



**BERGISCHE
UNIVERSITÄT
WUPPERTAL**

**Permittivity reconstruction and radio-propagation
simulations to guide sub-surface radar exploration
of ice moons and terrestrial glaciers for
the Enceladus Explorer project**

A thesis submitted in fulfilment of the requirements for the
degree of Doctor of Science (Dr. rer. nat.)

Alexander Luke Kyriacou

Department of Physics,
Faculty of Mathematical and Natural Sciences,
University of Wuppertal

Primary supervisor:
Prof. Dr. Klaus Helbing

Co-referee
Prof. Dr. Anna Nelles

2023

Acknowledgements

It has been a phenomenal five years as a doctoral student and researcher in Germany. Doctoral research is challenging enough, but I also had to adjust to a new country, a different language, and living away from my home for the first time. As the saying goes: It takes a village to raise a child. There are many people I need to thank, without them this thesis would not exist.

First, I extend my gratitude to my supervisor Prof. Dr. Klaus Helbing, whose guidance and support were invaluable throughout this work. Then I must acknowledge my friend and colleague in the EnEx-AsGAR project in Wuppertal, Dr. Pia Friend. From welcoming me to the city of Wuppertal, helping shape my project, providing great feedback, and being a crucial collaborator, I would not be here without her.

I also need to thank my project partners in the EnEx-AsGAR project (described in chapter 3): Michael Stelzig at the University Erlangen-Nuremberg and Andreas Benedikter at the DLR-HR at Oberpfaffenhoffen. Their expertise in the field of radar allowed them to teach me a lot and it was a privilege to collaborate with them. I owe much to another collaborator in the project, Uwe Naumann, who taught me many valuable things about RF electronics and helped to design the radar system described in this project. I would also acknowledge my friend, colleague and office mate Fabian Becker, from the closely related DLR project: TRIPLE-FRS. Special thanks to Gianluca Boccarella, who worked as a student helper in EnEx-AsGAR through his bachelor and master thesis. I must also thank my friend and colleague Frederik Lauber, who provided important insights into my work, particularly the aspects hardware, and was an effective assistant for part of the project.

Enceladus Explorer is an initiative of the Deutsche Luft-und-Raumfahrtzentrum (DLR) space administration, funded by the Bundesministerium für Wirtschaft und Klimaschutz (BMWK). I would like to thank the chief of the Explorer Initiative: Oliver Funke of DLR. I also thank my colleagues from RWTH Aachen for the TRIPLE project: Jan Audehm and Mia Giang Do, who were a vital part of the second field test as operators of the melting probes, as well as Simon Zierke, who worked in both EnEx and TRIPLE and operated melting probes in the first field test.

A special mention should go to my friend and colleague, Prof. Steven Prohira at the University of Kansas. He helped introduce me to the Parabolic Wave Equation method for simulating radio waves in ice. Over the last two years, he has given my valuable feedback on my work and I thank him for it.

The computations in chapter 5 were carried out on the PLEIADES cluster at the University of Wuppertal, which was supported by the Deutsche Forschungsgemeinschaft (DFG) and the Bundesministerium für Bildung und Forschung (BMBF).

My life here was brightened up by sharing my working space with some wonderful office mates over the years; Ruth Hoffmann, Stephanie Hickford, Sarah Pieper, as well as the aforementioned Pia, Fabian and Gianluca. I thank my colleagues Anna Pollmann, Timo Stuerwald, Enrico Ellinger and Norman Haussmann, who provided me with useful feedback in group meetings. Moreover, I made many friends in the astro-particle group, including but not limited to Frederik Lauber, Eric Mayotte, Vivek Patel, Ioana-Alexandra Caracas, Karl-Heinz Becker, Sonja Mayotte, Leonel Morejon-Hernandez, Jannis Pawolwsky, Shivani Ramachandran, Therese Paulsen, Joerg Foertsch, and others.

I would also thank my friends here in Germany outside of the group; Marlene Robles Useche, Kristinko Blazun, Gokhan Rizaoglu, Isil Kalpkirmaz, Kinda Nassredinne, Sweta Patel-Contractor

and David Kobernick.

And last but certainly not least, I must extend my deepest gratitude to my family and friends in Australia, who though separated by an ocean and two continents and eight and a half time zones, were always there to support me. I thank my mother Alison, my father Steve, and my sister Stephanie.

Declaration of Originality

I, Alexander Luke Kyriacou, do certify that the work presented in this thesis is my own work, conducted under the guidance of my supervisor Prof. Dr. Klaus Helbing. This thesis does not contain any content that has been plagiarized, copied, or borrowed without prior acknowledgment.

I affirm that I have provided appropriate citations and references for all my sources, including but not limited to articles, websites, theses, abstracts, and other published works. The research, analysis, and composition have been conducted solely by me unless otherwise stated and acknowledged.

Contents

1	Introduction	3
1.1	Modelling Radio Propagation in Ice	4
1.2	In-situ measurement of ice permittivity	4
2	Enceladus: A home for extraterrestrial life?	7
2.1	Observational History	7
2.2	Orbital Characteristics	9
2.3	Geology	10
2.3.1	Internal Structure	10
2.3.2	Origin and Geological History	10
2.4	Surface Features	11
2.5	South Polar Terrain	12
2.5.1	Tiger Stripes and Geysers	12
2.5.2	Plumes	13
2.6	Astrobiological Potential	16
2.7	Future Exploration	17
3	Enceladus Explorer - AsGAR	19
3.1	Enceladus Explorer (EnEx)	19
3.1.1	Mission Outline	19
3.2	Mission Architecture	21
3.2.1	Combined Spacecraft	21
3.2.2	Orbiter	22
3.2.3	Lander	22
3.2.4	IceMole	22
3.3	Field Tests	22
3.4	Sub-projects	23
3.5	EnEx-AsGAR	24
3.5.1	Radar Exploration	24
3.5.2	Permittivity Reconstruction	25
3.6	Summary	27
4	Radar Simulations with Parabolic Equation Methods	29
4.1	Introduction	29
4.2	Modelling Electromagnetic Waves in Ice	29
4.2.1	Finite Difference Time Domain	30
4.2.2	Ray Tracing	30
4.3	Parabolic Equations	31
4.3.1	Numerical Spatial Solution in Frequency Domain	33
4.3.2	Time Domain Solution	35
4.3.3	Backwards Propagation	37
4.4	Example of two-way PE simulation	38

4.5	Simulations through Glaciers with data-defined profiles	39
4.5.1	Examples of Glaciers	39
4.5.2	Frequency Domain	39
4.5.3	Time Domain	41
4.6	Limitations and Potential Improvements to PE Methods	44
5	Inversion of PE Simulations using Genetic Algorithms	49
5.1	Genetic Algorithms	49
5.1.1	Examples of GAs	50
5.1.2	GA Procedure	50
5.2	GA-based Inversion of paraProp	52
5.2.1	Misfit and Fitness Function	52
5.2.2	Initialization	53
5.2.3	Genetic Operators	56
5.2.4	Selection	58
5.3	Testing with Pseudo-Data	59
5.3.1	Signal Settings and Antenna Positions	59
5.3.2	Ref-Index Scenarios	61
5.3.3	RF Simulation Setup	61
5.3.4	GA Settings	62
5.3.5	Results	63
5.4	Discussion	68
5.4.1	Limitations of Inversion	70
5.4.2	Limitations of GAs	71
6	Cross-Borehole Permittivity Radar	73
6.1	Modulation Technique	73
6.1.1	Frequency Modulated Continuous Wave (FMCW) Radar	73
6.2	Design	77
6.2.1	Layout	78
6.2.2	Electronics	78
6.2.3	Antenna	83
6.2.4	Control: Permittivity Measurement Mode	85
6.2.5	Transmitter: TX	85
6.2.6	Receiver: RX	86
6.3	Measurement Procedure	86
6.3.1	Data Acquisition	86
6.3.2	Processing	86
6.4	Testing of Permittivity Radar	87
6.4.1	PLL Tests	87
6.4.2	Antenna Tests	90
6.4.3	In-Air Antenna Transmission Tests	90
6.5	Summary of System	92
6.5.1	Experimental Uncertainties	92
7	Field Campaign at the Aletsch Glacier	97
7.1	Goals of the Field Test	97
7.2	Location and Timeline	98
7.2.1	Aletsch Glacier	98
7.2.2	Site Plan	100
7.3	Cross-Borehole Measurements	100
7.3.1	Parallel Depth Profiles	102

7.3.2	Cross Depth Profiles	106
7.4	Permittivity estimation via Peak Analysis Method	107
7.4.1	Results: Permittivity Profile	109
7.5	Attenuation Measurement	111
7.6	Summary	113
8	Analysis of Field Test Data	115
8.1	Glacier Modelling	115
8.2	Comparison of Field Test with RT and PE Simulations	117
8.2.1	RT Simulation	118
8.2.2	PE Simulation	119
8.2.3	Simulation Results	119
8.3	Reconstruction of the Refractive Index profile with PEs	120
8.3.1	Simulating the transmitted signal	122
8.3.2	Settings	124
8.3.3	Results	125
8.3.4	Discussion	128
8.3.5	Summary of GA reconstruction	128
9	Conclusions	129
9.1	Summary of Results	129
9.1.1	Simulating radio-wave propagation through ice	129
9.1.2	In-situ measurements of ice permittivity	130
9.2	Future Work	131
9.2.1	Parabolic Equation Simulations	131
9.2.2	Inversion of PE and RT simulations	132
9.2.3	Permittivity Radar	132
9.2.4	Use of Permittivity Radar in Field Tests	133
	Appendices	141
A	Dielectric Properties of Ice	143
A.1	Permittivity: Theory	143
A.1.1	Atomic Model	144
A.1.2	Debye Model	144
B	Formation of Glacial Firn	145
B.1	Densification	145
B.1.1	Densification Models	146
B.1.2	Melting and Refreezing	147
C	The Permittivity Profile of the Tiger Stripe Region	149
C.1	Ice Deposition on a Global Scale	149
C.1.1	Geysers deposition modeling	149
C.1.2	Results for Deposition	151
C.1.3	Sintered snow layer	152
C.2	Ice Deposition on a Local Scale	154
C.3	Permittivity Profile	156
C.3.1	Layering	156
C.3.2	Chemical Composition	157
C.4	Discussion	158
C.5	Conclusions	158

D	Field Test 1	161
D.1	Field Test 1: Mittelbergerferner	161
D.1.1	Results	162
E	Comparison of PEs to FDTD	165
F	Non-Flat Surface Simulations with paraProp	169
F.1	Non-flat Surfaces	169
F.2	Example: Brueggen glacier	169

List of Figures

2.1	Enceladus plumes imaged by Cassini	8
2.2	Saturnian system	9
2.3	Enceladus interior structure.	11
2.4	South Polar Terrain ice crust	12
2.5	Map of Enceladus Plumes	14
2.6	Mass spectra of plume ice grains	15
2.7	Subsurface plume venting	15
2.8	Map of the ice grain deposition rate on Enceladus	16
3.1	Technical drawings of the Enceladus Explorer combined spacecraft	20
3.2	EnEx-IceMole concept drawing (3.2b and the illustration of the APS concept (3.2a)	23
3.3	EnEx-IceMole in Antarctic Field Test 2013	24
3.4	The three primary phases of the radar imaging during the EnEx mission	25
3.5	Permittivity measurement concept using passive reference targets	26
3.6	The FAU and BUW permittivity reconstruction concepts	27
4.1	The RF power at the South Pole, modelled using parabolic equations (PEs).	34
4.2	Time domain simulation with PEs.	35
4.3	A parallel depth B-Scan simulated with PEs	37
4.4	A two-way PE simulation of the RF amplitude transmitted through the South Pole firn, with three different ‘reflectors’: an aquifer, crevasse, and meteor.	40
4.5	A two-way PE simulation in time-domain, showing a reflection of a pulse off an aquifer.	41
4.6	Refractive index profiles of multiple terrestrial glaciers.	42
4.7	Horizontal RF propagation at the South Pole and Guliya ice caps.	43
4.8	The PE simulated RF power as a function of range for multiple glaciers.	44
4.9	A comparison between a received 400 MHz bandwidth Gaussian pulse from a TX at $z_{tx} = 11$ m to a RX at $z_{rx} = z_{tx} =$ m over a range of $R = 42$ m through the South Pole and Guliya ice caps.	45
4.10	Parallel depth B-Scans show for South Pole and Guliya ice caps.	46
5.1	An example of Genetic Algorithms: the simulation of an optimal bicone-antenna for neutrino detection in the GENETIS project [70].	51
5.2	Workflow of refractive index reconstruction with GAs	53
5.3	Examples of glacier refractive index profiles used to initialize the GA-based reconstruction	55
5.4	Examples of interpolated glaciers $n(z)$ profiles.	57
5.5	Genetic operators used to modify $n(z)$ models.	58
5.6	The TX time domain signal and spectrum used in the GA reconstruction.	60
5.7	The positions of transmitters and receivers used in the 2022 Aletsch Glacier field campaign, used to define the TX, RX configuration in the example of GA reconstruction in this chapter.	60

5.8	The profiles used to define the ‘pseudo-data’ for the Guliya glacier and the Brueggen glacier.	61
5.9	The evolution of the GA fitness score for the reconstruction of Brueggen.	64
5.10	Brueggen refractive-Index $n(z)$ reconstruction.	64
5.11	The Parallel Depth B-Scans of the Brueggen Glacier simulation.	66
5.12	Brueggen: signal envelope ratio.	66
5.13	Examples of A-Scans from different TX and RX combinations for the Pseudo-Data (black), best result of first generation (red), and best overall result (blue).	67
5.14	Guliya fitness score evolution.	67
5.15	Guliya refractive index evolution.	68
5.16	Guliya parallel depth B-Scans	69
5.17	Guliya: envelope ratio parallel depth B-Scan. Left: the envelope ratio for the best result from generation 0, Right: the best overall result.	69
5.18	Guliya A-Scans	70
5.19	Comparing the fitness score of the simulated signals and the refractive index profiles.	71
6.1	A concept for measuring the time-of-flight between a transmitting antenna, the EnEx melting probe, and near-surface receivers.	74
6.2	Illustration of permittivity radar setup.	74
6.3	FMCW method explained.	76
6.4	Example FMCW Fourier spectrum.	77
6.5	Technical layout of the permittivity radar.	78
6.6	Photograph of permittivity radar setup.	79
6.7	An simplified technical layout of a PLL-based frequency synthesizer.	80
6.8	A layout of a Phase Frequency Detector (PFD) component of a PLL circuit.	81
6.9	Photograph of frequency synthesizer board.	81
6.10	A photograph of a Mixer board.	83
6.11	Photos of wide-band cage antennas	84
6.12	The standing wave ratio of cage antennas used in permittivity radar setup.	84
6.13	The transmitter TX tube	85
6.14	A spectrogram of the frequency synthesizer RF output.	88
6.15	A diagram of the self-mixer test of the PLL board	88
6.16	Result of PLL self-mixing test.	89
6.17	Impulse Response function (IR) of the cage antenna.	91
6.18	Example of permittivity radar data acquisition.	93
6.19	Measured time of flight of permittivity radar using an air-air test with a separation of 9.8 m.	94
6.20	Range Test: the transmitter and receiver are placed on wagons and separated by increasing distances from 5 to 25 m.	94
6.21	Uncertainty of the measured time of flight for different central frequencies.	95
7.1	Map of the Aletsch glacier with a scale of ~ 20 km \times ~ 20 km, with a satellite photo and ice thickness map.	99
7.2	Map of the Jungfrauoch with a scale of ~ 1 km \times ~ 1 km, with a satellite photo and ice thickness map.	101
7.3	A bird’s eye view photograph of the Jungfrauoch test-site.	101
7.4	Photograph of TX and RX deployed at Field Test.	102
7.5	Layout cross-section cross-borehole permittivity measurements at field test.	103
7.6	Examples of FFT time-of-flight profiles, measured between TX and RX at a range of $R = 25$ m.	104
7.7	Parallel Depth B-Scan, for boreholes L1 and L2, $R = 25$ m, using $f_{base} = 1.7$ GHz and a bandwidth $B = 200$ MHz, with intervals of $\Delta z = 0.5$ m.	105

7.8	The propagation time and power of ‘maximum’ peak and ‘first’ arriving peak in the waveforms recorded between L1 and L2	105
7.9	Parallel Depth B-Scan, for boreholes L1 and L3, $R = 42$ m, using $f_{base} = 1.3$ GHz and a bandwidth $B = 200$ MHz, with intervals of $\Delta z = 1$ m.	106
7.10	The propagation time and power of ‘maximum’ peak and ‘first’ arriving peak in the waveforms recorded between L1 and L3.	107
7.11	Cross Borehole B-Scan for L1-L3, with a fixed transmitter depth $Z_{tx} = 14.0$ m. .	108
7.12	The ‘first’ and ‘maximum’ peaks selected from the L1-L3 cross depth B-Scan . .	109
7.13	Cross Depth B-Scan for L1-L2, with a fixed receiver depth $Z_{RX} = 0$ m and a variable transmitter depth.	110
7.14	The time of flight of the peaks selected in the L1-L2 cross borehole radar (left), with the power shown on the right.	110
7.15	The estimated permittivity profile ϵ'_r , estimated using the ‘first’ and ‘maximum’ peak method.	111
7.16	The derived attenuation profile of the Jungfraufirn.	112
7.17	The attenuation rate $\alpha(z = 12 \text{ m}, f)$ at $z = 12$ m, as function of frequency f	112
8.1	Density evolution of Aletsch Glacier as predicted by Herron-Langwey model. . .	116
8.2	Comparison between estimated permittivity profiles from Field Test data and prediction by Herron-Langwey model.	117
8.3	Refractive index of Aletsch Glacier, estimated from first peak method, shown with the positions of TX and RX used in cross-depth measurements.	118
8.4	Comparison of RT and PE simulations using $n(z)$ profile found from first-peak method.	120
8.5	Time of flights of cross-borehole measurements at Field Test, compared with predictions from Ray Tracing and Parabolic Equations.	121
8.6	Time of flight residuals between cross-borehole measurements at Field Test and predictions from Ray Tracing and Parabolic Equations.	122
8.7	The simulation chain used to replicate the Field Test data, utilizing the PE simulation method.	123
8.8	The modeled TX signal from the permittivity radar used in the GA reconstruction.124	
8.9	Evolution of the fitness score for the fitting of the GA based inversion to the field test data.	125
8.10	The best fit refractive index $n(z)$ profile from the field test data using the GA based inversion method.	126
8.11	A comparison between a FMCW waveform measured at the field test and the paraProp simulation found from the best-fit refractive index from GA reconstruction.127	
B.1	The densification processes of dry snow and firn from snow settings to the formation of glacial ice.	146
C.1	The modeled ice particle velocity distribution at the geyser for ice particles with radii from $r_{grain} = 0.5 \mu\text{m}$ to $r_{grain} = 15 \mu\text{m}$	150
C.2	The ice grain eruption rate from a geyser located at ‘D2’.	150
C.3	A map of the accumulative ice deposition above the South Polar Terrain (SPT) over 100 kyr.	152
C.4	Illustration of sintering process.	153
C.5	Time of sinter neck evolution given different surface temperatures on ice bodies in the solar system.	153
C.6	A topographical cross-section of Damascus Sulcus at the location of Geyser 389, with surface temperature of different points indicated with coloured dots.	154
C.7	Trajectory of ice particle from Geyser 372 in Enceladus gravitational field.	155

C.8	The simulated depth of the ice particles subtracted from the surface topography.	156
C.9	An illustration of a geyser plume eruption from a vent within Damascus Sulcus. .	157
D.1	The Mittelbergferner test site.	161
D.2	Deployment of the reference targets at the Mittelbergferner	162
D.4	Reflection spectra at Mittelbergferner	163
E.1	The time of flight of a pulse in the old version of paraProp.	166
E.2	Comparison of RF amplitude between Meep and paraProp.	166
E.3	The phased velocity of the E-field $z = 9.9$ through South Pole firn layer predicted by paraProp and Meep.	168
E.4	A pulse shown with the correction of the Q operator	168
F.3	The gain of the RF emission for a ‘rough surface’ scenario for the Brueggen glacier relative to the ‘flat surface’ case.	172
F.4	The gain of the RF emission for a rough surface relative to a flat surface.	173

Chapter 1

Introduction

Saturn's moon Enceladus is a promising candidate for hosting extraterrestrial life[51]. Observations of plumes of water vapor and ice particles by the Cassini spacecraft have proven the existence of a global saltwater ocean beneath the surface[63]. These geysers originate from the fracturing of the ice crust at the south polar region induced by tidal forces and the filling of these cracks with water from the underlying ocean, forming aquifers around ~ 500 m to ~ 800 m beneath the surface (assuming the ice crust at the Enceladus south pole is between 5 km and 8 km) [78]. The fracturing of the ice above the aquifers leads to the observed cryovolcanism. A summary of the relevant geological properties of Enceladus is given in chapter 2. These aquifers represent a uniquely accessible target for future exploration of ice moons by an autonomous melting probe.

The Enceladus Explorer (EnEx) project aimed to construct an autonomous self-navigating melting probe to access analogous environments on Earth, such as the sub-glacial lakes in the Antarctic [43]. Successful demonstration of the probes on Earth would pave the way for developing a melting probe as a payload for a future lander mission to Enceladus (or similar ice moons). The EnEx project is described in chapter 3. Some prerequisites for successfully deploying such a probe on Enceladus include accurately identifying the depth and position of subsurface aquifers and the ability to land the spacecraft in a safe landing location within the melting probe's operating range. Crucially, the probe must safely traverse the ice along a path that avoids hazardous obstacles such as crevasses, dust belts, and meteorites.

Ice is a transparent medium to radio waves, with attenuation lengths L_α on the order of 0.8 km to 1.5 km in the Greenlandic and Antarctic ice sheets for the 100 MHz to 500 MHz range[6, 10, 13, 83]. This suggests the use of ice-exploring radar as a means to achieve the goals of the EnEx project. Successfully characterizing the position and shape of targets and hazards in ice requires a reliable model of the intervening ice properties, chiefly a profile of the dielectric constant or permittivity ϵ_r . The refractive index of the ice n can be calculated directly from the permittivity.

Therefore, some key goals of the EnEx project were to:

1. Develop methods to model or simulate the propagation of radio-wave through the Enceladus' ice environment from a transmitting source (TX) to a receiver (RX)
2. Develop an in-situ method to measure the permittivity of the ice.

Finding working solutions to satisfy these goals was the subject of the work described in this thesis.

1.1 Modelling Radio Propagation in Ice

Reconstruction of the position of the water pocket beneath the surface of Enceladus will depend on accurately modeling radio propagation through these layers, where the permittivity will be in-homogeneous concerning depth and lateral distance. This work uses a parabolic equation (PE) method to model radio-wave propagation through different ice environments. PE methods yield approximate solutions to Maxwell’s equations in contrast to a full-field solution from finite-different time domain (FDTD) methods, with the benefit of being far more computationally efficient. At the same time, the PE approximation yields a more complete radio transmission model than ray tracing (RT) methods, accounting for frequency-dependent and range-dependent wave properties such as interference. PE methods permit simulation of continuous wave and pulsed emission through data-defined depth and range-dependent refractive index profiles on a km-scale, accounting for realistic features such as surface roughness, crevasses, and refrozen-ice layers, and can also model back-scatter off objects in the ice. A description of the PE method and its implementation via the paraPropPython code [68], which was improved and updated in this work, is given in chapter 4.

Given the ability to simulate radio-propagation given a known ice permittivity, it is possible to define testable predictions of ice-penetrating radar data from a given permittivity profile. However, in real-world applications, one wishes to find the permittivity profile from in-ice radar data, requiring a *inversion* method. In this work, an inversion method was formulated to reconstruct the permittivity profile of the ice environment between transmitter(s) and receiver(s). This inversion method works by using paraPropPython to simulate the radar data using a large set or population of permittivity profile estimates, which are represented by a set of ‘genes’, and using a genetic algorithm (GA) to select for the best-fitting profiles and generating new profiles by combining features of different profiles and adding ‘mutations’. The GA evolves the population of permittivity profiles over multiple generations to yield improved estimates. In chapter 5, a test of this method is made by generating artificial data (‘pseudo-data’) using paraPropPython, and the GA inversion method can reconstruct the permittivity profile to a residual error of $\Delta\epsilon_r \leq 0.1$.

1.2 In-situ measurement of ice permittivity

A prototype bistatic radar system for measuring permittivity between prepared boreholes was developed during this work. The radar utilizes the frequency-modulated continuous wave (FMCW) method to measure the time delay between the signal transmission from an in-ice transmitter (TX) to an in-ice receiver (RX). The modulating involves the synthesis of a continuous wave signal with a frequency that increases linearly from a minimum frequency f_{min} to a maximum frequency f_{max} over a defined time interval, known as the modulation time T_{mod} . The propagation time is estimated by multiplying the received signal with an equivalent signal generated by a local oscillator within the receiver. Due to the continuous frequency ramp, the time delay between these two signals will result in an instantaneous frequency offset between the two signals, which can be observed in the Fourier transform of the multiplication signal. In the case of multi-path propagation caused by in-ice reflections, the Fourier spectrum will have multiple peaks corresponding to different signal propagation times. The FMCW system designed in this work was able to transmit between frequencies of 800 MHz to 2200 MHz and can measure the direct propagation time of a signal in the air to a precision $\Delta t \leq 5$ ns. This time resolution results in a nominal permittivity reconstruction $\Delta\epsilon_r \leq 0.14$ for a horizontal distance separating TX and RX of $R = 20$ m, assuming the correct identification of the direct traveling signal. An overview design and testing of this cross-borehole radar is given in chapter 6.

This cross-borehole radar was tested in a field campaign on the Aletsch Glacier of the Swiss

Alps in the spring of 2022 and was used to measure the complex permittivity of the upper 15 m of the glacial firn. This is described in chapter 7. Finally, a preliminary analysis of the data obtained from the Aletsch glacier field test, utilizing the GA-based inversion of PE simulations, is given in chapter 8. A summary of the important findings of this work is given in chapter 9.

There are five appendices following the conclusion. Appendix A summarizes the theoretical aspects of dielectric permittivity. A description of glacial firn densification processes is given in Appendix B. A theoretical study of the possible ice properties on the surface of Enceladus, based on modeling the deposition of ice grains on the surface, was given in Appendix C. A discussion of a preliminary field test for the EnEx-AsGAR project is given in Appendix D. A comparison study between the PE simulation code paraProp and a finite different time domain (FDTD) code MEEP is shown in Appendix E, in which the accuracy of the PE methods is verified against the more established FDTD method. Finally, an example of RF propagation through a non-flat surface topography is shown in Appendix F.

Chapter 2

Enceladus: A home for extraterrestrial life?

Among the many planetary bodies of this solar system, Saturn's moon Enceladus is considered one of the most promising candidate to host extraterrestrial life[51]. Enceladus is the smallest planetary object in the solar system, with a diameter of 504.2 km, which is geologically active. More than 200 geysers were identified at its south pole by Cassini-Huygens spacecraft throughout its 13-year-long exploration of the Saturnian system [63]. These erupt water in the form of vapor and ice particles. These plumes are ultimately sourced from a global saltwater ocean that separates Enceladus' ice crust from a porous rocky core[66].

The presence of such an ocean, along with the presence of organic molecules (which were also detected in the plumes[65]), and the availability of energy to drive metabolism would make Enceladus a world that would be habitable for a range of Earth microorganisms. The energy source may be chemical interactions at the ocean floor or oceanic volcanism. This chapter provides an overview of Enceladus' geology, geological activity, and surface features, emphasizing the south-polar terrain (SPT). The characteristics of the plumes, including their chemical composition and distribution over the surface, are also described. The south polar terrain is a region of prime scientific interest. It is thus a target for proposed future space missions such as the Enceladus Explorer project discussed in chapter 3. An analysis to determine the dielectric properties of its surface is summarized in appendix C.

2.1 Observational History

Enceladus was discovered on the night of the 28th of August 1789 by the German-born British astronomer William Herschel, using a 12 m long, 1.2 m aperture reflective telescope, the largest in the world at the time. Even with the most powerful telescopes of the age, Enceladus was difficult to observe owing to its faint apparent magnitude ($M_V = 11.7$) and its proximity to Saturn and its rings [25]. Apart from its orbital characteristics and estimates of its mass, density, and albedo, little else was known about Enceladus for the next two centuries. Evidence for a diffuse and extensive outer ring of ice particles overlapping with the orbit of Enceladus was first observed by astronomers in 1907, with definitive identification of a ring occurring in 1966, later being designated the 'E-ring'[25]. The first detailed observations of Enceladus' surface and the E-ring came with the Voyager 2 flyby in 1981, revealing a geologically young surface devoid of impact craters. The measured sputtering rate from the Voyager 2 plasma detector showed that the lifetime of an ice particle in the E-ring was approximately 100 years, which meant that its existence required a replenishing source of ice particles, most likely from Enceladus itself [25].

A giant leap in the knowledge of this world came with the arrival of the ESA/NASA robotic

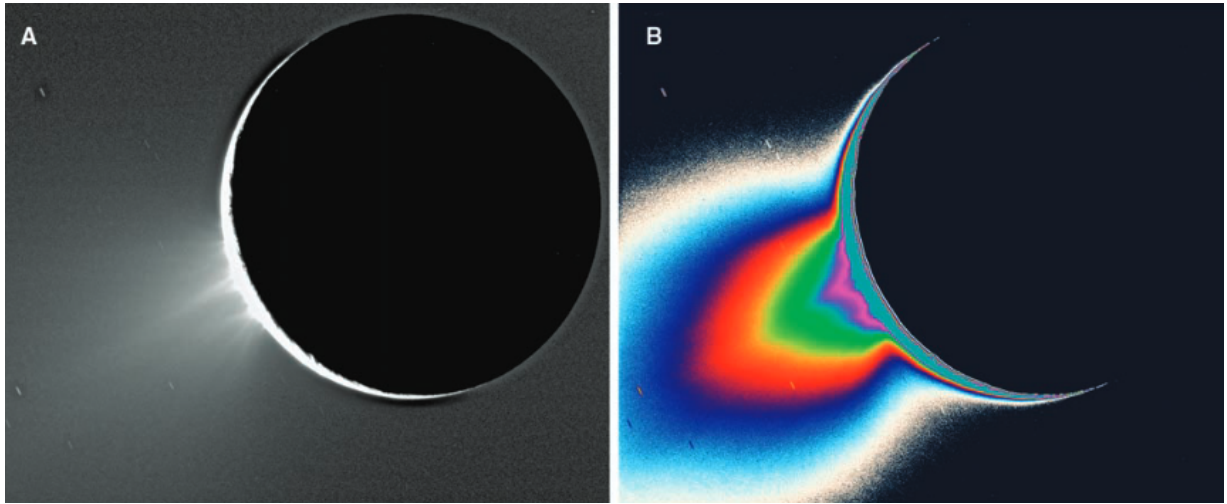


Figure 2.1: A high phase-angle image by Cassini’s ISS (taken on 27.11.2005) of the plumes visible by scattered light. Image A shows the clear-filter image, where the plumes can be resolved into individual jets. Image B is a color-coded version of Image A, where fainter parts of the plume are made visible. Images are taken from Fig. 6 in Porco et al. 2006 [63].

probe Cassini-Huygens into orbit around Saturn, beginning a 13-year exploration of the planet, its rings, and system of moons[25]. Between 2005 and 2015, Cassini would make 23 dedicated flybys of Enceladus, designated E0 through to E22. Hints of a trace atmosphere of ions generated by an unknown process were found in perturbations in the Saturn magnetic field in flybys E0 and E1, with the second flyby showing the atmosphere was not symmetric but concentrated toward the southern hemisphere [25]. These findings prompted the Cassini science team to plan a closer flyby of Enceladus in July 2005[25].

This third flyby (E2) saw Cassini fly within 177 km ($0.7 R_E$) of the surface, where the magnetometer confirmed the presence of ionized water vapor[25]. The Ultraviolet Imaging Spectrograph (UVIS) observed occultations of background stars, which were used to confirm the existence, composition, and position of a plume of water vapor from Enceladus’ south polar region. Together, these observations proved the existence of active ‘cryovolcanism at Enceladus’ south pole and showed that these plumes were the source of Saturn’s E-ring. Subsequent images by the Imaging Science Subsystem (ISS) showed the terrain of the South Polar Region to be geologically young and active, with narrow tectonic fractures (the ‘tiger stripes’), high color and albedo contrasts, high relative temperatures, and surface of finely grained ice particles. An ISS image of plumes emanating from the south pole is shown in Fig. 2.1. The ISS also traced the origin of the plumes to jets emanating from sources within the tiger stripes, likely originating from saltwater reservoirs beneath the surface. Later analysis of ISS images confirmed the presence of microscopic ice particles [63].

This discovery marked Enceladus as a primary target of interest for the Cassini mission, with flybys E3 and E4 making even closer passes (47 km and 46 km altitude at closest approach, respectively) allowing for in situ sampling of plume particles and high-resolution imaging of the south polar terrain. Flyby E5 featured the closest-ever approach of Cassini to Enceladus at an altitude of 20 km. The sampling of the plumes using the Cosmic Dust Analyser (CDA) confirmed the presence of salt-rich ice particles, which proved the existence of a saltwater ocean separating the ice crust from a rocky core. The data obtained by Cassini’s instruments throughout the 23 flybys and more remote observation of Enceladus and the E-ring while in Saturnian orbit form the basis of our current understanding of Enceladus as a geologically active world. However, many fundamental questions about Enceladus, including its age and mode of formation, as well



Figure 2.2: The location of Enceladus within the Saturnian system, with the ring system and five of its ‘mid-sized’ moon neighbors (Credit: NASA/JPL).

as the possible existence of life, can only be answered by future space missions with more sensitive instruments than Cassini and a greater focus on Enceladus, including potential orbiters, landers or subsurface melting probes.

2.2 Orbital Characteristics

Enceladus orbits Saturn every 1.37 sidereal days in a slightly eccentric orbit (the eccentricity e of Enceladus is: $e = 0.0047$) at an average distance of 237948 km from the center of Saturn [1]. It is one of Saturn’s six ‘mid-sized’ satellites, which are in order of increasing distance from Saturn: Mimas, Enceladus, Tethys, Dione, Rhea, and Iapetus[3]. These worlds have diameters ranging from 400 km to 1500 km and are approximately spherical in shape[3]. Collectively, they comprise $\sim 4\%$ of the mass of all objects in orbit around Saturn, making them substantially smaller than Titan, Saturn’s largest moon, which accounts for 96 % of the mass[3], but substantially larger than all other Saturnian satellites and the rings which collectively comprise only 0.04 % of the system’s mass[27] with Saturn’s mass itself excluded. Except for Iapetus, the mid-sized satellites orbit between the main ring system and the orbit of Titan. A graphic showing the positions and sizes of the mid-sized Saturnian moon and the rings is given in Fig. 2.2. The moons are all comprised primarily of silicate rock and water ice. Except for Enceladus, they all have ancient surfaces dominated by impact craters [79], with surface ages approaching the age of the solar system ~ 4.5 Gyr. Alone amongst the mid-sized satellites, Enceladus is geologically active and internally differentiated[79] into a structure of Enceladus, which will be described in the following section.

Due to its relatively close distance to its host Enceladus is tidally locked with Saturn, with the same hemisphere always facing the planet[56]. It is also presently locked in a 2:1 orbital resonance with Dione, completing 2 orbits for every Dione orbit. The orbital resonance is a major driver of Enceladus’ geological activity via tidal heating [55, 56]. Its orbit is located at the peak density of Saturn’s E-ring, comprised of water vapor and ice particles from Enceladus’ geysers [77].

2.3 Geology

2.3.1 Internal Structure

The bulk density of Enceladus is measured to be $\rho_E = 1609 \pm 5 \text{ kg/m}^3$, which implies ice to silicate rock mass balance ratio of $\sim 60:40$ [59, 72]. As mentioned above, it is a differentiated body with a core composed of silicate (SiO_4) rock and metal with a radius of $\sim 190\text{-}200 \text{ km}$ and density of $\sim 2400 \text{ kg}$, overlaid by a water layer some $62\text{-}52 \text{ km}$ thick on average divided into an ocean of liquid water and an outer layer made of ice[72, 86]. The differentiation of Enceladus into these 3 layers, with the estimated densities and thicknesses, is shown in Fig. 2.3. The existence of an ocean can be inferred from the presence of salts, particularly sodium Na, in the plume particles, for which the most plausible explanation would be a body of liquid water in contact with porous silicate rock[66]. Initially, this ocean was hypothesized to be only a regional sea below the south polar terrain, as the 0.3 GW heat output of the core appeared to be unable to sustain a global ocean on geological time scales [79]. However, two lines of evidence indicate that the ocean is global in extent. First, Enceladus is found through gravitometric measurements to not be in hydrostatic equilibrium and would require isostatic compensation to account for the excesses in topography and variations in gravitational field[35]. The simplest explanation for this is an ocean that separates the ice crust from the core. Secondly, Enceladus undergoes libration in its orbit, a phenomenon that can be thought of as a ‘wobble’ of the rotational axis with respect to its orbital plane [35]. The measured libration $0.120^\circ \pm 0.014$ is too large to be consistent with an ice crust in contact with the core but is consistent with a global ocean. Indeed, the libration is consistent with an ocean with an average depth of between 26 km and 31 km deep, an ice crust with an average depth of between 25 km and 21 km thick and a core radius of 200 km [86]. However, the ice crust is not uniform in thickness across the moon but is estimated to vary from a maximum of $\sim 30 \text{ km}$ at the equator to between $\sim 6 \text{ km}$ and 8 km at its southern pole and $\sim 10 \text{ km}$ at its northern pole [40].

Recent analyses of the tidal and orbital evolution of Enceladus indicate that the equilibrium heating rate of Enceladus is sufficient to maintain an ocean over geological timescales ($\sim \text{Gyr}$), as long as the ice crust is conductive [56]. Inferring from the time between the formation of the Earth’s oceans $\sim 4.5 \text{ Gyr}$ and the earliest evidence of life (4.1 to 3.5 Gyr), the persistence of the Enceladus ocean for billions of years makes the existence of life more likely and plausible than the case of a recent formation of the ocean [51].

2.3.2 Origin and Geological History

Exactly how Enceladus formed and how old it is remains uncertain, although there are several hypotheses[52]. Enceladus must have formed from the accretion of a rotating co-planar disk of material around Saturn. The exact mechanism is unclear, as is the time when this occurred. Indeed, even a recent formation of Enceladus from an earlier ring or the debris of one or two mid-sized moons that underwent a collision has not been ruled out at the time of writing [53]. Most theories posit the formation of Enceladus with the other mid-sized moon at approximately the same time as the formation of Saturn[52]. The available evidence of the chemical composition of Enceladus and Saturn’s other icy moons, drawn from the chemical composition of Enceladus plumes and measurements of Titan’s atmosphere by Huygens, suggests that the building blocks of Enceladus have a common origin with some types of comets and carbonaceous asteroids[53]. These materials were drawn into orbit around proto-Saturn and appear to have formed Enceladus and the other moons without significant chemical interaction with the gas of the Saturnian nebula[53]. However, more chemical and isotopic data are needed to determine whether Enceladus is primordial or formed from an earlier ring or a catastrophic impact[53].

Also unclear is how Enceladus became differentiated and whether its global ocean is primordial or emerged recently. A planetary body of Enceladus’ size and density should quickly cool

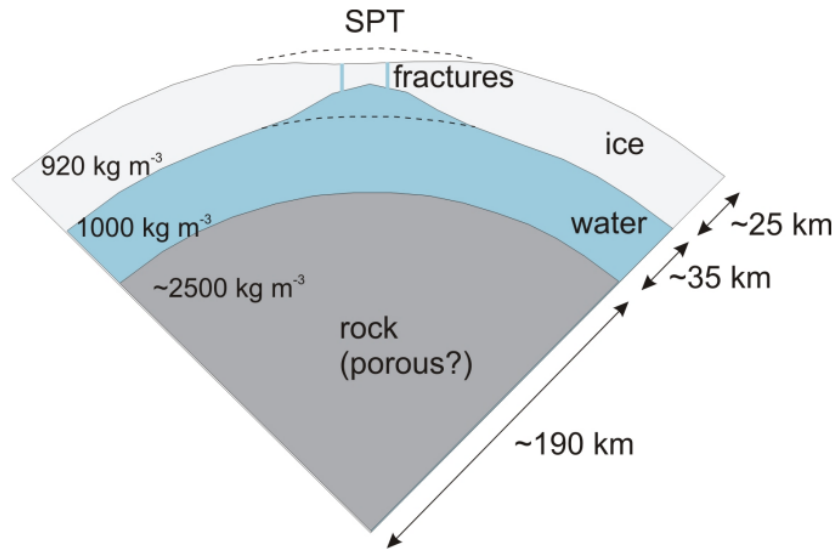


Figure 2.3: A cross-sectional profile of Enceladus' south polar terrain showing the relative sizes and densities of the three layers [56].

down and solidify internally before differentiation can occur without an additional heat source [56]. The early Saturnian nebula was rich with short-lived radionuclides, including Al^{26} and Fe^{60} , which would have produced enough heat to prevent the interior from freezing before differentiating [56].

2.4 Surface Features

Enceladus has the highest albedo $A = 0.81 \pm 0.04$ of any object in the solar system, reflecting so much sunlight that it has an average afternoon surface temperature of ~ 80 K and nightly temperatures of ~ 50 K at equatorial latitudes, the coldest surface temperature of any Saturnian satellite [33]. The high reflectivity of its surface is due to a ubiquitous layer of microscopic ice grains deposited on the surface from plume eruptions from geysers at the south-polar region [64]. The surface features of Enceladus are incredibly diverse, with substantial differences in crater count numbers, topography, temperature, and ice grain composition between different regions of Enceladus [59]. Enceladus surface can be roughly divided into three distinct regions: the south-polar, equatorial, and north-polar [59]. Due to Enceladus being tidally locked, one can define a Saturn-facing hemisphere, an anti-Saturn hemisphere, and may also define a leading hemisphere (the side that faces the direction of orbital motion) and a trailing hemisphere. There is a remarkable symmetry with respect to the direction of orbital motion and the direction of Saturn, with similar surface features being observed on the Saturn and anti-Saturn surfaces and similarities between the leading and trailing hemispheres.

The local surface age can be estimated from the size and density of superimposed impact craters and a model of impactor flux, a method which can be intuitively understood, as an older impact crater is more likely to have smaller impact craters inside it than a younger one, and larger impacts were more likely earlier in the solar system's history [24]. Aging a surface by crater counting is strongly dependent on the model of impactor flux and may be uncertain by a factor of 4 [42]. The oldest surfaces form a band from the Saturn-facing hemisphere, over the north pole to the anti-Saturn hemisphere, with a surface age between 1 to 4 billion years [42]. However, it is notable that most craters have been deformed by tectonic fracturing and are shallower than

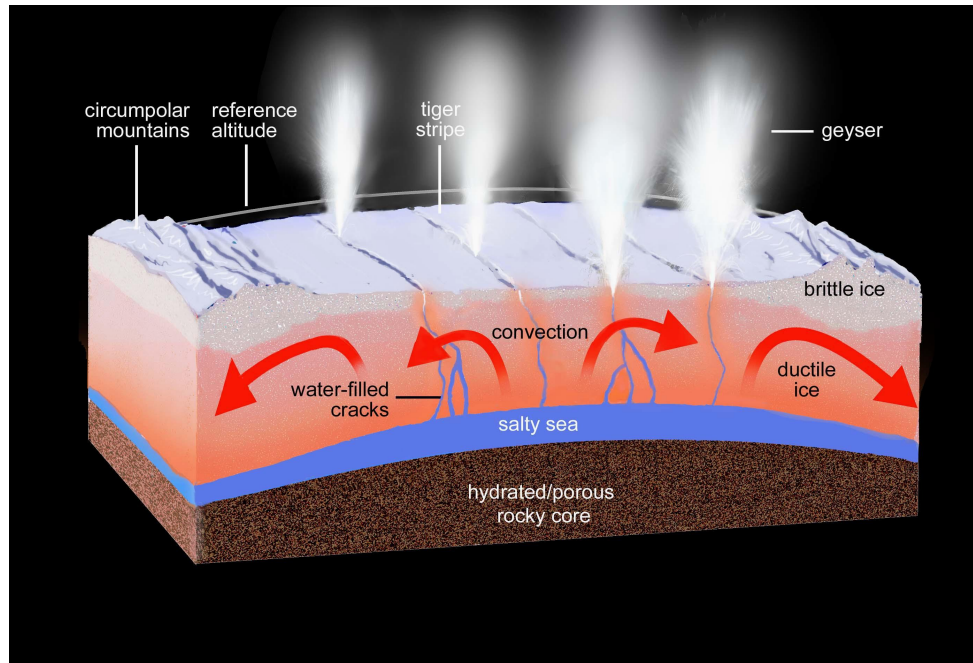


Figure 2.4: A cross-section of the South Polar Terrain ice crust, showing the convection of warmer and deeper ice and the fracturing of the ice from the ocean to the surface. (credit NASA/JPL <https://photojournal.jpl.nasa.gov/target/enceladus>)

expected, possibly due to infilling from geyser deposits[79].

The leading and trailing hemispheres of Enceladus are geologically younger at mid-latitudes than the Saturn and anti-Saturn hemispheres, with provinces ranging from 10 Myr to 2 Gyr in crater count estimated ages [42]. These regions show signs of tectonic activity, with crisscrossing sets of fractures and ridges with peaks and troughs up to 1 km in amplitude. Hills, isolated ridges, and fractures are also present in these regions [79]. The presence of these features is evidence that these provinces had ancient periods of geological activity, with high heat fluxes of around $200\text{--}270 \text{ mWm}^{-2}$, similar to the present-day heat flux at the south polar region[85]. This ancient period of activity could be explained by ‘polar wander’, a movement of the moon’s rotational axis over time[85].

2.5 South Polar Terrain

The south polar terrain (SPT) comprises the surface of Enceladus south of $\sim 55^\circ\text{S}$ latitude. The SPT is surrounded by south-facing scarps and ridge belts at 50° latitude. South of this latitude, the region is largely devoid of impact craters, with none larger than 1 km in diameter, indicating it to be the youngest region of Enceladus, with some surfaces as young as 500,000 years[63]. Despite being a polar region, SPT is the site of the warmest surface temperatures of Enceladus and is the host to the sources of the plumes and the four famous surface fractures known as ‘tiger stripes’ [79].

2.5.1 Tiger Stripes and Geysers

The tiger stripes, first imaged in detail by the Cassini ISS in 2005, are four approximately parallel fissures, known as ‘sulci’, on the SPT [63]. They were named; ‘Alexandria Sulcus’, ‘Baghdad Sulcus’, ‘Cairo Sulcus’ and ‘Damascus Sulcus’, after cities that appear in the tales of the classic *A Thousand and One Nights*[63]. They can be described as linear depressions on the surface

with depths of around 500 m, flanked by ridges ~ 100 m high and 2-4 km wide, with the peaks separated by ~ 2 km [79]. The sulci extend for an average distance of 130 km and are separated from each other by ~ 35 km intervals. In addition to their shape, the tiger stripes are distinguished by being covered in coarse-grained crystalline ice [64], in contrast to the fine grains that blanket the rest of Enceladus' surface. CO₂ ice, as well as simple organics, have been identified by VIMS [21]. The crystalline ice structure is evidence of recent resurfacing, as radiation directed by the Saturnian magnetic field would distort the crystal ice into an amorphous form [65]. The tiger stripes were also distinguished as the site of a thermal anomaly by observations of the CIRS instrument, with temperatures reaching peaks of 113 K to 180 K within the ridges [16]. The best current estimate of the radiated power of the region is 15 ± 3.1 GW [63].

The tiger stripes are the site of the most cryovolcanic activity on the moon's surface, with almost all of the jets emanating from within the tiger stripes [81]. A map showing the location of the identified geysers is shown in Fig. 2.8. The sources have been described as discrete geysers, erupting from specific coordinates on the surface with a specific inclination angle [65]. An alternative hypothesis is that the plumes are sourced as part of a common 'curtain eruption' similar to that seen in Iceland [80]. Throughout the observation period from Cassini, a cycle was observed in which the geyser ceases activity and then resumes activity after approximately 6 years [39]. A potential explanation for this phenomenon is the sealing of the vent of the plume with deposited material (from the geyser itself), which leads to a build-up of pressure from the warm water beneath, which leads to a later explosive eruption that restarts the plume [39].

2.5.2 Plumes

As previously mentioned, Cassini's discovery of active plumes from Enceladus' southern pole confirms the existence of a subsurface ocean. The plumes consist of three phases: gaseous, solid, and ionized. In all phases, water is by far the dominant component, but other species are present. The gaseous component of the plume was sampled by Cassini's Ion and Neutral Mass Spectrometer (INMS) during 5 flybys. The dominant component is H₂O with a volume mixing ratio of 0.9 ± 0.01 , followed by CO₂ (mixing ratio 0.053 ± 0.001), and several other species; CO, H₂, ⁴⁰Ar, N₂, CH₄, NH₃ and various simple organic molecules ranging in mass from 23 Da (Dalton or atomic mass unit) to 80 Da (see Fig. 2.6) [65]. The presence of ammonia NH₃ and argon ⁴⁰Ar was strong evidence that the plumes were sourced from a reservoir of liquid water (rather than sublimation of ice) [88]. The gaseous component erupts at speeds of ~ 700 ms⁻¹ with a mass ejection rate of $\dot{M} = 200$ kgs⁻¹. As Enceladus' escape velocity is 239 ms⁻¹, this mass is permanently lost to the object and enters orbit around Saturn. One can observe that this mass loss rate would imply that Enceladus has lost approximately ~ 30 % of its original mass if it is ~ 4 Gyr and has been continuously active at its present rate for this entire time, although it is not certain that the former is true nor is their evidence to believe the latter. The ice grains erupt at a wide range of velocities depending on their mass, and overall, around 10% escape the body while the remaining fall back to the surface as a form of 'snow'. A map showing the estimated surface deposition rate (made in a previous work [65]) of this geyser can be shown in Fig. 2.8. The implications of this 'snow layer' for future space missions to Enceladus, particularly for radar exploration, are considered in an analysis outlined in Chapter C.

The solid phase of the plume consists of microscopic ice particles or 'ice grains', ranging in size from 0.5 μ m up to 500 μ m. The mass spectra of different ice grains were measured by Cassini's CDA and can be seen in Fig. 2.6. The spectra show that the species of the impurities were various salts, predominantly Na-based and smaller amounts of K, and organic molecules. Plume ice grains can be classified into three types [65]:

- Type I: Salt-poor particles $\text{Na}/\text{H}_2\text{O} < 10^{-3}$

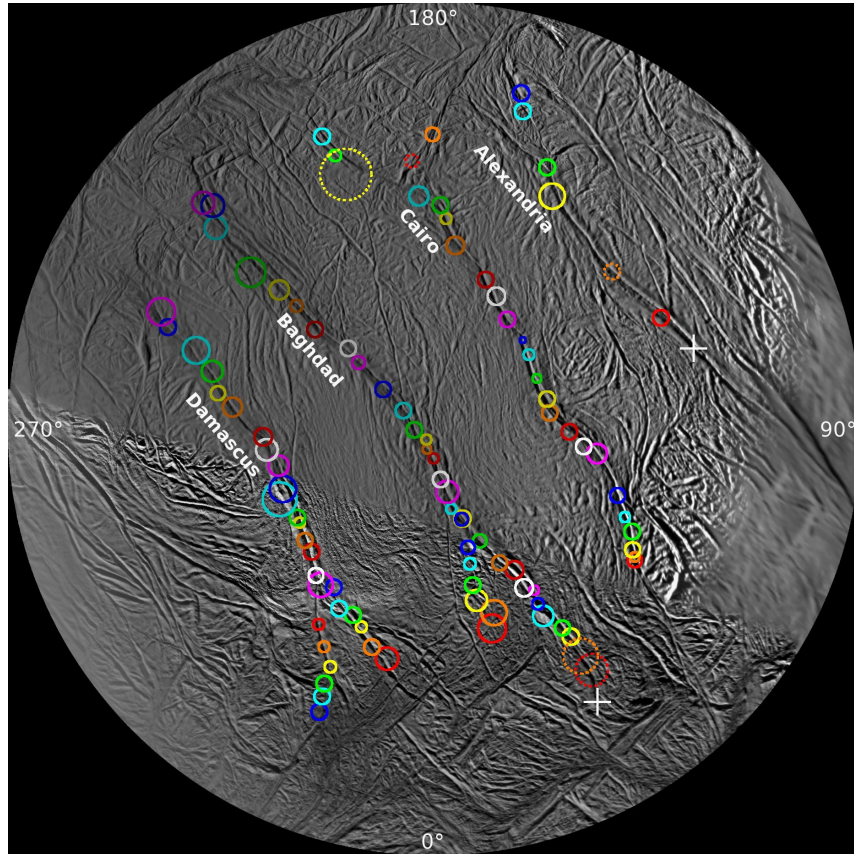


Figure 2.5: Map of Enceladus plume sources, with the circles radius corresponding to the 2σ uncertainty and the center corresponding to the most likely position [60] (for interpretation of the references to color in this figure, the reader is referred to the web version of [60]).

- Type II: Organics rich particles
- Type II: Salt-rich particles $\text{Na}/\text{H}_2\text{O} > 10^{-3}$

The differences between Type III and Type I particles are hypothesized to be due to different formation mechanisms; Type III are rapidly frozen droplets of water from the reservoir, hence have a higher salinity, while Type I and Type II are probably formed from sputtering of the ice within the vent of the geyser. The different formation mechanisms are illustrated in Fig. 2.7. There is also evidence that Type III particles are more massive than Type I and II particles, as Cassini detected an increasing relative abundance of Type III particles as it approached the densest part of the plume and observed a decrease as it flew out of the plume during flyby E5. The same phenomenon was again observed in flyby E17[65].

The suspected mechanism for the geysers is described by the ‘cold geyser model’: the source of the geysers are water-filled cracks in the ice crust, where the water evaporates upon contact with the vacuum. Tidal forces acting on Enceladus result in heating and fracturing of the ice at the south polar region, allowing water to flow upward from the ocean to near-surface aquifers. An illustration of the structure of the ice crust in the south-polar region is shown in Fig. 2.4. [78] showed that from simple buoyancy arguments, Enceladus’ time-averaged water table depth is approximately 10% of the ice crust depth. The south-polar region features the thinnest ice, with estimates ranging from 5 km to 8 km ([40]) depth, implying that the aquifer-vacuum interfaces are approximately $\sim 500 - 800$ m below the surface.

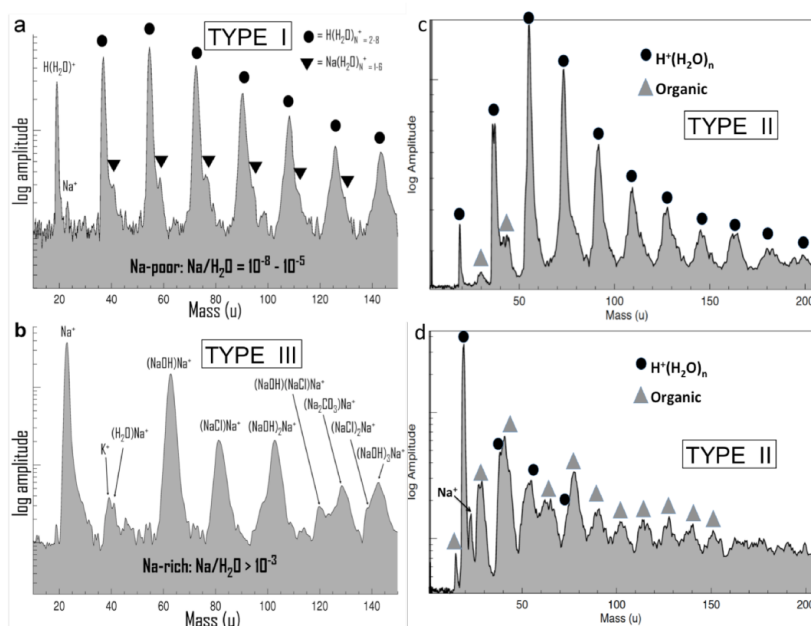


Figure 2.6: Four examples of mass spectra of the ice grains in the plumes measured by Cassini Cosmic Dust Analyser (CDA) [65]. The spectra plots show the frequency of the species in the spectra (described as ‘log amplitude’), and the species mass is indicated on the x-axis in the standard atomic unit u . A ‘salt poor’ Type I grain is shown in the top right plot (a), a ‘salt rich’ particle is shown in in the bottom left (b), and two ‘organics rich’ spectra are shown in the upper right (c) and lower right (d) plots respectively.

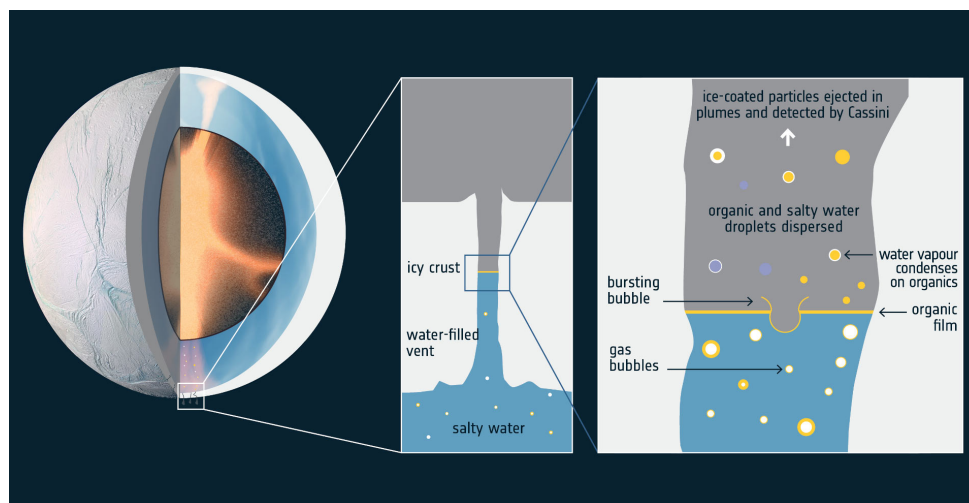


Figure 2.7: Gas bubbles from underlying ocean ascend through fissures in the ice to the water surface, transporting organic molecules. The organics concentrate in a layer at the surface. When the bubbles burst, they form aerosols made of concentrated organic material that then nucleates the formation of Type-II ice grains. At the same time, salt-water droplets are detached from the main water body, flash freezing and forming the salt-rich Type III grains. This illustration is taken from the ESA website https://www.esa.int/ESA_Multimedia/Images/2018/06/Hydrothermal_activity_in_Enceladus_core_and_the_rise_of_organic-rich_bubbles and was adapted from a figure in [67]

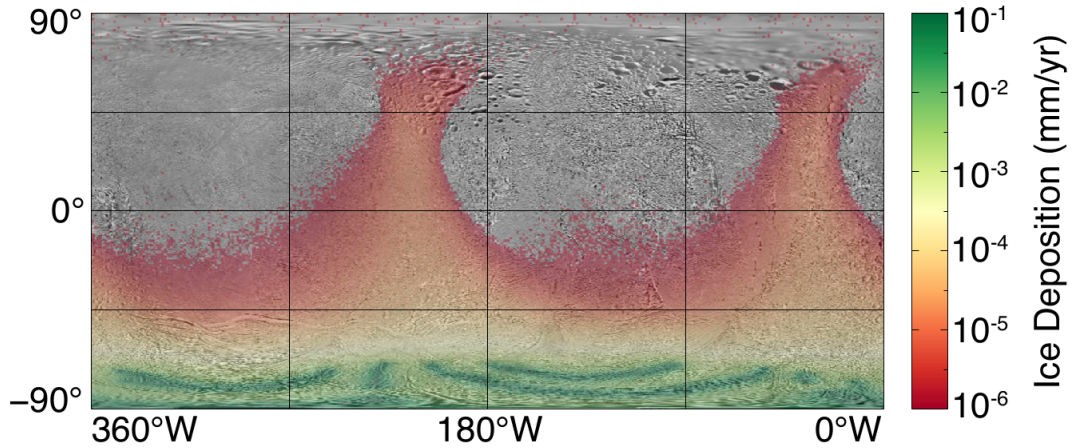


Figure 2.8: A map of the Enceladus surface in Mercator projection, with the modeled deposition rate of ice particles integrated across radii $0.5\mu\text{m}$ to $50\mu\text{m}$ displayed on the color scale in units of mm/yr [75]

2.6 Astrobiological Potential

The available evidence of the conditions of Enceladus' ocean indicates that it is habitable for known Earth microbes. All of the major elements necessary for the construction of known biomolecules (C, H, N, O, P, S) have been detected in one of the plume phases or are very likely to be present due to the chemical interactions between the core and the ocean[51]. Measurements from Cassini's CDA also indicate the presence of relatively massive organic molecules. The pH of the ocean is estimated to be between 8.5 and 10. The salt content of the ice grains in the plumes and the salinity of the E ring of the Enceladus ocean is around 0.5 % to 2 % (mostly NaCl), a suitable level for Earth lifeforms[51]. Moreover, the detection of nanometer-scale silica particles detected in the E-ring and possibly in plume measurements suggest the existence of hydrothermal vents on the ocean floor in which the water is in contact with the core at temperatures of at least $\sim 100^\circ\text{C}$. Thus, Enceladus currently meets all of the 'three requirements' for habitability: water, a source of energy, and the presence of biogenic elements[51].

However, *habitable* does not necessarily mean *inhabited*. Abiogenesis, the chemical process that lead to the origin of life on Earth, remains one of the great mysteries of science. Finding the mechanism for the development of life is a daunting task, as the event(s) must have occurred at least 3.5 Gyr ago. There are three predominant hypotheses for the origin of life on Earth:

1. **Black smokers:** Life originated in hydrothermal vents on the ocean floor.
2. **Primordial soup:** Life originated in tidal pools on land, requiring periods of wetting and drying to concentrate the relevant biomolecules.
3. **Panspermia:** Life originated somewhere else in the solar system and was carried to Earth through meteorites. However, this alone does not explain the mechanism by which life began.

Which, if any, of these mechanisms produces life is highly relevant as only the 'black smoker' mechanism seems feasible on Enceladus since tidal pools could not have existed on Enceladus at any time and the Saturn system seems too remote for Panspermia to be viable either. An additional uncertainty is over what fraction of Enceladus' existence has its ocean existed. On Earth, the earliest disputed evidence of life was dated to ~ 4.1 Gyr before present [14], and the oldest known fossils of microorganisms were dated to ~ 3.7 Gyr before present[57], leaving a gap

of ~ 0.4 Gyr to 0.8 Gyr between the Earth's formation and the earliest evidence of terrestrial life at the time of writing. A recent formation of Enceladus, or of its ocean, would make life less likely to exist there. However, many models permit a primordial and long-lived ocean on Enceladus. It is also possible that the time gap between Earth's formation and abiogenesis was shorter than current evidence suggests, and the time gap may not be typical of the development of life in general[51]. In this author's opinion, although one can not state with confidence that a search for life on Enceladus will yield a positive result, even a negative result would have significant implications for the abundance, or lack thereof, of life in the universe. On the other hand, a positive result would provide biologists with a 'second data point' concerning life's development. Such ice-shell worlds can exist outside of the so-called 'habitable zone' of stars or even as rogue planets unbound to any star. Thus, if Enceladus is found to both be inhabited and the site of independent abiogenesis, ice shell worlds similar to Enceladus could be the most common ecosystems in the universe.

2.7 Future Exploration

Under NASA's 'planetary protection protocol', a requirement to eliminate the risk of contaminating pristine extraterrestrial environments with Earth microbes, Cassini was de-orbited on September 15th, 2017, burning up and vaporizing in Saturn's atmosphere. Future space missions to the Saturnian system in general and Enceladus in particular have been proposed. Even a mission not dedicated to astrobiology may yield answers to important questions such as the lifetime of the Enceladus ocean[25]. The subsurface vents are a relatively accessible target for future space missions and permit scientific exploration of Enceladus' ocean without the need to traverse several km of ice. The most straightforward follow-up mission will be a close flyby of the SPT to sample the plumes with more sophisticated chemical and biological sensors than Cassini or perhaps preserve a sample for a return flight to Earth[49].

An estimate of the likely biological yield of a sampled ice grain can be made using the 'Lost City' field of hydrothermal vents located in the mid-Atlantic ridge as an analog environment[48]. By scaling measured microbe concentrations by the ratio of the geothermal energy flux of Enceladus ~ 0.1 W/m² to that of Lost City, Enceladus could have microbial concentrations in hydrothermal vents of $\sim 10^5$ cells/mL. The dilution as the water column rises from the ocean floor to the surface would reduce this concentration so that a flyby or orbiting probe flying through the plume in its 'average state' at 50 km altitude would sample ~ 1 cells per flyby with a 0.04 m² sample plate, a level insufficient to confidently detect the microbe with any current detection method[62]. In such a case, a flyby would be limited to searching for the presence of biomolecules. Some likely signatures would be the presence of complex amino acids, the ratio between left- and right-handed chiral molecules, and the ratio of different carbon isotopes[49]. However, it is also possible that bubbles rising from the vents could 'scrub' a column of organic molecules and microbe. Such 'bubble scrubbing' has been observed on Earth and can increase local microbial concentration by orders of magnitude. If present on the ocean floor of Enceladus, bubble scrubbing could increase the microbial sample of a flyby probe to 10^2 to 10^3 microbes per pass[62]. A lander within close proximity to the tiger stripes could continuously sample falling geyser 'snow', collecting $\sim 10^5$ cells over a 100 Enceladus day period (138 Earth days), although this could increase to $> 10^7$ with bubble scrubbing[62].

However, a more reliable in situ life test would be to directly sample a body of liquid water, either the Enceladus ocean or an aquifer sourced from the ocean. This would allow examination of the water before bio-signatures can be damaged or destroyed by the processes of evaporation or freezing at the water-vacuum interface, cold temperatures, and exposure to cosmic rays, gamma rays, and UV light in outer space. As previously mentioned, geyser-feeding aquifers may exist as

close as 500 m to the surface and are certainly less than 5 km below the surface[38]. A steerable and autonomous drilling or melting probe or ‘cryobot’ deployed from the surface may be able to perform in situ tests for microbial life. Prototypes of such probes have been developed by NASA, ESA, and DLR (German Aerospace Center)[49]. The latter mission proposal is the ‘Enceladus Explorer’ project, which is the main subject of this thesis. The next chapter’s subjects are the design, development, and anticipated challenges of such a mission.

Chapter 3

Enceladus Explorer - AsGAR

3.1 Enceladus Explorer (EnEx)

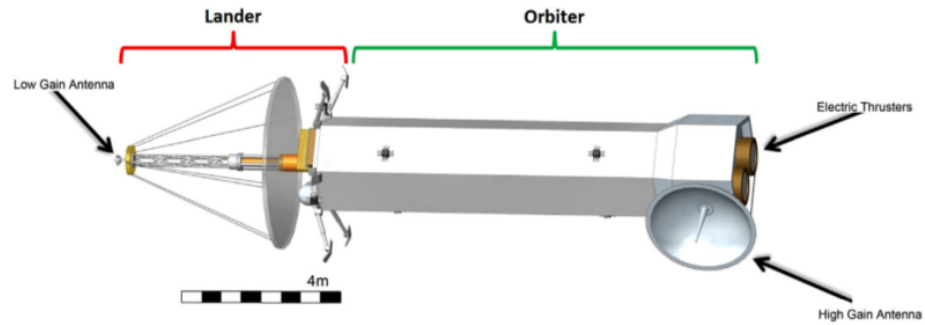
Since 2012, the ‘Enceladus Explorer’ (EnEx) project, an initiative of the DLR Space Administration, has investigated necessary technologies for a future space mission to explore the subsurface of Enceladus. The goal of the project is to develop a semi-autonomous, self-navigating and steerable melting probe (known in the original proposal as ‘IceMole’), delivered as part of a payload on a lander mission to Enceladus, which can burrow through a few hundred m of ice and arrive at an aquifer, where it will take water samples which are then analyzed in-situ for the presence of microbes [43]. The primary challenges of such a mission include:

1. Continuous and precise measurement of the melting probe’s attitude and position.
2. Location of an aquifer to provide a target for the melting probe.
3. Mapping and imaging of the subsurface ice within the working area of the probe allows for the optimization of the trajectory and, crucially, the avoidance of hazards such as buried meteorites, crevasses, and salt belts.

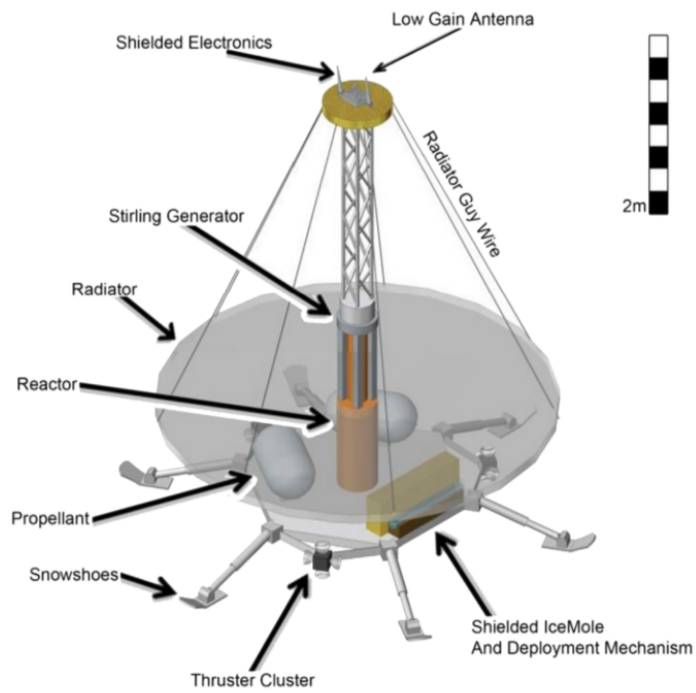
From 2012 to 2015, a consortium of several German universities led by Aachen University for Applied Sciences (FH Aachen) developed the mission concept, design, and working prototypes for IceMole. IceMole is delivered to the surface as a lander payload and connected with a tether. The tether serves the dual purpose of providing power sourced from a radio-isotope thermal generator (RTG) to operate IceMole and to provide data relay and communication between IceMole and the lander. Its length must be at least as long as the likely path trajectory.

3.1.1 Mission Outline

A preliminary probe design and mission plan was outlined in 2015 by Konstanidis et al. [44]. IceMole would be delivered as a payload of an EnEx Lander probe, which would itself be carried on the EnEx orbiter ‘bus’ probe. The total payload mass of the combined spacecraft is estimated to be 5533.2 kg (including 5866.0 kg of Xenon propellant fuel for maneuver). The dimensions of the craft are designed to be housed within the fairing of an Ariane V rocket ($5.4 \times 17m^2$). The proposed flight plan calls for a launch on an interplanetary trajectory, followed by two Earth gravitational assist maneuvers 1 and 3 years after launch respectively. The resulting momentum boosts allow the probe to acquire sufficient velocity to reach Saturn within 14.55 years of the launch date [44]. After insertion into orbit around Saturn, a 2.85-year ‘moon tour’ would commence where the EnEx combined probe would perform flybys of Enceladus and other moons, utilizing the time to take close radar scans of the south polar terrain at inclined angles, allowing the identification of a suitable target aquifer and a safe landing location (more on this in section 3.5.1). The next stage is insertion into orbit around Enceladus. Finding a stable



(a) The preliminary design of the combined EnEx spacecraft, before Lander separation



(b) A drawing of the Lander, with the IceMole as payload

Figure 3.1: Technical drawings of the Enceladus Explorer combined spacecraft (a), and the lander (b) [44].

polar orbit ideal for paths above the south polar region is complicated by Saturn’s strong 3rd body effect. Solutions were found for a maximum inclination orbit of 61° and altitude of 200 km, permitting a stable orbit for longer than 15 years [15]. The probe will initiate landing and deployment following the orbital insertion phase and the safe landing site selection. This is the subject of section 3.5.1.

3.2 Mission Architecture

This section summarizes the proposed EnEx mission as outlined in the mission concept paper [44]. The reader is cautioned that EnEx is best thought of as a concept study, a proposal for a funded EnEx space mission has not been made, and a full technical description is not yet possible and may deviate from that outlined in the concept paper [44].

3.2.1 Combined Spacecraft

The EnEx mission goal would be delivering the melting probe to the surface of Enceladus. The IceMole would be delivered to Enceladus onboard a ‘combined spacecraft’ (shown in Fig. 3.1a), which will travel to the Saturnian system as a single spacecraft before separating into an orbiter and lander. The orbiter section hosts the propulsion module and high gain antenna (HGA) used for communication with Earth. Following the separation of the orbiter and lander, communication from the IceMole to the Earth will be relayed between the lander and IceMole via tether and between the lander and orbiter by a low gain antenna (LGA) housed on the lander, with the orbiter broadcasting to and receiving signals from the Earth using the HGA.

The combined spacecraft’s power plant would be housed on board the lander and work on the principle of converting heat from radioactive sources into electrical power. Radioisotope power sources utilize ^{238}Pu to generate heat. Stirling converters, such as the Advance Stirling Radioisotope Generator (ASRG), then convert this heat into electricity, with a maximum specific power of 9 W/kg for ^{238}Pu . However, the low production rate of plutonium at the time of the paper’s writing (~ 1 kg/yr in 2015) led the author to suggest using ^{241}Am as an alternative, yielding perhaps 4 W/kg, although there would need to be development of ASRG technology to allow utilization of ^{241}Am . In lieu of further technological development, the study’s authors propose a simpler system, the Multi-Mission Radioisotope Thermoelectric Generator (MMRTG). This would give the EnEx combined spacecraft a maximum plausible power budget of ~ 2 kWe (kW-electric) [44]. The orbiter would require an independent power supply of at least 3 MMRTGs to allow for operation following the lander’s separation, adding complexity to the design. 3 MMRTGs would give the orbiter an end-of-life (EOL) power of 300 W after 15 years[44].

Several propulsion systems were considered, including all-chemical propulsion, all-electric propulsion, and combined electric and chemical propulsion. Chemical propulsion achieves thrust through the combustion of a chemical fuel and expulsion of the product exhaust gas. Electrical propulsion would involve the acceleration of ions using an electrical potential and the expulsion of the ions as an exhaust. Electrical propulsion would be powered from a small fission reactor housed onboard. Electrical propulsion would offer a higher specific impulse (I_{sp}) but lower thrust, which would necessitate a fly-by of the spacecraft to achieve the acceleration needed for a trajectory that intercepts the Saturnian system[44]. An additional option would be electric or chemical propulsion with an ‘aerocapture’ maneuver, which would involve a close fly-by of Saturn’s moon Titan, which would pass through its atmosphere at high altitude and utilize atmospheric drag to alter the spacecraft’s trajectory to enter into orbit around Saturn[44]. The all-electrical propulsion option was considered optimal as it would minimize launch mass, achieve high I_{sp} , and be able to achieve flight times within a reasonable time frame (on the order of a decade). Moreover, a nuclear reactor would be needed, in any case, to achieve the

power needed to melt the ice efficiently. Aerocapture was rejected, and it was deemed to be a high operational risk. It would complicate the mission by requiring a close fly-by of Titan, as Enceladus lacks a substantial atmosphere[44].

3.2.2 Orbiter

As seen in Fig. 3.1a, the orbiter has a hexagonal primary structure with a length of 8.7 m, with the lander attached to one end, allowing maximum separation of the nuclear reactor from the bulk of the orbiter and the electric thrusters on the opposite end. The orbiter would host a suite of three remote sensing instruments, including a reconnaissance camera (RC), ice-penetrating radar (IPR), and a thermal mapper. As of the time of writing, the design and implementation of these instruments have not been outlined in detail, but Konstanidis et al. make references to earlier missions, such as the Mars Reconnaissance Orbiter (MRO) SHARAD as a possible baseline[44]. Communication with Earth is made through a 3 m diameter HGA similar to that used by the Cassini orbiter. Based on the performance of Cassini, the orbiter could transmit 4 GB within 9 hours, translating to a data transmission rate of 130kbps.

3.2.3 Lander

The preliminary configuration of the EnEx lander is based on the Mars Cryobot Mission concept[44] with a diagram shown in Fig. 3.1b. At the time of writing, the lander design features a reactor and Stirling generator in the center, with a large disk acting as a radiator of heat and shielding for the lower body of the lander, the IceMole, and the IceMole deployment mechanism. A mast is connected to the Stirling generator. It extends perpendicular to the radiator disk, with a low gain antenna (LGA) fixed atop the mast, which is connected to the ends of the disk with radiator guy-wires. Six lander legs are attached to the bottom of the lander, with snow shoes attached to the ends to allow the spacecraft to land on a snowy surface. A crucial consideration in the lander design is the need to deal with the radiation produced by the reactor during the interplanetary flight phase. At the same time, the water ice on Enceladus will act as a strong attenuator of neutrons. As of the time of writing, the radiation shielding concept has not been defined, and the authors anticipated that ~ 500 kg of payload would need to be allocated towards shielding alone. The lander would also host a suite of instruments, including a site imagine system (SIS), a ground penetrating radar (GPR), a magnetometer, and acoustic pingers.

3.2.4 IceMole

IceMole was built as a 2 m long rectangular tube weighing 60 kg with a 15 cm x 15 cm cross-section with a metallic melting head with an ice screw motor to enable steering possible [43] as well as side-heaters to help prevent the probe from becoming frozen in place. For navigation, IceMole was equipped with an inertial measurement unit (IMU) and a pair of magnetometers for attitude measurement. The melting head was integrated with an ultrasonic phased array, which allowed the identification of targets and obstacles through echo-location [43]. An overview drawing of EnEx-IceMole, including all integrated subsystems, is shown in Fig. 3.2b. Navigation and localization are facilitated through a concept called the ‘Acoustic Positioning System’ (APS)[26]. Under APS an array of acoustic transducers at the surface, deployed from the land, transmit ultrasonic signals through the ice to allow for the positioning of IceMole via triangulation [26]. An illustration of APS is given in Fig. 3.2a.

3.3 Field Tests

Several field tests of various IceMole prototypes were conducted at the Swiss Monteratsch and Icelandic Hofsjökull glaciers which successfully demonstrated the maneuverability of the melting

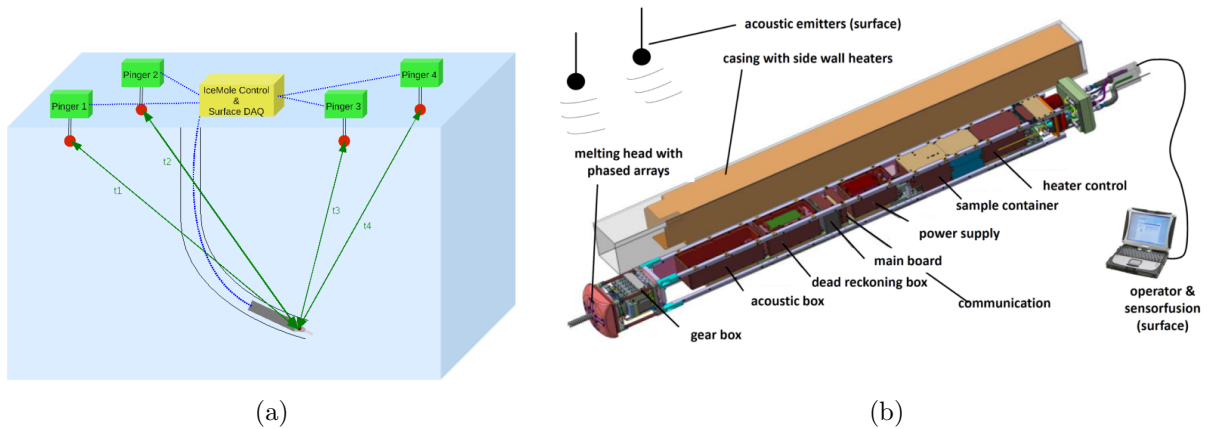


Figure 3.2: An illustration of the Acoustic Position System (APS) concept (3.2a) showing four acoustic transmitter or ‘pinger units deployed on the surface, connected to a central control and DAQ system, with signals propagating to the IceMole. A technical drawing of the EnEx-IceMole (3.2b), showing the various contained systems.

probe and demonstrated the navigation and forward mapping systems. A key finding from these field tests was the demonstration of the APS to resolve the location of the IceMole to an uncertainty of ≈ 1 m but the limitation of the APS range due to attenuation lengths of less than 50 m in glacial firn [34]. This finding highlighted the need for the APS and acoustic sounding systems to be complemented by radar systems, which would have attenuation lengths in ice at least an order of magnitude greater. The final integration of the melting probe, EnEx-IceMole, with all systems integrated, was deployed at the Canada glacier in Antarctica in November-December 2013 and Blood-Falls at the terminus of the McMurdo ‘Dry Valleys in Antarctica. The deployment of the IceMole on the latter field test is shown in Fig. 3.3.

3.4 Sub-projects

Since 2015 several sub-projects within EnEx have worked at improving existing subsystems of EnEx, adding new subsystems and using laboratory and field tests and simulations to optimize the mission concept. These subprojects include:

- EnEx-AsGAR*: Development of a radar mapping and imaging system to identify subsurface aquifers and crevasses - University of Wuppertal (BUW), University of Erlangen-Nuremberg (FAU) and DLR-HR (DLR-High Frequency) (October 2017 - April 2022). This project will be described in greater detail later in this chapter.
- EnEx-RANGE: Further Development of Acoustic localization and reconnaissance system around an array of transducers - RWTH Aachen (February 2015 - Autumn 2018).
- EnEx-CAUSE: Sensor fusion - University of Bremen (April 2015 - September 2018).
- EnEx-NavEn: Development of Inertial Measurement Unit - Bundeswehr University of Munich (UniBW) (August 2015 - July 2017).
- EnEx-Eislabohr: Development of a laser to bore through surface ice to analyze the ice composition - Technical University of Dresden.
- EnEx-nExT: Optimization of IceMole melting process under Enceladus conditions, namely testing melting process in a vacuum - FH Aachen (June 2015 - May 2019).

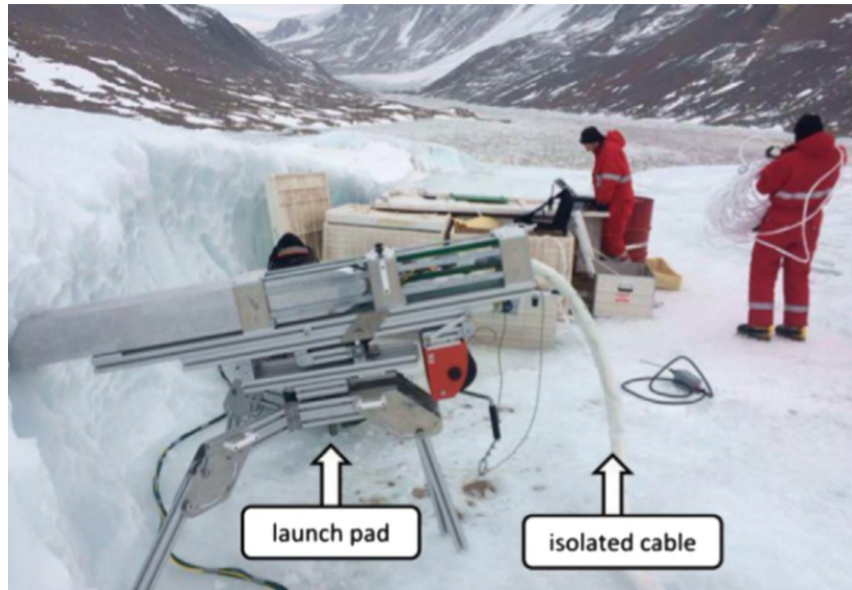


Figure 3.3: Field Testing of the IceMole by FH Aachen at the Canada glacier, Antarctica, November-December 2013

- EnEx-DiMice: Directional Melting in Ice - RWTH Aachen (August 2015 - March 2018).
- EnEx-MIE: Development of magnetometer to calculate the attitude of IceMole using Saturn's magnetic field - Technical University of Braunschweig.
- EnEx-WISE: Optimization of the melting process of IceMole using simulations and models of ice crust and development of conductivity sensors - RWTH Aachen.

3.5 EnEx-AsGAR

3.5.1 Radar Exploration

The mapping of the surface is envisioned to occur in three phases (shown in Fig. 3.4):

1. Radar-based coarse detection and mapping of surface structures and sub-glacial structures from orbit
2. Enhanced structural resolution & imaging of deeper structures in the landing area during descent
3. Detailed detection of the ice region and in particular ice crevasses after landing in the environment below the landing position

Phase 1 would provide the crucial input on deciding on a landing location, which must be at a safe distance to an active geyser while being close enough to an aquifer to be placed within range of the melting probe. In addition, detailed measurement of the surface topology and texture and identification of surface hazards (such as ice boulders) are also critical to the mission's success. Phase 2 will allow for the refinement of the subsurface mapping that will provide input for the planned trajectory of the melting probe. Phase 3 would further enhance the resolution of subsurface mapping, and in this phase, in-situ permittivity measurement will be performed to allow radar calibration.

Each of the phases will exploit the synthetic aperture radar (SAR) technique, in which a moving radar transceiver antenna samples data from several points in space. When applied to a static

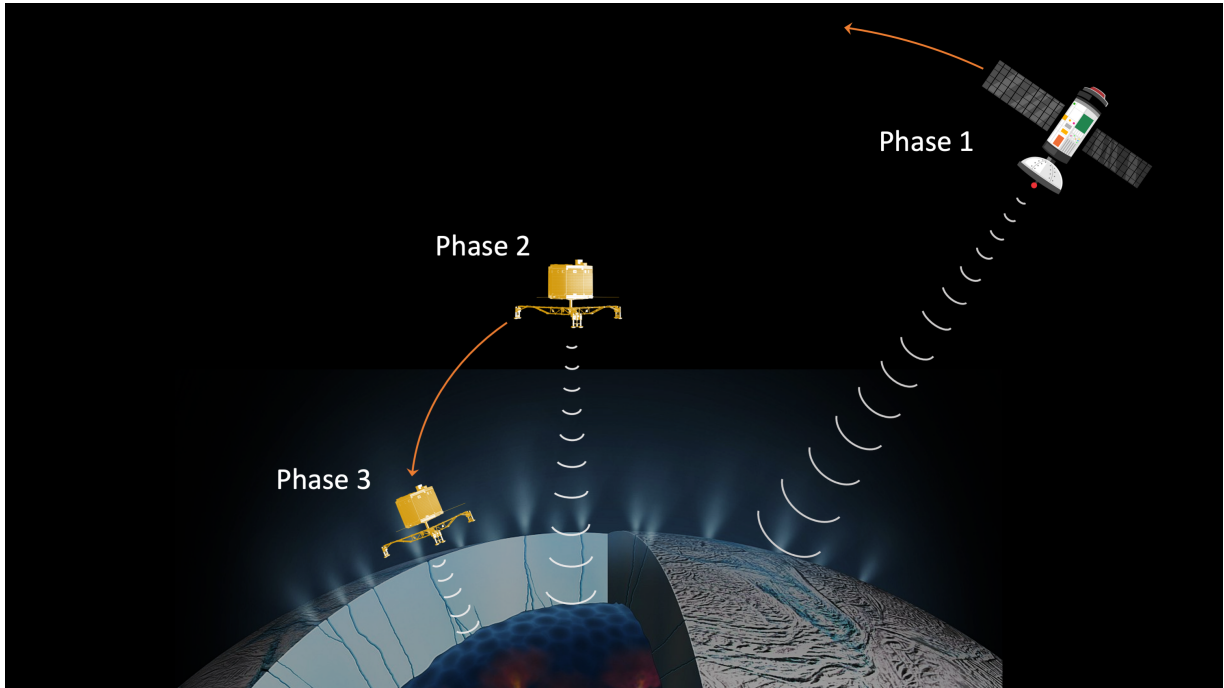


Figure 3.4: The three primary phases of the radar imaging during the EnEx mission

target (such as the subsurface structure of Enceladus), this multi-point sampling simulates radar transmission from an array of many different antennas. Multiple frequency ranges for the radar are envisioned, as the attenuation rate for radio waves is directly proportional to the frequency, and the range uncertainty is inversely proportional to the bandwidth of the radar, with larger operating bandwidths requiring higher base frequencies.

3.5.2 Permittivity Reconstruction

To produce the desired radar calibration, the three-dimensional permittivity profile $\epsilon_r(x, y, z)$ of the intervening ice between the surface and the nearest aquifer needs to be well constrained via in situ measurements. The concept of permittivity measurement is based on the calculation of the travel time one way or two ways t between two points (P_1 & P_2) with known positions in space.

$$t(P_1 \rightarrow P_2) = \frac{1}{c} \int_{P_1}^{P_2} n(x, y, z) dl = \frac{1}{c} \int_{P_1}^{P_2} \sqrt{\epsilon_r(x, y, z)} dl \quad (3.1)$$

The best method for solving the underlying permittivity distribution depends on the complexity of the permittivity distribution in space, as well as its dependence on temperature and frequency, as well as a reliable signal analysis technique. In a simple scenario of a layered medium (i.e., a flat environment with vacuum, lower density snow and ice) and an assumption that the wave-like properties of the signal can be neglected, i.e., the ray-tracing approximation whereby the wave frequency is assumed to be infinite ($f \rightarrow \infty$), then one may rely on Fermat's principle and Snell's law to solve the permittivity. For more complex spatial distributions of permittivity and continued applicability of the ray-tracing approximation, the distribution is obtained through numerical solutions of the *eikonal equation* (see equation 3.2), with various methods existing, including Forward Marching Method and inversion of ray-tracing simulations.

$$|\nabla t(x, y, z)|^2 = \frac{\epsilon_r(x, y, z)}{c^2} \quad (3.2)$$

However, there exist cases where the wave-like properties cannot be ignored and therefore the ray-tracing approximation is invalid. In these cases, a solution relies on inversion of wave-

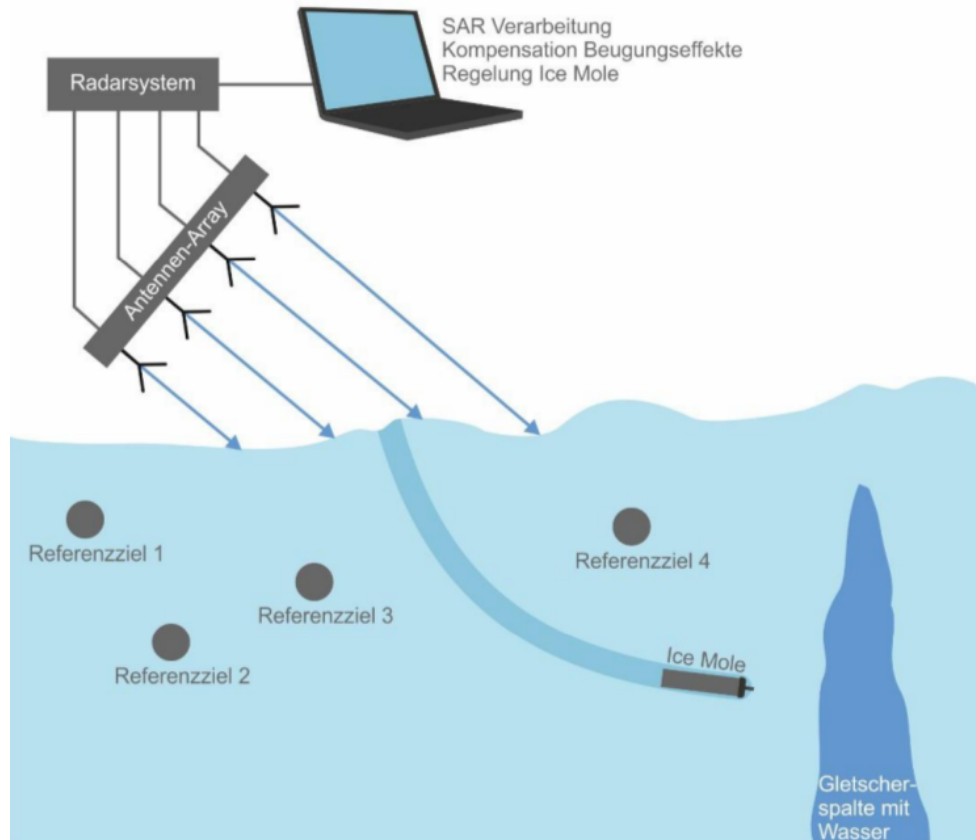


Figure 3.5: Permittivity measurement concept using passive reference targets. In this depiction, the Synthetic Aperture Radar (SAR), is approximated as a stationary array of antennas (*Antennen-Array*). A series of reference targets (shown in text as *Referenzziel*) with known positions are deployed within the ice and reflect the transmitted signal to the antennas, hence providing a basis for reconstruction. With the reconstruction of ice permittivity, identification of the water pockets (*Gletscherspalte mit Wasser*) is facilitated. In practice, this was found to be impractical, as the RCS of the reference-targets was insufficient to be detected (discussed in Appendix D).

equation-based simulations, such as the Parabolic Wave Equation method or Finite Domain Time-Difference method. In the course of the project, numerous algorithms were developed that allowed for the solution of the permittivity.

In addition to devising reconstruction algorithms, an implementable measurement technique needed to be developed. The original proposal described the concept of delivering *self-melting reference targets*, simplified melting probes that only need to move vertically and downward. These reference targets would have a known range and depth relative to the EnEx lander and act as a passive reflector with a known Radar Cross Section (RCS), as depicted in Fig. 3.5. The back-scatter of the orbiter radar signals off these targets could then be used to provide a signal to reconstruct the permittivity. However it was found over the course of the project that this method was impractical, as the RCS of these reflectors is too low to produce a signal observable above radar clutter. FAU and BUW both developed permittivity measurement concepts that rely on bistatic radar (see Fig. 3.6). FAU developed an active transponder that receives and re-transmits signals sent from the orbiter (figure 3.6a). BUW developed an in-ice cross-borehole permittivity radar concept, in which a transmitter (TX) and one or more receivers (RX) are embedded within the ice, and the transmitted signal is picked up at multiple points by the receivers

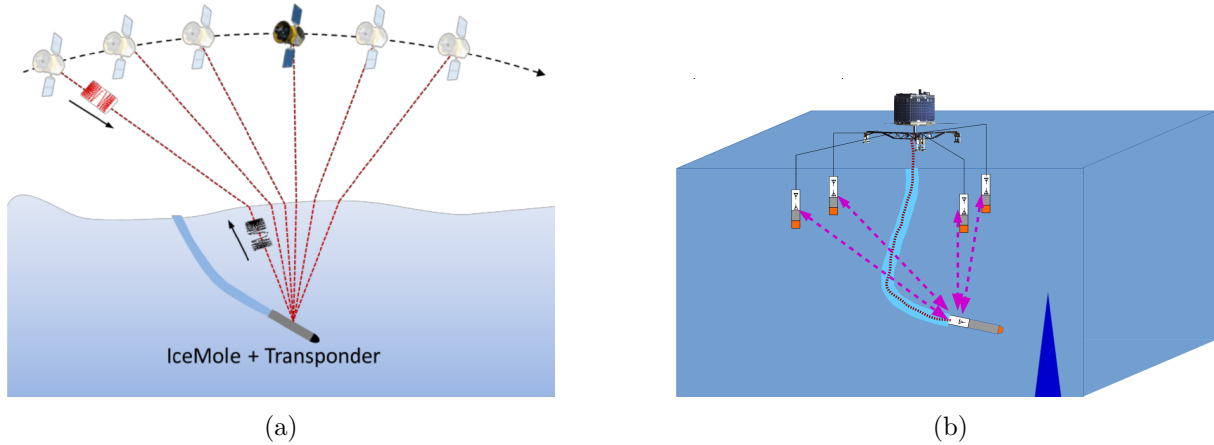


Figure 3.6: Two different permittivity reconstruction concepts, explored by the project partners BUW and FAU. FAU developed the bistatic-radar configuration of the active transponder interacting with the orbiter (3.6a). BUW developed the bistatic cross-borehole radar (3.6b)

(Fig. 3.6b). The transmitter and receiver components of the permittivity radar are designed to be included in the melting probe and the self-melting reference targets in the original proposal. The active transponder may be directly integrated into the melting probe.

3.6 Summary

The EnEx-AsGAR project was devised to examine several key challenges for a future lander melting probe to Enceladus and devise solutions. In particular, to identify a safe landing location on the south polar terrain (SPT) in close proximity to a subsurface aquifer and to optimize a safe trajectory to the subsurface aquifer while avoiding obstacles and keeping track of the melting probe's immediate position. The tasks in this thesis were to estimate the likely permittivity distribution of the SPT (examined in appendix C), develop methods to model radio-wave propagation through arbitrary ice permittivity distributions (Chapter 4, reconstruct the permittivity from ice-penetrating radar data with the help of accurate simulation methods (Chapter 5) and devise a prototype permittivity measuring bistatic radar and demonstrate its use in an alpine glacier (Chapters 6 and 7 respectively).

Chapter 4

Radar Simulations with Parabolic Equation Methods

4.1 Introduction

In this chapter, a recently developed simulation technique (at the time of writing) for radio propagation in ice is described. This technique utilises the ‘parabolic wave equation’ (PE) approximation of Maxwell’s equations. This approach allows for the simulation of continuous wave (CW) and pulsed emission through function and data-defined permittivity profiles on a scale of km, accounting for realistic features such as surface roughness, crevasses, and refrozen-ice layers, and can also model back-scatter off objects in the ice. This approach has been shown to be more accurate than ray-tracing-based simulations[68] in modelling radio propagation in polar ice sheets while being less computationally efficient. Conversely, it is more efficient and thus applicable to large-scale environments than the Finite Difference Time Domain (FDTD) method, which is a full solution of Maxwell’s equations, but are less accurate than FDTD [68]. In this chapter, PE simulations are applied to radio propagation through ice through an open source code: paraPropPython (referred to hereafter as ‘paraProp’) [46], which was first developed in a previous work [68]. This simulation method and the paraProp software were further developed in this thesis to add features; including two-way propagation and range-dependent profiles, with examples of both discussed in this chapter. A comparison study between PE and FDTD methods is also made in the appendix E.

The paraProp simulation code is additionally able to simulate the effects of dielectric attenuation and rough surfaces. In the following chapter PEs are applied to mode radio propagation effects derived from the refractive indexes of both real-world glaciers, including uneven surfaces, and for models of Enceladus (derived in chapter C). Furthermore, an inversion technique to derive a permittivity profile from cross-borehole radar data was developed as described in chapter 5. This inversion method is then applied to cross-borehole radar radar acquired at a field campaign at the Aletsch Glacier, which is discussed in chapter 8.

4.2 Modelling Electromagnetic Waves in Ice

Real-world cryospheres, whether terrestrial glaciers or the surfaces of ice moons are heterogeneous. This means that they have varying densities, compositions and numerous anomalies. Examples of the latter can include crevasses, scattering objects like boulders and water-filled cracks. Interpreting the results of a radar in such an in-homogeneous environment requires a reliable simulation method which converts a given ice model to a predicted radar pattern (whether pulse or continuous wave emission). In the case of Enceladus, the challenge is to model radio propagation in the ultra high frequency (UHF) regime, typically 300 MHz to 3 GHz for 2D or

3D geometries on size scales ranging from 100 m to 2000 m. The two traditional approaches in radio-wave simulations in ice environments are Finite Difference Time Domain (FDTD) and ray-tracing (RT).

4.2.1 Finite Difference Time Domain

The FDTD method works by discretizing the space and time in a defined grid and solving Maxwell's equations numerically at each discrete spatial grid space, known as 'Yee cells', at each time interval. This approach finds an approximation of a full solution of Maxwell's equations in the simulation domain by the discretization of space and time. With this approximation, the method can find accurate solutions for radio propagation provided that the cells are sufficiently small given the frequency of interest. A rule of thumb is that each wavelength λ should be sampled by at least 10 Yee cells,

$$\Delta r \leq \frac{\lambda}{10} = \frac{c}{nf} \cdot \frac{1}{10}, \quad (4.1)$$

As a result, the drawback of this method is the computational requirements, with the memory being directly proportional to the number of cells. For a cubic volume with extent $R = X = Y = Z$ and resolution $\Delta r = \Delta x = \Delta y = \Delta z$, the memory M is proportional to the number of Yee cells N_{cells} in the following way,

$$M \propto N_{cells} = \left(\frac{R}{\Delta r} \right)^3. \quad (4.2)$$

While the time resolution is also directly tied to the spatial resolution. Assuming equal size resolution in three dimensions $\Delta x = \Delta y = \Delta z = \Delta r$:

$$\Delta t \leq \frac{1}{c \sqrt{\frac{1}{\Delta x^2} + \frac{1}{\Delta y^2} + \frac{1}{\Delta z^2}}} = \frac{\Delta r}{c}. \quad (4.3)$$

Where the simulated time T should be large enough to allow at least one light travel time from one side of the volume to another,

$$T \geq R/c. \quad (4.4)$$

Hence, the computational time $T_{compute}$ requirement is:

$$T_{compute} \propto \left(\frac{R}{\Delta r} \right)^3 \cdot \frac{T}{\Delta t} = \left(\frac{R}{\Delta r} \right)^4. \quad (4.5)$$

Thus for our case, if one wants to simulate 1.35 GHz emission in a 100 m x 100 m x 100 m volume, an accurate simulation would require 10^{11} cells (approximately 10 TB of memory in standard FDTD packages like gprMax and MEEP), which is not feasible for the problems that are the subject of this thesis.

4.2.2 Ray Tracing

In-ice ray tracing is the current standard technique for simulating radio and radar propagation through ice. RT methods take the infinite frequency limit and solve for different paths that a signal can travel from one point to another that obey Fermat's principle of least time and the derived laws of geometric optics, such as Snell's law of refraction. The classic example is a 'ray' of light in a medium with refractive index n_0 encountering some new medium with refractive index n_1 . The angle of the incident ray to the normal of the surface θ_i is related to the angle of the transmitted (or 'refracted') ray to the surface normal θ_t with the equation:

$$n_0 \sin(\theta_0) = n_1 \sin(\theta_1) \quad (4.6)$$

Co-currently, a ‘reflected’ ray will propagate away from the interface of n_0 to n_1 by the angle $\theta_r = -\theta_i$. The amplitude of the reflected ray is given by the reflection coefficient r :

$$r = \frac{|n_1 - n_0|}{|n_1 + n_0|} \quad (4.7)$$

And the transmitted ray is given by the transmission coefficient t :

$$t = 1 - \frac{|n_1 - n_0|}{|n_1 + n_0|} \quad (4.8)$$

RT simulations can be performed in a variety of different ways. One approach is to define a source and some geometry with a refractive index profile $n = n(x, y, z)$. Several rays with different starting angles. The polar angle θ and azimuth angle α , may be randomly sampled from the source and be allowed to propagate according to the aforementioned optics equations. Another approach involves defining a source and a receiver and computing for a convergent solution of a ray that travels from the source to the receiver if a solution exists. In many cases in RF propagation through firm, it is not possible to find convergent solutions for a given source and receiver, as the intervening ice layers may cause ‘total internal reflection’ that forbids any starting angle that results in a ray that arrives at the receiver.

In RT simulations in ice, a distinction is often made between ‘direct’ signals, which travel from source to receiver in an arc or straight line without intercepting the surface (ice/air interface) and ‘reflected’ signals, which have been reflected off the ice/air interface. If the ice has a constant density or if it has a smoothly or continuously changing refractive index profile, receiver-transmitter geometry will only allow one or two ray path solutions. However, in cases of highly stratified ice density, i.e., a layer of refrozen melt-water, the number of possible ray paths increases with the number of reflective layers. RT methods provide analytical solutions for some forms of refractive index profiles and, in general, can provide numerical solutions for vertexing (the location of a radio source) by comparing the time difference of arrival (TDOA) of different receivers. RT will give accurate results provided that the wavelength λ is much smaller than any feature size, and where wave-like properties such as diffraction and interference can be ignored.

Recent experiments related to searches for Askaryan emission of neutrinos in terrestrials glaciers have demonstrated the short-comings of RT, including the observation of emission from a transmitter in regions at shallow depths where propagation is ‘classically forbidden’ by optics [12], as well as horizontally propagating modes for certain transmitter and receiver depths. Furthermore, FDTD simulations can often replicate signal features in data that are not observed from ray-tracing.

4.3 Parabolic Equations

The Parabolic Equation (PE) is an approximation of the wave equation which can be solved to allow for spatial step-wise solutions for field propagation. That is, a monochromatic (single-frequency) field can be solved in a given geometry, with the boundary conditions being that the edges of the boundary in the x and z dimensions absorb all propagating E-fields, and the field at the origin surface, i.e. $x = 0$ and $z_{min} < z < z_{max}$ is known.

To derive the PE approximation, one starts with the assumption that electromagnetic waves can be defined by the scalar Helmholtz Equation (i.e. the wave equation). In this case, ψ repre-

sents a vertically polarized electric field. Specifically, it is linearly polarized along the z -axis:

$$\nabla^2 \psi + \frac{n^2}{c^2} \frac{\partial^2}{\partial t^2} \psi = \nabla^2 \psi + k_0^2 n^2 \psi = 0. \quad (4.9)$$

With the vacuum wave number $k_0 = \omega/c$ and refractive index n . If ψ is cylindrically symmetric about the z -axis one can define the ‘reduced field’ $u = u(x, z)$, with x as the radial coordinate,

$$\psi = \frac{1}{\sqrt{x}} e^{ik_0 x} u. \quad (4.10)$$

By introducing u one can re-write equation 4.9 such that:

$$\left(\frac{\partial^2}{\partial x^2} + 2ik_0 \frac{\partial}{\partial x} + \frac{\partial^2}{\partial z^2} + k_0^2 (n^2 - 1) \right) u(x, z) = 0 \quad (4.11)$$

To allow for the PE solution one must factorize equation 4.11 by introducing the ‘pseudo-differential operator’ Q ,

$$\left(\frac{\partial}{\partial x} + ik_0(1 - Q) \right) \left(\frac{\partial}{\partial x} + ik_0(1 + Q) \right) u = 0. \quad (4.12)$$

Where Q is:

$$Q = \sqrt{\frac{1}{k_0^2} \frac{\partial^2}{\partial z^2} + n^2}. \quad (4.13)$$

The factor including $(1 - Q)$ represents the forward propagating component of the wave u_{plus} , i.e in the positive \hat{x} -direction, while the factor containing $(1 + Q)$ represents the backwards propagating component u_{minus} , with the overall solution being expressed as a linear combination $u = u_{\text{plus}} + u_{\text{minus}}$. If one then assumes no reflections or negligible reflections, one may neglect u_{minus} such that $u = u_{\text{plus}}$ and derive the following differential equation:

$$\frac{\partial u}{\partial x} = -ik_0(1 - Q)u(x), \quad (4.14)$$

which can be solved to obtain the solution for the forward propagating field:

$$u(x) = e^{-ik_0(1-Q)x} = e^{ik_0(Q-1)x}. \quad (4.15)$$

This enables us to solve the equation in the x direction in discrete steps of Δx , given an initial solution at the source at $x = 0$:

$$u(x + \Delta x, z) = e^{ik_0 \Delta x (Q-1)} u(x, z). \quad (4.16)$$

A standard method to solve u is to apply a Fourier transformation to the equation in z -space (depth space) with the Fourier transform being defined thus:

$$F_z(u(z)) = \int_{-\infty}^{\infty} u(z) e^{-ik_z z} dz = U(k_z) \quad (4.17)$$

With k_z being the z -component of the wave vector. In applying the FFT in z -space to the left and right-hand sides of equation 4.14, one can take advantage of the Fourier identities:

- $F_z\left(\frac{\partial^2 u}{\partial x^2}\right) = -k_z^2 F(u)$
- $F_z\left(\frac{\partial u}{\partial x}\right) = \frac{\partial}{\partial x} F(u)$

Thus, allowing computational solution of the equation using the Fast-Fourier Transform (FFT) algorithm. However, this method is reliant on being able to express Q as a linear sum of other components,

$$Q \approx \sum_i Q_i. \quad (4.18)$$

and consequently:

$$e^{ik_0\Delta x(Q-1)} \approx e^{-ik_0\Delta x} \prod_i e^{ik_0\Delta x Q_i}. \quad (4.19)$$

There are multiple approximations for Q in the literature, with the choice of the approximation dependent on the application. Henceforth, it is useful to express Q as $Q = (1 + q)^{1/2}$ (with $q = \partial_z^2/k_0^2 + n^2 - 1$).

In the lowest order expansion of Q : $(1 + q)^{1/2} \approx 1 + q/2$ the ‘standard parabolic equation’ (SPE) is obtained, which gives valid solutions for angles $\theta < 15^\circ$ from the ‘paraxial’ direction. For a dipole antenna source, the paraxial direction is perpendicular to the antenna orientation, and as such the paraxial direction is pointing in the x -direction. The SPE is written therefore as:

$$\frac{\partial^2 u}{\partial x^2} + 2ik_0 \frac{\partial u}{\partial x} + k_0^2(n^2 - 1)u = 0. \quad (4.20)$$

However, there are applications where one may wish to solve for wider angles, requiring a better approximation of Q . Attempts to do so have often lead to complex polynomials that lead to numerical instability [7]. An alternative approach was proposed by Feit & Fleck [29], who used the approximation: $\sqrt{1 + A + B} \approx \sqrt{1 + A} + \sqrt{1 + B} - 1$ where $A = \partial_z^2/k_0^2 + 1$ and $B = n^2 - 1$, leading to the Feit-Fleck Q_{FF} operator:

$$Q_{FF} = \sqrt{1 + \frac{1}{k_0^2} \frac{\partial^2}{\partial z^2}} + n - 1. \quad (4.21)$$

Where there exists separate ‘diffractive term’, $\sqrt{1 + \frac{1}{k_0^2} \frac{\partial^2}{\partial z^2}}$ and ‘refractive term’, $n - 1$.

For solving EM waves in glacial firn, such as at the South Pole, Q_{FF} did not provide sufficiently accurate solutions[68] when compared with FDTD and ray tracing. Hence a new operator was feined based on a second order expansion of Q [68]: Q_{ice} :

$$Q_{ice} = \sqrt{1 + \frac{1}{k_0^2} \frac{\partial^2}{\partial z^2}} + n \sqrt{1 + \frac{1}{n_0^2}} - \sqrt{1 + \frac{n^2}{n_0^2}}. \quad (4.22)$$

Where n_0 is a reference refractive index, a somewhat arbitrary constant in the operator. The wave number k_0 is redefined to be wave number at the refractive index. In paraProp, n_0 can be defined arbitrarily, with the default being close to surface $n_0 = n(z = 1)$.

4.3.1 Numerical Spatial Solution in Frequency Domain

As previously mentioned, the PE is solved step-wise from origin up to some maximum range in increments of Δx . The solution of the reduced field $u(x = 0)$ is set beforehand as a boundary condition. For the next step $u(\Delta x)$ and all subsequent steps $u(x_i) = u(x_{i-1} + \Delta x)$, the previously reduced field $u(x_{i-1})$ is converted to Fourier space U_{i-1} , where the next step is solved numerically using the equation 4.23, in which the solution is separated into its *refractive* and *diffractive* components via the Q_{ice} operator. The component $u(x_i)$ is then solved by applying an inverse

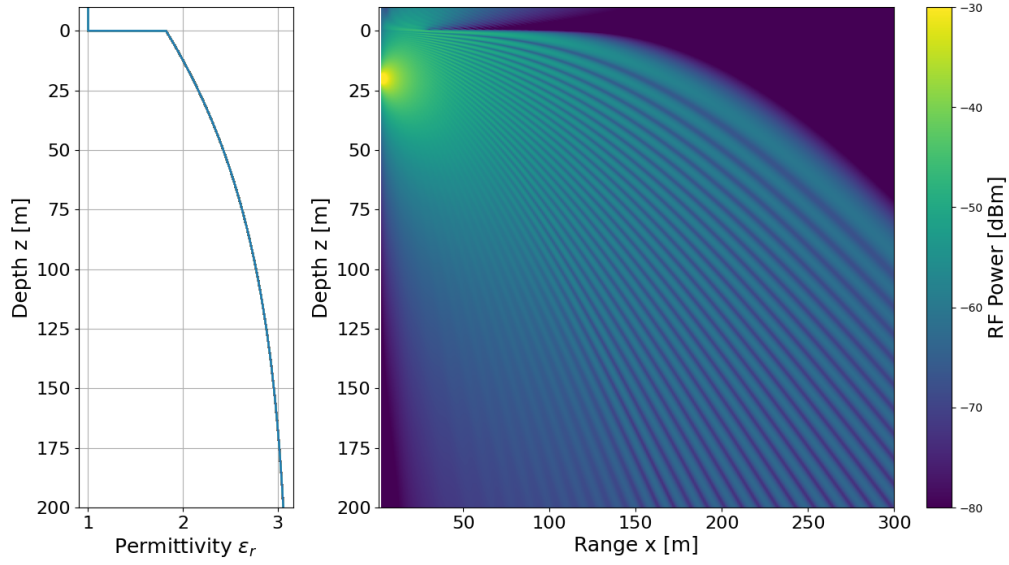


Figure 4.1: Right: The RF power simulated for a functional profile of the ice at the Geographic South Pole in Antarctica, with the power shown as a function of range and depth. Left: permittivity profile, which is defined with an empirical function (see equation 4.28) used to describe the refractive index profile inferred from the measure density profile of the Spice Core[68]. The refraction of the signal ‘downwards’ is due to the increasing refractive index with depth.

Fourier transform on $U(x_i)$. The procedure is summarized in the equation 4.23:

$$u(x + \Delta x) = \exp \left[ik_0 \left(n \sqrt{1 + \frac{1}{n_0^2}} - \sqrt{1 - \frac{n^2}{n_0^2}} \right) \Delta x \right] \quad (4.23)$$

$$\times F_z^{-1} \left\{ \exp \left[-ik_0 \Delta x \sqrt{1 - \frac{k_z^2}{k_0^2}} + 1 \right] U(x, k_z) \right\}. \quad (4.24)$$

With the field at the origin being defined with the source profile $s_0(z)$

$$u(x = 0, z) = s_0(z), \quad (4.25)$$

and thus one obtains,

$$u(x = \Delta x) = \exp \left[ik_0 \left(n \sqrt{1 + \frac{1}{n_0^2}} - \sqrt{1 - \frac{n^2}{n_0^2}} \right) \Delta x \right] \quad (4.26)$$

$$\times F_z^{-1} \left\{ \exp \left[-ik_0 \Delta x \sqrt{1 - \frac{k_z^2}{k_0^2}} + 1 \right] F_z(s_0(z)) \right\}. \quad (4.27)$$

This procedure is repeated iteratively until the complex reduced field $u(x, z)$, and hence the field $\psi(x, z) = \frac{u(x, z)}{\sqrt{x}} e^{ik_0 x}$, are calculated for the entire domain. As an example in Fig. 4.1 (on the right), one can see the emitted power of a 400 MHz signal from a dipole antenna source at a depth of $z_{src} = 30$ m through an ice-sheet defined with a functional refractive index profile $n(z)$. This refractive index profile is defined by an analytical fit to the measured density profile at the South Pole (left on figure 4.1) utilized in [68]:

$$n(z) = n_{ice} + (n_0 - n_{ice}) e^{-z/z_{scale}}. \quad (4.28)$$

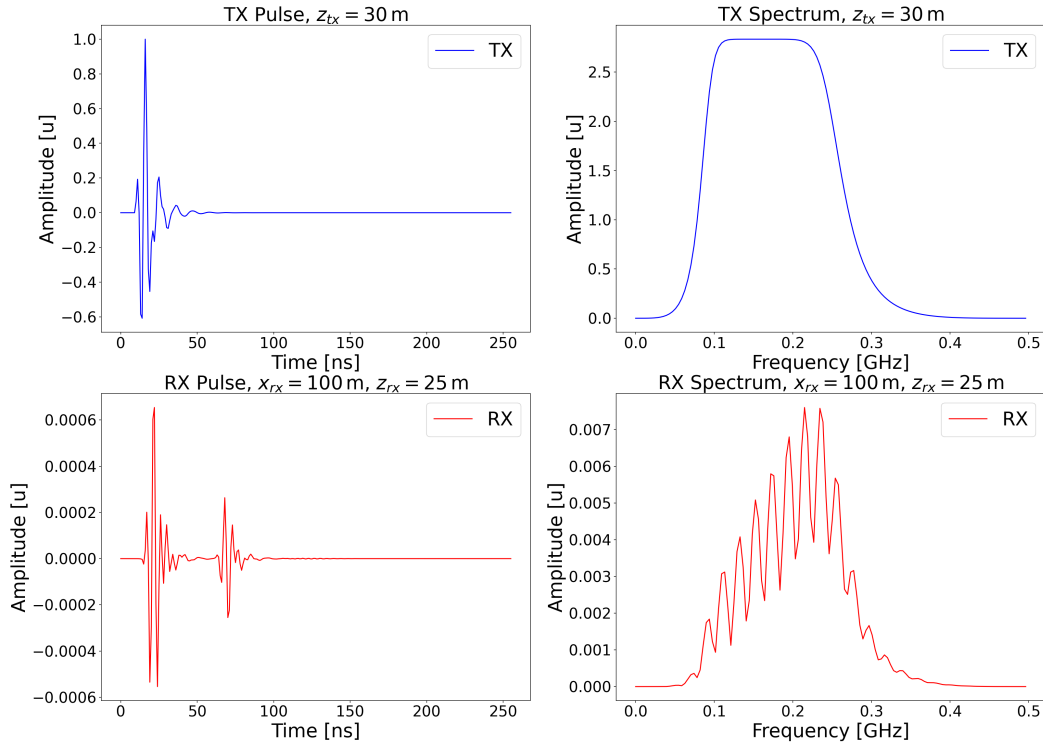


Figure 4.2: An illustration of the synthesizing of a waveform at the receiver in the time domain. A pulse is defined at the source $z_{tx} = 30$ m (top left) and divided into its spectral components via an FFT (spectrum shown top right). The amplitudes are used to define the source field $u(x = 0, z)$ and then simulated through the domain, and sampled at the receiver point $RX(x = 100$ m, $z = 25$ m) (bottom left). The pulse at the receiver is then synthesized via an inverse FFT (bottom right). Note that the times shown for the TX and RX pulses are relative.

Where $n_{ice} = 1.78$ is the refractive index of solid ice, $n_0 = n(z = 0)$ is the refractive index at the surface and z_{scale} is the ‘scale depth’ of the ice, a constant related to the densification rate of the firn.

4.3.2 Time Domain Solution

Limitations in memory restrict the ability to solve a time-domain waveform for every point in the entire geometry. Instead time-domain solutions require the definition of a single receiver or a set of receivers at distinct ranges and depths within the simulation domain. The solution in the time domain is performed by decomposing the source signal, such as a pulse, into its constituent Fourier modes, and simulating each mode utilizing the numerical spatial solver described in the previous section (4.3.1). At the receiver positions, the complex amplitude for each mode is sampled to produce the spectrum of the received signal. Subsequently, the receiver signal is synthesized by a simple inverse Fourier transform. This procedure is illustrated in Fig. 4.2 for a bandwidth limited (80 MHz to 200 MHz) impulse emitted from a dipole antenna at $z_{src} = 40$ m and propagating through a refractive index profile defined by the function 4.28, that approximates the refractive index inferred from density measurements at the South Pole. A receiver at the same depth as the transmitter and at a range of 20 m measures a direct traveling pulse and reflection off the air-ice interface.

A-Scans and B-Scans

A short digression must be made to define the terms *A-Scans* and *B-Scans* in the context of PE simulations in this work. In surface penetrating radar (SPR) applications, the terms A-Scan and B-Scan refer to the arrangement of time-domain waveforms in some spatial coordinate system, typically Cartesian (x, y, z) . Normally, in SPR, the operator uses a transmitter and receiver at the surface, which transmits some signal, i.e., a pulse, downwards into the ground and measures the backscatter from various sources. In SPR, an A-Scan refers to a single time-domain waveform captured at a specific spatial coordinate[22]. For a given array of data in two spatial dimensions $A(t, x_i, z_j)$, with t being the two-way travel time of the signal:

$$f(t) = A(t, x_i, z_j) \quad (4.29)$$

where i and j are constant. A B-Scan is an ensemble of waveforms defined with[22]:

$$f(t, x) = A(t, x_i, z_j) \quad (4.30)$$

with i being in a range (1 to N). This will be hereafter called a ‘horizontal B-Scan’. Usually, a B-Scan is represented with a color-map image, with the horizontal distance x also being used to define the x -axis of the plot, the travel time defining the y -axis of the plot, and the amplitude defining the color scale. The reader should note that A-Scan or B-Scan may be plotted as a function of range $R = ct/2$, in other words, the two-way travel distance of the signal from transmitter to receiver after being reflected. For example, an A-Scan may be plotted as a function of amplitude against range R , and a B-Scan may be plotted as a function of amplitude against range R and antenna displacement.

Since this thesis is concerned with one-way propagation from a transmitter and receiver separated by some distance and sometimes different depths, it useful to adopt convention from cross borehole radar. In this convention an A-Scan is a time-domain waveform of propagation from a transmitter at some coordinates $TX = TX(x_{tx} = 0, z_{tx})$ to a receiver $RX = RX(x_{rx}, z_{rx})$, and a B-Scan is an ensemble of different waveforms for different combinations of z_{tx} , x_{rx} and z_{rx} , with the data being stored in some array $A(t, z_{tx,i}, x_{rx,j}, z_{rx,k})$ over ranges $i = 1, \dots, N_{TX}$, $j = 1, \dots, N_{RX,x}$ and $k = 1, \dots, N_{RX,z}$. The following types of B-Scans are defined:

- Parallel-Depth B-Scans, an ensemble of A-Scans for TX and RX at the same depth and a fixed range $f_{t,z} = A(t, z_{tx,i}, x_{rx,j}, z_{rx,k})$, for $i = k = 1, \dots, N_{TX}$ (with $N_{TX} = N_{RX,z}$), and with j being constant.
- Fixed receiver vertical B-Scan: An ensemble of A-Scans for a fixed range and depth for the receiver and changing depths of the transmitter. $f(t, z) = A(t, z_{tx,i}, x_{rx,j}, z_{rx,k})$, with $i = 1, \dots, N_{TX}$ and $j = k = \text{constant}$.
- Fixed transmitter vertical B-Scan: An ensemble of A-Scans for a fixed transmitter depth, fixed range, and moving depth of the receiver. $f(t, z) = A(t, z_{tx,i}, x_{rx,j}, z_{rx,k})$, with $k = 1, \dots, N_{TX}$ and i and j being constant.
- Fixed depth horizontal B-Scan: An ensemble of A-Scans for fixed transmitter and receiver depth but varying ranges. $f(t, z) = A(t, z_{tx,i}, x_{rx,j}, z_{rx,k})$, with $j = 1, \dots, N_{RX,x}$ and i and k being constant.

An example of a parallel depth scan is shown in Fig. 4.3, through a refractive index profile defined by the density profile shown in the top right corner. An A-Scan for $z_{tx} = z_{rx} = 15$ m and $x_{rx} = 30.1$ m is shown on the top left. Within the B-Scan, it is possible to identify two features: a directly transmitted signal forming an arc whose shape closely matches the refractive index profile and a fainter but still visible shallow arc that is caused by the reflection of the wave off the surface.

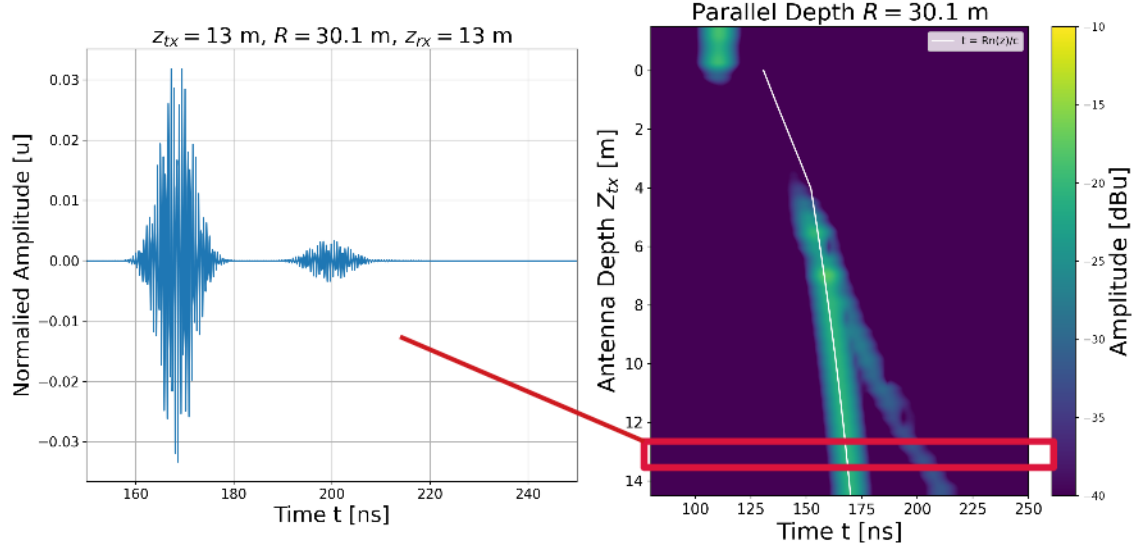


Figure 4.3: A simulated parallel depth scan for a set of transmitters and receivers and a separation of 30.1 m. Left: a pulse transmitted at a depth of 13 m is recorded by a receiving antenna at a depth of 13 m and range of $R = 30.1$ m. Right: the ‘Parallel depth B-Scan’ is formed by combining the received waveforms from 2 m above the surface to 15 m below the surface in 0.5 m intervals into a single image. It is referred to as ‘parallel depth’ since the transmitting and receiving antennas are at equal depths. The y-axis shows the depth of both antennas, the x-axis shows the time and the color axis is the amplitude. The direct transmission pulse and reflected pulse become clearly distinguishable for depths below 8 m, while the region above 4 m depth is dark, reflecting the lack of a solution of an electric field at these depths with ray-tracing.

4.3.3 Backwards Propagation

A primary goal of this work is to detect targets in ice via the back-scatter of a radar and to model how such back-scatter is affected by the permittivity of the intervening ice. Back-scatter can be simulated with PEs by taking the second term of the solution of equation 4.12; the ‘backwards propagating’ component u_{minus} [58]. If one neglects the forward propagating term one can solve for u_{minus} in a similar way to u_{plus} :

$$u_{\text{minus}} = e^{-k_0 \Delta x (1+Q)x} \quad (4.31)$$

and:

$$u_{\text{minus}}(x - \Delta x, z) = e^{-k_0 \Delta x (1+Q)\Delta x} u_{\text{minus}}(x, z) \quad (4.32)$$

which may be solved using the same iterative technique as equation 4.23. Hence solving a two-way PE involves first solving for the forward-going wave u_{plus} from the origin $x = 0$ up to the maximum range $X = N_x \Delta x$ after increments of Δx in N_x steps through a medium defined with a two-dimensional refractive index profile $n = n(x, z)$. In the code, the profile is represented with a two-dimensional matrix. An anomalous object, such as a cavity in the ice, a boulder or aquifer, etc., may be represented in this matrix. The solver propagates through the medium and encounters these objects as a sudden change in refractive index in the x -directions $dn/dx > 0$, and these distances are hence used to define the *sources* for the subsequent backwards propagating wave. In this first stage, if at any range x_i and any depths z it is found that: $|n(x_i, z) - n(x_{i-1}, z)| > 0$, a reflective source $s_{\text{ref}}(z)$, and a source amplitude. The final term is as a function of the incoming amplitude ψ_{plus} multiplied by Fresnel’s reflection coefficient $R = R(n_1, n_2) = \frac{n_2 - n_1}{n_2 + n_1}$.

$$s_{\text{ref},i}(z) = R(n_i(z), n_{i-1}(z)) \cdot \psi_{\text{plus}}(x_{i-1}, z) \quad (4.33)$$

The forward going field at x_i is also reduced by an amount defined by the Fresnel transmission coefficient $T = 1 - R$

$$\psi_{\text{plus}}(x_i) = T(n_i, n_{i-1}) \cdot \psi_{\text{plus}}(x_{i-1}) \quad (4.34)$$

As the forward propagation solution continues, this step is repeated for any change of the refractive index in the x -direction, with each discontinuity being treated as a separate source. These ‘sources’ are added to an ensemble (or list) of sources s_{list} which will be used to calculate the backwards reflection:

$$s_{list} = \{s_1(z), s_2(z), \dots, s_j(z), \dots, s_{N_{\text{ref}}}\}, \quad (4.35)$$

where N_{ref} is the number of range steps where $\Delta n(z)/\Delta x > 0$ (for any z). Once all reflecting sources have been found and calculated, the calculation of the backwards propagating field commences. Each source $s_j(z)$ in the ensemble is used to initialize a separate backwards propagating field $\psi_{\text{minus},j}$:

$$\psi_{\text{minus},j} = \frac{1}{\sqrt{|x - x_j|}} u_{\text{minus},j} e^{ik_0|x-x_j|} \quad (4.36)$$

With x_j being the range coordinate of the source. An ensemble of independent backwards fields $u_{\text{minus},j}$ is simulated using the backwards PE equation (equivalent to equation 4.23):

$$u_{\text{minus},j}(x - \Delta x) = \exp \left[ik_0 \left(n \sqrt{1 + \frac{1}{n_0^2}} - \sqrt{1 - \frac{n^2}{n_0^2}} \right) \Delta x \right] \quad (4.37)$$

$$\times F_z^{-1} \left\{ \exp \left[-ik_0 \Delta x \sqrt{1 - \frac{k_z^2}{k_0^2}} + 1 \right] U_{\text{minus},j}(x, k_z) \right\} \quad (4.38)$$

The resulting backwards propagating reduced field ψ_{refl} is thus calculated from the sum of the fields in the ensemble:

$$\psi_{\text{minus}} = \sum_j^{N_{\text{ref}}} \psi_{\text{minus},j} \quad (4.39)$$

And the total solved field of the two-way PE is simply the sum of the forward and backward solved fields:

$$\psi = \psi_{\text{plus}} + \psi_{\text{minus}} \quad (4.40)$$

Two important drawbacks to this approach must be mentioned. First, since the reflected field is calculated as the sum of an ensemble, each member of this ensemble must be simulated individually, leading to the computation time increasing by a factor of $1 + N_{\text{ref}}$. For example, if one considers reflections off a vertical wall or a vertical pipe, then the flat geometry of the shape’s representation of the $n(x, z)$ matrix leads to the simulation time doubling. However, in the case of a sphere of radius R , the simulation time will increase by a factor $2R/\Delta x + 1$ causing a penalty to be paid for any increase of spatial resolution in the x -direction, as well as for the size of the object. Secondly, this approach only considers *first order reflections* and ignores second or higher order reflections caused as the backwards propagating field encounters an anomaly. Higher order reflections have been implemented in other PE codes [58], but were not yet implemented into paraProp, as this would also significantly increase the computation time.

4.4 Example of two-way PE simulation

To demonstrate the ability of PE methods to simulate the two-way wave propagation, an example of back-scatter off three different types of anomalies in ice are defined using the South Pole empirical model. The simulation domain is a 50 m x 50 m cross-section of the ice, assumed to be cylindrically symmetric about the z -axis. The horizontal resolution is 20 cm, and the vertical resolution is 5 cm. The transmitting antenna is at 20 m depth and is transmitting at 500 MHz

The anomalies are as follows:

1. An aquifer: Shown as a salt-water filled vertical crack beginning at 30 m depth and extending 2 m in width, at a horizontal range of 48 m from the transmitter. The water has a complex permittivity of $\epsilon_r^* = 82 + i90.884$ (the imaginary part is derived from a typical value for the conductivity of seawater $\sigma_{sea-water} = 5 \text{ S/m}$ [87]) and as such has a very high attenuation constant $\alpha \approx 188$ and a skin depth of $\delta \approx 5.3 \text{ mm}$
2. A crevasse: shown as a triangular air-filled crack in the ice (although the limited resolution of the simulation causes this to appear ‘stepped’). The depth of the crevasse is 20 m, the width is 4 m across and the bottom of the crevasse is 50 m away from the source in the horizontal direction.
3. A ‘meteor’ (or boulder): Note that the dimensions of this meteor are likely unrealistically large. It appears as a cross-section of a spherical meteor with a radius $r = 5 \text{ m}$ with its center at 30 m depth and 50 m horizontal range from the source. The permittivity is defined as $\epsilon_r = 8.2 + 0.1558j$, the value of a meteor with 80% silicate minerals and 20% Fe-metal composition[36].

The square of the field amplitude in dB units as a function of space is shown for each class of anomaly in Fig. 4.4. Also shown is an example of a two-way PE solution for a pulse shown in Fig. 4.5, using the crevasse anomaly as a source of back-scatter.

4.5 Simulations through Glaciers with data-defined profiles

In this section a comparison is made between RF propagation inside South Polar ice (as measured by in the Spice Core), with a mostly smoothly increasing refractive index and that of the Guliya ice cap, which has numerous refrozen ice layers as seen in Fig. 4.6.

4.5.1 Examples of Glaciers

South Pole

At an elevation of 2835 m above sea level the South Pole firn comprises the upper $\sim 200 \text{ m}$ of the Antarctic ice sheet at the South Pole, with ice sheet itself extending $\sim 2.8 \text{ km}$ downwards through the ice. The ice is the accumulation of $\sim 54 \text{ kyr}$ of continuous snowfall.

Guliya

Guliya is an ice cap located in the far western Kunlun Shan mountains located in the Qinghai-Tibet plateau in China. It resembles a polar ice cap, with 30 to 40 m high ice walls and a depth of 308.6 m (in 1995) and with an area of $> 200 \text{ km}^2$, it is the largest ice cap located in a subtropical region. The Tibetan plateau is a dry region, but an accumulation of ice occurs due to moisture flowing from the Indian subcontinent during the Monsoon seasons. The deepest 20 m of the core are thought to be a record from $> 500 \text{ kyr}$ ago.

4.5.2 Frequency Domain

In fig 4.7, CW propagation at $f = 1.3 \text{ GHz}$ from a dipole antenna located at $z = 15 \text{ m}$ is shown for the upper 30 m of the firn for the South Pole (Fig. 4.7a) and for Guliya (Fig. 4.7b). In both examples, lensing effects are clearly seen, where enhanced RF power is seen at the depth of the transmitter depth $z_{tx} = 15 \text{ m}$. For the Guliya glacier, this depth is within a relatively dense layer with $n(z) \sim 1.6$ for depths between $14.3 \text{ m} < z < 15.8 \text{ m}$, resulting in strong internal reflections.

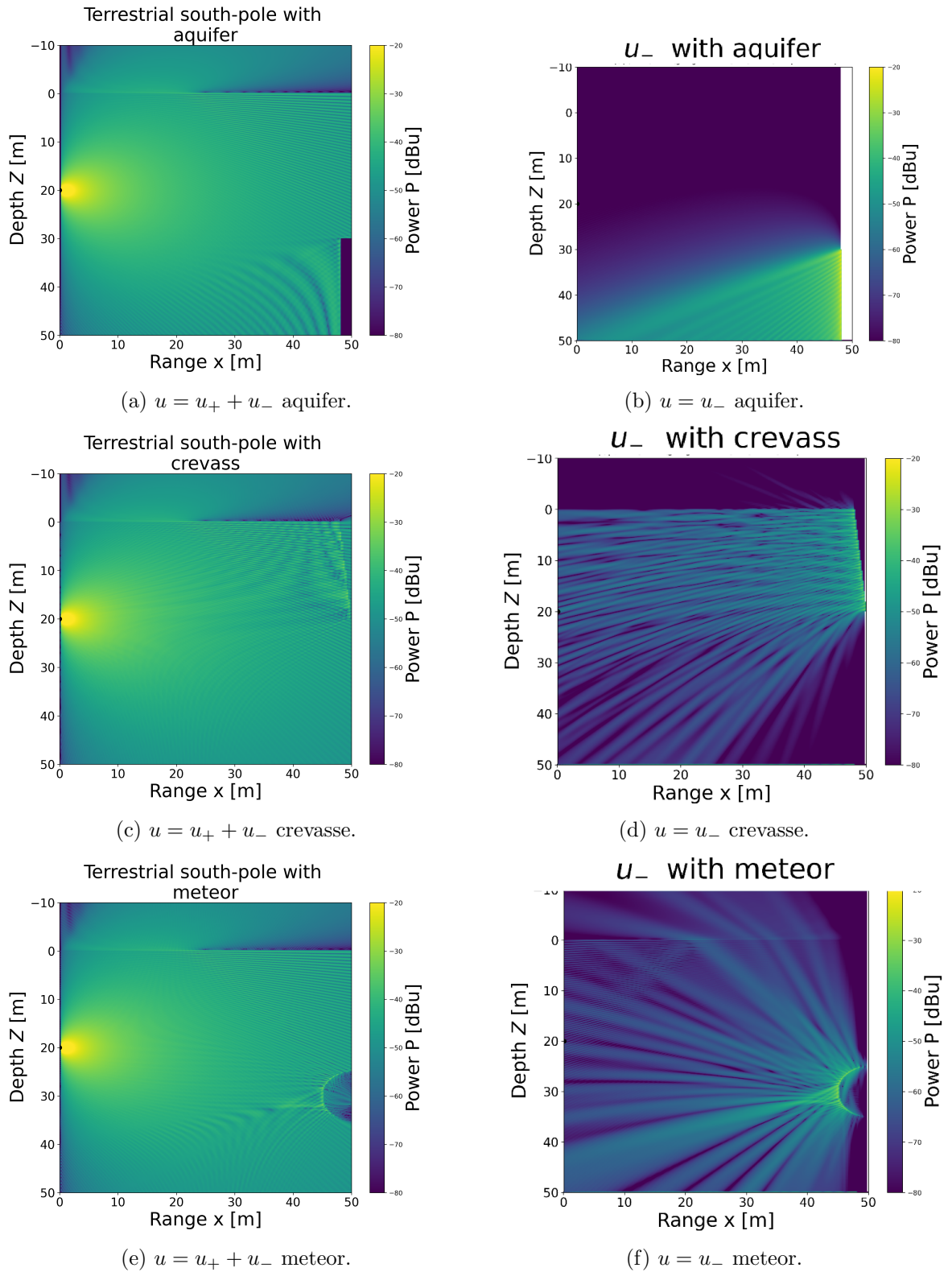


Figure 4.4: For each plot, the backwards propagating or reflected field ψ_{minus} is shown on the right-hand side, and the combined field is shown on the left-hand side. The amplitude of the pulse is shown in dB space, with the forward combined component and backward component displayed in different colors.

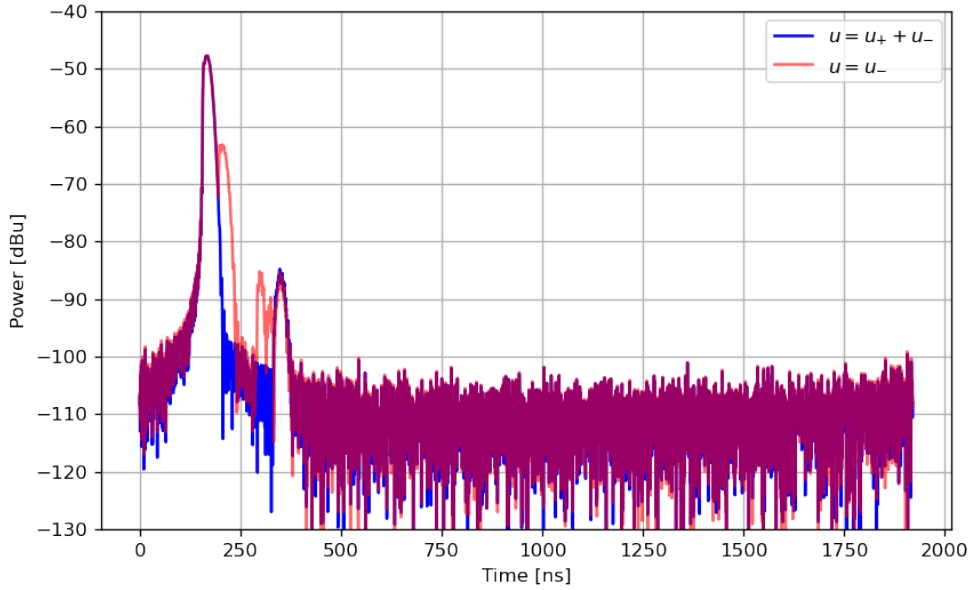


Figure 4.5: A pulse traveling from a transmitter at 30 m depth to receiver at 30 depth at a range of 40 m. The combined PE solution is shown in blue, while the backwards component alone is shown in red.

The lensing effect caused by ice layers can be seen clearly in Fig. 4.8 showing emission from $z_{tx} = 15.0$ m at $f = 1.3$ GHz different glaciers. The left plot in Fig. 4.8 shows the RF power against the horizontal range R for the different glaciers, compared against the in-air transmission $P_{air}(R) = P_{TX}/4\pi R^2$. In the right plot in Fig. 4.8 the gain of the emission in glaciers relative to the in-air transmission is shown. The strongest lensing effect is apparent for the Guliya glacier, with a gain relative to P_{air} of ~ 10 dB. Gains of ~ 5 dB are apparent for the Brueggen, Colle-Gniffeti, and the South Polar glaciers.

4.5.3 Time Domain

The effects of ice layering on RF emission are also apparent in the results of time domain simulations. To illustrate these effects, a comparison is made again between the upper 25 m of the South Pole and the Guliya ice cap. In this case, a 400 MHz bandwidth Gaussian pulse, with a central frequency of $f_{central} = 1.3$ GHz is simulated. Multiple scans are made, with the transmitter depth varying from $z_{tx} = -2$ m to a maximum depth $z_{tx} = 20$ m in intervals of $\Delta z_{tx} = 0.5$ m, and the receivers located at the same depths at a range of $R = 42$ m. The results are shown with a parallel depth B-Scan in Fig. 4.10. For the case of south polar ice 4.10a, the B-Scan shows two clear trends, the directly transmitted signal from the transmitter to receiver, i.e., the ‘horizontal signal.’ A reflected signal from the air-ice interface, which becomes clearly distinguishable at depths $z > 15$ m. At each depth, the horizontal signal has the highest amplitude and matches exactly to the time of flight expected from horizontal propagation $t_{horizontal}(z) = Rn(z)/c$. One can observe brighter signals at points of increased density relative at $z = 1$ m, 5 m, 11 m, 15 m and 18 m, which are caused by the amplification of the emission due to lensing. In the case of the Spice Core B-Scan it is interesting to note that at $z_{tx} = z_{rx} \sim 3$ m there is a deviation of approximately ~ 10 ns between the propagation time predicted by paraProp and the time implied by the local refractive index $t(z) = Rn(z)/c$. This offset occurs in a ‘cavity’, i.e., a layer where the firn density is reduced relative to the surface density. Hence, a possible explanation may be that there is interference between internally reflected waves that creates a delay in the pulse arrival

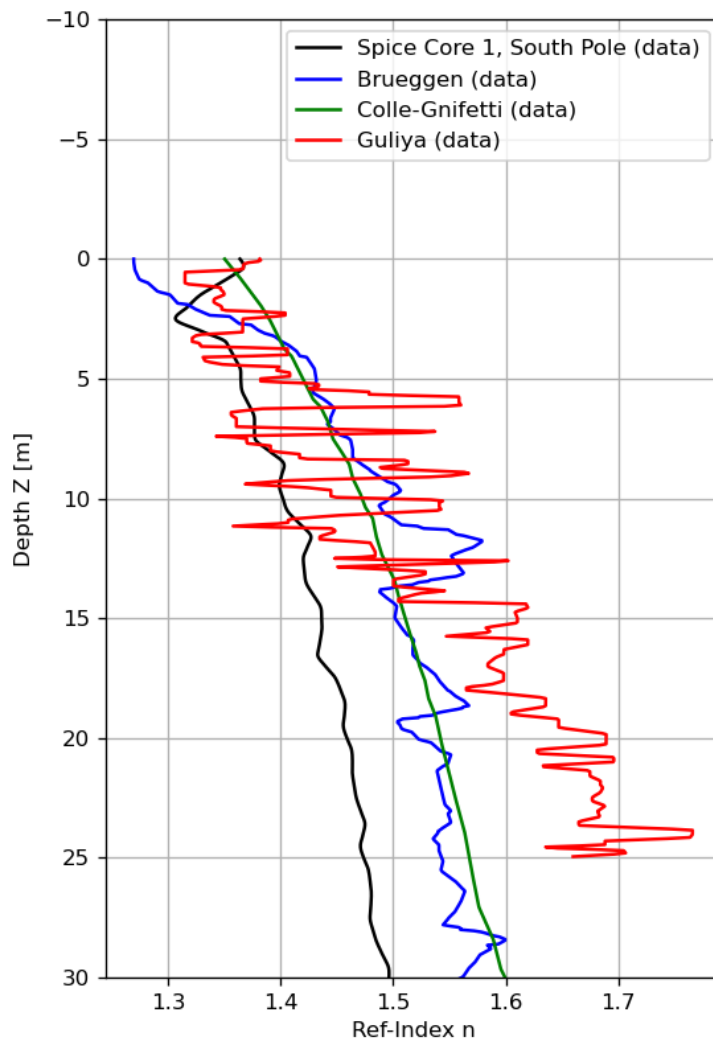
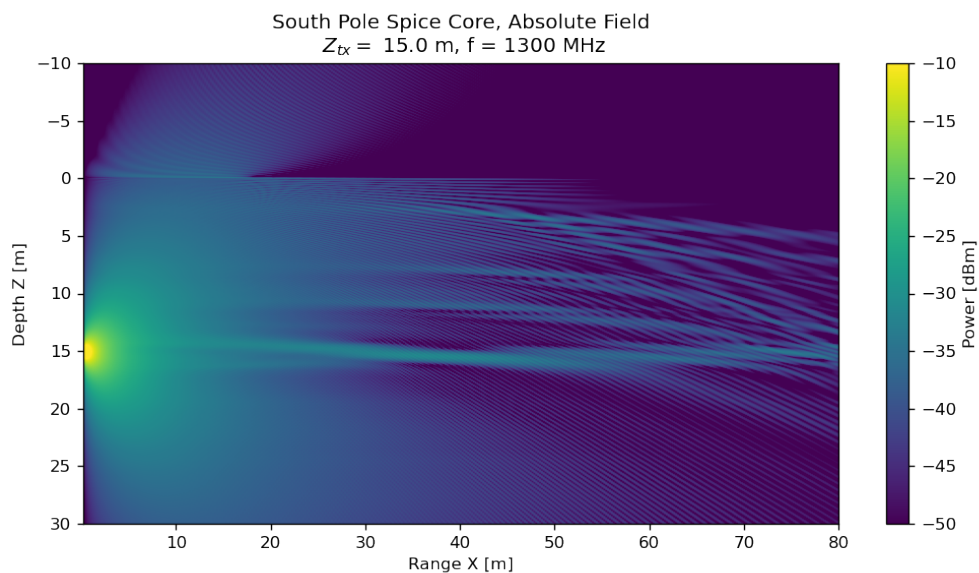
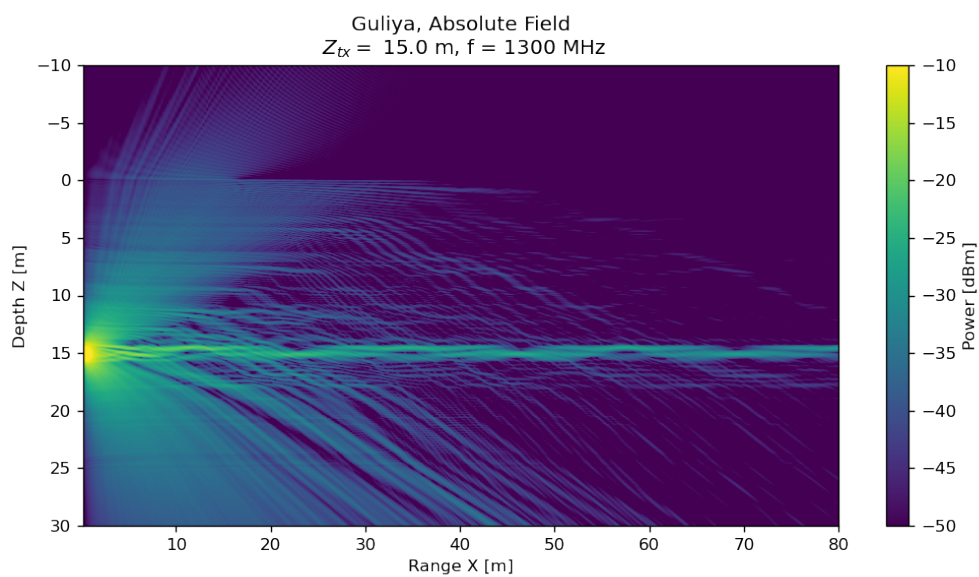


Figure 4.6: The refractive index profiles of different polar and mountainous glaciers as measured using ice core data. These are: the South Polar ice sheet as measured by Spice Core 1, the Brueggen glacier in Patagonia, the Guliya glacier of Tibet and the Colle-Gnieffeti glacier in the Swiss Alps.



(a) RF propagation through South Polar ice (defined using Spice Core density profile)



(b) RF propagation through Guliya

Figure 4.7: RF propagation through ice defined with the refractive index of the Spice Core (4.7a) and that of the Guliya glacier (4.7b). In both case the transmitter is located at $z_{tx} = 7$ m and is transmitting CW emission at $f = 1.3$ GHz. Horizontal propagation is shown in both examples, with non-zero RF signals being observed in regions forbidden by ray-tracing.

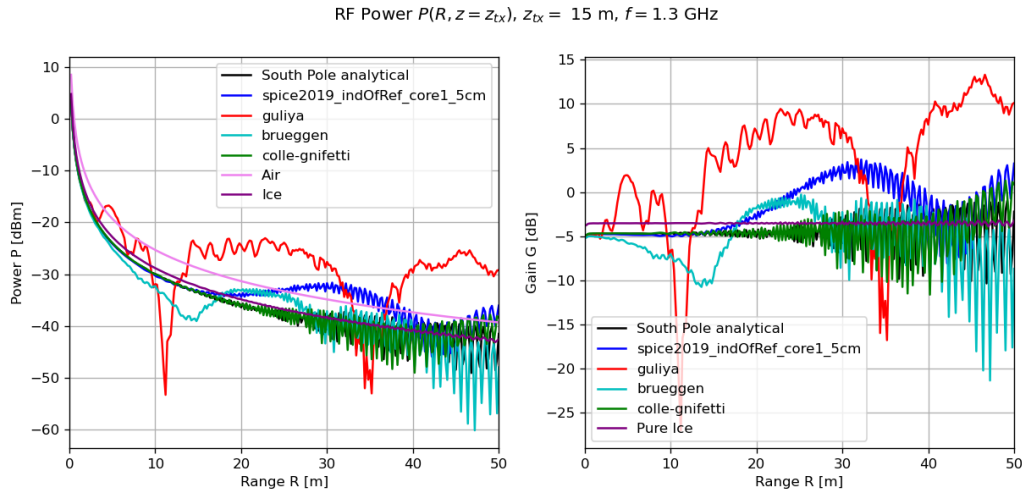


Figure 4.8: The RF power simulated in FD as a function of depth and range for $f = 1.3$ GHz from a transmitter at $z_{tx} = 15$ m, for the Guliya ice cap and the South Pole ice cap, as measured from the Spice Core

time, but this phenomenon has not yet been explained and is worthy of further investigation. However, this delay is similar to the delays observed between the refrozen layers in the Guliya B-Scan, lending credence to the internal reflection explanation.

The B-Scan of the Guliya glacier is more complex, owing to the numerous ice layers. Again, there is a clear horizontal component of the signal, which mostly corresponds to the time expected from the local refractive index $t_{horizontal}(z) = Rn(z)/c$ and mostly has the highest amplitude, but this is not true for every depth. Notably at the gaps between the ice layers, the signal is delayed from that expected from horizontal propagation by \sim ns at the gaps in $z = 9.5$ m, $z = 11$ m and a larger delay of ~ 40 ns at $z = 0.5$ m. A narrow and denser layer exists at $z = 7.25$ m, lying between the simulated antenna pairs at 7 m and 7.5 m depths, both of which see the highest amplitude peak being delayed from $t_{horizontal}$ by ~ 10 m. Here, it is worth noting that the central wavelength in air of the radio waves is $\lambda = 23$ cm, and it may be possible that there is some interference between the part of the wave passing through the dense layer and parts traveling within the gap, explaining the delay.

The reflected component of the Guliya signal is also very complex and it is difficult to find obvious interpretations for the features show trailing after the direct transmitted signal. There is no clear sign of reflection from the ice-air interface. The South Pole transmission shows a direct pulse centered at 210 ns followed by the ice-air interface reflection at 230 ns.

4.6 Limitations and Potential Improvements to PE Methods

Although a powerful and relatively new means of simulating radio propagation through the ice, the PE approximation has some disadvantages when compared to more standard methods like RT and FDTD.

Three Dimensions

The implementation of PE simulations is currently limited to two dimensions. The PE approximation assumes a cylindrically symmetric field $\psi(x, z, \phi)$. In principle, solving for forward propagation in ice in three dimensions is trivial; one only needs to substitute $\psi(x, z, \phi = \phi_i)$

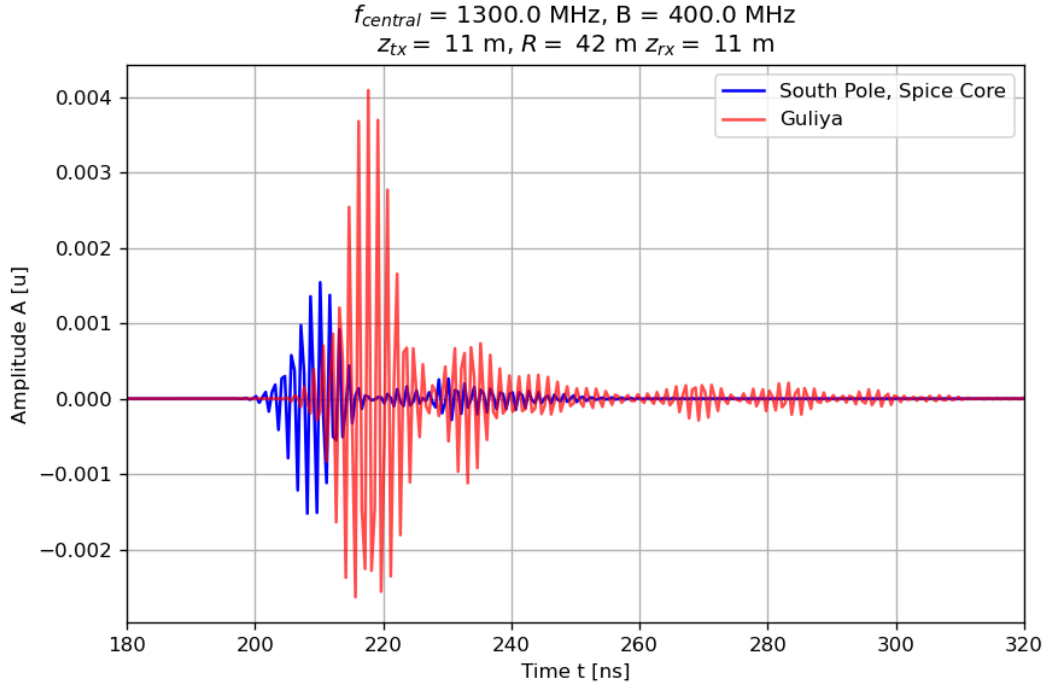


Figure 4.9: A comparison between a received 400 MHz bandwidth Gaussian pulse from a TX at $z_{tx} = 11$ m to a RX at $z_{rx} = z_{tx} = 11$ m over a range of $R = 42$ m through the South Pole and Guliya ice caps.

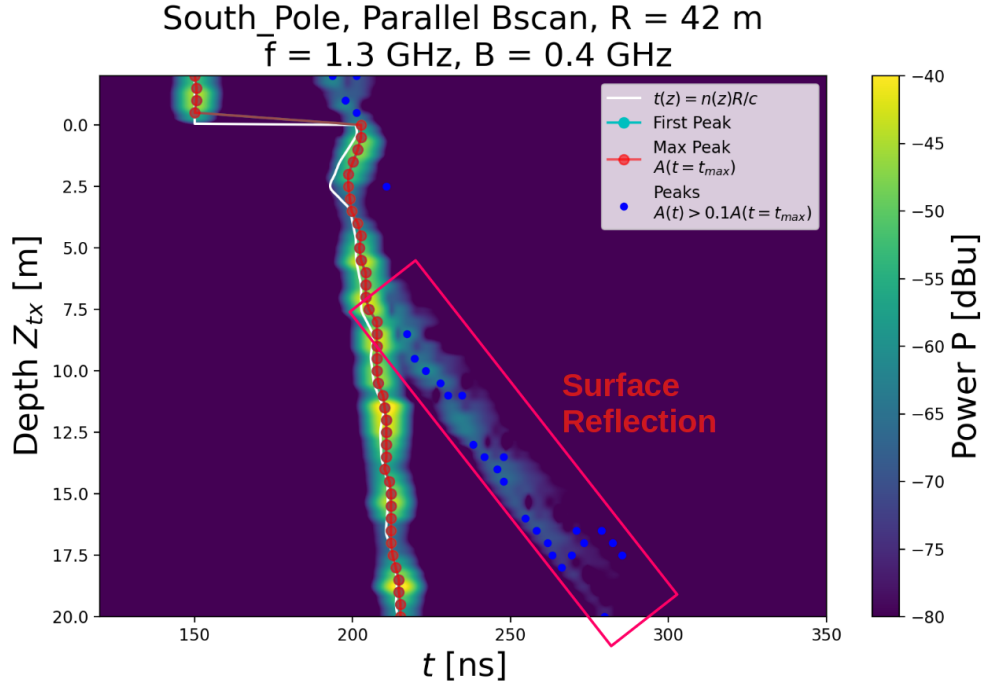
where ϕ_i is a member of a list of all the azimuth directions ϕ that one cares to simulate. However, modeling two-way propagation will require considering interference between waves of several different wave vectors. Updating paraProp to operate in three dimensions is a subject for future work and is beyond the scope of this thesis.

Polarization

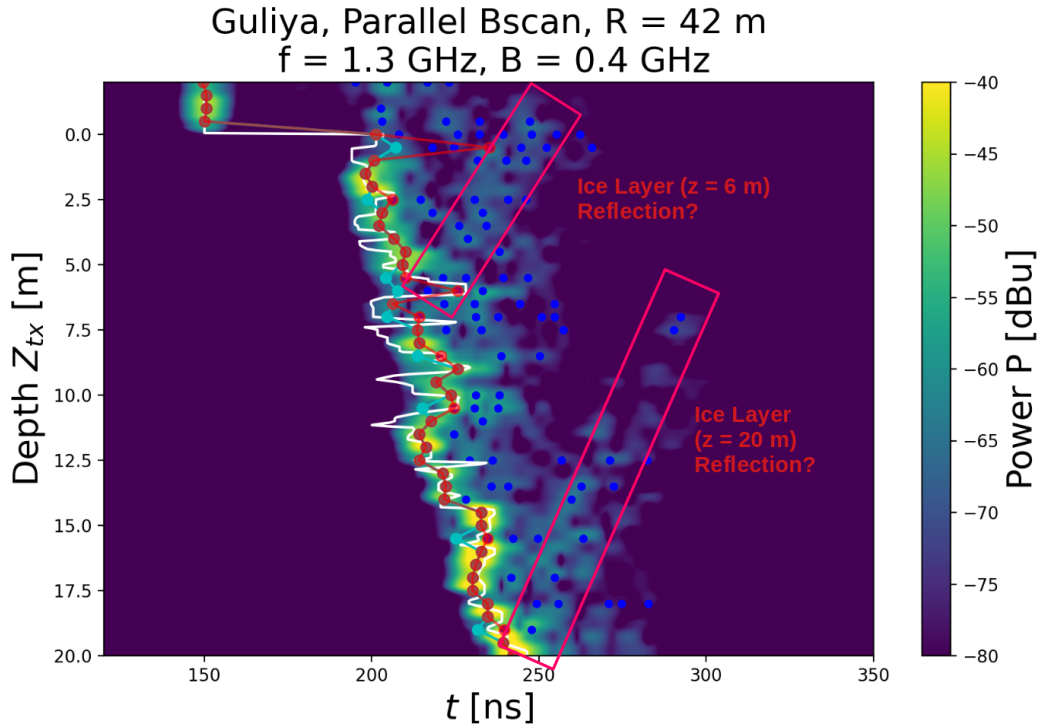
Another limitation of the PE method is that the solution is derived on the assumption of a vertically polarized field $\psi(x, z) = E_z(x, z)$, which will naturally propagate with a wave vector in the horizontal direction. While this may be sufficient for a cross-borehole radar with a vertically polarized antenna, there are applications where different polarization angles may be of interest. One can imagine solving the PE for E_x or E_y however in these cases, the assumption of cylindrical symmetry about the polarization axis is not true for a vertically variant refractive index, and thus, it is not clear if the solutions would be valid. For these cases, PE may be used alongside other radio-propagation methods such as FDTD or RT, which may allow for the computation of a boundary condition to allow initialization of the PE.

Computation Time

Although PEs are computationally more efficient than FDTD methods, as the higher spatial resolution is only required in the polarization axis, computation time is still a consideration, especially for TD and two-way propagation solutions. In the current paraProp solver, the slowest component is the computation of the FFT and inverse FFT for equation 4.23. Currently, this utilizes the NumPy FFT function and takes approximately ~ 1 ms. Future improvements to FFT may include the solution of the PE in a more efficient code, such as C++, or utilizing a more efficient formulation of the FFT algorithm. An example of this could be the FFTW ‘Fastest Fourier Transform in the West’ library. FFTW performs a planning phase to determine an



(a) B-Scan of the South Polar ice cap.



(b) B-Scan of the Guliya Ice Cap.

Figure 4.10: The parallel depth B-Scan of the upper 20 m of the South Pole and Guliya ice caps, for RF transmission from TX to RX at the same depth. The color scale shows the received RF power, the y-axis shows the depth of both antennas, and the x-axis shows the recorded signal time at the receivers. At each depth, the maximum signal component or ‘peak’ is shown with a red dot, while all other peaks with an amplitude greater than 10% of the maximum are indicated with blue dots. The horizontal propagation time $t(z) = Rn(z)/c$ is indicated with a white plot line. The delay of the pulse arrival time at $z \sim 3$ m for the Spice Core relative to the expectation from the refractive index is not yet understood.

optimal sequence of computations. During this phase, it analyzes the input data, caches, memory alignment, and processor architecture to create an execution plan tailored to the specific machine. Increasing the computation speed by an order of magnitude would allow for higher resolution modeling of anomalies for back-scatter simulations, as well as three-dimensional simulations.

Chapter 5

Inversion of PE Simulations using Genetic Algorithms

As described in chapter 4, a forward simulation technique for radio propagation through an ice medium with an arbitrary two-dimensional refractive index profile $n(x, z)$, using the Parabolic Wave approximation has been implemented in the paraPropPython code, hereafter referred to as ‘paraProp’. So far, solutions for the electric field amplitude throughout the medium in the frequency domain mode have been shown (section 4.5.2), as well as solutions for the received pulse from a single transmitter source $TX = TX(z)$ at a set of receiver positions in the ice $RX = RX(x, z)$ (section 4.5.3). To reconstruct the refractive index in real-world cryospheres, an inversion technique is necessary, where one can take the observed pulses at the receiver positions and reconstruct a refractive index profile that can adequately explain the characteristics of the received pulses, such as the time of arrival and amplitude.

In this chapter, an inversion technique based on a genetic algorithm (GA) is presented. GAs are a form of optimization technique that attempts to replicate the process of natural selection to evolve a set of solutions to a problem towards a better set of solutions. The concept of a GA is presented in section 5.1. In section 5.2, a GA’s application to permittivity reconstruction is described in detail, including the initialization method, fitness function, genetic operators, and selection routines. In section 5.3, the testing of the GA to reconstruct the refractive index profiles of simulated ‘pseudo-data’ is presented, which are generated from two real-world glaciers. The tests aimed to verify this technique’s effectiveness and calculate the expected residuals of the optimal refractive index profile. In chapter 8, the application of the GA-based inversion to the time-of-flight profiles obtained using the cross-borehole radar technique, described in chapter 6, is shown.

5.1 Genetic Algorithms

Genetic algorithms (GAs) are a class of optimization algorithms that utilize the principles of evolution to determine solutions to complex problems efficiently. GAs operate on an initial ‘population’ (set) of ‘individuals’ (solutions), which are each defined by their genes, which are parameters of interest in the solution. There are many ways the genes can be represented in the algorithm. The simplest example is of genetic representation is an individual being defined with an array of binary bits, each of which is a ‘gene’. However, the genes may also be integers or floating-point numbers within a limited domain. The procedure of a GA can be divided into the following steps, each of which will be described in greater detail in section 5.1.2:

1. Initialization: An initial population of individuals is created.
2. Evaluation: Fitness scores are calculated for the individuals

3. Selection: Fitness scores are used to select a subset of individuals.
4. Reproduction: New individuals are synthesized via various genetic operators, including cross-breeding and mutation
5. Repeat steps 2-4 until termination.
6. Termination: An individual reaches a sufficiently high fitness score or a maximum number of iterations has occurred

5.1.1 Examples of GAs

A famous use of GAs in optimization is the ‘Knapsack problem,’ a classic computer science problem dating from 1897. In this problem, a traveler must fill his or her knapsack with a number N of items m , with each item having a different monetary value v and weight w , and the knapsack must be under a maximum weight W . The traveler wishes to maximize the value of the knapsack. The traveler could calculate the value of every possible combination of the items, but if there are many items, this method quickly becomes unworkable as the evaluation time increases as $\propto 2^N$. GAs have been demonstrated to solve this problem in substantially shorter periods of time[71].

An example of practical use of GAs that is relevant to this work’s topic is antenna design. The GENETIS (Genetically Evolving NEuTrIno TeleScopes) project utilizes a GA to design the dimensions of a bicone antenna to be used by the Askaryan Radio Array (ARA) to detect in-ice Askaryan radio emission induced from relativistic particle showers induced by ultra-high energy neutrinos interacting within the Antarctic ice-sheet [8, 9, 70]. The dimensions of the antenna were to be selected to maximize the effective detection volume of ARA and, therefore, maximize the sensitivity of the detector to the ultra-high energy neutrino flux[70]. The ‘genes’ in this case were 7 floating point numbers that defined the dimensions of the bi-cone antenna (as shown in Fig. 5.1). An optimal resulting antenna increased the effective volume by 22% was found by generation 23, with 50 individuals per generation.

5.1.2 GA Procedure

Initialization and Evaluation

The first step in a GA is ‘initialization’; the first generation must be created. At each generation, all members of the population of solutions are evaluated with a ‘fitness function’, which quantifies the solution’s goodness of fit, typically with an output of a single number, known as the fitness score S .

Selection

With a fitness score assigned to each individual, individuals may then be selected as ‘parents’ for the next generation, with the probability of selection being proportional to the fitness score. As the name suggests, parent individuals generate ‘children’ which populate the next generation. The way that parents are selected is known as a ‘selection routine’, of which two are used in this thesis:

- Roulette selection: also known as ‘fitness proportionate’ selection, is where an individual’s likelihood of being selected as a parent is proportional to its fitness score.
- Tournament: a subset of the population is randomly sampled, and the highest-scoring individual within this subset becomes a parent. This process is repeated to ensure enough parents through this selection method.

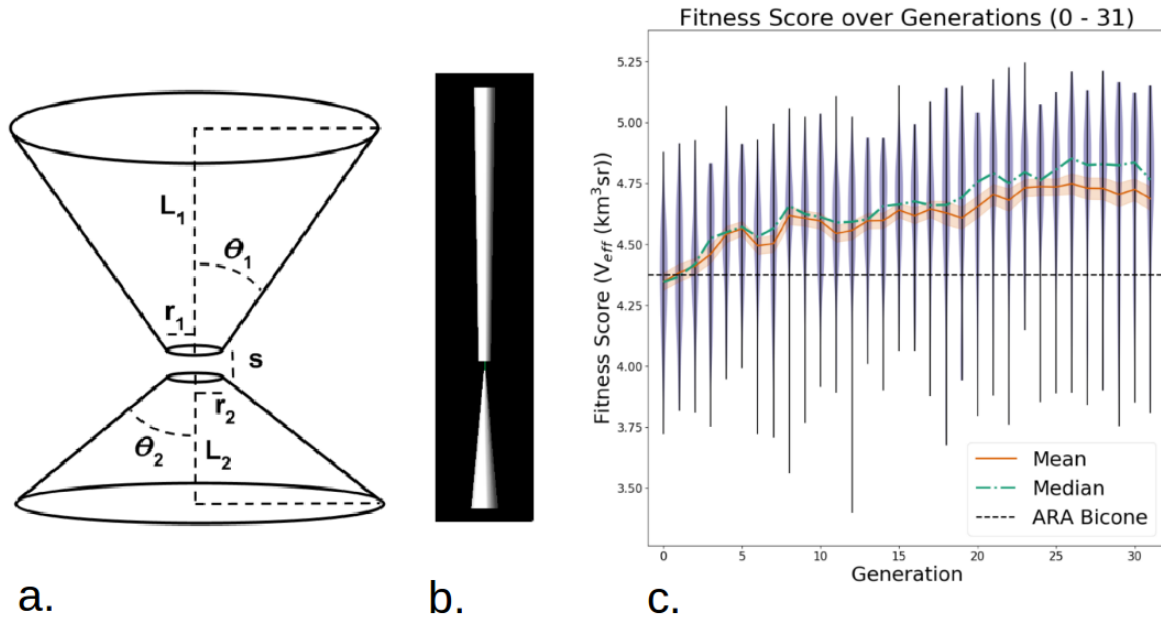


Figure 5.1: A sketch with the dimensions of the GENETIS bicone antenna: the lengths or heights (L_1, L_2), the inner radii (r_1, r_2) and interior angles (θ_1, θ_2) of the upper and lower cones, and the separation s between the bicones. Fig 7.1b. A three-dimensional model of the best antenna shape was found using the GA. Fig 7.1c. The evolution of the fitness score throughout the GA [70].

Reproduction and Mutation

Having chosen the parents, the production of children takes place via genetic operators, with the main operators being:

- **Cross-breeding:** Two parents create a new individual, with approximately $\sim 50\%$ of the individual's genes coming from parent 1 and the rest coming from parent 2. The way the genes may be allocated can differ. For example, each gene may have a 50% chance of coming from parent 1 or parent 2. Alternatively, the genes of each parent may be split into even-sized chromosomes, with half coming from parent 1 and the other half from parent 2.
- **Cloning:** An individual with a very high relative fitness score may be directly copied or cloned into the next generation, with the clone having identical genes to its parent. Not all GAs use cloning. Cloning is used to guarantee that the quality of the solutions cannot decrease from generation to generation, a strategy called 'elitism' or 'elitist selection'. Too much GA elitism can decrease the population's diversity and lead to over-fitting of the problem. As a rule of thumb, the proportion of cloned children should be small, typically on the order of 5 % or less.
- **Mutation:** the simplest way to picture 'mutation' is for individuals to be expressed as an array of binary bits. One or more bits in the array are randomly selected and flipped to the opposite sign. This mutated individual is then passed to the next generation. For integer or floating-point representation, mutation is more complicated. An integer number gene may be replaced with a new number from some distribution or two genes may be swapped inside the individual.
- **Immigration:** this operation is done without using parents from the previous generation. Instead, completely new individuals may be added to the new generation by sampling

from a separate distribution. This may or may not be the same distribution from which generation 0 was sampled.

Additionally, multiple operators may be applied to the same individuals in different orders. For example, a child individual created via cross-breeding may also be subjected to mutation, as can a clone or immigrant. Each problem that a GA analyzes is different and may require a different relative proportion of the different genetic operators.

Termination

In a GA, a loop iterates through each generation, evaluating the fitness scores, selecting parents, and spawning the new generation via the operators until termination. Termination can occur after a predefined number of generations or until at least one individual reaches a predefined fitness score.

5.2 GA-based Inversion of paraProp

The application of a genetic algorithm in this work is as an optimization routine to find a best-fit refractive index profile of a region of ice under test. The observables are the radar amplitude data $A_{TX,RX}(t)$ from subsurface receiver RX and transmitter TX . In the construction of the problem, one can define each refractive index profile as a model m which is comprised of a 1-D refractive index profile $n_i(x, z) = n_i(z)$, with the genes being the refractive index values at a discrete number of depths $n_{i,j} = n_i(z_j)$. The procedure follows a simple workflow described in Fig. 5.2. A population of refractive index models is created at the initialization step, using some combination of analytical and data-derived profiles, with random fluctuations added to some fraction of these.

Following initialization, each refractive index in the population is used to generate a set of ‘B-Scans’ (defined in section 4.3.2) using the paraProp simulation code (see chapter 4). This means that a forward propagating signal from TX is simulated for a set of transmitter depths, and the signal is sampled at a discrete set of receiver points RX . The data set is described here as an array of waveforms or A-Scans $A_{k,l,sim}(t)$, where the subscript k corresponds to a transmitter TX_k position from a set of N_{TX} positions, and l corresponds to a receiver position RX_l from a set of N_{RX} receiver positions. For each TX and RX position, there will also exist a data recorded waveform $A_{k,l,data}$. At each point, the difference between the data $A_{k,l,data}$ and simulation output $A_{k,l,sim}$ is calculated using a misfit score $\chi_{k,l} = \chi(A_{k,l,data}, A_{k,l,sim})$. The fitness score for the refractive index model m is the inverse of the sum of the misfit scores for all TX and RX positions. The fitness scores are then used to select some of the models to act as ‘parents’ for the next generation, which are then generated using the genetic operators. This process is repeated N_{gen} times, with the output being the refractive index model with the highest fitness score. Each step is outlined in detail in this section. In this chapter, the models have a depth resolution of $\Delta z = 0.5$ m, for a range of depths from $z_{min} = 1$ m to $z_{max} = 15$ m, resulting in a gene number of 28. For the depths above z_{min} , the refractive index values are fixed using real-world data of snow permittivity from the Aletsch glacier field test of the Enceladus Explorer (EnEx) project, described in chapter 7.

5.2.1 Misfit and Fitness Function

The refractive index model m in a generation is then used in a TD-simulation with paraProp, creating an ensemble of waveforms, $A_{sim}(m) = A_{k,l,sim}(m, t)$ for transmitter TX_k and receiver RX_l , which can take the form of a pulse or a CW waveform. Finding an optimal fit to the data will require a function that quantifies how *different* the simulated signal is from the measured data by use of a *misfit function* $\chi(A_{sim}, A_{data})$. A misfit function can be defined in multiple

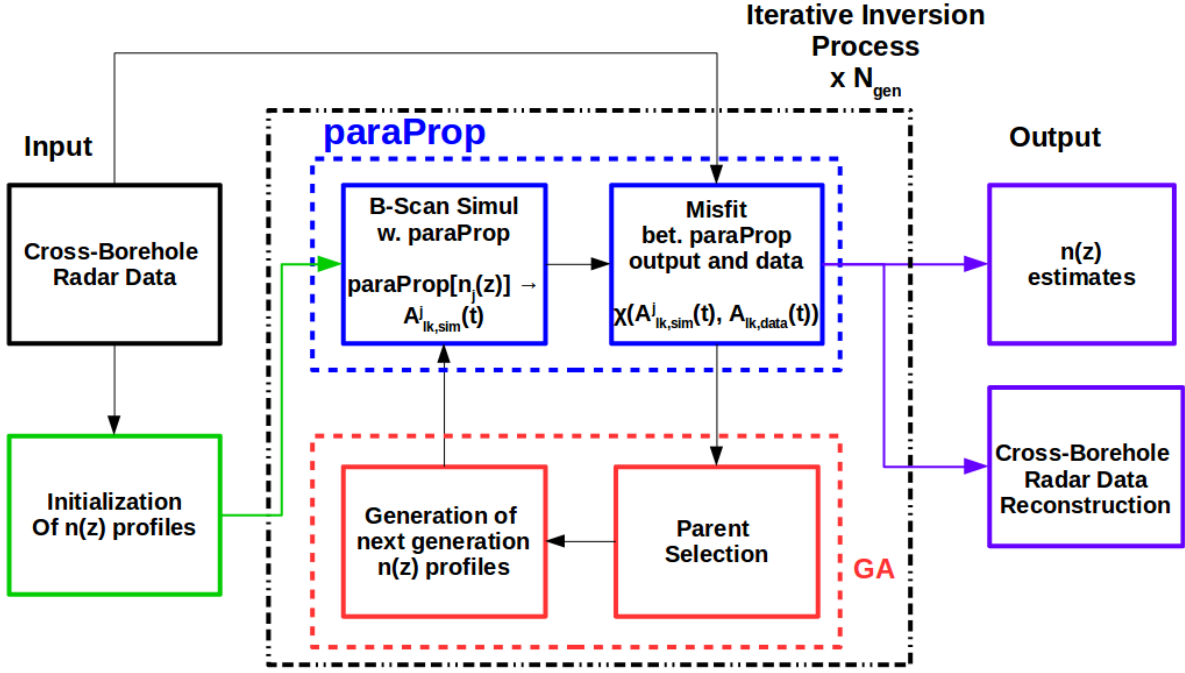


Figure 5.2: A workflow diagram of the GA-based refractive index reconstruction. The procedure is initialized with an initial fit to the time of the peaks in the data waveforms $A_{data}(t)$, with a set of $n(z)$ -profiles created from these fits. The initial $n(z)$ profiles are then used to generate time-domain signals A_{sim} with paraProp. The waveforms are evaluated using a fitness score, which then drives the selection of the best profiles with the genetic algorithm. The selected profiles then produce the next generation of signals. The procedure repeats iteratively.

ways: instantaneous phase, envelope misfits, waveform amplitude, travel-time difference, etc. [17]. This analysis defines a misfit function χ_E from the signal envelopes $E(t)$. The envelope misfit function is the integral over time of the natural logarithm of the ratio of the envelopes of the data and simulated wave-forms squared, between times t_{min} and t_{max} :

$$\chi_E(A_{sim}(m, t), A_{data}(t)) = \int_{t_{min}}^{t_{max}} \left| \log \left(\frac{E_{data}(m, t)}{E_{sim}(t)} \right) \right|^2 dt. \quad (5.1)$$

Where the envelope $E(t)$ is defined as the root of the real and imaginary components of $A(t)$ squared,

$$E(t) = \sqrt{\text{Re}(A(t))^2 + \text{Im}(A(t))^2}. \quad (5.2)$$

The global misfit X between the refractive index model m and the data is quantified as the sum of all the waveforms across all combinations of TX and RX:

$$X(m) = \sum_k^{N_{TX}} \sum_l^{N_{RX}} \chi_{kl}(m) = \sum_k^{N_{TX}} \sum_l^{N_{RX}} \chi(A_{sim,k,l}(m), A_{data,k,l}). \quad (5.3)$$

As a better fit means a lower misfit score, one can therefore define the fitness function of the GA simply as the inverse of the global misfit:

$$S(m) = \frac{1}{X(m)}. \quad (5.4)$$

5.2.2 Initialization

For this case initialization is the process of creating the first generation of refractive index models. To achieve a resolution that reflects density fluctuations observed in real-world glaciers, the

depth intervals of the profile should be of a scale $\Delta z < 0.5$ m. For a profile of depth $z \geq 15$ m, the number of free parameters will therefore be of an order of ≥ 30 . Thus, there is a large parameter space to be searched, so it is prudent to utilize the time of flight information of the data or pseudo-data so that an optimal solution can be acquired in a reasonable time frame and with realistic computational resources. On the other hand, it is also important to have some degree of diversity of the solutions to avoid over-fitting and premature convergence to a local minimum. Thus, a combination of ‘first-guess’ profiles utilizing peak selection of the pseudo-data waveforms are used, both in raw form and with some ‘noise’ components added in the refractive index space. Additionally, classes of functional refractive index profiles are added, with some noise components added in.

In Fig. 5.3 examples of profile initialization for an example refractive profile are shown which are used in section 5.3.5.

The analytical profiles are:

- Exponential Profile: $n(z) = n_{\text{ice}} + (n_{\text{ice}} - n_{0,\text{rand}}) \exp(z/z_{0,\text{rand}})$
With the constant value $n_{\text{ice}} = 1.78$ the following variables determined randomly:
 - Surface Refractive Index: $1.35 < n_{0,\text{rand}} < 1.45$ (random).
 - Scale Depth: $14 \text{ m} < z_{\text{rand}} < 100 \text{ m}$ (random).
- Sine Profile: $n(z) = A_{\text{rand}} \sin(k_{\text{rand}}z + \phi_{\text{rand}}) + n_{c,\text{rand}}$. With the following random variables defined within bounds:
 - Amplitude: $0 < A_{\text{rand}} < 0.4$
 - Wave vector: $1/15 < k_{\text{rand}} < 2$
 - Constant: $1.0 < n_{c,\text{rand}} < 1.78$
 - Phase: $0 < \phi_{\text{rand}} < 2\pi$
- Flat Profile $n(z) = n_{\text{rand}}$, with the bounds: $1.0 < n_{\text{rand}} < 1.78$.

Randomized refractive index: Random fluctuations in ice density have been observed ice cores at the Taylor Dome [12] and at the South Pole [68] on an order of 2% to 5% of the absolute density value within the measured depths at both sites. The fluctuations in density are maximized at shallower depths and decreases as a function of depth. To model the depth dependence of the fluctuations, a random density vector $\Delta n_{\text{rand},0}$ is calculated using a function:

$$\Delta n_{\text{rand},0}(z) = \frac{A}{1.0 + Bz} (R - 0.5). \quad (5.5)$$

Where A is a proportionality constant, B controls the depth dependence of the fluctuations and R is a random number $0 < R < 1$. The constant B is assumed to be the inverse of the ‘scale depth’ of the glacier. In the initialization process, these constants are set to: $A = 0.05$, $B = 0.01$. Before applying this random fluctuation vector to a analytically or data-derived profile, $\Delta n_{\text{rand},0}$ is passed through a low-pass filter F_{LP} which suppresses fluctuations on scales $\Delta z < z_{\text{min}}$:

$$\Delta n_{\text{rand}} = F_{LP}(\Delta n_{\text{rand},0}, z_{\text{min}}). \quad (5.6)$$

And the randomized refractive index derived from a starting profile $n_0(z)$ derived analytically or from data:

$$n_{\text{rand}}(z) = n_0(z) + \Delta n_{\text{rand}}. \quad (5.7)$$

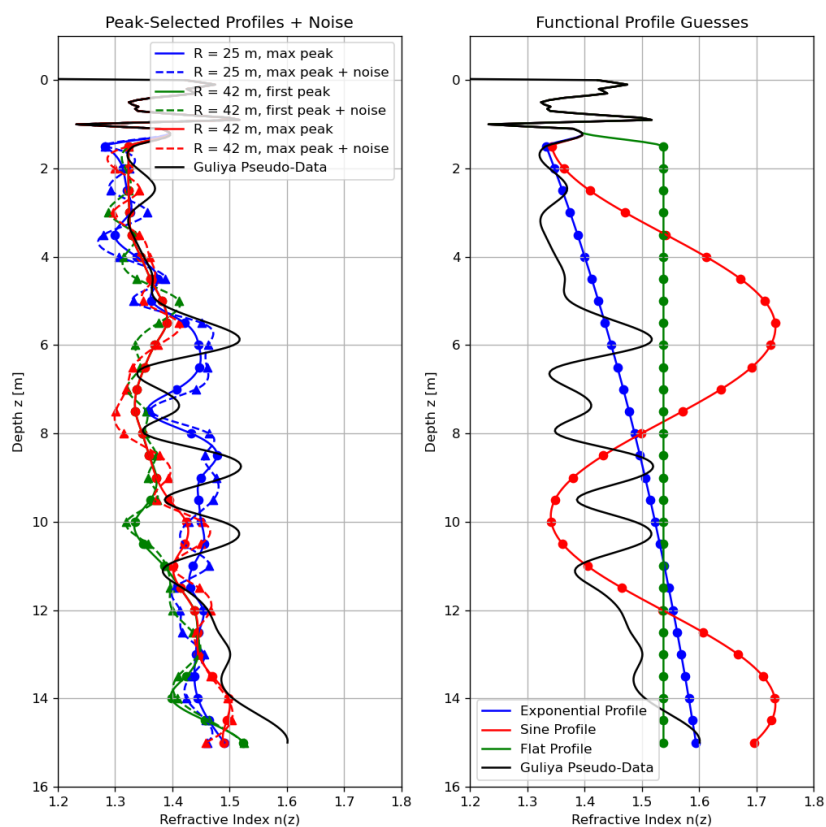


Figure 5.3: Examples of glacier refractive index profiles used to initialize the GA. On the left side are examples of profiles formed by ‘peak selection’ for the pseudo-data signal, shown with circles. These include both the first peak in the signal with a $SNR > 10$ and the peak of maximum amplitude ‘max peak’. The triangles are these profiles with some random noise added to them. On the right are examples of functional profiles: Sine, Flat and Exponential.

Creating Profiles

In paraProp, the minimum required depth resolution Δz is determined by the wavelength λ of the signal, with a requirement that $\Delta z < \lambda$. In TD mode Δz is dependent on the wavelength from the Nyquist frequency $f_{nyquist} = 1/2\delta t$ of the waveform. For example, it was found that resolution of $\Delta z_{paraProp} = 5$ cm was required to simulate frequencies up to 1.9 GHz. In this analysis a resolution of $\Delta z_{paraProp} = 2$ cm is used. An important consideration in the inversion analysis is to select the necessary depth resolution of the refractive index Δz . In the GA-based reconstruction used in this analysis, the refractive index values at a series of equally spaced depths are the model's free parameters or the individual's genes. If the aforementioned minimum depth resolution of paraProp was used to define the spacing, then each individual would contain 300 to 750 genes. A large parameter space will inevitably require more individuals per generation to find optimal solutions and more generations to evolve toward better solutions, which will stretch the limits of available computational power. Another consideration is the number of observables used in the optimization, in this case, the number of points in space in which the propagated signal is sampled. In this analysis, a choice was made to equate the number of genes to the number of observables. Thus, the spacing of the refractive index values used as genes or free parameters is the same as the highest spacing of receiver and transmitter points in space. This leads to the number of genes as 28, with the genes being the refractive index points from $z = 1.5$ m to $z = 15$ m. These correspond to the depths measured by the cross-borehole radar (chapter 6) at the Aletsch glacier campaign (chapter 7).

The remainder of the refractive index profile used in the simulation was found via spline interpolation of the points below depths of 1.5 m. The refractive index for depths between the surface at $z = 0$ m and $z = 1.5$ m is taken from measurements with a coaxial probe permittivity sensor of a snow pit at the Aletsch glacier [82]. An example of such an interpolated profile is shown in Fig. 5.4. In this case, the ice core data of the Guliya data between $z = 1.5$ m and $z = 15$ m is selected and then decimated, leaving only the points from 1.5 to 15 m in 0.5 m increments (5.4a) and 0.2 m increments (5.4b). The resulting profile with a resolution of 0.5 cm is used in the subsequent testing of the GA inversion. However, it should be noted that not all of the density fluctuations are reproduced after the processing, notably two thin and dense layers at ~ 7.5 m and 3.5 m are not shown in the resulting profile for 5.4a. Both cases do not reproduce the thin layer at 12.5 m in 5.4b. However, the 0.2 cm interpolation mostly reconstructs the number of layers, their relative thicknesses, and the refractive index value n . Using the density profile of the Guliya glacier as an example, a good reconstruction of this glacier's density requires a resolution of at least 20 cm for shallow depths [45].

5.2.3 Genetic Operators

A cross-breeding operator is applied to two different refractive index profiles (designated profile 'p' $n_p(z)$ and profile 'm' $n_m(z)$) applying a 'splicing' method. That is, a random depth z_{cut} is selected between z_{min} and z_{max} , and the n values for $z > z_{cut}$ are taken from $n_p(z)$ and $z \leq z_{cut}$ is taken from $n_m(z)$, these are combined to make the child profile $n_c(z)$:

$$n_c(z) = \begin{cases} n_p(z) & \text{if } z > z_{cut} \\ n_m(z) & \text{if } z \leq z_{cut} \end{cases} \quad (5.8)$$

On the other hand the mutation operator acts only on an individual and acts simply to replace one or more $n_i = n(z_i)$ values with a random value n_{rand} with a value $1.2 < n_{rand} < 1.8$. The constraints here on physical assumptions that the highest density in the firn will be the density of solid ice ($\rho_{ice} = 918$ kg/m³, for which $n = 1.8$) and the lowest density will be that of freshly fallen snow ($\rho_{snow} \approx 230$ kg/m³ for which $n \sim 1.2$) The probability of the discrete value n_i is set by a threshold number P_{thres} with a value $0 < P_{thres} < 1$, such that for the mutant profile n_m

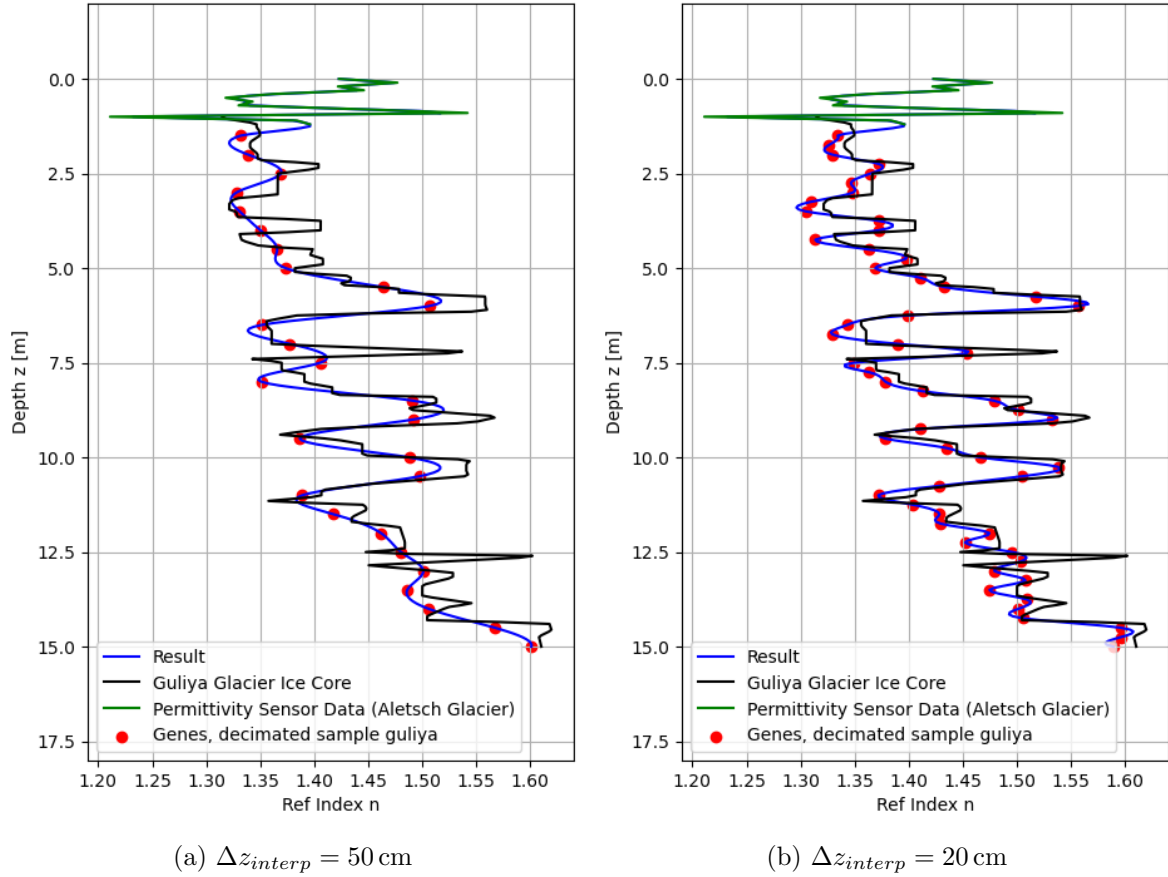


Figure 5.4: The interpolated Guliya glacier with the top 1.5 m defined separately using near field permittivity data from the Aletsch Glacier field campaign 2022[82] (credit Fabian Becker). Shown in Fig. 5.4a is the profile used to define ‘pseudo-data’ with a resolution of $\Delta z = 50$ cm, while on the Fig. 5.4b is the same but with a resolution of $\Delta z = 20$ cm. The 20 cm resolution captures more of the profile data, but a small dense layer at 12.5 m is missing from both examples.

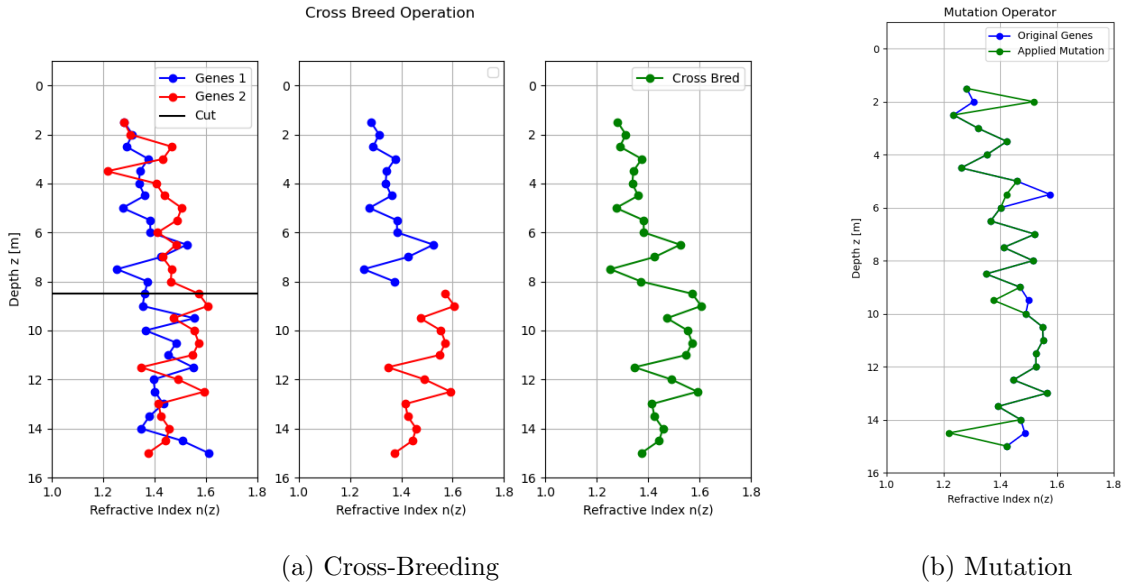


Figure 5.5: Examples of the ‘cross breeding’ and ‘mutation’ genetic operations being applied to form new refractive index profiles.

derived from the parent profile $n_p(z)$:

$$n_m(z) = \begin{cases} n_p(z) & \text{if } R < P_{thres} \\ n_{rand} & \text{if } R \leq P_{thres} \end{cases} \quad (5.9)$$

where R is a random number between 0 and 1. Examples of a cross-breeding operation is shown in Fig. 5.5a and a mutation operation is shown in Fig. 5.5b.

5.2.4 Selection

The selection method used in this analysis are the aforementioned roulette and tournament selection methods. Roulette usually means fitness proportionate selection, and in this case the probability $P_{i,roulette}$ of an individual being selected to be a parent of the next generation is related to the *ranking* of the individual’s fitness score S_i to the distributions of the scores in the population:

$$P_{i,roulette} = 1 - \frac{n(S|S \geq S_i)}{N_{ind}}, \quad (5.10)$$

With N_{ind} being the number of individual’s in the generation. Tournament selection is applied by first randomly selecting a subgroup of the profiles. By default, the number in the subgroup is set to 10. The individual with the highest score is then selected, and the whole distribution of individuals is shuffled, and the process is repeated until the quota of tournament-selected individuals is filled. The final selection process is simply the cloning of some percentage of the best scoring profiles, i.e., the elites.

After calculating the fitness scores for each generation, the selection of elites takes place first, such that the best scoring profiles is always preserved, while the selection of parents by roulette and tournament takes place next. These parents are then subjected to cross-breeding and mutation. The final step is the selection of ‘immigrant’ profiles.

5.3 Testing with Pseudo-Data

Before applying GA based inversion to field test data (see Chapter 7), it was necessary to test the reliability of the reconstruction method using ‘pseudo-data’ generated using paraProp, using user-defined refractive index profiles, including some drawn from density data of real-world glaciers. The following criteria for the efficacy of the reconstruction method are defined:

- Averaged Residual Error of the Refractive Index
- Time of Flight Reconstruction
- Amplitude Reconstruction
- Repeatability

5.3.1 Signal Settings and Antenna Positions

A goal was set beforehand that the GA inversion should return refractive index values with residual offsets within a range of $\Delta n \leq 0.05$ for all depths. The choice of this was motivated by the timing resolution of the signal, for which a somewhat crude approximation is made that the time of flight resolution is equal to the width of the pulse, which is inversely related to the bandwidth of the pulse in Fourier space. The transmitted signal is modeled as a Gaussian pulse, where the magnitude of the pulse $A(t)$, and the magnitude of its spectrum $S(f)$ are Gaussian distributions. For the pulse, the pulse width Δt in the time domain is equivalent to the standard deviation σ of a Gaussian distribution, while for the spectrum the bandwidth is equivalent to the standard deviation. The transmitted pulse $A_{TX}(t)$ can therefore be expressed:

$$A_{TX}(t) = A_0 e^{-\frac{|t-t_{0,TX}|^2}{2\Delta t}} e^{-i2\pi f_{central}t} \quad (5.11)$$

with A_0 being the maximum amplitude, t_0 being the time of peak magnitude of the pulse at the TX, and $f_{central}$ being the central frequency of the pulse’s spectrum. Since the spectrum is also a Gaussian in frequency space, with the standard deviation of the Gaussian defining the bandwidth B , one can see that the pulse-width Δt is the inverse of the bandwidth B :

$$\Delta t = \frac{1}{B} \quad (5.12)$$

For a Gaussian pulse of bandwidth $B = 200$ MHz the pulse-width is $\Delta t = 5$ ns, which hereafter will be referred to as the ‘timing-resolution’. The transmitted pulse and its spectrum are shown in fig 5.6. The location of the transmitters and receivers reflects the positions utilized in the Aletsch glacier field test described in chapter 7 and is shown in the graphic in Fig. 5.7. The transmitting antenna is always located at $R = 0$, with depth ranging from $z_{tx} = 1$ m to $z_{tx} = 15$ m in the B-Scan, with depth intervals of 0.5 m. The receivers are located at ranges of 10 m, 25 m and 42 m. At the first range $R = 10$ m, the receiver is only located at the surface. At $R = 25$ m and 42 m, the receiver position changes from $z_{rx} = 0$ m to $z_{rx} = 15$ m, with intervals of 0.5 m for the former range and 1 m for the latter.

If horizontal propagation is assumed at the depth z , one would then measure the refractive index to a resolution $\Delta n = c\Delta t/R$, which for $R = 25$ m is $\Delta n = 0.06$ and for $R = 42$ m is $\Delta n = 0.032$ respectively. Thus the choice of $\Delta n = 0.05$ was made as a desirable minimum reconstruction residual.

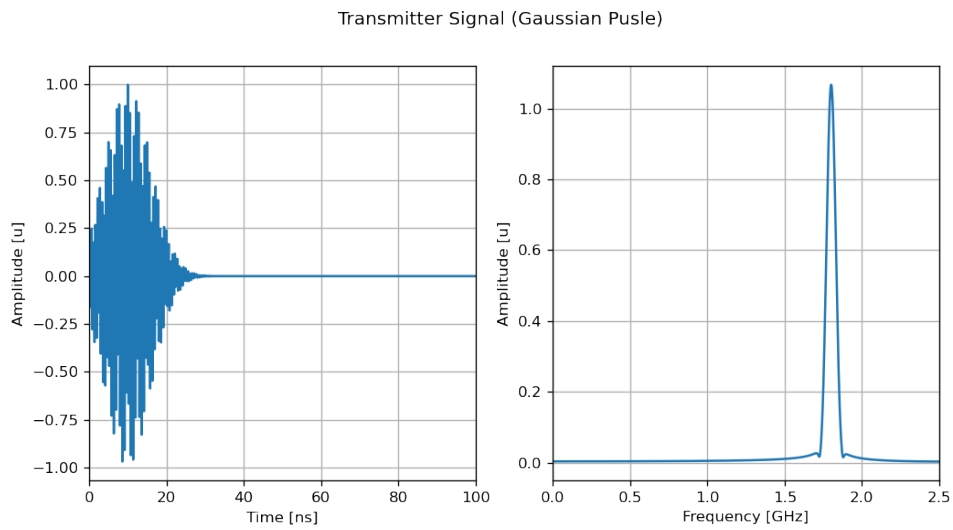


Figure 5.6: Left: the transmitted signal: a 200 MHz bandwidth Gaussian pulse emitted with a delay of 10 ns, with the amplitude shown in arbitrary units. Right: the Fourier spectrum of the pulse, showing the central frequency of 1.8 GHz

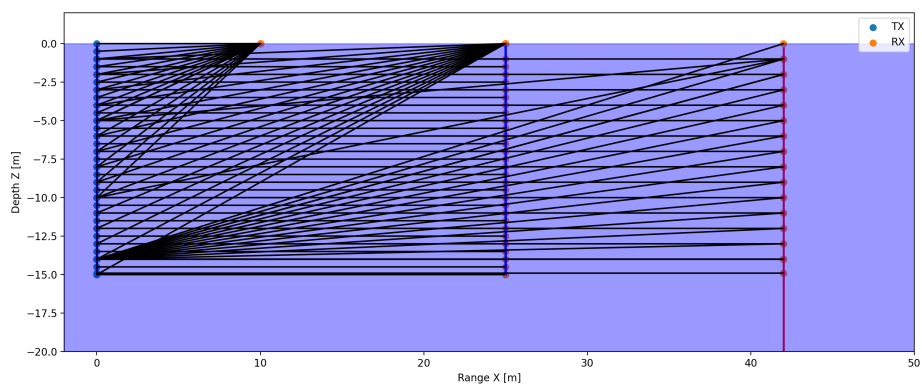


Figure 5.7: The positions of transmitters and receivers used in the 2022 Aletsch Glacier field campaign, used to define the TX, RX configuration in the example of GA reconstruction in this chapter.

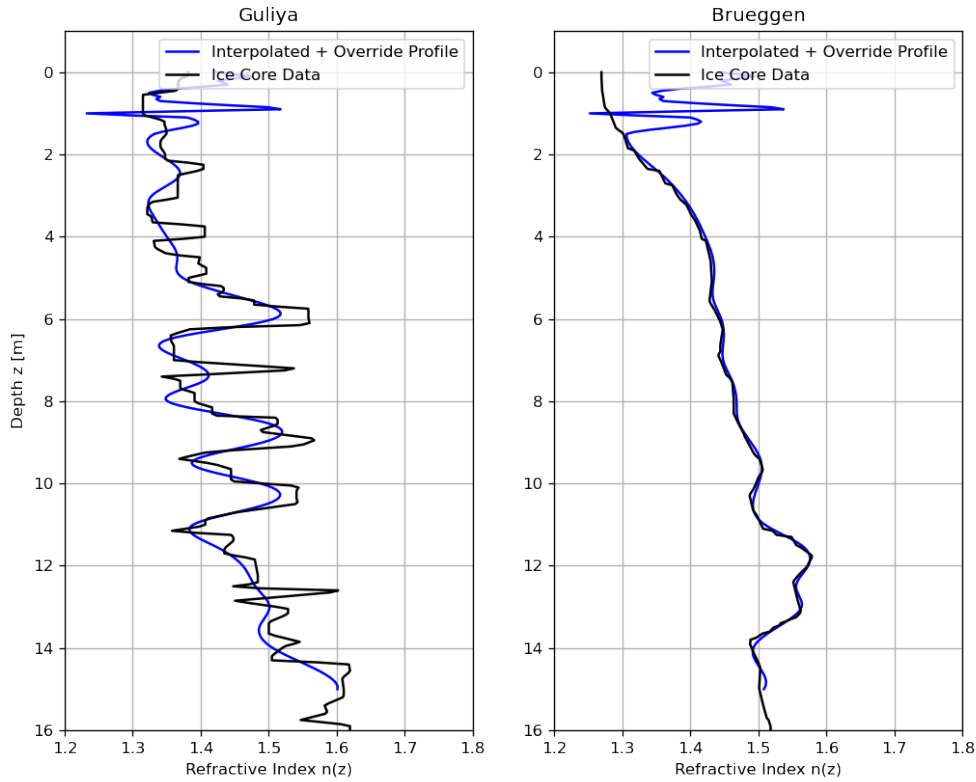


Figure 5.8: The profiles used to define the ‘pseudo-data’ for the Guliya glacier (left) and the Brueggen glacier (right), with the Aletsch glacier snow profile obtained with a permittivity sensor overlapping the first 1.5 m [82].

5.3.2 Ref-Index Scenarios

In testing, two real-world glaciers are used, the Guliya glacier located in the region of Western Tian Shan in the Tibetan Autonomous Region of China (data obtained from [45]) and the Brueggen glacier in Chile [73]. In both cases, the genes are the refractive indices at discrete depth points from $z_{min} = 1.5$ to $z_{max} = 15$, and the refractive index values used in the simulation are interpolated between these points. The profiles used to generate the pseudo-data are shown in Fig. 5.8.

5.3.3 RF Simulation Setup

The geometry of the simulation domain was chosen to be large enough allow for the signal to be sampled at the distance of the receivers RX from the transmitter TX , and to represent the maximum depth sampled by TX and RX in the Aletsch glacier field test (see chapter 7). The simulation uses axes x , which represents range, and z , which represents depth. The maximum length of the simulation is called the ‘Ice Length’ L_{ice} , and the vertical distance from the surface $z = 0$ to the maximum depth of the simulated ice is the ‘Ice Depth’. The resolution in the x -direction or horizontal direction is Δx , and the resolution in the z -direction or vertical direction is Δz . In this example, the geometry settings are as follows:

- Ice Length $L_{ice} = 50$ m
- Ice Depth $Z_{ice} = 15$ m

- Horizontal Resolution $dx = 1$ m
- Vertical Resolution $dz = 0.05$ m

As mentioned before, the transmitted signal is modeled as a Gaussian pulse described with equation 5.11, with the defining parameters: peak magnitude A_0 , time of peak magnitude t_0 , central frequency $f_{central}$ and bandwidth B . In this study, the electric field amplitude is defined with arbitrary units u and expressed in the paraProp simulation code as a complex vector, with the number of elements being the ‘sample number’ N_{sample} . Each vector element is the pulse electric field amplitude at an instant in time, with the timing intervals dt being equal for all elements. Thus, we simulate the waveform from a start time of $t_{start} = 0$ to a maximum time t_{max} . In this example we use the following signal parameters:

- Central Frequency $f_{central} = 1.7$ GHz
- Bandwidth $B = 200$ MHz
- Time of peak magnitude at TX: $t_{TX,0} = 10$ ns
- Peak amplitude $A_0 = 1$ u
- Time interval $dt = 0.2$ ns
- Sample number $N_{sample} = 3000$
- Maximum Time $t_{max} = N_{sample}dt = 600.0$ ns

5.3.4 GA Settings

For the two examples of the GA reconstruction of the refractive index profile of the pseudo-data, each generation contained 200 individual profiles and ran over 100 generations. Each profile was simulated using paraProp using the above settings (section 5.3.3). The time needed to complete a simulation is proportional to the multiple of the number of samples in time-space, the size of range space and depth space over the respective resolutions, and the number of transmitters. With the utilized settings, each paraProp simulation was completed within approximately 10 to 15 minutes, utilizing one CPU core and 500 MB of memory. To make the solution of the GA feasible, the supercomputer cluster PLEIADES at the University of Wuppertal was used [2]. Each individual was simulated on a separate CPU core. It was not practical to save the signal data from each profile, as each required ~ 50 MB), but the reconstructed refractive index profiles and the fitness scores were saved to a hierarchical data format (HDF) file, and any profile of interest could be simulated at a later time. **Main Settings**

- Number of Generations $N_{Generations} = 100$
- Number of Individuals $N_{Individuals} = 200$
- Number of Genes $N_{genes} = 28$
- Minimum Depth of Genes $z_{min} = 1.5$ m
- Maximum Depth of Genes $z_{max} = 15$ m

Parent Selection Settings

- Fraction of Elites: $f_{elites} = 0.05$
- Fraction of Parents: $f_{parents} = 0.85$
 - Fraction of Parents selected by Roulette: $f_{Roulette} = 0.7$

– Fraction of Parents selected by Tournament: $f_{Tournament} = 0.3$

- Fraction of Immigrants $f_{immigrants} = 0.1$

Operator Settings

- Mutation Fraction: $f_{mutation} = 0.4$
- Cross-Breeding Fraction: $f_{cross-breed} = 0.6$

Initialization Settings

- $f_{fluctuations} = 0.8$
- $f_{sine} = 0.05$
- $f_{flat} = 0.05$
- $f_{exp} = 0.1$

5.3.5 Results

For both Brueggen and Guliya the inversion method were able to return solutions of the refractive index profile to within a residual error well below $\Delta n_{residual} < 0.05$, and the shape of the best resulting profile is similar to the shape of the ‘truth’ profile, i.e. the profile used to produce pseudo-data. The agreement between the simulated signal data shows a substantial improvement from initialization through to the last generation. The results for Brueggen and Guliya are presented, showing the evolution of the fitness score, the profile reconstruction, and signal reconstruction.

Results: Brueggen

The evolution of the fitness score is shown in figure 5.9, with the evolution of the scores being shown by plotting the ‘best’ score along with the mean and median values of the scores per generation. The mean and median scores mostly fluctuate around $S \approx 0.05$ from generation 18 onwards, but the ‘best’ score per generation goes from $S_{gen=1} \approx 0.007$ to $S_{gen=95} \approx 0.011$, an improvement of $\sim 57\%$. The best-fit $n(z)$ profile (found at generation 95) to the Brueggen pseudo-data is in good agreement with the initialization profile, with $\Delta n_{RMS} < 0.02$ across all depths, well exceeding that target resolution of $\Delta n < 0.05$. Its noteworthy that the first generation obtained a fit that fell within the target resolution for most sampled depths, with the exception of $1\text{ m} < z < 0.2\text{ m}$ and close to $z = 12\text{ m}$.

It could also be remarked that the Brueggen pseudo-data was relatively easy to find fitting profiles for compared to the Guliya example. This was due to it having a smooth profile from $z = 2\text{ m}$ to $z \approx 11\text{ m}$, with the only noticeable anomaly being a dense layer between $z = 11\text{ m}$ and $z = 14\text{ m}$ as seen Fig. 5.10. The initial best guess was an exponential profile, which already is mostly within the aforementioned desirable boundary of $\Delta \leq 0.05$. The next generation sees the reduction of the refractive index at $z = 2\text{ m}$, being reproduced in the next generation in the profile (also seen in Fig. 5.10), while the bulge in density gradually takes shape and becomes obvious by generation 80. The best resulting profile appears at generation 95 (see 5.10), with the shape being constrained to within $-2.5 \leq \Delta n \leq 0.05$, with a noticeable systematic offset of $\Delta n_{sys} \approx 0.01$.

Signal Reconstruction

The reconstruction of the signal is represented by comparing the parallel depth B-scans (Fig. 5.11) of the best score of the first generation (shown in the middle plot) and the best score of

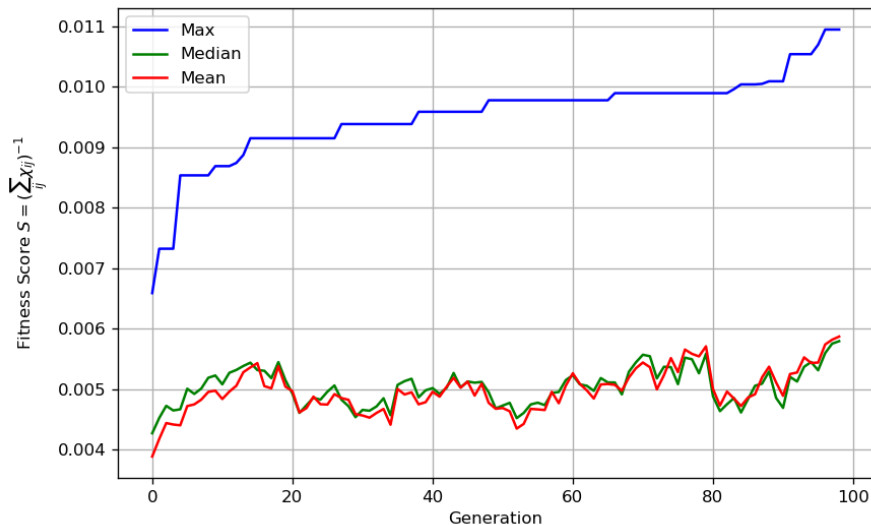


Figure 5.9: The evolution of the fitness score S for the reconstruction of the Brueggen over 100 generations. The best distribution score in each generation is indicated in blue as ‘Max,’ while the mean and median average of the score distribution in each generation is shown in red and green, respectively.

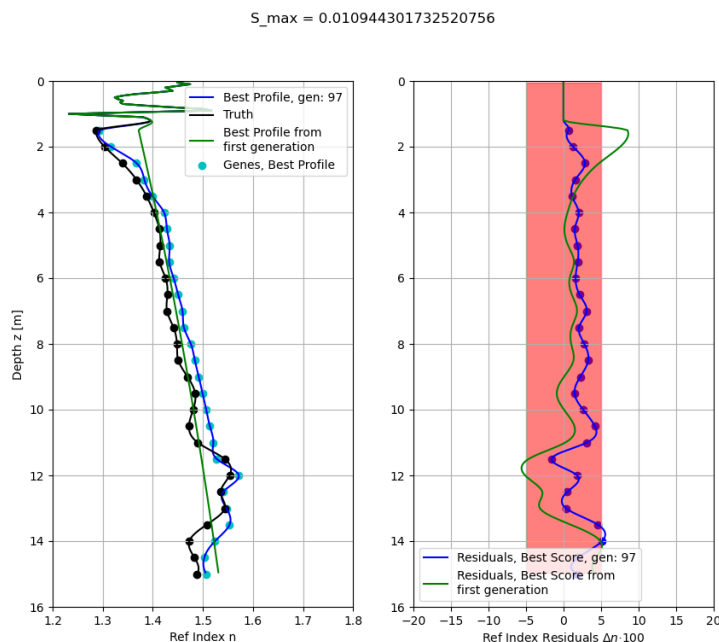


Figure 5.10: Brueggen Refractive-Index Reconstruction. Left: the genes used to define the profiles are displayed as dots, with the interpolated profile as ‘solid lines,’ with the best result from the first generation in green, the best result from the entire process in blue, and the pseudo-data in black. Right: the residuals of the profile; the resolution window of $n_{sim}(z) - n_{data}(z) \leq \pm 0.05$ is shaded in red.

the whole inversion process (shown on the right) against the B-scan of pseudo-data (shown on the left). The evolution of the signal reconstruction is somewhat difficult to discern, and indeed, the shapes are broadly similar, with a direct signal feature that tracks well with the shape of the profile and a reflection signal feature that diverges at $z \approx 10$ m, which likely originates from the dense layer at $z = 1$ m, or from the surface.

The improvement of the signal reconstruction is seen more clearly by looking at the logarithm of the ratio of the signal envelopes $E(t) = \sqrt{\text{Re}(A(t))^2 + \text{Im}(A(t))^2}$ between the output of the GA and the pseudo-data (see 5.12) where,

$$\frac{d\chi}{dt} = \left| \log \left(\frac{E_{data}(t, m)}{E_{sim}(t)} \right) \right|^2. \quad (5.13)$$

$$\chi(t) = \int_{t_{min}}^{t_{max}} \frac{d\chi}{dt} dt. \quad (5.14)$$

From which the misfit score χ was obtained by integrating over the flight time of each TX and RX. The envelope ratio B-Scans show good agreement between the best result from generation 95 and that of the Pseudo-Data, with both the direct and the main reflection component.

A comparison between selected A-Scans of the pseudo-data, the best result from the first generation and from the best overall result are shown in Fig. 5.13, with two ‘parallel depth; examples and two ‘cross-depth’ examples:

- $z_{tx} = 11$ m, $R = 25$ m, $z_{rx} = 11$ m (Fig. 5.13a)
- $z_{tx} = 5$ m, $R = 42$ m, $z_{rx} = 5$ m (Fig. 5.13b)
- $z_{tx} = 1$ m, $R = 42$ m, $z_{rx} = 9$ m (Fig. 5.13c)
- $z_{tx} = 9$ m, $R = 42$ m, $z_{rx} = 7$ m (Fig. 5.13d).

Results: Guliya

The fitness score evolution is shown in Fig. 5.14, continuous improvement of the score distribution from generation 0 until 30, where the mean and median scores start to fluctuate about a value of $S \approx 0.003$, while the maximum score in the distribution continues to improve until generation 57.

Compared to the prior example of Brueggen, Guliya features a larger number of relatively re-frozen dense layers, leading to more in-ice reflections and signal delays. Due to the interpolation, the ‘truth’ profile has fewer dense layers, the density gradient is not as sharp, but there are still 5 significant dense layers. A more complex signal set should therefore be harder to fit for. Nevertheless, the GA inversion was also able to reconstruct the refractive index profile within $\Delta z \leq 0.05$ for 26 out of 30 sampled depths, and a maximum deviation of $\Delta n_{max} 0.065$. The GA reconstruction procedure was thus able to show a substantial improvement of the best-fit profile from generation 0 to generation 60. The best fit from the initial generation was generated from the ‘first peak’ selection method and represented the general trend of the profile without the density fluctuations. The best result is obtained at generation 57 (see Fig. 5.15), with the 5 density fluctuations ($z = 3$ m, 6 m, 7.5 m, 9 m, 10.25 m) being visible in the best-fit profile, although the dense layer at $z = 6$ m is both broader and has a lower n value than for the pseudo-data profile. It also reconstructs a feature at 13.5 m that is not present in the pseudo-data profile, although the gap between $z = 13.5$ m and $z = 14.5$ m could be argued to be a ‘shifted down’ gap from the pseudo-data profile.

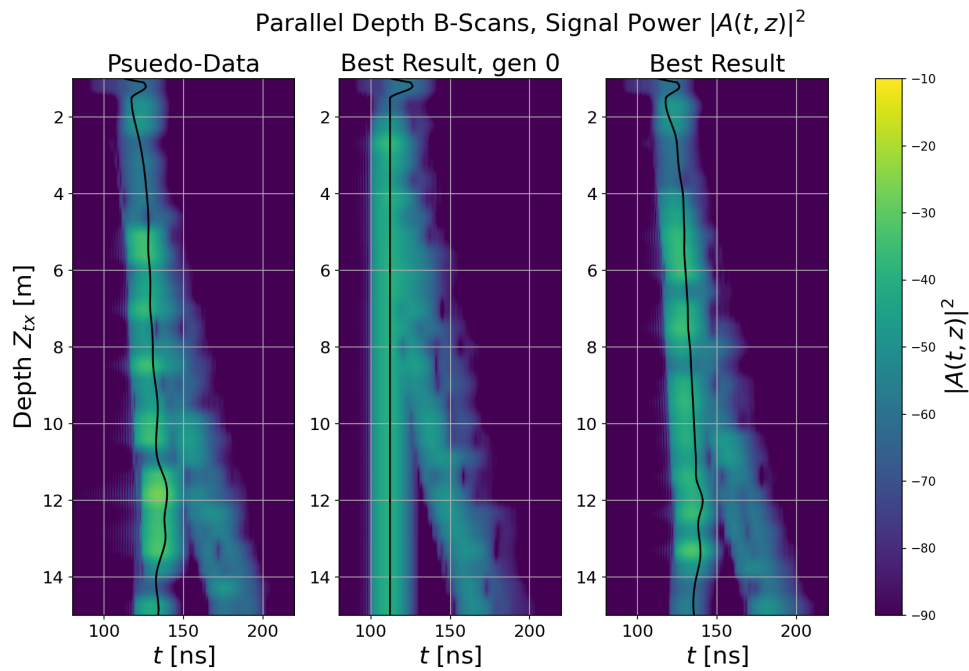


Figure 5.11: The Parallel Depth B-Scans of the Brueggen Glacier simulation. Left side: the pseudo-data, middle: the best result from generation 0, right side: the best result overall. the horizontal time of flight defined using the refractive index profile $t(z) = Rn(z)/c$ is shown in black.

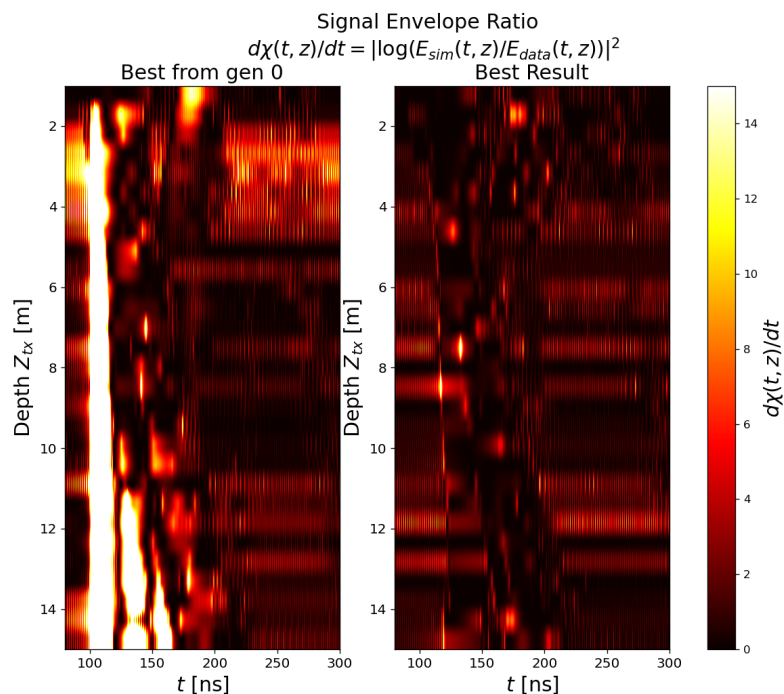


Figure 5.12: Brueggen: the parallel B-Scan of the ratio of the signal envelope of the simulation over the data signal envelope. Left: the envelope ratio for the best result from generation 0, Right: the best overall result.

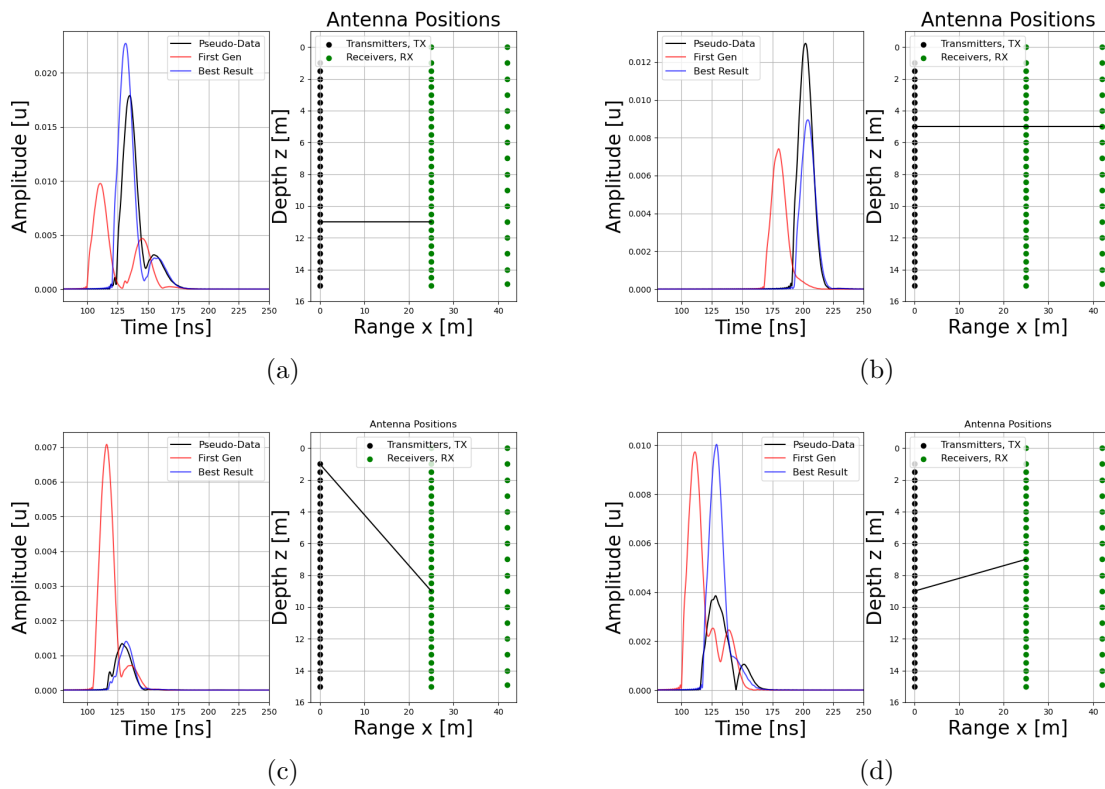


Figure 5.13: Examples of A-Scans from different TX and RX combinations for the Pseudo-Data (black), best result of first generation (red), and best overall result (blue).

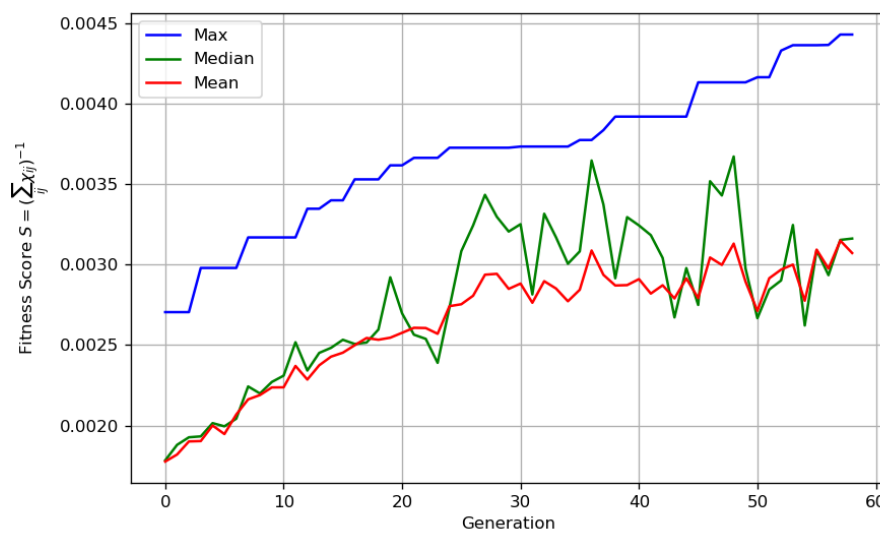


Figure 5.14: The evolution of the fitness score S for the reconstruction of the Guliya over 60 generations.

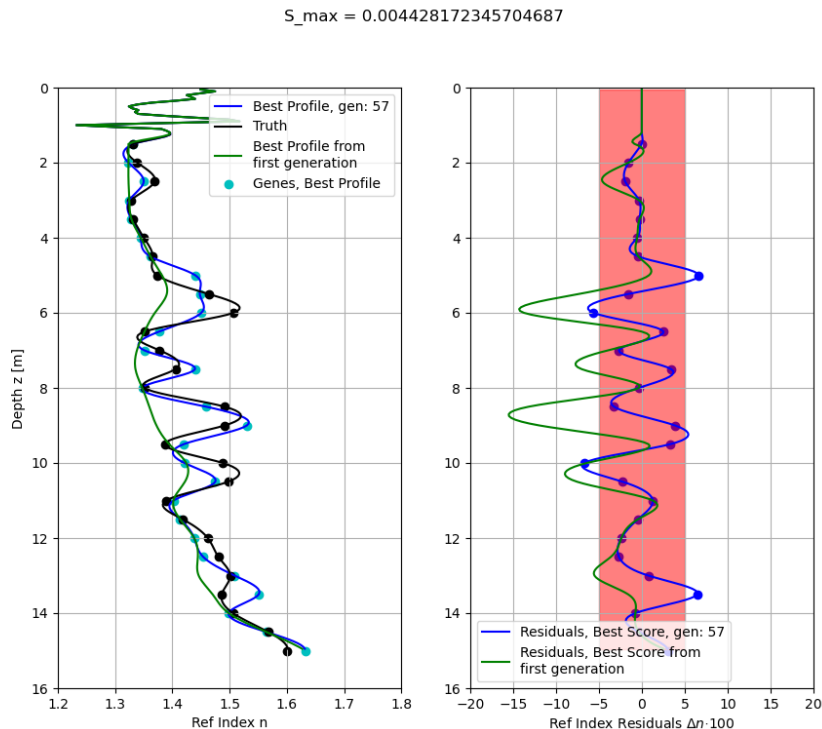


Figure 5.15: The evolution refractive index reconstruction of the Guliya glacier, with the best overall result obtained in generation 57.

Signal Reconstruction

The improvement from generation 0 and 57 is easier to discern from the parallel depth B-Scan plots in Fig. 5.16. The B-Scans of the pseudo-data and generation 57 best result show amplification of the signal intensity at locations of high refractive index gradient, although the amplification is both more localized and more prominent in the pseudo-data than for generation 57. In Fig. 5.17, the parallel depth B-Scans of the envelope ratios between the generation 0 best result and the pseudo-data is shown on the left, and the one for the generation 57 best result, and the pseudo-data is shown on the right, once again displaying good agreement for generation 57 and the pseudo-data. In Fig. 5.18, the improvement in the pulse reconstruction from generation 1 to generation 57 at 4 different TX-RX configurations is shown.

5.4 Discussion

This work claims a tentative refractive index reconstruction precision of $\Delta n \leq 0.05$ for a depth resolution of $\Delta z = 0.5$ m, using 200 MHz bandwidth pulses. However, the GA's performance is limited by the complexity of the parameter space, and care must be taken to avoid premature convergence to a local maximum of the fitness score while still allowing for optimization of the model.

It has been demonstrated in this chapter that genetic algorithms can optimize a set of models of depth-variant and range-constant refractive index profiles towards an optimal solution sufficient to reconstruction the time of flight of signals, but not the amplitudes. The performance of the GA-based inversion was tested smoothly, varying refractive index profiles and ones with large numbers of density fluctuations, with an interpolation resolution $\Delta z = 0.5$ m.

A general remark is that the reconstruction algorithm can replicate the time-of-flight of the

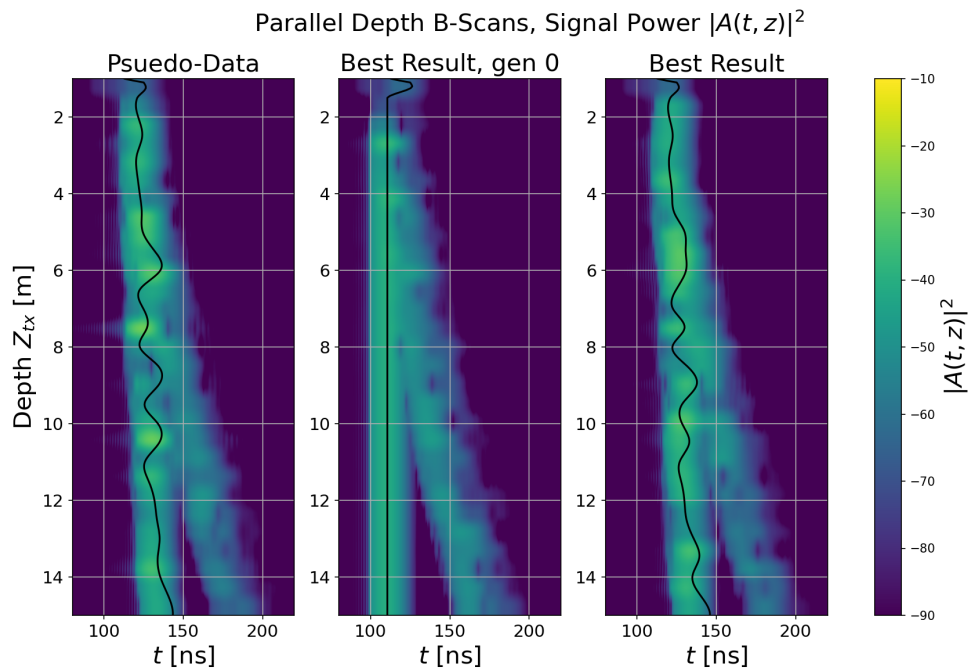


Figure 5.16: Parallel Depth B-Scans for Guliya. Note the amplification of the signal at points of high refractive index gradient: ($z = 3$ m, 6 m, 7.5 m, 9 m, 10.25 m) between the pseudo-data and the best overall result. the horizontal time of flight defined using the refractive index profile $t(z) = Rn(z)/c$ is shown in black.

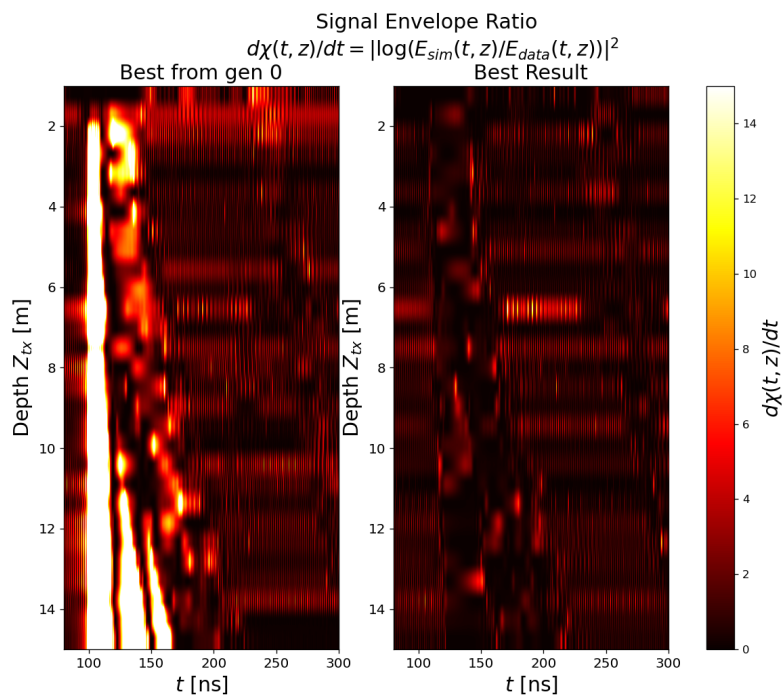


Figure 5.17: Guliya: envelope ratio parallel depth B-Scan. Left: the envelope ratio for the best result from generation 0, Right: the best overall result.

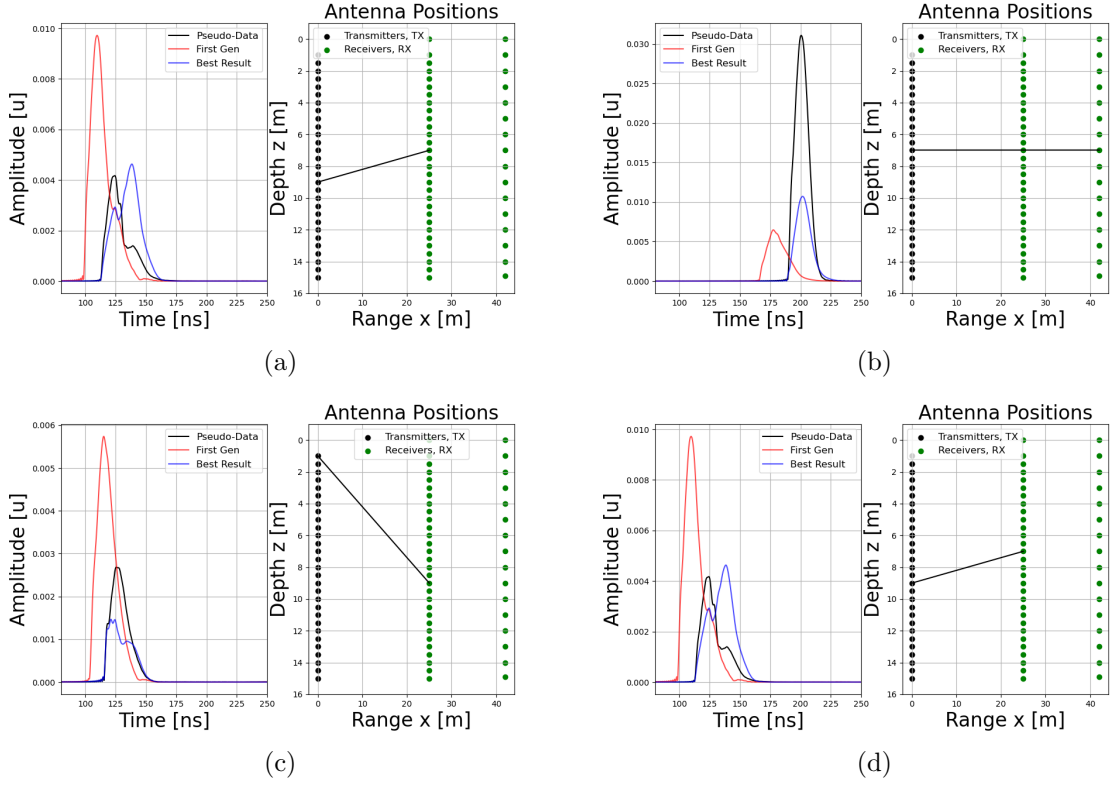


Figure 5.18: Examples of A-Scans from different TX and RX combinations for the Pseudo-Data (black), best result of first generation (red), and best overall result (blue).

first and second most significant features of the A-Scans. However, the reconstruction of the amplitude of the signals was less accurate. It also appeared to be easier, especially in the case of Guliya, to reconstruct signals across depths $z_{tx} = z_{rx}$, than it was to simulate horizontal propagation $z_{tx} = z_{rx}$. The likely explanation for this is the increased complexity of signals, which are ‘trapped’ between layers, leading to diffractive effects and multiple internal reflections. The more components of the signal to find a fit for, the more difficult it will be to find an optimal solution.

5.4.1 Limitations of Inversion

The goal of the inversion analysis is to accurately reconstruct the ice’s refractive index or permittivity profile in the depths examined by radar. The received signals at a discrete set of points defined by the receiver positions and the origin at the transmitter are the observables that the GA uses to evaluate the fitness of individual refractive index models. In doing so, one assumes a causal link between the observables and the model parameters. This can be expressed using a function ξ , which formalizes the relationship between the observables: the array of signal data for the different TX and RX positions $A_{TX,RX}$ and the refractive index model m ;

$$A_{TX,RX} = \xi(m). \quad (5.15)$$

If ξ is bijective, then there would exist a unique solution m^* for every unique array of signal data, making the problem ‘well-posed’. In fact, inversion problems are usually ‘ill-posed’, where there is no guarantee that a unique solution exists for m^* , and one must settle for a set of parameters that explain the observables to some acceptable level of precision.

$$m_* = \min_m (A_{TX,RX} - \xi(m)). \quad (5.16)$$

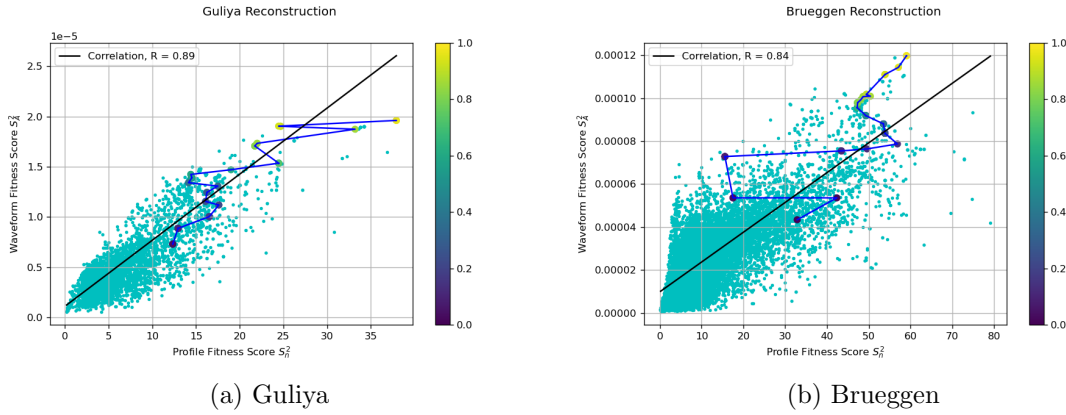


Figure 5.19: The square of the fitness score calculated from the waveform S_A , compared with that calculated from the refractive index profiles.

The key assumptions made in this inversion analysis: that the refractive-index profile is depth variable but not range variable, that the antenna can be reduced to an infinitesimal dipole, and smooth transition between the points used to define the genes of the model, all of these will prevent a unique solution for a given set of radar data. In chapter 8, it will be seen that uncertainties in the behavior of the permittivity radar system (chapter 6) would severely limit the ability of the GA method to reconstruct the refractive index to better than $\Delta n < 0.05$.

5.4.2 Limitations of GAs

Having discussed the fundamental limitations of inversion analysis, one must discuss the performance of the GA algorithm on pseudo-data produced directly with paraProp. One approach is to look at the relationship between the data's fitness score and the refractive index's residual error. The latter may also be expressed as a 'fitness score': S_n , distinct from the GA evaluative fitness score, which will be described as S_A for clarity in this discussion. S_n is simply the inverse of the sum of the difference between the refractive index of model $m_l = n_l(z)$:

$$S_n(m_l) = \left(\sum_i |n_{truth} - n_l(z_i)|^2 \right)^{-1} \quad (5.17)$$

In Fig. 5.19, the distribution of S_n^2 and S_A^2 for the GA analysis conducted for Guliya and Brueggen is shown, along with a line that shows the change of the fitness scores S_n and S_A for the 'best' score per generation. In both cases, one sees a clear correlation between S_n^2 and S_A^2 , but a wide degeneracy of the solutions. A final remark is to comment that the examples shown in the chapter are quite artificial, as the refractive index profiles are interpolated approximations of real-world data and are range independent, which, as noted in section F, will not generally be true in real-world glaciers. Based on the real-world glacier from Guliya (section 5.3.5), a resolution of $\Delta z < 0.02$ m is necessary to accurately replicate the density profile of ice using the interpolation method. Thus, reconstruction of a range-independence profile will require > 55 genes, a subject for later investigation. Finally, this analysis has so far neglected range-dependent profiles $n(x, z)$. Reconstruction in two dimensions is a challenging problem and will likely require multiple sampling points in the range direction to be solvable.

Chapter 6

Cross-Borehole Permittivity Radar

As discussed in chapter 3, the successful location of a subsurface water pocket with radar and localization of the melting probe requires some estimate of the intervening permittivity distribution. One concept to measure the permittivity is to use the melting probe as a radar transmitter or receiver and to estimate the permittivity by measuring the propagation time between the probe and surface antennas or other in-ice probes (this concept is illustrated in Fig. 6.1). This concept was tested with the construction and testing of a prototype cross-borehole radar (also referred to here as the ‘permittivity radar’) with a remote transmitter (TX) and receiver deployed in the ice and controlled from the surface. In section 6.1, the frequency modulated continuous wave (FMCW) technique used to obtain time-of-flight measurements is described. In section 6.2, the design of the permittivity radar is described, along with a detailed description of the electronics and antennas. The measurement procedure for obtaining the signal propagation time is explained in section 6.3. An overview of the testing of the operation and performance of the permittivity radar, both of individual components and the combined system, is given in section 6.4. A summary of the system specifications and experimental uncertainties is given in section 6.5. The cross-borehole radar was tested at a field test at the Aletsch Glacier in the winter of 2022, which is the subject of the following chapter (chapter 7).

6.1 Modulation Technique

Various modulation techniques exist in surface penetrating radar (SPR) and cross-borehole radar (CBR) applications, the optimal choice depends on the application. The most common technique is an impulse radar, which emits a short pulse from the transmitter. These fall into the category of ‘amplitude modulation’ (AM). The second most common technique is ‘frequency modulation continuous wave’ (FMCW)[22]. The use of the FMCW technique is preferable to pulsed radars when frequencies greater than $f > 1$ GHz [22]. FMCW radars typically have a wider dynamic range, that is, the difference in power between the maximum emitted power of the system and the noise floor. They also have lower noise levels and higher mean radiated power[22]. An additional benefit is that, in contrast to pulsed radars where the sampling frequency should be greater than the bandwidth of interest, the information contained in an FMCW radar is generally at frequencies far lower than the bandwidth, typically in the acoustic range: 1 kHz f 10MHz. The explanation for the latter, as well as a more detailed description of FMCW will be contained within the following section.

6.1.1 Frequency Modulated Continuous Wave (FMCW) Radar

In common usage FMCW is a modulation technique used by mono-static radar to precisely measure the distance to a reflective target. They are also capable of measuring the target’s relative velocity in the line’s direction from the target to the radar. In a mono-static configuration, a transmitting (TX) and receiving (RX) antenna are at the same location and are connected to

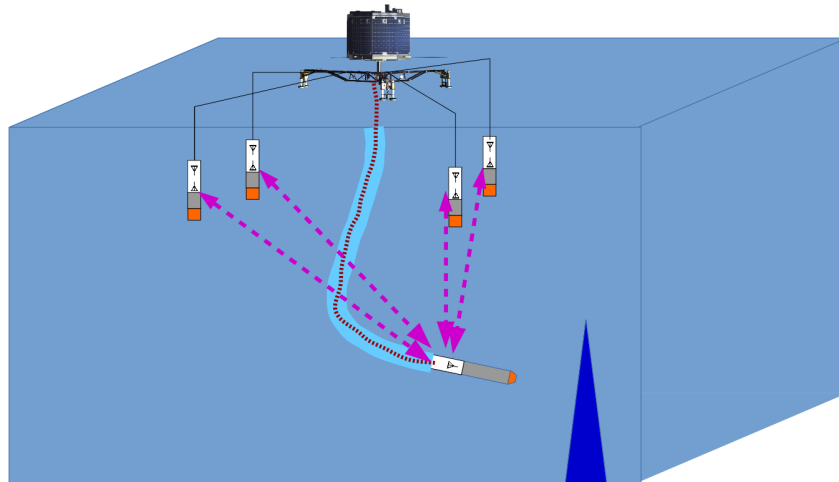


Figure 6.1: A concept for measuring the time-of-flight between a transmitting antenna the EnEx melting probe, and near-surface receivers. This concept is inspired by the APS navigation system proposed for acoustic transducers in the related EnEx project[26] (see chapter 3 for a description).

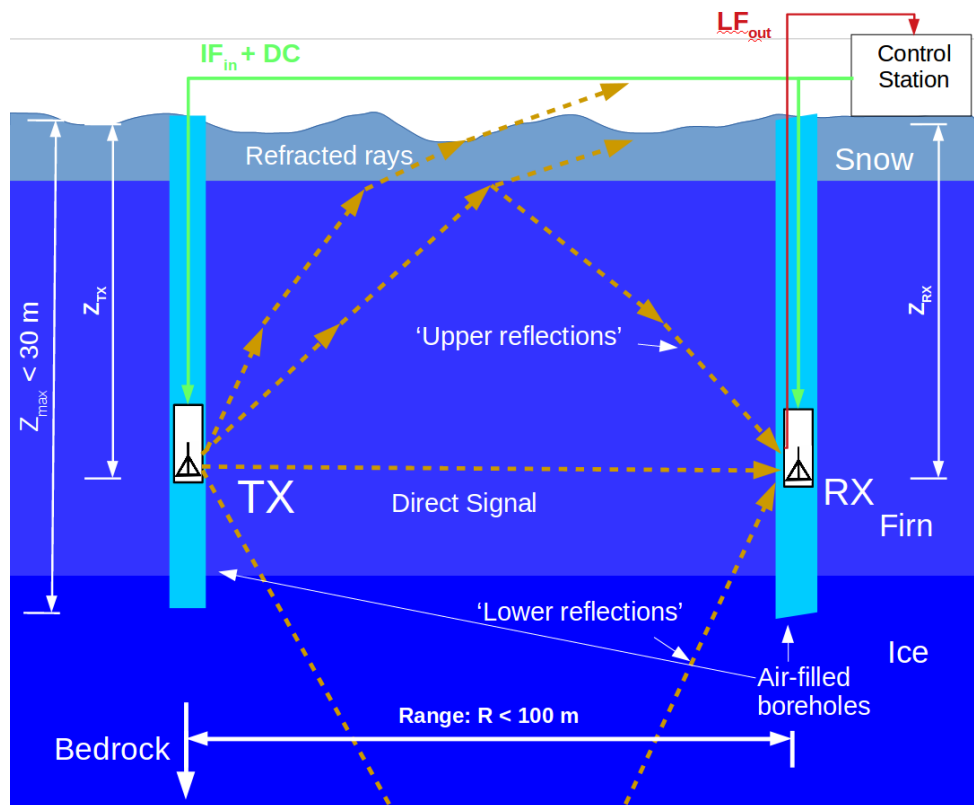


Figure 6.2: An illustration of how the permittivity radar is deployed on a glacier. The transmitter and receiver are deployed at depths Z_{tx} and Z_{RX} respectively, in prepared boreholes separated by a distance R in the field, connected to the control station at the surface via cables. The ‘green’ lines show the cables carrying the IF reference signal, while the red line shows the cable carrying the LF output from the mixer. The orange dashed lines correspond to ‘rays’ of radio-wave signals propagating away from the TX, some of which are sampled by the RX, which should observe a direct propagating signal and reflections from layers above and below its depth. The length of the cables limited the deepest accessible depth Z_{max} to $Z_{max} < 30$ m and range to $R < 100$ m.

a local oscillator (LO), which produces a time-varying signal $e(t)$, in which the frequency varies according to some function $f(t)$ over a fixed period T . This can occur as a single burst over a time T or can be repeated in multiple cycles. The signal is placed through a splitter which outputs two new signals, which are hereby defined as the TX signal $e_{TX}(t)$ and the ‘local oscillator or LO signal $e_{LO}(t)$, which becomes the input for a mixer circuit. The TX signal $e_{TX}(t)$ becomes the input for a power amplifier (PA), and the output is then emitted from the TX. The emitted signal propagates through space and scatters off the target of interest. The back-scattered signal is then recorded by the receiving antenna, typically passing through a low-noise amplifier to be recorded as $e_{RX}(t)$. Due to the round-trip travel time Δt , the received signal will have an instantaneous frequency offset Δf that is directly proportional to Δt . After multiplying $e_{RX}(t)$ and $e_{LO}(t)$ in the frequency mixer, the output signal from the mixer $e_{mixer}(t)$ can then be digitized in an analog-digital converter (ADC). If one can describe the two inputs to the mixer as sine waves ($e_{LO}(t) = A_1 \sin(\omega_1(t)t)$ and $e_{RX}(t) = A_2 \sin(\omega_2(t)t)$), the resulting output will, to first order, be the sum of the cosines of the sum and difference of the frequencies,

$$e_{mixer}(t) = e_{LO}(t) \cdot e_{RX}(t) = A_1 A_2 [\cos((\omega_1(t) + \omega_2(t))t) + \cos((\omega_1(t) - \omega_2(t))t)] \\ \approx A_1 A_2 \cos(\Delta\omega(t)t). \quad (6.1)$$

When processed through a low pass filter, the resulting signal will then be a function of the difference of the frequencies. Different ways to modulate the frequency exist, with a linear ramp being a typical and practical case. This may be a ‘sawtooth’ with the frequency sweeping up to down or down to up, or a triangle wave with the frequency sweeping up to down to up to down, and so on. For a sawtooth ramp, the frequency at a given time $f(t)$ increases from a minimum frequency f_{min} to a maximum f_{max} where the difference between these is the bandwidth $B = f_{max} - f_{min}$,

$$f(t) = B/T \cdot t + f_{min} \text{ if } N \cdot T < t < (N + 1) \cdot T. \quad (6.2)$$

Where N is any integer number. Hence, the beat frequency Δf is linearly proportional to the round-trip signal time,

$$\Delta f = B/T \cdot \Delta t. \quad (6.3)$$

Both transmitter and receiver are connected to tuned oscillators that produce a signal with a continuous linearly ramped frequency $f_{RF} = f_{base} + \frac{df}{dt} \times t$ (with $\frac{df}{dt} = \frac{B}{T}$) over a period T and within a bandwidth B . The time difference between the transmitted signal and the receiver’s reference signal will result in a frequency offset Δf . In a vacuum, or in the air where the refractive index is very close to that of the vacuum $n_{air} = 1.0003 \approx 1.0$, the frequency offset Δf is therefore:

$$\Delta f = \frac{df}{dt} \Delta t = \frac{B}{T} \Delta t = \frac{B R}{T c} \quad (6.4)$$

that can be measured in the output of a frequency multiplier $e_{mixer}(t)$:

$$e_{mixer}(t) = \sin(2\pi(f_{base} + B/T)t) \times \sin(2\pi(f_{base} + B/T)t + \delta t) \approx \cos(2\pi \Delta f t) \quad (6.5)$$

The frequency shift Δf should then be visible in the Fourier spectrum of the frequency multiplier. For an example where $B = 200$ MHz and the modulation time is $T = 1$ ms, the frequency shift Δf is in the audio frequency range; $\Delta f = 20$ kHz if $\Delta t = 100$ ns. Consequently, such measurements are possible with relatively low sampling rates. The uncertainty in propagation time δt is inversely proportional to the bandwidth:

$$\delta t = \frac{1}{B} \quad (6.6)$$

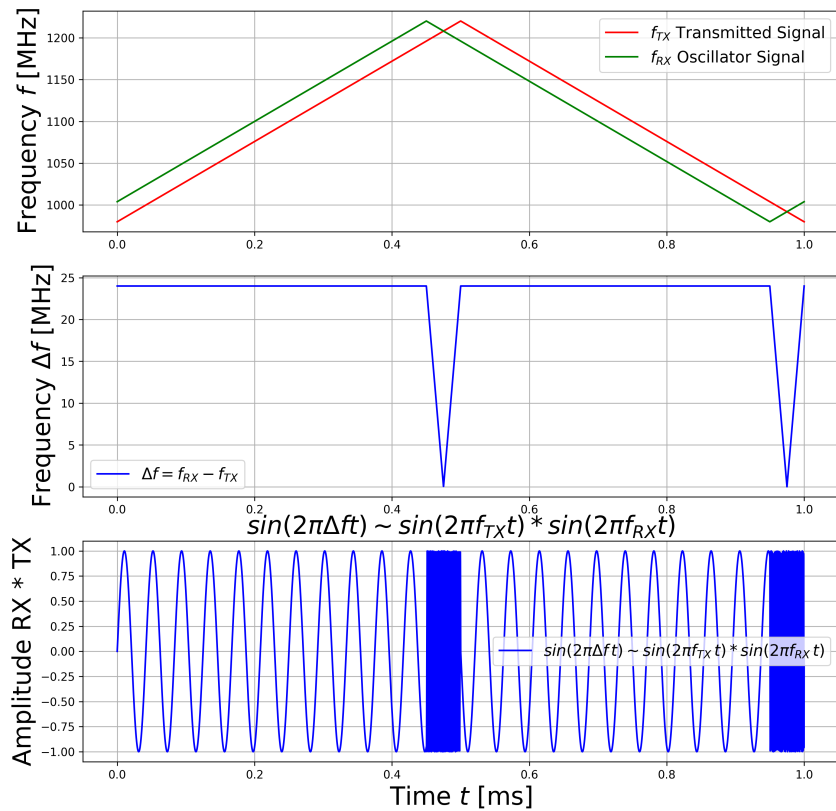


Figure 6.3: An example triangle modulation frequency ramp, with the frequency of the local oscillator (LO) in green and the signal propagating through space from TX to RX (either directly or by back-scatter off another object) is shown in red (top picture). Due to the time offset Δt between the two signals, there is a frequency Δf , which can be seen as a function of time (middle picture). The resulting signal (when passed through a low pass) appears as a simple sine wave for most of the observation time (bottom picture).

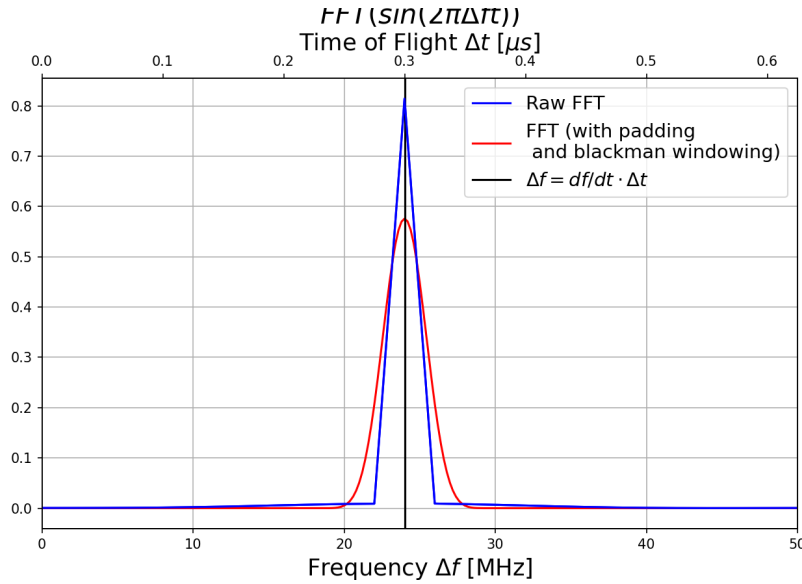


Figure 6.4: The Fourier transform of the waveform shown in Fig. 6.3. The FFT of the waveform (a perfect sine wave) is a simple Dirac-delta function with a non-zero value at the waveform’s frequency ($\Delta f = 25$ MHz in this case). In practice, however, the raw waveform will be processed before the FFT, including with ‘padding’ of the waveform and windowing with a function such as the Blackman function, resulting in a smoothed-out Gaussian waveform in the FFT. The data processing is described in section 6.3.2.

6.2 Design

To measure the permittivity profile of the upper ice/firn of the Aletsch glacier in the EnEx Field Test (chapter 7) a cross-borehole radar was developed to measure the signal propagating from a single transmitter (TX) to one or more receivers (RX) for different positions of both TX and RX in the ice. This could include one or both being deployed within boreholes that are made beforehand via melting probes or ice drills, with the other being kept above the surface. A graphic illustrating the whole system being deployed in the field can be seen in Fig. 6.2. The primary challenges of the design were to ensure that the electronics would fit within a cylinder that itself would fit within a borehole diameter of 8 cm, since the melting probes used at the field test (chapter 7) had this same diameter. There needed to be sufficient clearance between the outer cylinder diameter and the borehole edge for the cylinder to be lowered and raised within the borehole without getting stuck or frozen in. The housing would consist of a grey PVC cylinder with an outer diameter of 7.5 cm, a length of 95 cm, and a thickness of 0.4 cm. It was deemed desirable to amplify the transmitter signal within the ice, with minimal separation between the power amplifier (PA) and the antenna. The reason for this was to reduce signal loss due to attenuation of the RF signal over the cable. For example, RG-58 transmission lines have a loss of 2.11 dB/10 m for $f = 1.2$ GHz. This condition meant that the choice of power amplifiers was constrained to those that could fit within these dimensions, as PAs often come with heat sinks composed of fins that can have larger dimensions than the rest of the PA. High-power PAs may also require active cooling, with a fan attached to one end of the heat sink to cool the sink by blowing away warm air. Ultimately, the limited space forced the selection of a medium power amplifier, the Pasternak PE15A4017. This PA could operate with a passive cooling solution, a small metallic heat sink attached to the top lid of the PA.

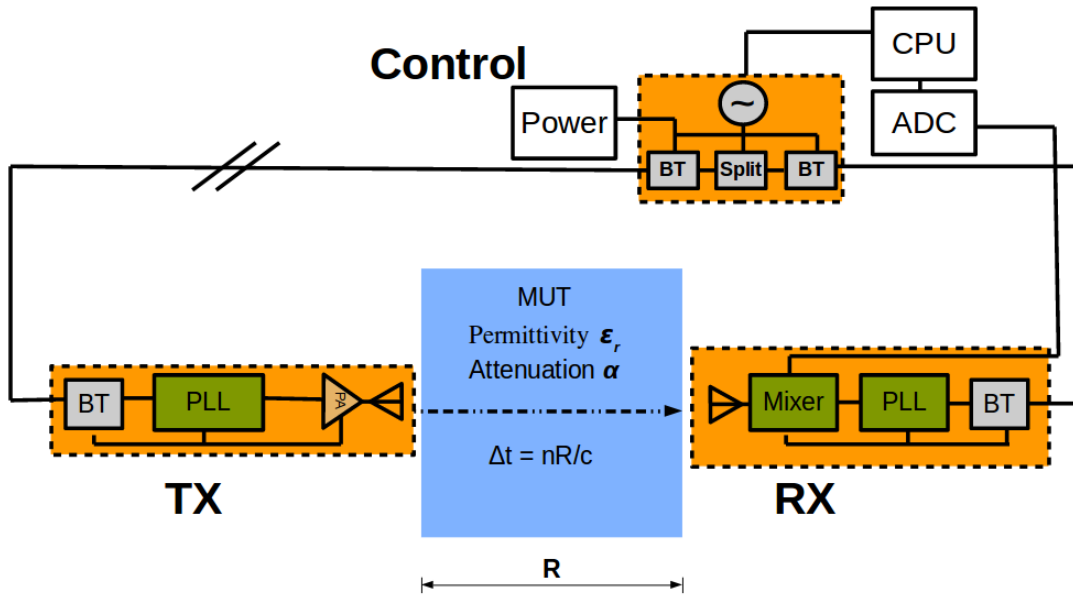


Figure 6.5: Technical layout of the permittivity radar, with the control station located at the surface, and transmitter and receivers located within the ice, separated by some range R . The major components of the control, TX and RX, are described in sections 6.2.4, 6.2.5, and 6.2.6, respectively.

6.2.1 Layout

The cross-borehole permittivity radar consists of three primary components: the transmitting (TX) tube, the receiving (RX) tube, and the control station. A diagram of the technical layout is shown in Fig. 6.5. The TX and RX tubes both house the antennas and the electronics. The electronic components include frequency synthesizers, amplifiers, bias-Tees, voltage converters, mixers, and N-type connectors to attach to long coaxial cables. The control station is the site of the signal waveform generation and data acquisition, both of which were accomplished using a PicoScope 5442D PC Oscilloscope. The control station contained a box containing frequency splitters, a power supply, and bias-tees. At the control station, the bias-tees generate a control signal consisting of a frequency ramp in the intermediate (IF) range of 10 MHz - 20 MHz is generated, split, and biased with DC. The control signal and DC voltage are transported by coaxial cables to the TX and RX tubes. Inside the tubes, the frequency synthesizers generate an RF signal, where the frequency is in some multiple of the IF control signal and is synchronized with the IF control signal. In the TX, the signal is amplified by a power amplifier and transmitted by an antenna. At the RX, the RF output from its own frequency synthesizer is the LO input for the mixer circuit, while the RF input is the received signal from the RX antenna. A photograph showing the RX and TX tubes with the control board is shown in 6.6.

6.2.2 Electronics

Frequency Synthesizer

A vital component of a FMCW radar is the frequency synthesizer, as the time of flight resolution is directly related to the linearity of the frequency ramp. A frequency synthesizer board was designed and tested with the goal of producing a highly linear frequency sweep (either sawtooth or triangle) over a bandwidth of 200 MHz within a frequency range from 900 MHz to 2200 MHz. The frequency synthesizer board consists of two components: a *voltage controlled oscillator* (VCO) and a *phase-locked loop* (PLL).



Figure 6.6: All of the components of the permittivity radar, except for the long coaxial cables, shown together on a table. The transmitter (TX) and receiver (RX) are shown, housed inside transparent PVC tubes (in the end, grey PVC tubes were used on the field). On the bottom right is the ‘controller’ board, which consists of a splitter and BiasTees to send the reference signal and power to RX and TX via cables.

As its name suggests, a VCO is an electronic oscillator whose oscillation frequency is controlled by a voltage input. In practice, the oscillation frequency is not a linear function of the voltage, so one cannot simply create a linear frequency sweep with a linear voltage sweep without compensation for the non-linearity of the response. Instead a PLL compares the phase of the VCO’s RF output (hereafter referred to as RF_{out}) and that of a reference signal (hereafter referred to as IF_{in}), and reduces the phase offset by adjusting the VCO’s input voltage until it achieves lock.

A basic configuration of a PLL-based frequency synthesizer is shown in Fig. 6.7. It consists of a phase detector, which takes $e_{IF,ref}$ as its input and produces a voltage which then passes through a loop filter before being the input to the VCO, which then produces $e_{RF,out}$, whose frequency is some integer factor N of $e_{IF,vco}$, although fractional ratio PLLs also exist. $e_{RF,out}$ is then split, with half leaving the circuit to pass through the PA and TX antenna, while the other half is fed-back into the PLL circuit and divided down in frequency by N by the Frequency Divider. This feedback signal $e_{IF,vco}$ is then the second input of the phase detector (PD). There are different types of phase detectors, the simplest form being a mixer whose output, after passing through a low-pass filter, is a sine function of the phase difference. If the divided down output signal from the VCO $e_{IF,vco}(t)$ and the reference signal $e_{IF,ref}(t)$ are:

$$e_{IF,vco}(t) = A_{vco} \sin(\omega_{IF,vco}t + \phi_{IF,vco}) \quad (6.7)$$

$$v_{IF,ref}(t) = A_{ref} \cos(\omega_{ref}t + \phi_{ref}) \quad (6.8)$$

and if one assumes that $\omega_{ref} = \omega_{out} = \omega$) then the output of the mixer $e_{IF,d}(t)$ is:

$$v_{IF,d}(t) = K_m v_{IF,ref}(t) v_{IF,out}(t) = \frac{1}{2} K_m A_{ref} A_{out} \sin(\phi_{out} - \phi_{ref}) + \frac{1}{2} K_m A_{ref} A_{out} \sin(2\omega + \phi_{out} + \phi_{ref}) \quad (6.9)$$

After going through the low pass filter, the output is the sine of the phase difference ($\Delta\phi = \phi_{vco} - \phi_{ref}$) scaled by:

$$K_d = \frac{K_m A_{ref} A_{vco}}{2} \quad (6.10)$$

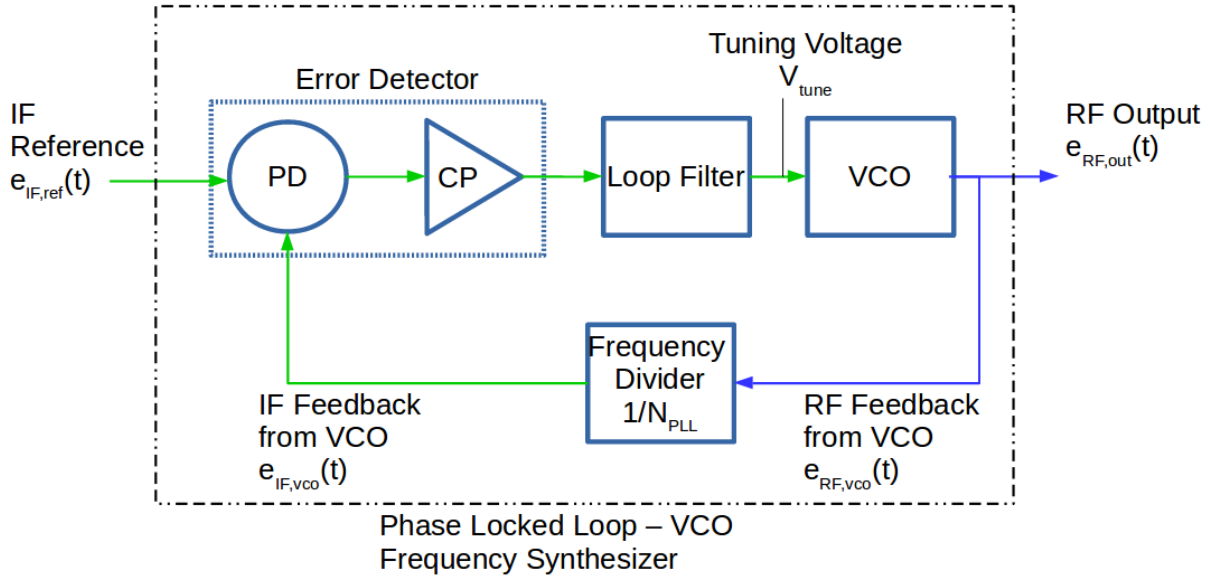


Figure 6.7: An simplified technical layout of a PLL-based frequency synthesizer[20]. Intermediate frequency (IF) signals are shown in green, and Radio Frequency (RF) signals are shown in blue. Note that the components in the error detector are the Phase Detector (PD) and Charge Pump (CP), with other components being the Loop Filter, Voltage Controlled Oscillator (VCO) and Frequency Divider.

For small phase errors, the sine will closely approximate a linear function. In this case, the PLL will lock when the phase shift $\Delta\phi$ of the inputs is very near to $\Delta\phi = \pi/2$.

However this method only achieves phase lock if the reference and divided output already have the same frequency, which can not be guaranteed when the system is initialized and almost certainly will not be the case. Therefore to achieve lock when the VCO's initial output frequency is very different from the reference signal, the frequency difference must be measured and used to lock the two signals, which is made possible with a Phase-Frequency Detector (PFD). The PFD compares the frequency and phase of the reference signal with those of the divided-down feedback signal. This can be seen in Fig. 6.8, where the PFD compares the input to F_{ref} at +IN and the feedback signal at -IN. It uses two D-type flip-flops with a delay element. One Q output enables a positive current source, while the other enables a negative source. These current sources are known as the charge pump (CP). Within this architecture, if the input at +IN is at a higher frequency than at -IN, then the current is pumped high. When integrated through the low pass filter, the high current will push the tuning voltage of the VCO upwards. As such, the -IN frequency will increase as the tuning voltage increases, and the PFD inputs will converge until they achieve lock at the same frequency. If the frequency of -IN is higher than +IN, the reverse will occur and achieve the same outcome.

To meet the requirements of the project, namely a wide frequency range from ~ 1 GHz to ~ 2 GHz, a custom built frequency synthesizer board was designed, built and tested. The final version of the board is shown in the image 6.9. This board utilized the Analog Devices ADF4112 for the PLL circuit and a Mini-Circuits ROS-2150VWR+ for the VCO. As seen in Fig. 6.9, the frequency synthesizer has two SMA connectors, which form an IF input and RF output for our purposes. The input connects the board to the IF reference signal, and the output connects to the PA. The frequency division factor N is set using a programmable Adafruit Pro Trinket microcontroller board. A pin connected at 'JP2', shown in Fig. 6.9, outputs an 'on' signal 3.33 V when the PLL has achieved lock and a 0 V when there is no lock. This output was used as a trigger for data

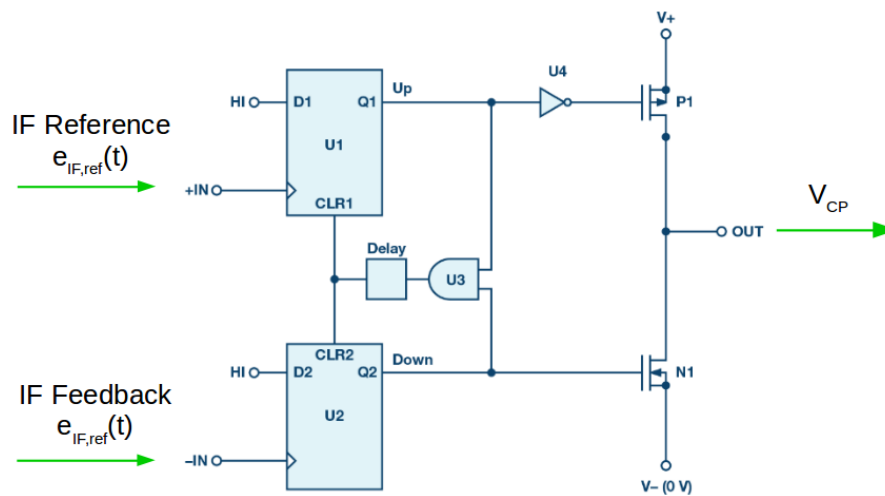


Figure 6.8: A layout of a Phase Frequency Detector (PFD), a type of Phase Detector (PD). The phase frequency detector in Figure 3 compares the input to FREF at +IN and the feedback signal at -IN. It uses two D-type flip flops with a delay element. One Q output enables a positive current source, and the other Q output enables a negative current source. These current sources are known as the charge pump.

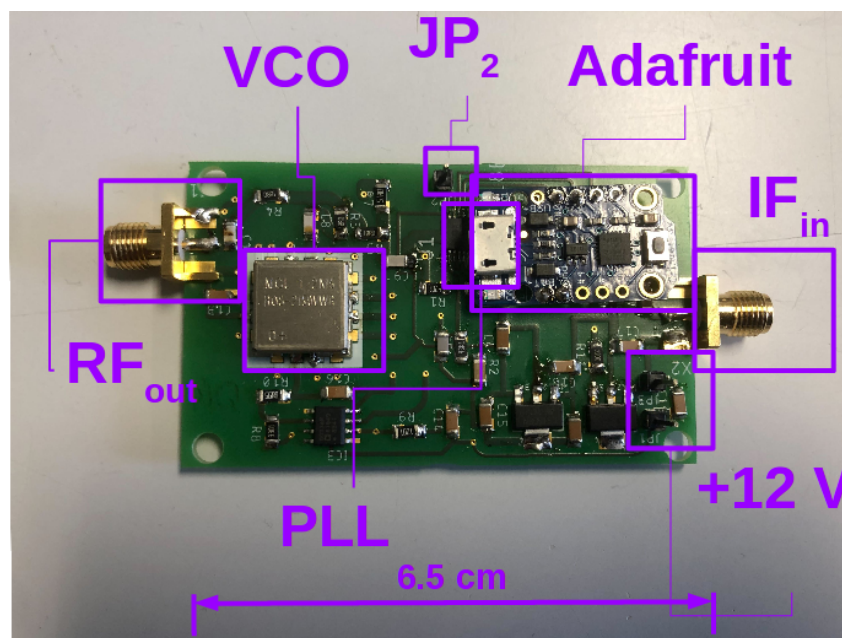


Figure 6.9: The frequency synthesizer board, with the major components highlighted in the purple boxes. These are the VCO, the SMA connectors in reference signal input (IF_{in}) and RF output (RF_{out}), an Adafruit Trinket Microcontroller, and the PLL circuit which is underneath the Adafruit, around the position of the USB-mini connection and is not directly visible. There is also a pin (JP2) which can be used to check for lock, and two pins to provide input power.

acquisition. The board was powered by a DC voltage input consisting of two pins, a ground and a positive, opposite the Adafruit and adjacent to the input SMA connector. Different voltages from 18 V to 22 V would provide power to the board, but voltages above 19 V were observed to cause significant heating of the board and thus were to be avoided. A power input of 18 V was ultimately used in field tests. A 10 kHz loop filter was utilized on the board, but it was found that the optimal modulation frequency $f_{mod} = 1/T$ was $f_{mod} = 100$ Hz.

Mixer Board

The mixer board is used to multiply the received signal and the local reference signal to obtain time of flight information from the mixed signals Fourier spectrum. There are different types of mixers, but the type used in the board is a double-balanced passive diode mixer, which uses a bridge of diodes. Diodes produce a non-Ohmic current, i.e., the current I_D is non-linear with the applied voltage. Instead, the current I_D passing through an ideal diode is an exponential function of the applied voltage V_D , as given by the Shockley diode equation [74]:

$$I_D = I_S \exp \frac{V_D}{nV_T - 1} \quad (6.11)$$

In which I_S is the reverse-bias saturation current, V_T is the thermal voltage and n is the ‘ideality factor’[74]. The exponential function can be approximated with a second-order Taylor expansion;

$$I_D \propto e^{V_D} - 1 \approx V_D + \frac{V_D^2}{2}. \quad (6.12)$$

If the sum of two signals V_1 and V_2 is applied to the diode, then the output voltage V_{out} is proportional to the current through the diode. If the constants in equation 6.11 are ignored, one finds:

$$\begin{aligned} V_{out} &= V_1 + V_2 + \frac{1}{2}(V_1 + V_2)^2 + \dots \\ &= V_1 + V_2 + 2V_1V_2 + V_1^2 + V_2^2 + \dots, \end{aligned} \quad (6.13)$$

And by substituting in $V_1 = \sin(at)$ and $V_2 = \sin(bt)$:

$$V_{out} = (\sin(at) + \sin(bt) + \frac{1}{2}(\sin^2(at) + 2\sin(at)\sin(bt) + \sin^2(bt)) + \dots \quad (6.14)$$

Here, all terms except $\sin(at)\sin(bt)$ are neglected, as they are outside of the frequency range of interest. After removing these terms, one is left with two signal components, one with the sum of the input frequencies and the other with the difference:

$$V_{out} = \sin(at)\sin(bt) = \frac{\cos(a-b) - \cos(a+b)}{2}. \quad (6.15)$$

When V_{out} is passed through a low-pass filter, then it is obvious how the mixer circuit produces a signal that is some sinusoid of the difference between the frequencies of the inputs. The mixer board that was used in the RX can be seen in figure 6.10. It contains a plug-in double-balanced mixer: the Mini-Circuits SRA-2000+. There are three SMA connectors:

- RX input: connects to the RX antenna
- LO input: connects to the Local Oscillator (LO)
- LF output: connects to the DAQ (PicoScope)

Both the LO and RX antenna inputs are amplified with integrated Low Noise Amplifiers (LNAs) by a factor of 15 dB. The board is powered by 12 V DC input.

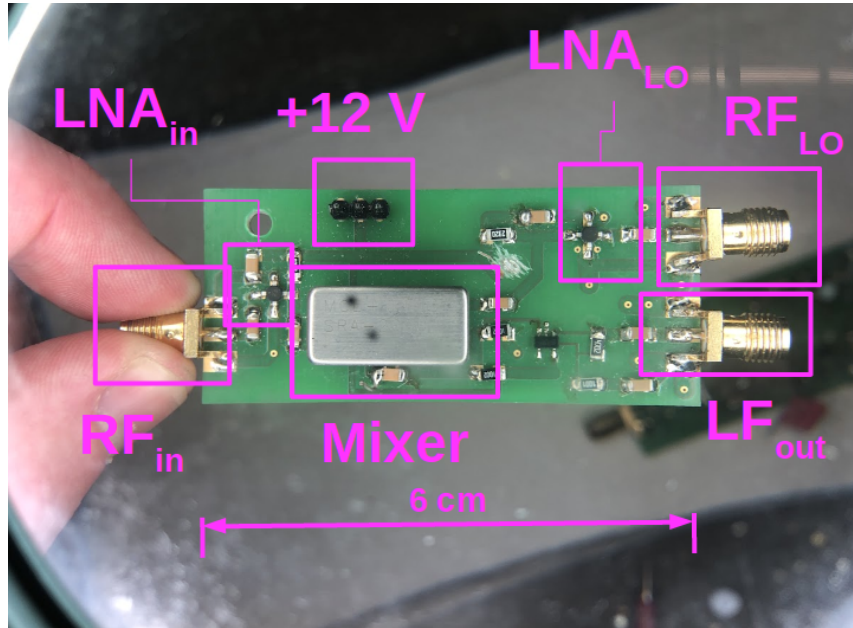


Figure 6.10: An image of the Mixer board, with the main components highlighted: the Mixer circuit, DC voltage input pins, the Low Noise Amplifiers (LNAs) and the SMA ports to connect to the LO and to the receiving antenna.

6.2.3 Antenna

The permittivity radar system requires an omnidirectional antenna with a wide operating frequency (1 to 2 GHz) and could also fit within the tubes' internal diameter of 7.3 cm. Commercially available antennas were found on the market that meet these requirements; however, as it was desirable to have multiple receivers, and the antennas found were prohibitively expensive, it was decided to develop an antenna that met our requirements. A similar design as the vertically polarized 'V-pol' antennas designed and utilized by the ARA collaboration was selected[8]. This can be described as a cage dipole antenna, consisting of two 'cages' of conductor connected to a common hub, with one electrically connected to the internal conductor of the RF cable and the other connected to the shield.

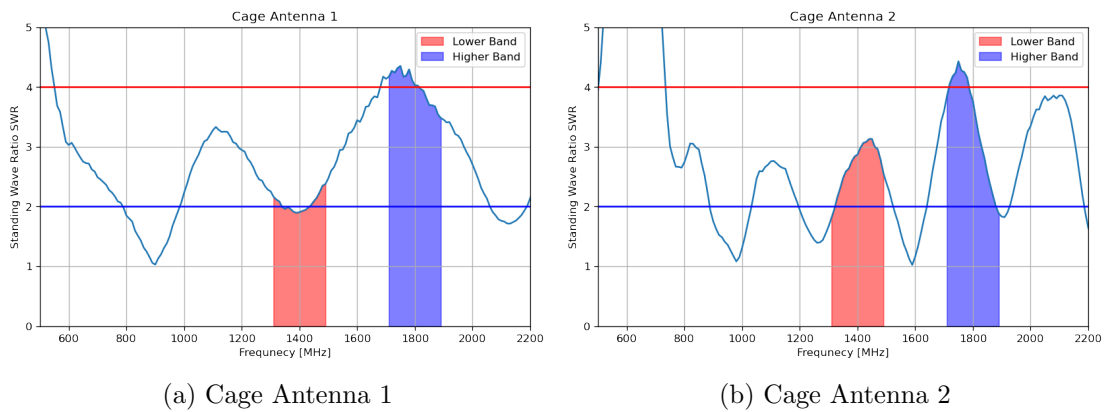
As the frequency range of interest was above that of the ARA project (up to 800 MHz) and the wavelength correspondingly smaller, the dimensions of the antenna would naturally be smaller. The cage dipole antennas, images of which are shown in Fig. 6.11, are comprised of two cages of 8 silver-skin copper wires in a shape similar to a lemon with the tips being tapered, with a maximum diameter of 4 cm, and a height of 5 cm. At the tapered ends, the wires are soldered to a ring wire with a diameter of 1 cm. The cages are separated by a 1 cm gap, giving the antenna a height of 11 cm. Approximating this as a half-wave dipole antenna, one expects maximum resonance of the antenna at 1.36 GHz. Two cages were soldered to the inner and outer conductors of an SMA-type coaxial cable, with the top being soldered to the inner conductor and the bottom cage to the outer conductor. To achieve a consistent shape, hollow molds were made using a 3D printer with a 'lemon' shape and grooves to direct the wires. The shape of the antenna chosen with the aid of FDTD simulations (see chapter 4) performed using RF module of Comsol Multiphysics. The emission properties of the antennas were then found by measuring the S_{11} -parameters using a Vector Network Analyser (see Fig. 6.12). However, the antenna's radiation pattern has not yet been measured due to a lack of access to an 'echoless' room in which such measurements should be made.



(a) Cage Antenna 1

(b) Cage Antenna 2

Figure 6.11: Photos of wide-band cage antennas



(a) Cage Antenna 1

(b) Cage Antenna 2

Figure 6.12: The voltage Standing Wave Ratio (SWR) of Cage Antenna 1 (used in the transmitter TX) and Cage Antenna 2 (used in the receiver RX). A blue line indicates $SWR < 2$ where at least 50 % of the RF energy is emitted, and the red line indicates $SWR < 4$, where at least 25 % of the RF energy is emitted. The highlighted region: red for the ‘lower band’ ($1.3 \text{ GHz} < f < 1.5 \text{ GHz}$) and blue for the ‘higher band’ ($1.7 \text{ GHz} < f < 1.9 \text{ GHz}$), indicate the frequencies used for FMCW transmission at the Aletsch Glacier Field Test (chapter 7).

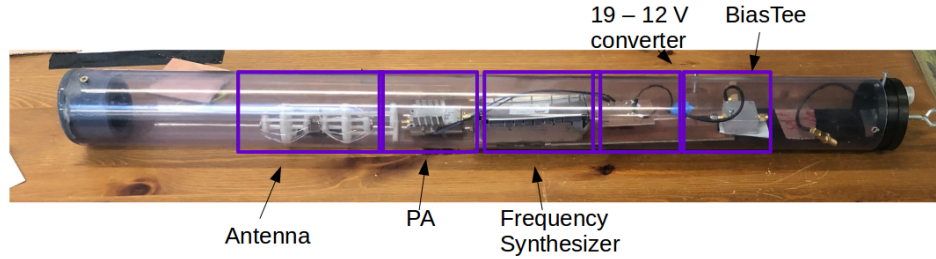


Figure 6.13: The transmitter TX tube

6.2.4 Control: Permittivity Measurement Mode

The control system is located at the surface, and contains; a ‘control box’, DC power supply, the reference signal generation and the data-acquisition (DAQ) system. For both, a 4-channel 200 MHz bandwidth PicoScope 5442D PC Oscilloscope was utilized. The PicoScope was connected via USB cable to a field laptop and could be operated from a GUI or could be programmed from a Python-based script.

With 4 input channels, one could operate up to 4 receivers simultaneously, with 2 additional channels for a trigger input and signal generation output. However, in practice, only one receiver was used. All inputs and outputs utilize BNC-type connectors. The signal generation output is connected to the ‘control box’. The control box consisted of a frequency splitter connected by SMA adapters to two Bias-Tee circuits. A Bias-Tee is a ‘diplexer’ or three-port network that permits adding a DC bias to an AC signal or vice versa. It is simple conceptually, a junction between a capacitor C , which blocks the DC bias but allows AC to pass, and an inductor L , which blocks the AC component but allows DC. Two bias-tees add the DC voltage input to the IF reference signal. Both then produce outputs via an N-type connector, which connects to coaxial cables.

6.2.5 Transmitter: TX

The transmitter tube TX was designed to be lowered into the ice and transmit a signal to the receivers. The antenna and electronics are housed within a 7.5 cm diameter PVC tube, with a cap at the end, and a 3D printed top lid. The purpose of the tube is to protect the electronics from any left-over melt-water, or fallen snow within the boreholes or other material. The tube is 95 cm long from the bottom cap to the top lid. The top lid has an N-type (female) to SMA (female) adapter on the outside to allow for connection to the coaxial cable, which provides power and is the reference signal for the PLL. Within the tube, all cabling and connections are SMA-type. A ring screw is drilled into the top lid to allow for connection with a rope which is suspended from a winch. The top lid also connects to a copper board upon which all electronics and the antenna are connected. A 15 cm SMA cable connects the SMA side of the lid adapter to a bias-tee, which divides the DC voltage from the reference signal. The reference signal is then passed to the PLL frequency synthesizer board via a SMA-to-SMA adapter. The PLL board is additionally housed within a metal box (Teko tin-plated steel enclosure with 1 mm thickness) to protect it from RF interference generated by the antenna and amplifier. The DC output of the Bias-Tee is split to provide 19 V power for the PLL board and to a DC-DC converter, which provides 12 V power for the PA. The PE15A4017 medium power amplifier had a gain of 27 dB and a power output of approximately 1 W.

6.2.6 Receiver: RX

The housing for the receiver is identical to the transmitter, except that the top-lid has two N-to-SMA adapters, one for the IF + DC input and one for the LF output. The RX also contains a Bias-Tee, a DC-DC converter, a frequency synthesizer, a cage antenna, and the mixer board described in section 6.2.2. The Frequency Synthesizer and Mixer Board are also both housed in metal boxes to protect them from external interference.

6.3 Measurement Procedure

6.3.1 Data Acquisition

The data acquisition is performed at the surface via the PicoScope, with at least one of its channels must be connected to LF-output cable. As mentioned in section 6.2.2, the PLL board produces a 3.3 V signal when it has acquired lock and remains at zero when lock is not achieved, with sufficient stability being achieved after 20 μ s. This makes this output the ideal source for the trigger, which is set to trigger for a rising voltage surpassing 300 mV. Upon triggering, the acquisition time was set to record at least 1 modulation cycle, with 2 cycles sometimes being measured. During data acquisition, multiple waveforms (typically 60) would be measured sequentially to allow for averaging. The data was then saved to a hierarchical data format (HDF) file via Python's h5py library, allowing the mixer output waveform(s), trigger waveforms, and timing data to be saved to NumPy arrays within the HDF format and all important metadata; including the measurement settings, a time-stamp and potentially comments made by the user can be saved as attributes to the file.

6.3.2 Processing

Analysis is later performed on the Fourier transform of the waveforms. The data processing consists of the following steps:

1. Averaging: Taking the average of the waveforms $v_{ave}(t) = \sum_i^{N_{ave}} v_i(t)$
2. Cutting: This removes part of the frequency ramp with non-linear or 'toggling' behavior. By default, the first 20 μ s are removed, and the end cut is placed at 97 % of one full cycle; i.e. at 9.7 μ s for a ramp with $T_{mod} = 10$ ms
3. Filtering: the waveform is placed through a Butterworth high pass filter to remove the DC component from the data, along with any time component shorter than the delay-time of the cable $\Delta t_{cut} = 500$ ns: $v_{filt}(t) = f_{HP}(v(t), f_{cut} < \Delta_{cut} \cdot \frac{df}{dt})$
4. Windowing: a 'Blackman' window function is applied to the data to reduce edge effects and minimize leakage, and suppress side-lobes
5. Padding: Padding involves the addition of 'zeros' to a waveform to allow for a finer frequency spacing in the Fourier and make peak structures clearly distinguishable.
6. Fourier Transform: a Fast Fourier Transform is applied to the mixer waveform. The resulting Fourier spectrum contains the time-of-flight information.
7. Time-of-flight cutting: the resulting Fourier spectrum is much larger than the time-of-flight zone of interest. For example, if one expects a signal propagation time of $t = 133$ ns (corresponding to travel through 40 m of air), then there is unlikely to be any signal of interest for travel times $> 1 \mu$ s. As such this data is cut from the analysis.
8. Peak identification: Significant features are identified in the data using Python's Peakutils library.

The total measured signal power P_{RX} is found from the root-mean-squared (RMS) voltage V_{RMS} measured in the waveform:

$$P_{RX} = \eta \frac{V_{RMS}^2}{R} \quad (6.16)$$

where R is the impedance of the oscilloscope, assumed to be $R = 50 \Omega$. η is the power conversion factor, which is determined by calibration using the output of an RF source with a known power and which has also been measured with a spectrum analyzer. The power associated with the direct signal component or ‘peak’ is derived by multiplying the total power by the integral of the normalized peak in the Fourier spectrum. The transmitted power output P_{TX} for two different frequency bands is described in the table 6.1.

6.4 Testing of Permittivity Radar

Before deployment to field tests at glaciers, several measurements were performed at the University of Wuppertal to test the performance of all the major components, including temperature tests using a refrigerator set to -20°C , the stability of the system, and crucially the time-of-flight resolution, maximum range, and the signal-to-noise ratio.

6.4.1 PLL Tests

The most important considerations for the PLLs were the linearity of the frequency ramp it produced, if the slope of the ramp was at the correct value, and the time required to achieve lock. In practice, the frequency output may have some small offset from the multiple of the reference signal. If the reference signal is itself ramping in frequency, PLLs can exhibit a behavior known as ‘toggling’, where the actual frequency tracks the desired frequency with some offset Δf_{off} . These toggling frequencies will appear as side lobes or side peaks in the Fourier spectrum.

$$f_{true}(t) = f(t) + \Delta f_{off}(t) = N_{PLL} f_{IF,ref}(t) + \Delta f_{off}(t) \quad (6.17)$$

Toggling is always present in a frequency ramp from a PLL initially. The goal was to keep $\Delta f_{off} < 1.0 \text{ kHz}$. To check for this effect, two tests were performed. The first was to measure the ramp frequency from the PLL output directly with a sliding Fourier transform (SFT). First, the RF_{output} was mixed with a constant frequency at $f_0 = 1.2 \text{ GHz}$, such that it would be possible to measure the ramp even with an oscilloscope with a bandwidth of 500 MHz . The output of the SFT can be seen in Fig. 6.14, for Triangle Ramps with $B = 120 \text{ MHz}$ and a modulation time $T = 5 \text{ ms}$. Ultimately it was decided to use a lower frequency modulations, $f_{mod} = 100 \text{ Hz}$, meaning that the toggling effect would be limited to the first $500 \mu\text{s}$ of the ramp. This motivated the choice of a longer modulation time (and shorter modulation frequency f_{mod}) of $T_{mod} = 10 \text{ ms}$, such that only the first 5% of the signal should be cut.

Cable Tests

Another way to verify the PLL boards performance was to check if the Fourier transform of the mixed signal would produce a ‘clean’ peak at the position expected by $\Delta f = B/T \cdot \Delta t$. This could be accomplished by splitting the output of the frequency synthesizer board, with half going directly into the mixer port and the other through a coaxial cable with a known time delay and connecting the far port of the cable to the other input of the mixer. This is called a ‘self-mixing’ test, with the test setup described in Fig. 6.15.

The result of a self-mixing is shown in Fig. 6.16c. A clearly definable peak is visible with a time delay corresponding to the propagation time through the cable. A Gaussian function was fit to the peak, with the cable time delay derived from the mean $t_{cable} = 522.6 \text{ ns}$, and the uncertainty $\Delta t = 2.9 \text{ ns}$ found from the standard deviation. Side lobes are observable to the left and right due to phase noise, which will be discussed further in section 6.5.1.

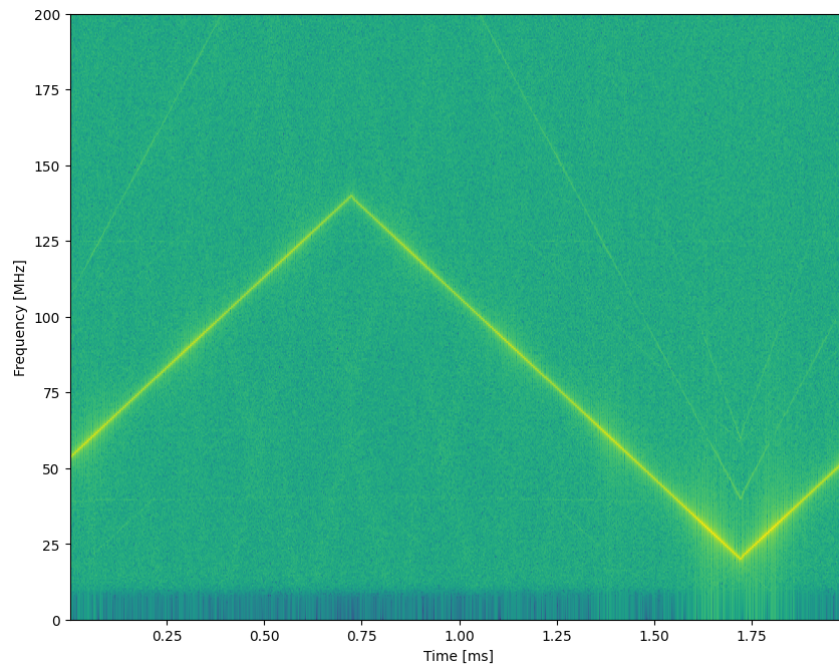


Figure 6.14: A sliding Fourier transform (SFT) spectrogram of the RF -output of a frequency synthesizer board, recorded with the Picoscope. Here a triangular ramp is used, with a bandwidth of $B = 120$ MHz and a modulation frequency of $f_{mod} = 1$ kHz and hence a modulation time of $T_{mod} = 1$ ms. Note that the base frequency of the board's output was at $f_{base} = 1300$ MHz, but the output was mixed with a constant reference frequency of $f_{LO} = 1290$ MHz, such that the ramp could be measured within the limited measurement bandwidth ($B_{meas} = 200$ MHz) of the Picoscope. The first-order harmonic of the VCO can clearly be seen.

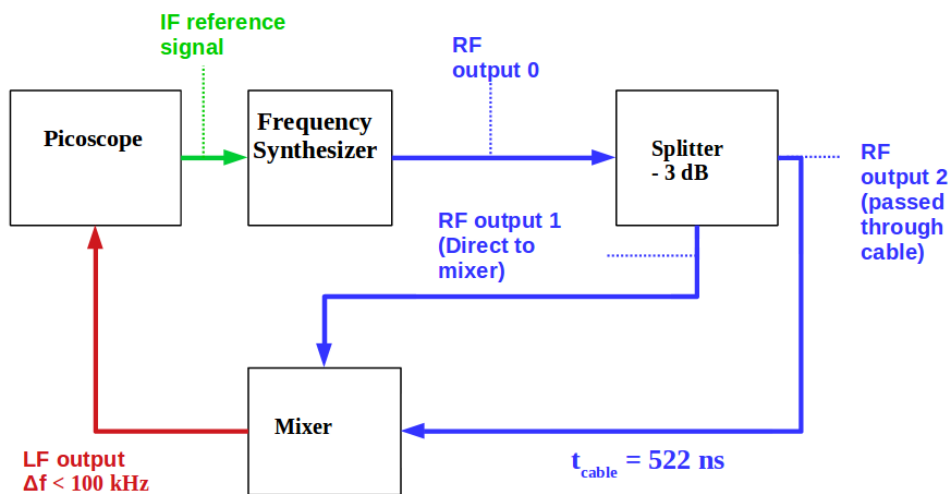
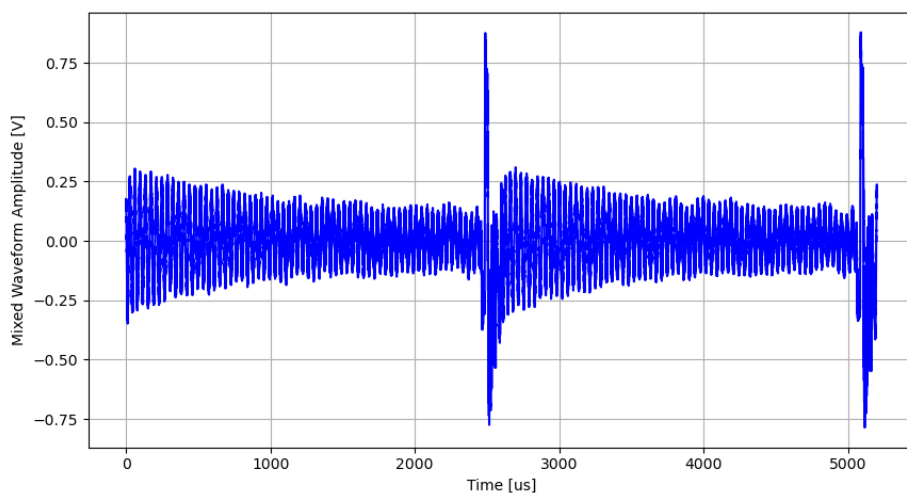
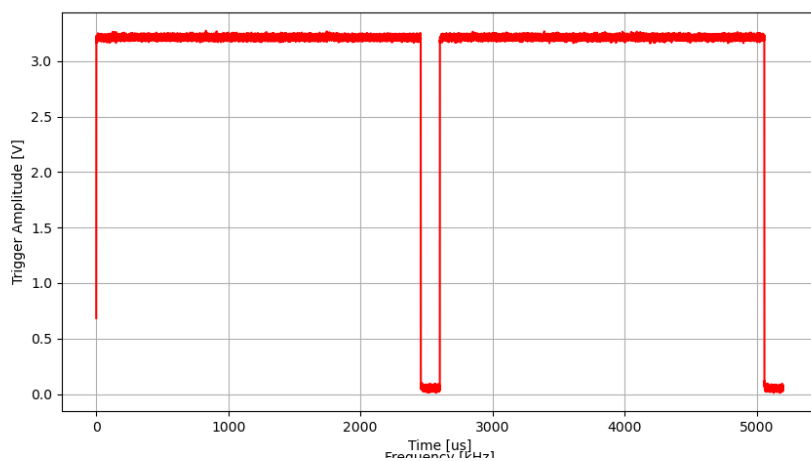


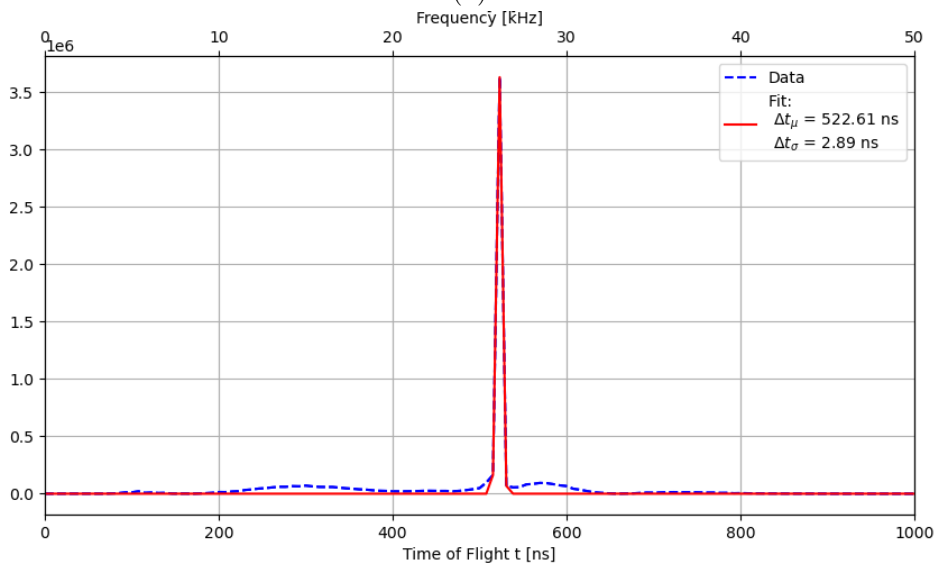
Figure 6.15: Self-mixing test of frequency synthesizer board.



(a)



(b)



(c)

Figure 6.16: Result of PLL self-mixing test (based on a setup depicted in Fig. 6.15).

6.4.2 Antenna Tests

The impedance of an antenna as a function of frequency is typically tested by measurements of the standing wave ratio SWR . SWR can be measured by connecting the antenna to a single port of a vector network analyzer (VNA) which calculates the scattering parameters or S-parameters of the network. Here only the S_{11} parameter, ratio of RF energy reflected into the port to RF energy transmitted, is needed to find SWR via

$$SWR = \frac{1 + |S_{11}|}{1 - |S_{11}|} \quad (6.18)$$

The SWR is always a real and positive number for antennas, and a smaller value is better as it implies a higher amount of energy transmitted from the antenna. A common standard for measuring the effective bandwidth of an antenna is any frequency range for which the antenna has $SWR < 2$, implying that at least 50 % of the RF power is transmitted. For the permittivity radar, the usable bandwidth is the region for which $SWR < 4$, as the PA of the TX was recommended by the manufacturer to operate only for a device with a $SWR < 4$. It should be noted that some fraction of the energy may be absorbed by the antenna material due to an imaginary component of the antenna's impedance, although this is usually negligible. The effective bandwidths of Cage Antenna 1 (used in the TX) and Cage Antenna 2 are shown in Fig. 6.12.

A related property is the antenna's impulse response function $h(t)$, a time-domain function that determines the antenna's frequency-dependent response to an incoming pulse, including any frequency dependence in the phase or time offset of the transmitted pulse to the input pulse. The transmitted signal $y_{tx}(t)$ can be related to the input signal $V_{in}(t)$ via the convolution of $x_{in}(t)$ with the IR function $h(t)$ (where τ is a dummy variable):

$$y_{tx}(t) = x_{in}(t) * h(t) = \int_{-\infty}^{\infty} x(t)h(t - \tau)dt \quad (6.19)$$

By exploiting the Fourier identity of convolution, we can obtain the transmission from the IR spectrum in frequency domain:

$$Y_{tx}(f) = X_{in}(f)H(f) \quad (6.20)$$

In the absence of an echo-less chamber, estimation of the IR function required an assumption that the transmitted signal $a_t(t)$ is same as the reflected signal $a_r(t)$:

$$a_t(t) = 1 - a_r(t) \quad (6.21)$$

In this case, the impulse response can also be inferred from the complex S_{11} parameter. The impulse function $h(t)$ for the full frequency range under test; from DC to 3 GHz:

$$h(t) = \int_{-\infty}^{\infty} H(f)e^{i2\pi ft}df \quad (6.22)$$

The derived IR function for Cage Antenna 1 is shown in the Fig. 6.17. The time-domain IR (bottom right) shows a large peak at $t = 0$ ns, followed by a sequence of smaller peaks (with an amplitude $< 20\%$ that of the first peak) that diminish rapidly on a scale of 5 ns.

6.4.3 In-Air Antenna Transmission Tests

To test the time of flight resolution, the transmitter and receiver were deployed on wagons while connected to the master box and then recording the time-of-flight spectrum at one or more distances. These tests were performed on a balcony of the University of Wuppertal.

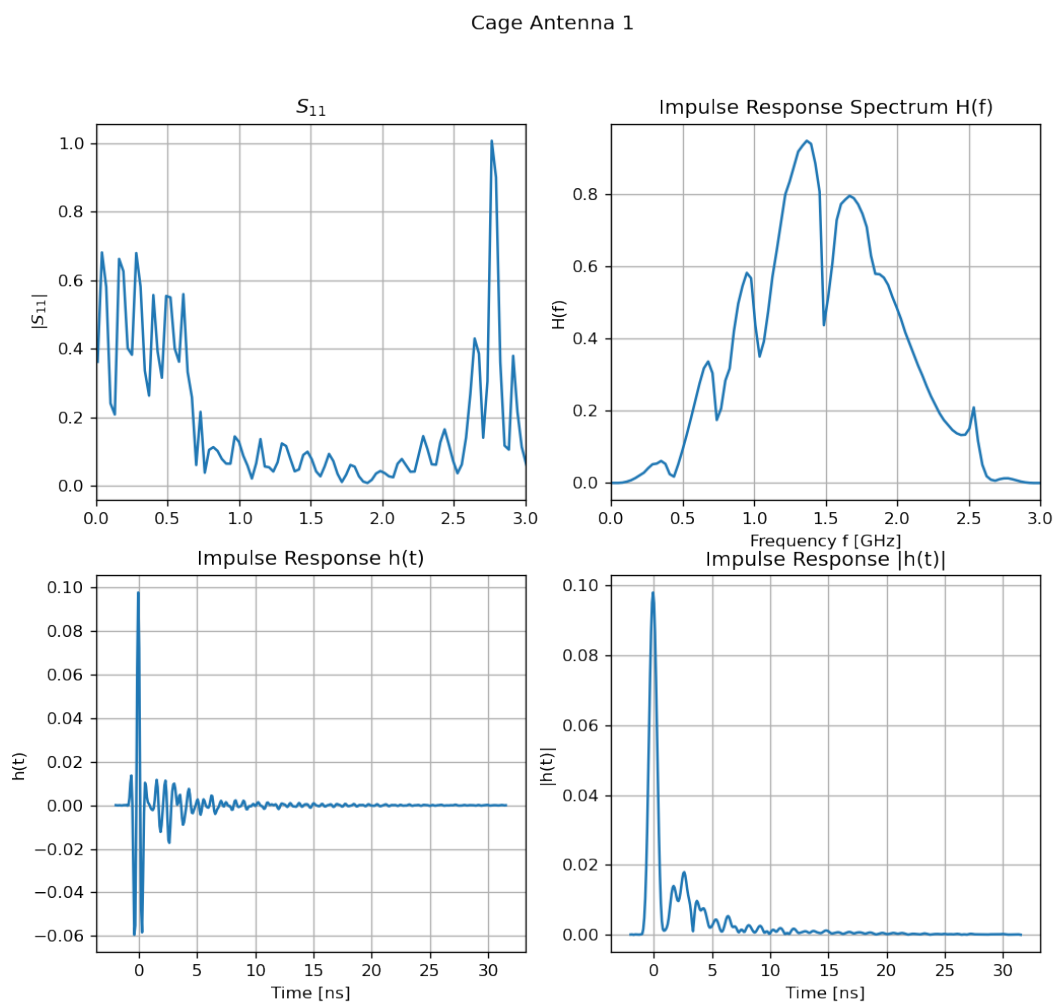


Figure 6.17: The estimation of the impulse response function IR . The top left plot is the S_{11} magnitude shown over a frequency range $10 \text{ MHz} < f < 3000 \text{ MHz}$. The top right is the derived frequency domain impulse response $H(f)$ calculated from S_{11} . The bottom images are the time-domain impulse response $h(t)F^{-1}(H(f))$, with the amplitude shown on the right.

Additionally, the time-delay was measured as a function of the base frequency f_{base} and bandwidth B . For this test, the transmitter, and receiver were placed at a distance of 9.7 m apart and recorded the time-of-flight spectrum for base frequencies between 800 MHz and 2000 MHz. Sawtooth-ramps were used as frequency modulation, with modulation times of $T_{mod} = 10$ ms and bandwidths of 130 MHz, 200 MHz and 300 MHz. The results are shown in Fig. 6.19, with the measured delay time t_{delay} being the mean of the Gaussian fit to the maximum signal peak, and the standard deviation is used to define the error of the measured delay time Δt_{delay} . The delay time measurements converge to the value of 660 ns which corresponds exactly to the cable delay and the propagation time in the air. The residuals of the measured time of flight decrease for higher frequencies, from a value of 7 ns for central frequency $f_{central} = 1$ GHz to ≤ 2 ns at $f_{central} = 1.8$ GHz. This comes with the exception for the region between $1.05 \text{ GHz} < f < 1.15 \text{ GHz}$, where large residual errors of 25 ns and 35 ns were measured, for which there is no satisfactory explanation at present. As a result, this frequency range was not used in the Aletsch glacier field test.

Another test performed was to measure the delay time of the signal traveling through the air from TX to RX as a function of the distance between them R . The RX was held stationary, while the transmitter was moved on a wagon in various distance increments, starting at $R = 2.5$ m and moving away in increments of 2.5 m up to 10 m, and with larger range increments for $R > 10$ m, with the widest separation measured being 50 m. In Fig. 6.20 the measured time delay is shown as a function of distance. This verified that the time of flight could be reconstructed to an accuracy of 5 ns. This would allow for permittivity measurements of $\Delta\epsilon_r = 0.075$ at $R = 40$ m.

6.5 Summary of System

From the cable tests and in-air antenna transmission tests, it was possible to derive the time-of-flight resolution of the permittivity radar of $\Delta t \leq 5$ ns for $f > 1.2$ GHz for a ramp bandwidth of $B = 200$ MHz. Assuming detection of the direct transmitted signal component in ice, this would give a nominal refractive index resolution of $\Delta n = 0.04$ for an antenna-antenna separation of $R = 40$ m and therefore a permittivity resolution of $\Delta\epsilon_r = 0.08$. The specifications of the system are summarized in the table 6.1. The FMCW permittivity radar was tested to be able to measure the propagation time of the signal with a precision of $\Delta t = 5$ ns for distances up to 50 m, with a likely maximum range of up to 250 m, although this was not confirmed experimentally and the maximum range utilized in the field was 42 m. It had a frequency range of between 800 to 2200 and a working bandwidth of 200 MHz. The application of this system at a field test in the Swiss Alps is the subject of the following chapter.

6.5.1 Experimental Uncertainties

The interpretation of signal propagation by the permittivity radar relies upon good understanding of waveform generated by the frequency synthesizer and its response to the components, in particular the antennas. Another crucial aspect is an understanding of the noise level of the radar.

Antenna Impulse Response

The least well understood of the permittivity radar was the antenna properties. It proved difficult to develop a broadband antenna with consistent S_{11} spectra, and indeed the antenna's properties could vary between measurements. A possible cause of this was the absence of a 'balun' connections at the junction of the top and bottom cages. Instead the top and bottom cage were soldered to the inner and outer conductors of the SMA cable.

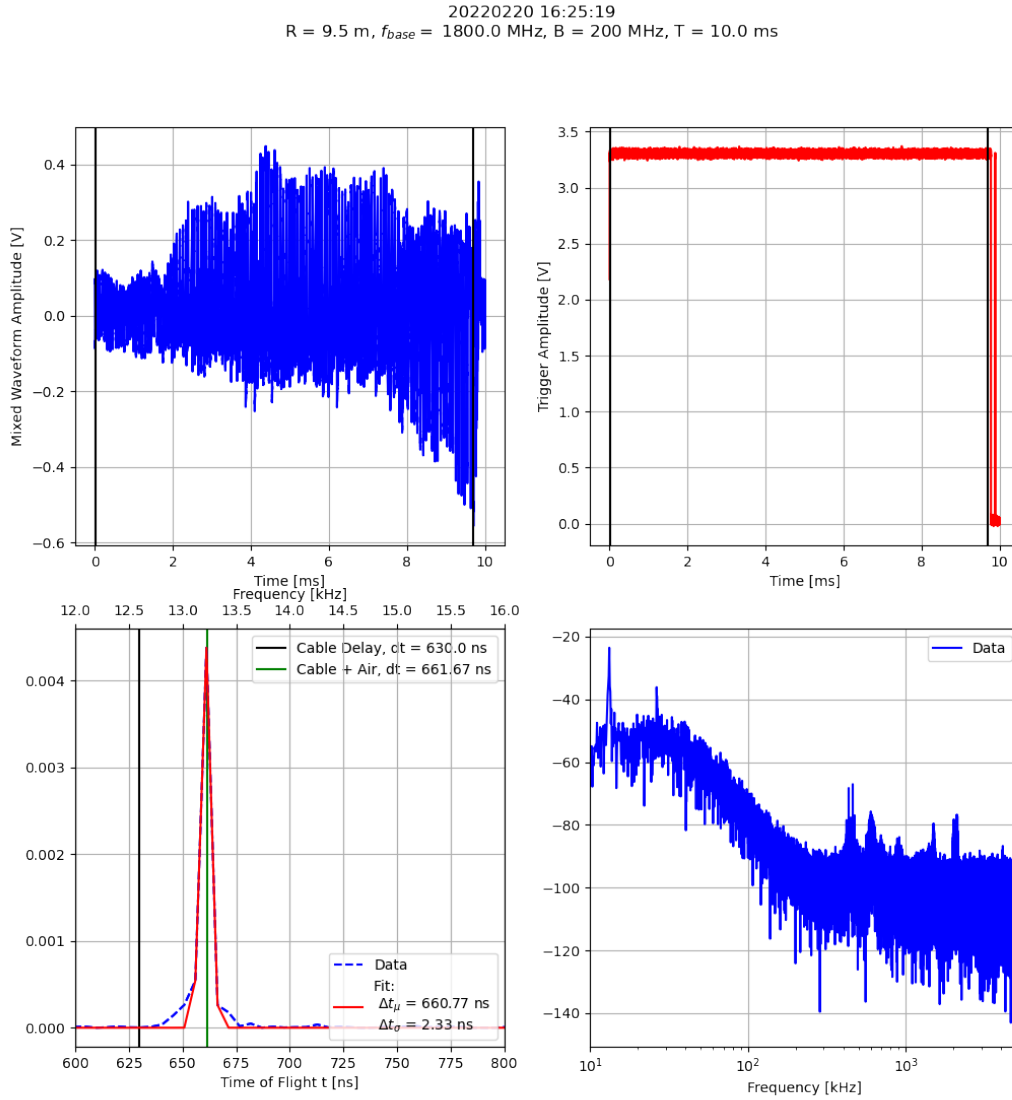


Figure 6.18: An example of the data-acquisition for in-air transmission $R = 9.5$ m, and a base frequency of $f_{base} = 1.8$ GHz and a bandwidth $B = 200$ MHz. The top left shows the mixer waveform $e_{mixer}(t)$ for $0 < t < T_{mod}$. The voltage output from the jumper port JP2, showing whether lock has been achieved is shown in the top right. The bottom two plots show the Fourier spectrum $e_{mixer}(f) = F(e_{mixer}(t))$. The bottom left plot shows the spectrum in linear scale for $12 \text{ kHz} < f < 16.0 \text{ kHz}$ corresponding to a time of flight of $600 \text{ ns} < t < 800 \text{ ns}$. The bottom right shows the same Fourier spectrum in a log-log scale over a frequency range $10 \text{ kHz} < f < 5 \text{ MHz}$.

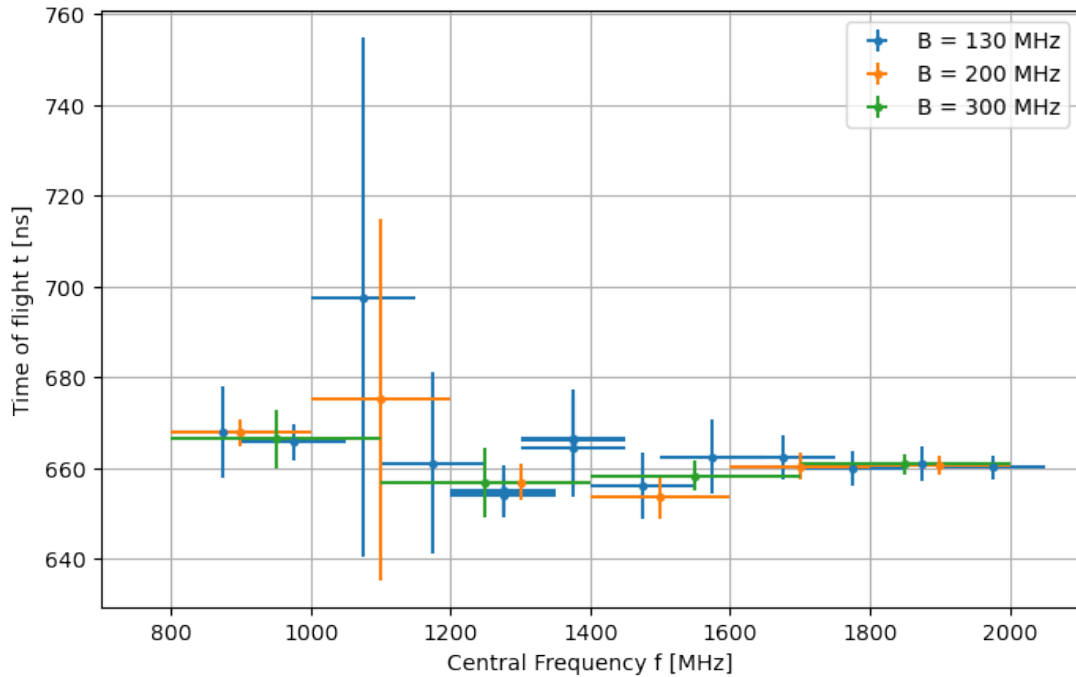


Figure 6.19: A plot of the time-of-flight for of the signal (plus a cable delay $+t_{cable} = 627$ ns to show the frequency dependence of the system. The antennas are separated by a distance of $R = 9.8$ m

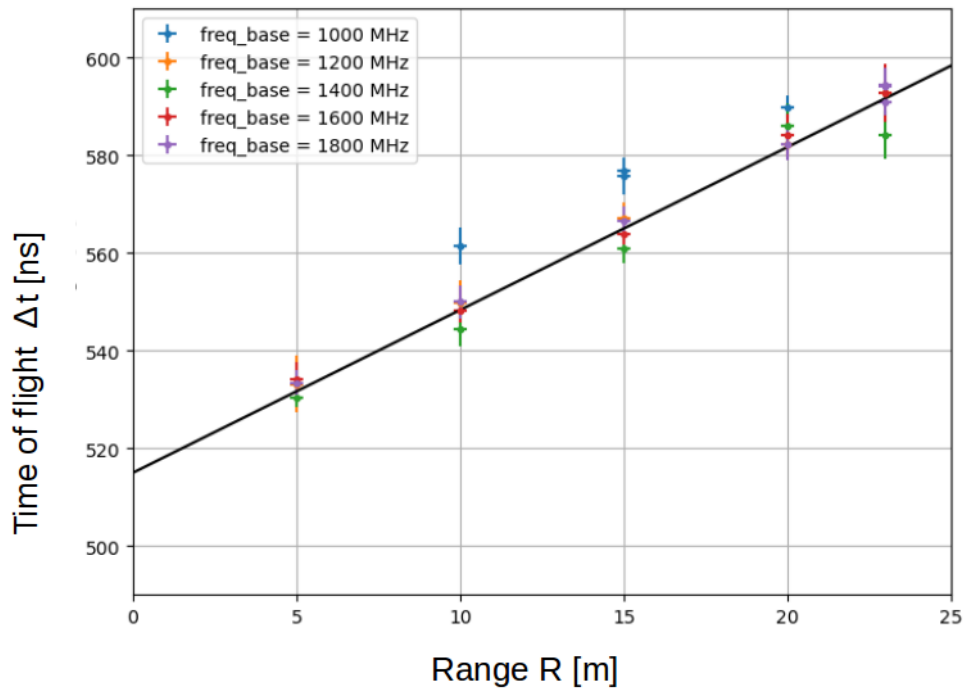


Figure 6.20: Range Test: the transmitter and receiver are placed on wagons and separated by increasing distances $5 \text{ m} \leq R \leq 25 \text{ m}$, and FMCW is sent between them, with different base frequencies being used. The time of flight could be measured as a function of distance, with the time of flight error being measured to be $\Delta t < 5$ ns.

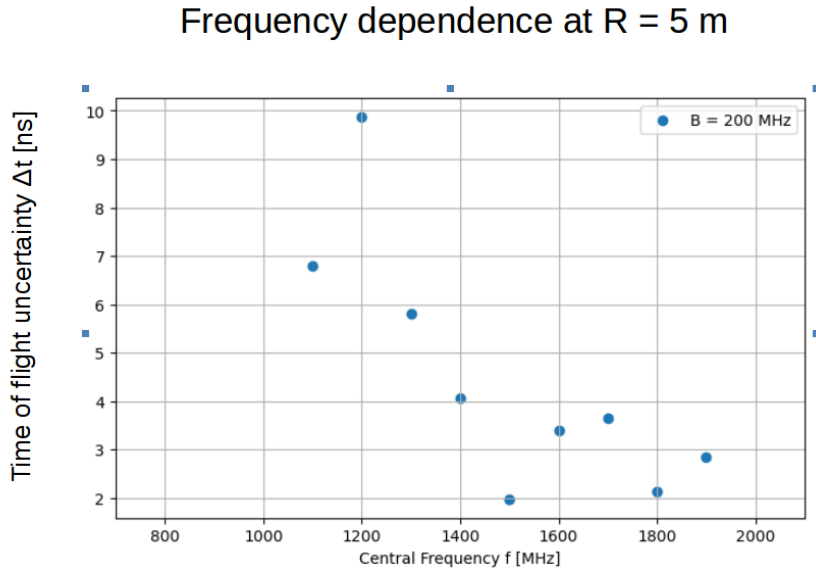


Figure 6.21: The time of flight measurement uncertainty as calculated from the residuals $\Delta t_{res} = t_{meas} - t_0$ of the total measured propagation time t_{meas} from the truth value $t_0 = t_{cable} + R/c$ with the cable delay $t_{cable} = 500$ ns and propagation time through air R/c , for a range of $R = 5$ m. All measurements used a sawtooth ramp with a bandwidth of $B = 200$ MHz. The residual error decreases as a function higher central frequencies, with the worst performance being at $f_{central} = 1200$ MHz with $\Delta t_{res}(f_{central} = 1200 \text{ MHz}) = 10$ ns and the best performances at $\Delta t_{res}(f_{central} = 1500 \text{ MHz}) = 2$ ns and $\Delta t_{res}(f_{central} = 1800 \text{ MHz}) = 2.2$ ns.

Description	Symbol	Value
TX & RX tube height	$H_{TX} = H_{RX}$	95 cm
Tube Diameter	$d_{TX} = d_{RX}$	7.5 cm
Power Requirement	P_{in}	$19 \text{ V} \times 0.4 \text{ A} = 7.6 \text{ W}$
Cable Delay	t_{cable}	505 ns
Maximum Range	R_{max}	100 m
Maximum Depth	Z_{max}	30 m
Operating Bandwidth	B	200 MHz
Modulation Time	T_{mod}	10 ms
Time resolution	Δt	± 5 ns
Range Resolution (in air)	ΔR	± 1.5 m
Refractive Index Resolution ($R = 40$ m, $f > 1200$ MHz)	Δn	± 0.04
Permittivity Resolution ($R = 40$ m, $f > 1200$ MHz)	$\Delta \epsilon_r$	± 0.08
Transmitting Power at Low Band	$P_{TX}(f = 1.3 \text{ GHz})$	237 mW (23.75 dBm)
Transmitting Power at High Band	$P_{TX}(f = 1.7 \text{ GHz})$	117 mW (20.75 dBm)

Table 6.1: FMCW Permittivity Radar Specifications, obtained from cable and range testing described within this chapter.

Measurements of the VSWR were used to infer the RF emission efficiency and receiving efficiency of the antennas. The VSWR of the transmitting and receiving antennas are shown in Fig. 6.12. The different shape of the *SWR* between the antennas is unexplained, but most likely due to the presence of the coaxial cable outside of the cage (visible in the images in Fig. 6.11), which may change the emission properties of the antenna from what would be expected from the cage design. Variable S_{11} spectrum imply changes of the antenna's impulse response function in an unpredictable fashion. This unfortunate situation means that many features of the time-of-flight spectra namely the side peaks of the spectra of the permittivity radar measurements can not adequately be modelled.

This issue is further compounded by the unfortunate lack of access to a echo-less chamber, without which a true measurement of the antenna's radiation pattern and impulse response function was not possible.

Phase Noise

In the time-of-flight spectrum of a FMCW based radar, the noise floor in the proximity of $\Delta f = df/dt\Delta t$ is dominated by *phase noise*. Phase noise is the noise arising from rapid, short-term, random phase fluctuations. These random fluctuations are caused by time domain instabilities called phase jitter. Phase noise can be observed in the Fourier spectrum of the carrier signal and of the difference frequency and is described with a spectra power distribution $S_N(f)$. There exists a frequency threshold f_{thres} such that for $|f - f_0| < f_{thres}$: S_N is flat and for $|f - f_0| > f_{thres}$:

$$S_N(f, f_0) \propto \frac{1}{|f - f_0|^2} \quad (6.23)$$

And beyond another threshold, the phase noise is dominated by thermal noise or white noise of the system. Typically the flat noise floor dominates for frequencies less than or equal to the loop-filter frequency $f_{thres} \leq f_{LP,loop}$, which for this system is $f_{loop} = 40$ kHz. An example of a phase noise spectrum of the permittivity radar can be seen in the bottom right subplot in figure 6.18. The flat noise floor is dominant within a frequency offset of $f \sim 40$ kHz from the frequency of the peak, with a power of $S(f) \approx P_{peak}/100$ (a signal to noise ratio $SNR \approx 20$ dB). Beyond the frequency threshold, that phase noise drops to $S_N(f > 200$ kHz, where the phase noise falls below the white noise floor $S_N \approx -100$ dBm. Since the mixer spectrum $e_{mixer}(t)$ is the multiple of $e_{LO}(t)$ and $e_{RF}(t)$, the phase noise spectrum falls by the fourth power:

$$S_N(f, \Delta f) \propto \frac{1}{|f - \Delta f|^4} \quad (6.24)$$

As a result of the phase noise floor, it is apparent that any reflected signals must have a power of at least $\sim 1\%$ of the main transmitted signal to be detectable.

Chapter 7

Field Campaign at the Aletsch Glacier

In this chapter, a field campaign of the EnEx-AsGAR project at the Aletsch Glacier is described. The Field Test took place from the 22nd of March until the 12th of April 2022 and was a collaboration with the TRIPLE-FRS project and the University of ETH-Zurich. The EnEx-AsGAR team included Alex Kyriacou from BUW, Michael Stelzig, and Andreas Benedikter from FAU, and DLR-Oberpfaffenhoffen, respectively. The TRIPLE-FRS team included Fabian Becker (BUW), Jan Audehm and Mia Giang Do from RWTH Aachen. Crucially, the team from RWTH operated the melting probes utilized for the EnEx-AsGAR experiments.

7.1 Goals of the Field Test

The goals of the field test for the EnEx-AsGAR project were to test the radar-based sensor systems that would be used to identify subsurface water reservoirs on Enceladus using a glacier as an analog environment. The main sensor systems to be tested were:

- Airborne synthetic aperture radar (SAR) system, using a flyover of a radar-equipped aircraft from DLR to perform F-SAR. Main institute: FAU and DLR-HR.
- UAV-based radar to map the upper firn layer. Main institute: FAU
- Borehole permittivity radar, to measure the permittivity profile of the upper firn layer. Main institute: BUW

In essence, the F-SAR scan would act as a ‘simulation’ of the scanning of the surface of Enceladus from orbit with a radar. Additionally, the flyover from the radar-equipped aircraft was to test the feasibility of locating an active radar transponder underneath the ice in a borehole to simulate a melting probe equipped with an active transponder. Co-currently, the position of the borehole radar would also simulate the transmission of signals between the melting probe and the surface (or other in-ice detectors). Moreover, the measurements from the borehole permittivity radar could aid in the calibration of radar images obtained in the flyover. Thus, the goals of the field test for the BUW side of the EnEx-AsGAR project were:

- Measure the complex permittivity of the upper glacial firn, preferably until the glacial ice was reached (primary)
- To test if in-homogeneities or density transitions from layers below the maximum depth of the borehole radar could be identified (primary)
- To test if the borehole radar could measure a response from the Active Transponder.

The field test was performed in collaboration with the TRIPLE-FRS project, also funded by the DLR Explorer-Initiative. The goal of the TRIPLE project is to demonstrate the feasibility of reaching a subsurface water reservoir with a melting probe that carries a miniaturized underwater vehicle, known as the ‘nanoAUV’, which would then be delivered as a payload to the water pocket. In similar fashion to EnEx, safe arrival requires a reconnaissance system to probe the ice in front of the probe. This is facilitated by a forefield reconnaissance system (FRS), which is envisioned to utilize a hybrid radar and sonar system integrated into the melting head to identify hazards in the path. It is also equipped with a near-field permittivity sensor to measure the local permittivity and therefore determine the true propagation speed of the radio waves, to correct the range assessment of the radar system. At the field test, tests were made to validate the effectiveness of the different sensor systems of TRIPLE-FRS, before future integration into a final version of the melting probe. The TRIPLE-FRS team was made up of two researchers from RWTH Aachen, and one from Wuppertal. The RWTH group also brought melting probes equipped with acoustic pinger units (APUs) which would transmit kHz-range acoustic signals and attempt to measure the speed of sound profile of the ice. These APU-melting probes were utilized to create the boreholes necessary for the experiments of the EnEx-AsGAR group.

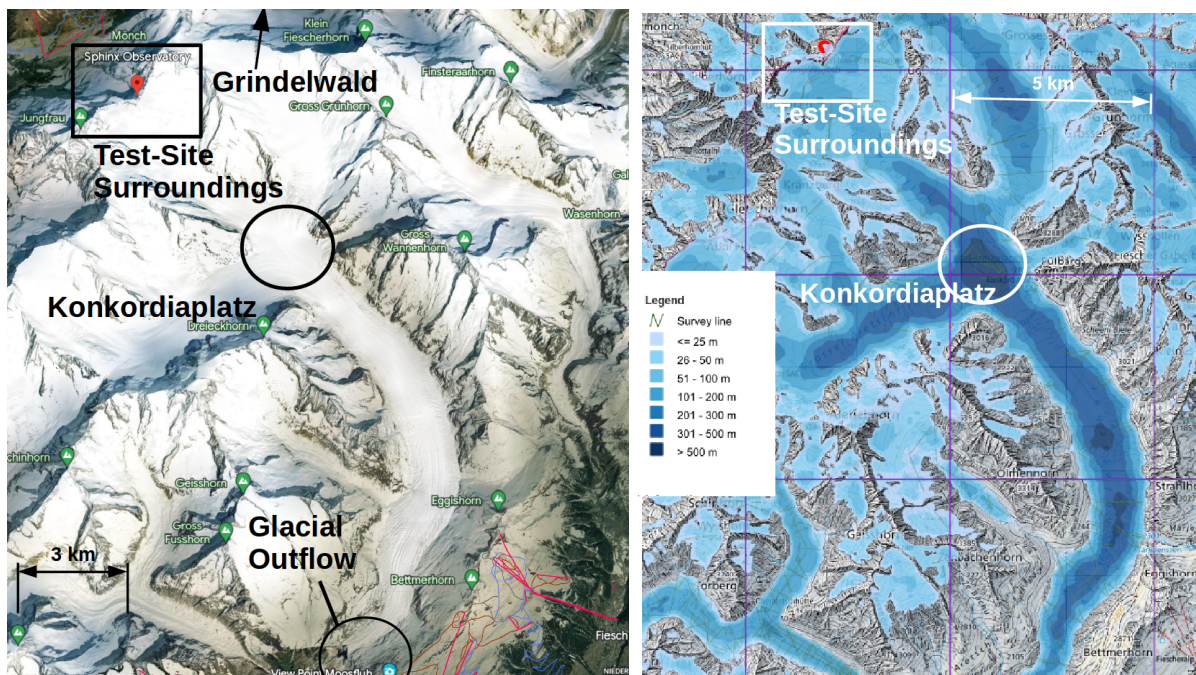
7.2 Location and Timeline

The field test had initially been planned for March 2021. However, due to the COVID-19 pandemic, this could not take place. Spring 2022 was set as an alternate date. It was desirable to select a glacier at a relatively high altitude such that the test location would be in the accumulation zone, where ice accumulates from snowfall, and that temperatures would remain consistently below $T < 0^\circ C$, so there would be minimal melt water to cause attenuation. The higher altitude would also mean colder year-round temperatures, resulting in fewer surface melting events that could lead to ice lenses, although these were later found to be present.

7.2.1 Aletsch Glacier

The Aletsch glacier is located within the Swiss cantons of Valais and Bern and had been chosen as the location for the field test. The Aletsch glacier is the largest glacier in the Alps and in continental Europe both by area and volume. In 2014 it extended for 23 km and had a volume of 15.4 km^3 and a surface area of 81.4 km^2 . As can be seen in the image shown in Fig. 7.1a, it is made up of different tributaries. At the center of the image is the deepest part of the glacier (as seen in the ice depth map in Fig. 7.1b) *Konkordiaplatz*, where the ice can be as deep as 800 m. Konkordiaplatz is the confluence of three glacial flows originating from higher elevations. These are the Jungfrau firn from the north-west, Ewigschneefäld from the north-east, the Grosser Aletschfirn from the south-west and Grüngg firn from the east. Out from the Konkordiaplatz flows the Grosser Aletschgletscher which has a crescent-like shape in the bottom half of the image. It flows downwards towards an altitude of 1632 m where it begins to melt. The melt water ultimately flows into the Rhone River. Like all alpine glaciers, the Aletsch is in retreat but is expected to survive for another century assuming that the current rate of warming from climate change continues.

The test site was set to be located on the Jungfrau firn tributary and in close proximity to the ‘Jungfrauoch’ (shown in Fig. 7.2) a ‘saddle’ between the peaks of the Jungfrau and the Mönch, each more than 4000 m above sea level. This makes the location one of the highest points of the Aletsch glacier. The choice of the site reflected both scientific goals and logistical practicality. Estimates of the depth of the ice at the test site were between $\sim 50 \text{ m}$ to $\sim 100 \text{ m}$, making it more likely that a reflection off the bed-rock could be detected by the radar and acoustic measurement systems.



(a) Satellite view. Credit: Google Earth

(b) Map of the ice thickness (08.10.2020)[31].

Figure 7.1: An overview of the Aletsch glacier with the left showing (Fig. 7.1a) the satellite view and the right (Fig. 7.1b) showing a topographical map (credit: Maps of Switzerland [84], overlaid with a map of the estimated ice thickness in 08.10.2020 [31]. In both images, the test site is within a box (with the label ‘Test-Site Surroundings’) on the top left side, located adjacent to the Jungfrauojoch. An expanded view of the area within this box is shown in Fig. 7.2. The position of the Sphinx Observatory can be seen with a red marker, also within the box. Also shown is Konkordiaplatz, the confluence of three different glacial flows and the deepest part of the Aletsch glacier (maximum of 800 m depth).

7.2.2 Site Plan

The test site was at a latitude of 46.55°N and longitude of 7.99°E at an altitude of ~ 3472 m above sea level and located within 400 m of the entrance to the Aletsch Glacier from the Jungfraujoch. A ‘bird’s eye view’ image of the test site from an overflying UAV is shown in Fig. 7.3. The site had been verified to be safely absent of crevasses by the local glacier guides from the Jungfrau AG. A tent was established to provide a place of warmth and shelter when needed. The power cable from the Jungfraujoch train station came to a tent (shown in the top left of the image), and there met a junction to convert the cable power into usable 220 V AC power. Next to the tent, the equipment for the researchers was kept in Zarges boxes on top of pallets for protection against the elements. Fresh snowfall surrounded the test site from the start of the Field Test.

Four boreholes were created using the APU melting probes during the first week of the field test, designated L1 through to L4. L4 was the deepest, at 35 m, and with a diameter of 9 cm to accommodate the active transponder. Due to the limited number of days where flights were possible, L4 was given the highest priority and melted first. L1 through to L3 were utilized to test the permittivity radar system described previously in chapter 6. L1 was used as the location of the in-ice receiver RX, while L2 and L3 were used for the position of the transmitter TX. L2 was located 25 m away from L1, while L3 was located 42 m away from L1. The length of the available coaxial cables limited the maximum measurable depth to 30 m. With this limit, it was hoped that the firn depth would be less than 30 m and that it would be possible to sample propagation paths through the glacial ice. Indeed, a depth of 25 m was achieved at L3, but due to adverse weather conditions in the second week of the field test, namely 3 days of a snow storm involving winds above 80 km/h and 2.5 m of snowfall, it was not possible to take measurements below 15 m. A cross-section of the glacier, showing the TX and RX configurations used for the permittivity and attenuation measurements is shown in Fig. 7.5. L4 was located 82 m away from L1, such that the transponder would not be obstructed from the aircraft by the equipment at the test site. It should be noted as well, that the horizontal distances between the boreholes were measured by tap, and the heights of the surface borehole were likely within $\Delta z_{surf} \leq 1.0$ m but this was not measured with GNSS receivers, bringing uncertainty into the analysis.

Located between L2 and L1 and next to the pallets was the setup for the 20 cm diameter TRIPLE-FRS melting probe, which reached a maximum depth of 6 m. This borehole was used to test the permittivity sensor system of TRIPLE-FRS. Finally in the top-left corner of Fig. 7.3 is a pit where up-to 3 boreholes were made to test transmission of acoustic signals for TRIPLE-FRS[82].

7.3 Cross-Borehole Measurements

Over the course of the campaign, more than 200 cross-borehole permittivity measurements were taken. All FMCW measurements used for the analysis utilized a bandwidth of $B = 200$ MHz, and base frequencies of 1.3 GHz and 1.7 GHz were used, with the former being useful for longer distance measurements (with subsequent higher signal loss) and the latter yielding higher resolution time-of-flight spectra, which shall be described in this section. Due to a combination of equipment failure (caused by a burnt PA in the TX) in the first week, and several days of poor weather in the second week, only four detailed profile measurements of the time of flight could be obtained. These are:

- Parallel Depth Profile; L1 - L3, $f_{base} = 1.3$ GHz, $B = 200$ MHz, $R = 42.0$ m, $\Delta z = 1.0$ m, $z_{min} = 1.0$ m to $z_{max} = 15.0$ m. Obtained on 05.04.
- Cross Depth Profile: L1 - L3, $f_{base} = 1.3$ GHz, $B = 200$ MHz, $R = 42.0$ m. TX depth fixed at $Z_{tx} = 14.0$ m, receiver moved in intervals of $\Delta z = 1.0$ m from $z_{min} = 14.0$ m to

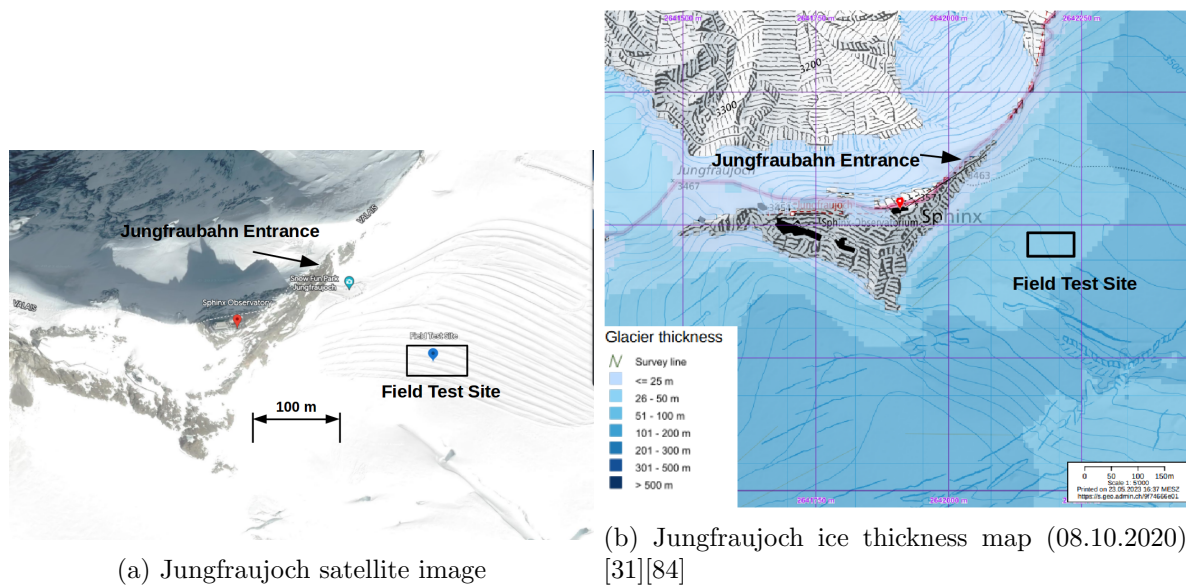


Figure 7.2: An overview of the Jungfrauoch (this view corresponds roughly to the red box from Fig. 7.1), with the satellite image on the left (Fig. 7.2a) and the ice depth map (fig 7.2b) on the right [31, 84]. The Sphinx Observatory is again indicated with a red marker approximately at the center of the images. The research station and touristic ‘Top of Europe’ complex are contained within the mountain upon which the Sphinx Observatory overlooks. The approximate location of the test site is indicated with a red box to the right of the mountain (an expanded view is shown in Fig. 7.3).

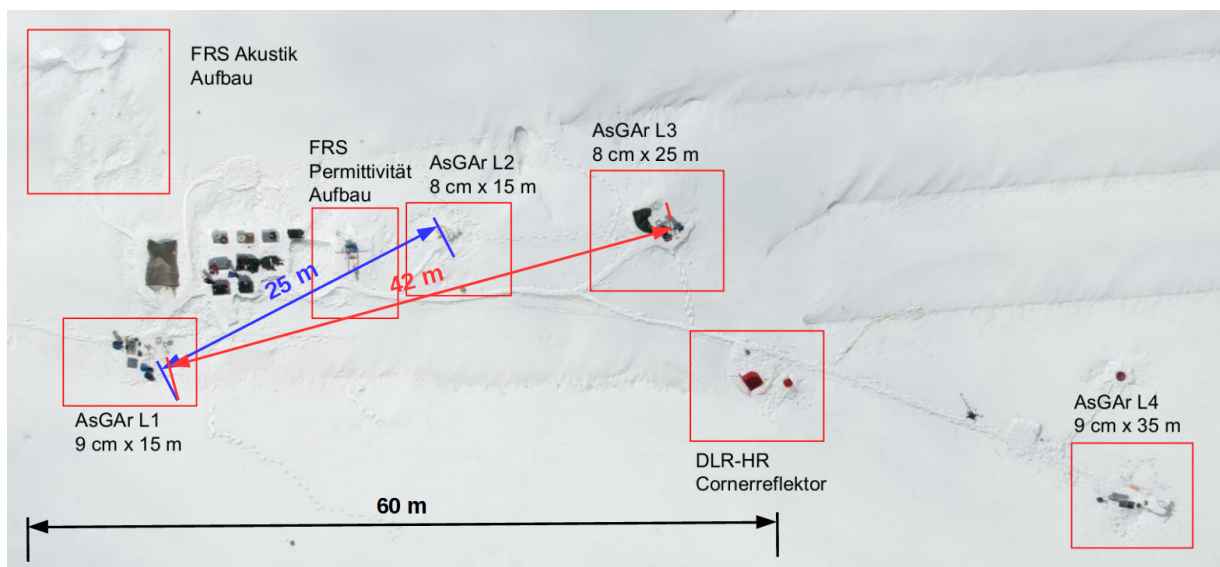


Figure 7.3: A bird’s eye view of the Jungfrauoch test-site, showing the position of the boreholes used by the experiments, the tent, and the equipment storage. This image was taken by a UAV during the field test and corresponds approximately to the box shown in fig 7.2. The blue line corresponds to a borehole separation of 25 m, the red-line to 42 m. Image credit: Michael Stelzig and Mia Giang Do.



Figure 7.4: Calibration air-air measurements between TX and RX at the Test Site 7.4a, taken before the boreholes had been prepared. The photo is taken at L1. The RX tube is shown in the foreground, and is taped to the wooden stand. 42 m away is the TX tube at the location of L3. Deployment of the RX in to the L1 borehole (7.4b)

$z_{max} = 1.0$ m. Obtained on 05.04.

- Parallel Depth Profile; L1 - L2, $f_{base} = 1.7$ GHz, $B = 200$ MHz, $R = 25.0$ m, $\Delta z = 0.4$ m, $z_{min} = 1.0$ m to $z_{max} = 15.0$ m. Obtained on 06.04.
- Cross Depth Profile; L1 - L2, $f_{base} = 1.7$ GHz, $B = 200$ MHz, $R = 25.0$ m. RX depth fixed at $Z_{tx} = 0.0$ m, transmitter TX moved in intervals of $\Delta z = 1.0$ m from $z_{min} = 1.0$ m to $z_{max} = 15.0$ m. Obtained on 06.04.

The positions of the TX and RX for all aforementioned measurements are illustrated in Fig. 7.5. Two separate methods are presented in the reconstruction of the permittivity. The first is a simple peak-selection method, which is applied to ‘parallel depth’ measurements and assumes horizontal propagation of rays through ice, described in section 7.4. The resulting estimates of the permittivity can be used to generate predictions for the time of flight for the ‘cross depth’ measurements via ray-tracing or other simulation methods. The second method attempts to reconstruct the permittivity of the ice using an inversion of PE-based simulations using genetic algorithms, which is described in chapter 5. Measurements of the RF power were made via a frequency sweep from $f = 800$ MHz to 2200 MHz, and the attenuation rate α was estimated as a function of depth and frequency. The attenuation measurement is described in section 7.5.

7.3.1 Parallel Depth Profiles

The most finely grained measurement was taken with the RX at the borehole and TX at the borehole, with a separation of $R = 25$ m. FMCW spectra were recorded between depths of $z = 1$ m to 15 m in intervals of $z = 0.5$ m, using a base frequency of $f_{base} = 1.7$ GHz and a bandwidth of $B = 200$ MHz.

Two examples of parallel depth time-of-flight spectra recorded using the FMCW technique can be seen in Fig. 7.6, with one (Fig. 7.6a) recorded at 12.5 m depth and the other (Fig. 7.6b) recorded at 14.5 m, with the TX and RX separated by a horizontal distance of 25 m in both cases and a base frequency of 1.7 GHz being used. Both show the complexity of the signal, with several peak components visible, which may correspond to reflected and refracted components. As shown in Fig. 7.15a, a relatively dense ice layer may exist between 13 and 15 m. As a result,

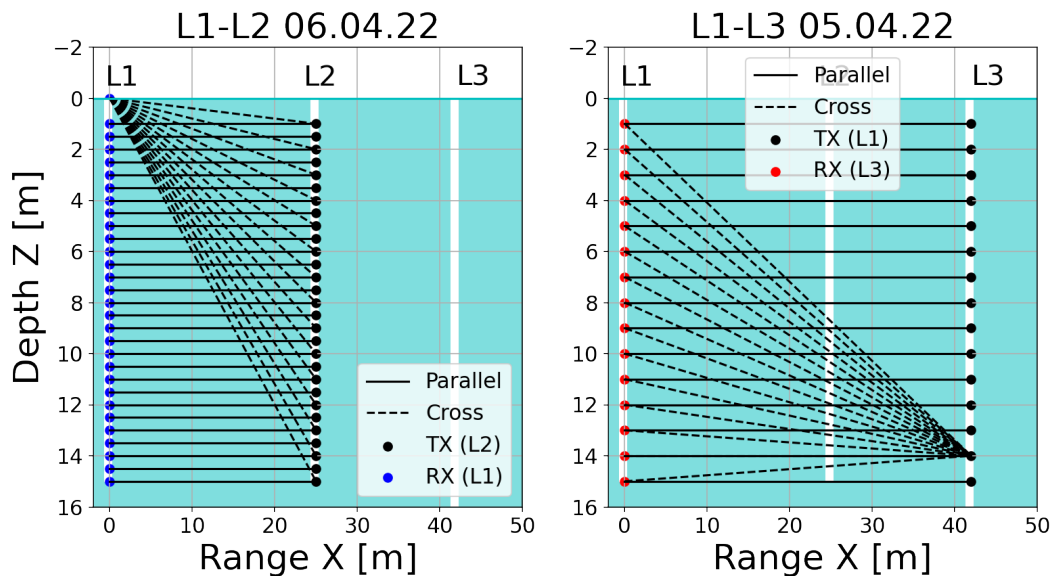


Figure 7.5: Measurement layout cross section on the Aletsch Glacier for days 05.04 (right) and 06.04 (left) for the field test. The labels L1, L2 and L3 indicate the boreholes seen in the image in Fig. 7.3. On both days, L1 is used for the receiver. L3 was used for the position of the TX on 05.04 and L2 was likewise used on 06.04. The parallel depth measurements are indicated with black solid lines and cross depth measurements with dashed lines.

a lensing effect can be observed at 14.5 m (leading to the high number of reflections and refractions). This observation is potential evidence of direct traveling signals (in a high permittivity layer) lagging behind refracted signals. Similar effects were seen in several measurements. The received signal power P_{RX} as a function of delay time at different depths is shown with a parallel depth B-Scan in Fig. 7.7. From this B-Scan, it is apparent that the brightest component of each waveform arrives at the receiver between $100 \text{ ns} < t_{max}(z) < 160 \text{ ns}$. Following, the succeeding times after the maximum peak appear chaotic, with significant features in the time interval from $t_{max} < t(z) < 400 \text{ ns}$, with $P > -50 \text{ dBm}$. Given the uncertainty of the antenna's impulse response function IR, it is difficult to discriminate whether these are clutter caused by internal reflections in the firn or are noise associated with the antenna's response to the maximum signal component. There is no unambiguous air-ice surface reflection, nor any obvious reflected component from a surface deeper within the ice.

In Fig. 7.8, the arrival times of the maximum amplitude signal are displayed at each depth, as well as the earliest arriving signal with an amplitude greater than 10% of the maximum peak. The two peaks match are identical for depths $6 \text{ m} < z < 11 \text{ m}$, but are divergent outside of this depth range. All of the observed peaks are between the propagation time for in-air travel $t_{air} = R/c$ and that for pure ice $t_{ice} = Rn_{ice}/c$ (with $n_{ice} = 1.78$). The maximum signal power $P_{RX} \approx -6 \text{ dBm}$ was measured at a depth of $z = 7.5 \text{ m}$, exceeding the average power of -16 dBm for depths $1 \text{ m} < z < 14 \text{ m}$, and the expected power expected from spreading loss at this range of $P_{RX} = P_{TX}/4\pi R^2 = -18 \text{ dBm}$ (given the expected TX power P_{TX} estimated in calibrations tests in chapter 6), with a gain of $G \sim 12 \text{ dB}$. The lowest power is seen at $z = 15 \text{ m}$, where it drops as low as $P_{RX} \sim -35 \text{ dBm}$. The cross-borehole measurements between L1 and L3 were performed in intervals of $\Delta z = 1 \text{ m}$, with a separation distance of $R = 42 \text{ m}$ and using a base frequency of $f_{base} = 1.3 \text{ GHz}$. The parallel depth B-Scan is shown in Fig. 7.9. As with the previous example of the L1-L2 measurement, the B-Scan can be described as having a bright peak component which mostly is the first arriving signal component, arriving at times $200 \text{ ns} < t(z) < 250 \text{ ns}$, in excess of the expected arrival time in a vacuum of $t_{air} = R/c = 133 \text{ ns}$.

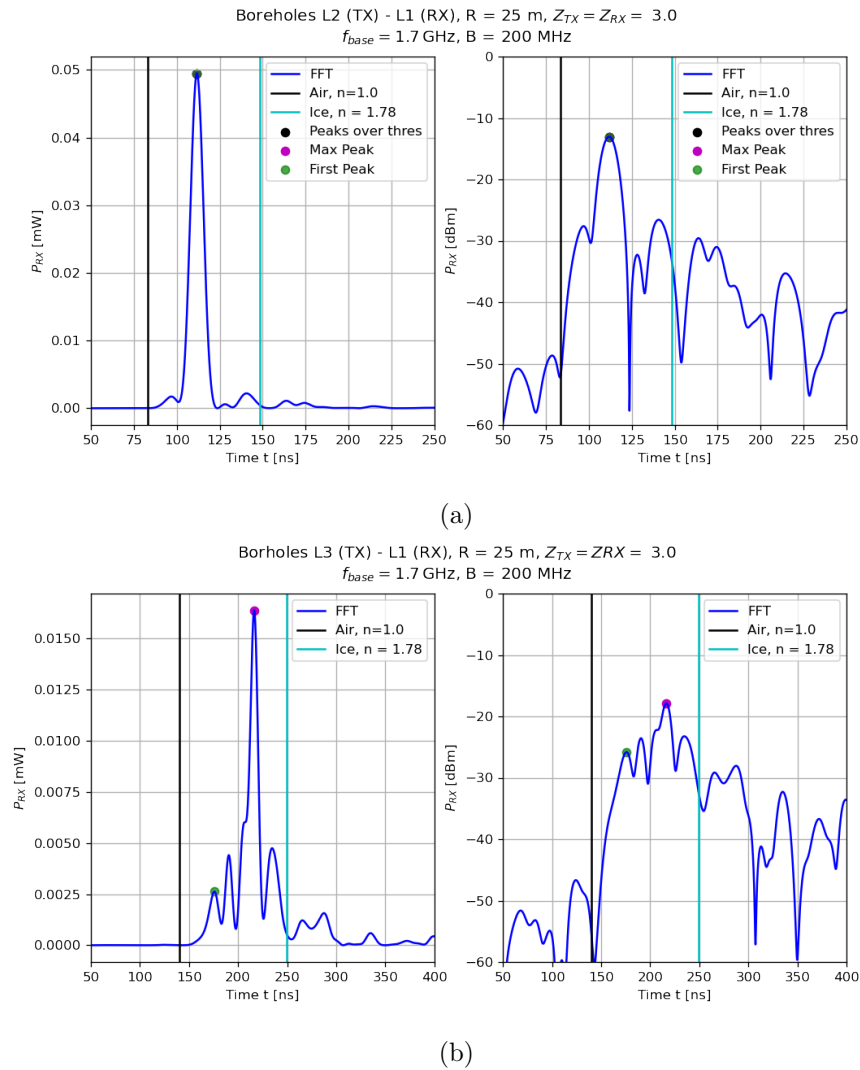


Figure 7.6: Examples of FFT time-of-flight profiles, measured between TX and RX at a range of $R = 25$ m. Fig. 7.6a was recorded when the RX and TX were at a depth of $Z = 14.5$ m and fig 7.6b was recorded at $Z = 12.5$ m. The red markers indicate ‘peaks’ with an amplitude at least 10 % that of the peak of maximum amplitude.

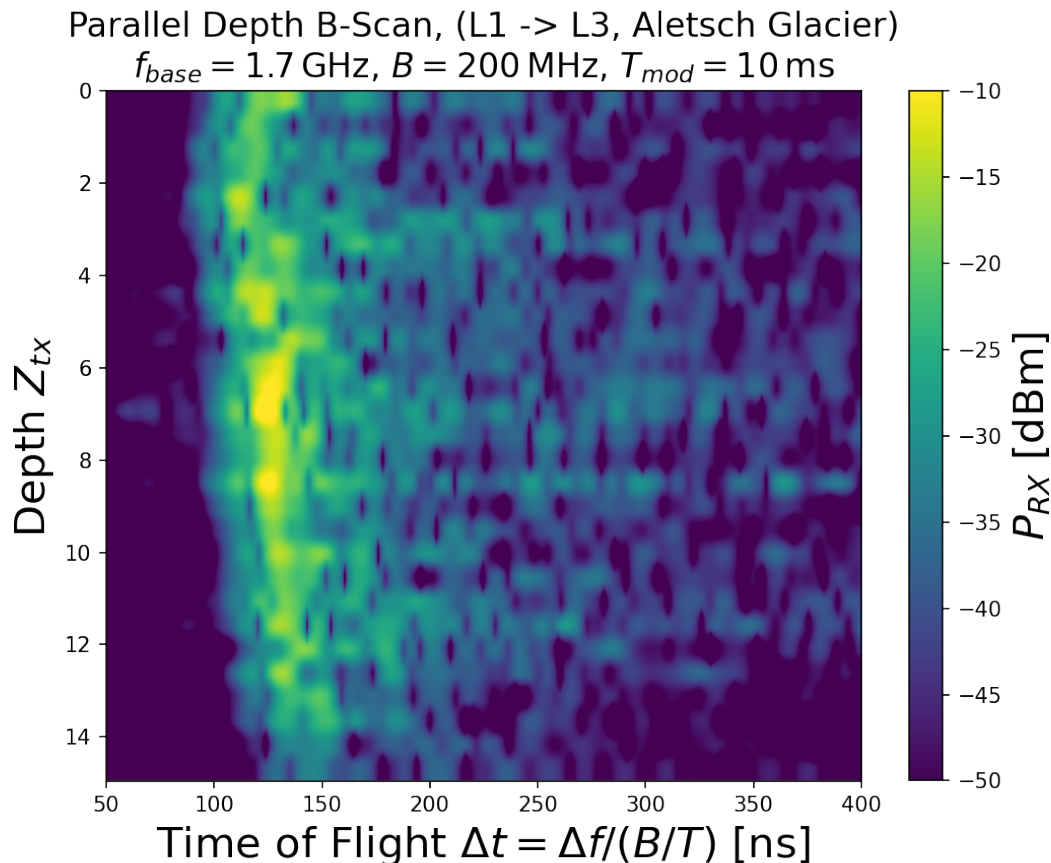


Figure 7.7: Parallel Depth B-Scan, for boreholes L1 and L2, $R = 25 \text{ m}$, using $f_{base} = 1.7 \text{ GHz}$ and a bandwidth $B = 200 \text{ MHz}$, with intervals of $\Delta z = 0.5 \text{ m}$.

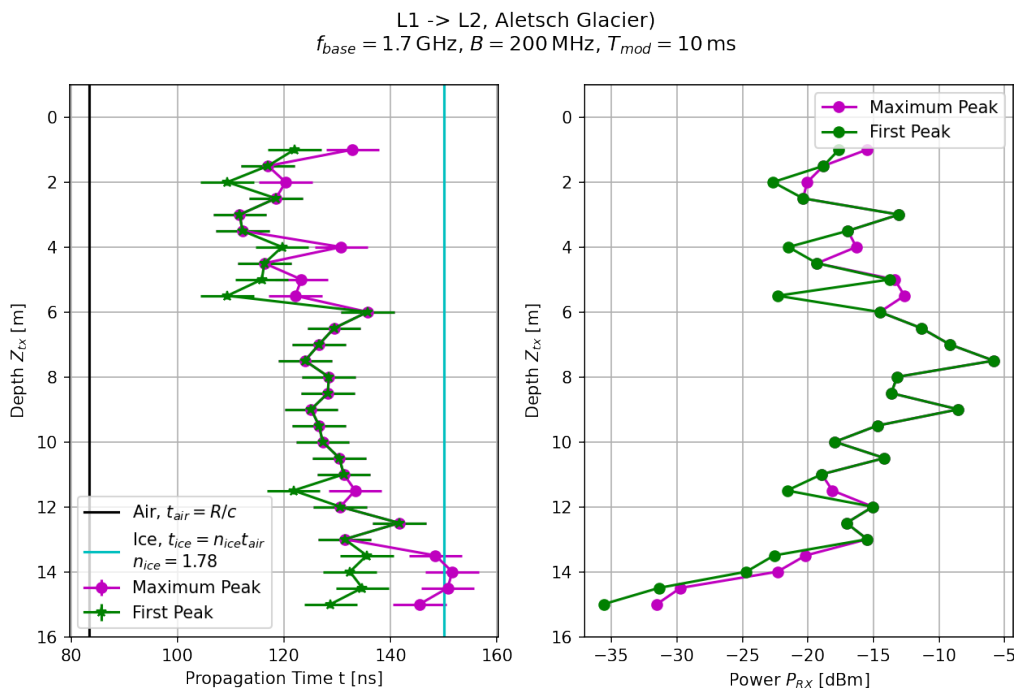


Figure 7.8: The propagation time and power of ‘maximum’ peak and ‘first’ arriving peak in the waveforms recorded between L1 and L2.

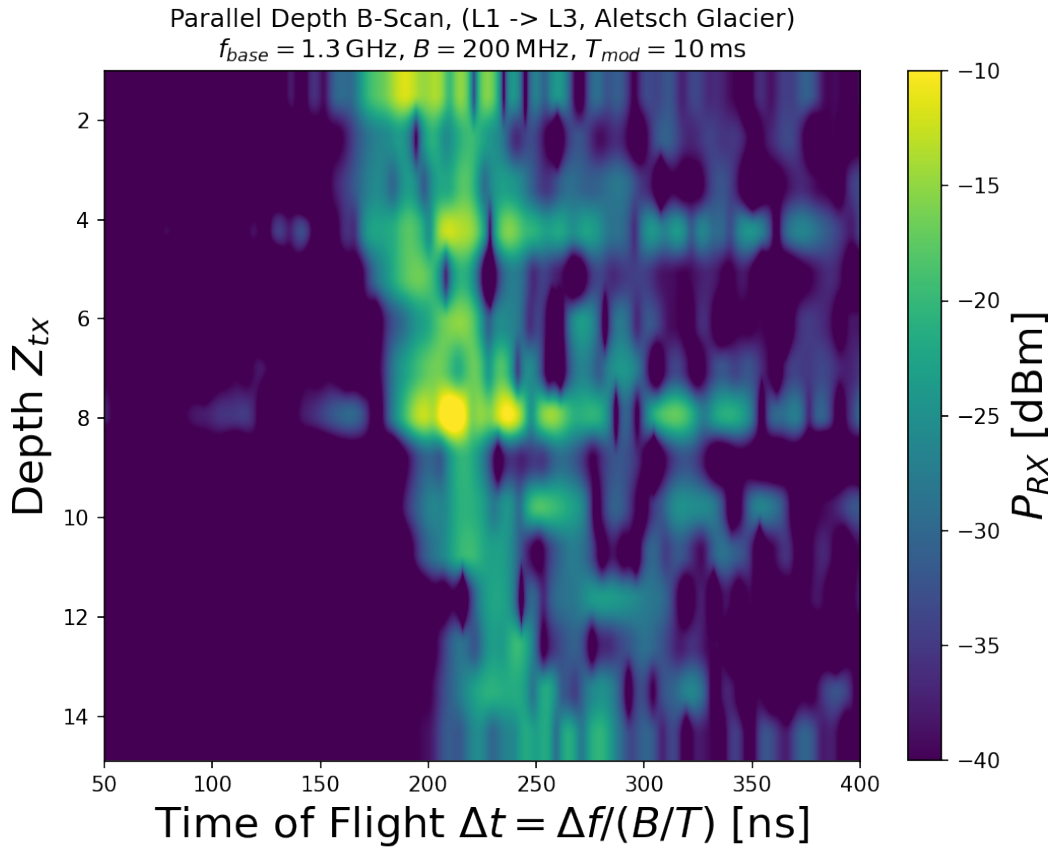


Figure 7.9: Parallel Depth B-Scan, for boreholes L1 and L3, $R = 42 \text{ m}$, using $f_{base} = 1.3 \text{ GHz}$ and a bandwidth $B = 200 \text{ MHz}$, with intervals of $\Delta z = 1 \text{ m}$.

This component is then followed by a trail of peaks which are difficult to distinguish from noise. It can be noted that there are more ‘double peaks’ in this B-Scan, with the maximum peak not necessarily corresponding to the first arriving peak, as seen in the propagation time and power of the first and maximum peaks in Fig. 7.10.

The signal power $P_{RF} \sim -5 \text{ dBm}$ is the greatest at 8 m depth, close to that observed for the L1-L2 example, and average power being approximately -15 dBm at depths $z > 8 \text{ m}$. Although L3 is located at nearly twice the distance from L1 and L2, calibration tests at the university found the $P_{TX} = 244 \text{ mW}$ for $1.3 \text{ GHz} < f < 1.5 \text{ GHz}$, meaning that the average power is broadly consistent with the expected power from the spreading loss. The permittivity profiles estimated from both ‘parallel-depth’ time-of-flight measurements will be discussed in section 7.4, with a consistent permittivity estimated found for depths $4 \text{ m} < z < 10 \text{ m}$, and discrepancies between the estimates found at other depths.

7.3.2 Cross Depth Profiles

The loss of measurement time at the field test was unfortunate, as cross-depth measurements would have allowed sampling of the ice environment along many more paths than are possible for parallel depth measurements. The signal power recorded at L1 from L3 is shown as a function of receiver depth and time in the cross-depth B-Scan in Fig. 7.11, with the time of flight and power of the ‘first’ and ‘maximum’ peaks shown in Fig. 7.12.

The B-Scan shows a complex signal spectrum with multiple significant features at $z > 12 \text{ m}$.

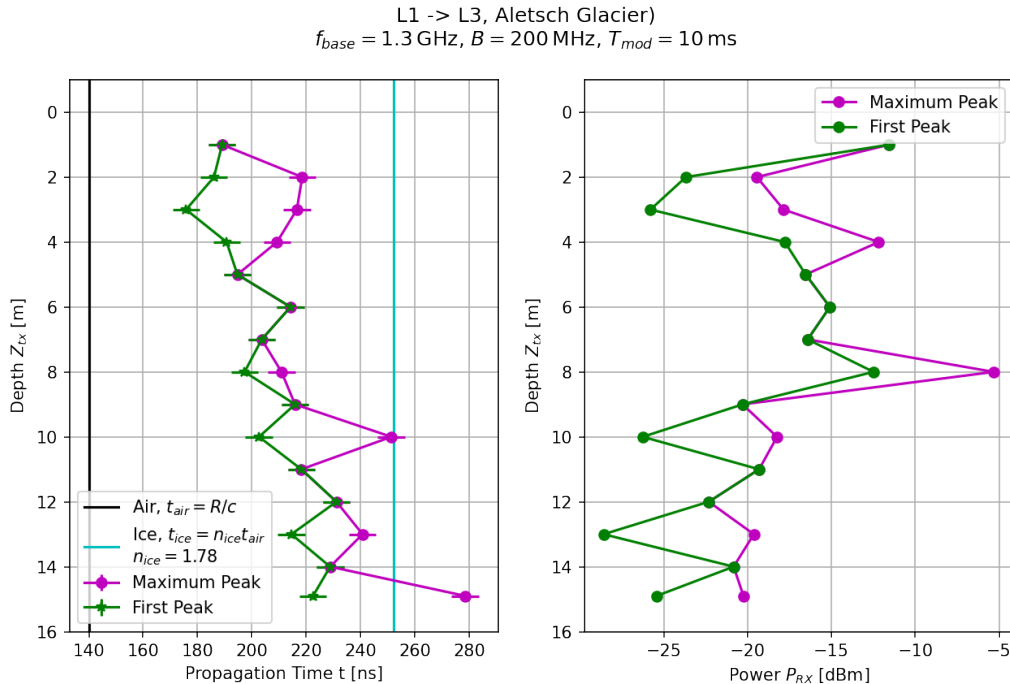


Figure 7.10: The propagation time and power of ‘maximum’ peak and ‘first’ arriving peak in the waveforms recorded between L1 and L3.

Bright emission of $P \sim -5 \text{ dBm}$ is observed at $z = 2 \text{ m}$, $z = 5 \text{ m}$ and $z = 12 \text{ m}$. To test the permittivity profiles estimated from the parallel depth data, the arrival time for a signal originating at $Z_{TX} = 14 \text{ m}$ as a function of depth for $R = 42 \text{ m}$ was computed using a ray-tracing (RT) algorithm. It is noteworthy that RT could only find solutions for a discrete number of depths at a range of 42 m: $z = 2, 6, 12, 13$ & 14 m , while the other depths appear to exist within the ‘forbidden zone’ of the glacier. The depths for which RT solutions exist are in good agreement with the measured time of flight of either the first or maximum peaks. A similar example to L1 from a TX located at $z = 1 \text{ m}$ L2 is shown in Fig. 7.13, and the time and power of the ‘first’ and ‘maximum peaks’ shown in Fig. 7.12. Here the measured power is weaker by a value of 10 – 15 dB from the two parallel depth profiles and the L1-L3 cross profile, as it seems that down-going RF emission is weaker than up-going or horizontal RF emission. Once again, the expected time of flight is estimated from RT using the permittivity profile derived from the parallel depth measurements. In this case, valid solutions could be computed for most of the RX depths (except for $z = 3 \text{ m}$ and $z = 15 \text{ m}$), and the estimated time of flight is in good agreement with the times of the first and maximum peaks for depths $z > 10 \text{ m}$, where the RT estimated peaks arrive approximately $\sim 10 \text{ ns}$ earlier than what is seen in data.

7.4 Permittivity estimation via Peak Analysis Method

The absolute signal amplitude is composed of several peaks, with a given amplitude, time-of-arrival and time resolution. Using Python’s *peakutils* package, the most significant signals (with an amplitude above a pre-determined value) are selected and the algorithm calculates for each depth z_i :

1. The arrival time of the peak with the largest amplitude or ‘maximum peak’: $t_{max,i} = t_{max}(z_i)$
2. The ‘first’ or earliest arriving significant peak: $t_{first,i} = t_{first}(z_i)$

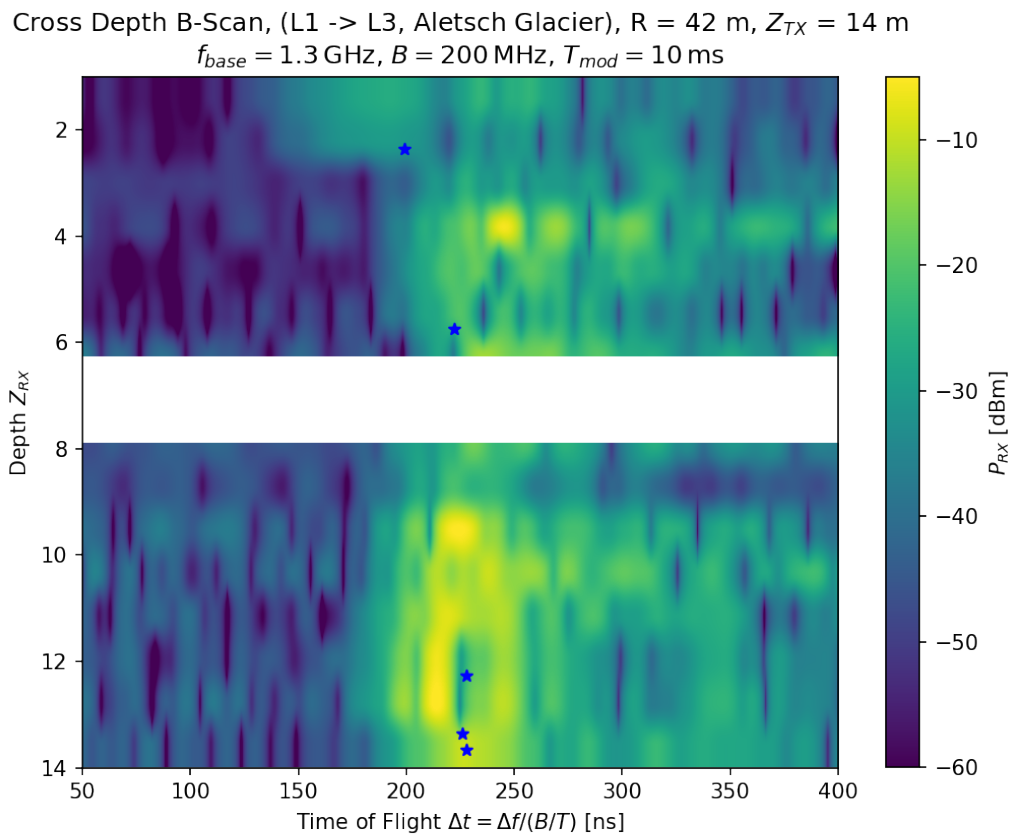


Figure 7.11: Cross Borehole B-Scan for L1-L3, with a fixed transmitter depth $Z_{tx} = 14.0$ m. The gap at $z = 7$ m corresponds to a failed measurement at this depth.

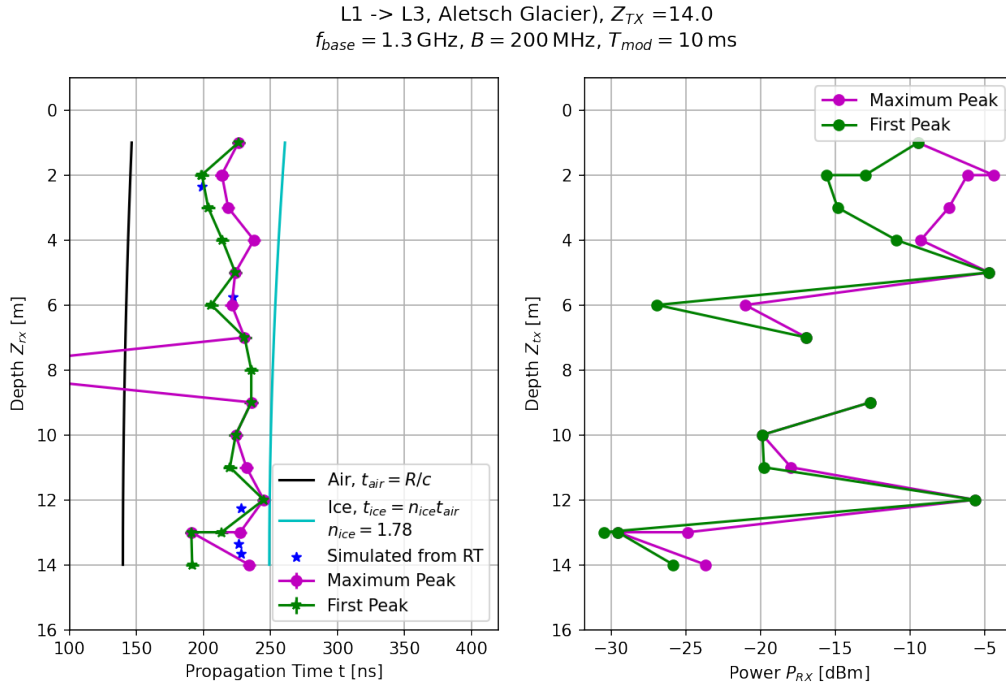


Figure 7.12: The ‘first’ and ‘maximum’ peaks selected from the L1-L3 cross depth B-Scan shown in Fig. 7.11, with the propagation time shown on the left and the power P_{RX} shown on the right. Note that the measurement at $Z_{RX} = 8$ m failed and hence the data point from this depth should be ignored.

Each of these values forms the basis of a hypothesis (hypotheses 1 and 2). Hypothesis 1 assumes that a horizontally propagating signal t_{direct} (from RX to TX directly) arrives at the time equal to the central time of the maximum peak t_{max} . Hypothesis 2 assumes $t_{direct} = t_{first}$. For each depth, the refractive index n_i is calculated simply:

$$n_i = ct_{direct}/R \quad (7.1)$$

Where c is the speed of light in a vacuum, and R is the horizontal distance between TX and RX . From this permittivity can be found simply: $\epsilon_r = n^2$. This procedure is repeated for each depth in the parallel depth scan. Thus, each depth has up to three possible values for the refractive index and permittivity. At this point, the estimated permittivity profiles are used to compute the results of cross-depth scans. The observed time of flight t_{obs} is compared to the prediction of each hypothesis t_j (where j corresponds to hypotheses 1,2 and 3), with the offset: $\Delta t_j = |t_{obs} - t_j|$. The final resulting permittivity profile is the one that minimizes the value:

$$\sum_i^N \Delta t \quad (7.2)$$

7.4.1 Results: Permittivity Profile

From the array of FMCW spectra, permittivity profiles of the upper 15 m of the Jungfraujochnfirn test-site were reconstructed at baselines of 25 m (results shown in blue) and 42 m (results shown in red). Utilizing the ‘maximum peak’ (Fig. 7.15) method, the permittivity profile along the two baselines shows consistent ice permittivity for depths between 4 m and 8 m, and for depths between 11 and 14 m. The peak-based reconstruction method shows a great degree of similarity between the profiles. Unfortunately, the 42 m profile could only be measured in depth increments

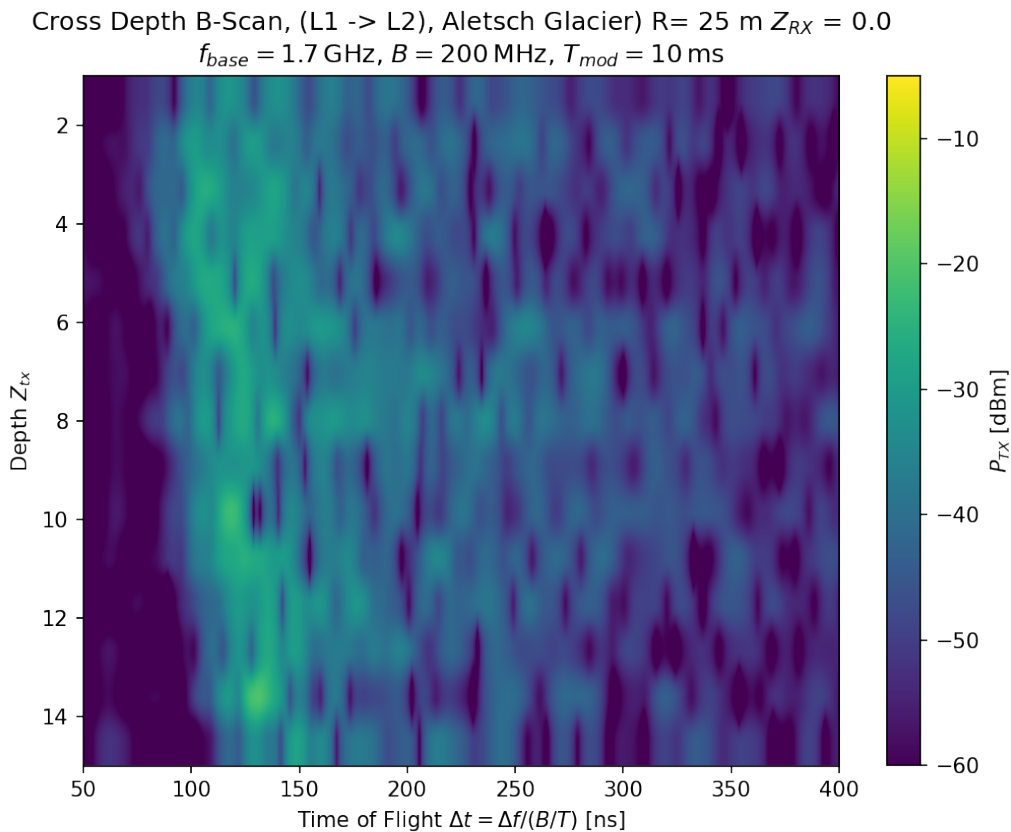


Figure 7.13: Cross Depth B-Scan for L1-L2, with a fixed receiver depth $Z_{RX} = 0$ m and a variable transmitter depth.

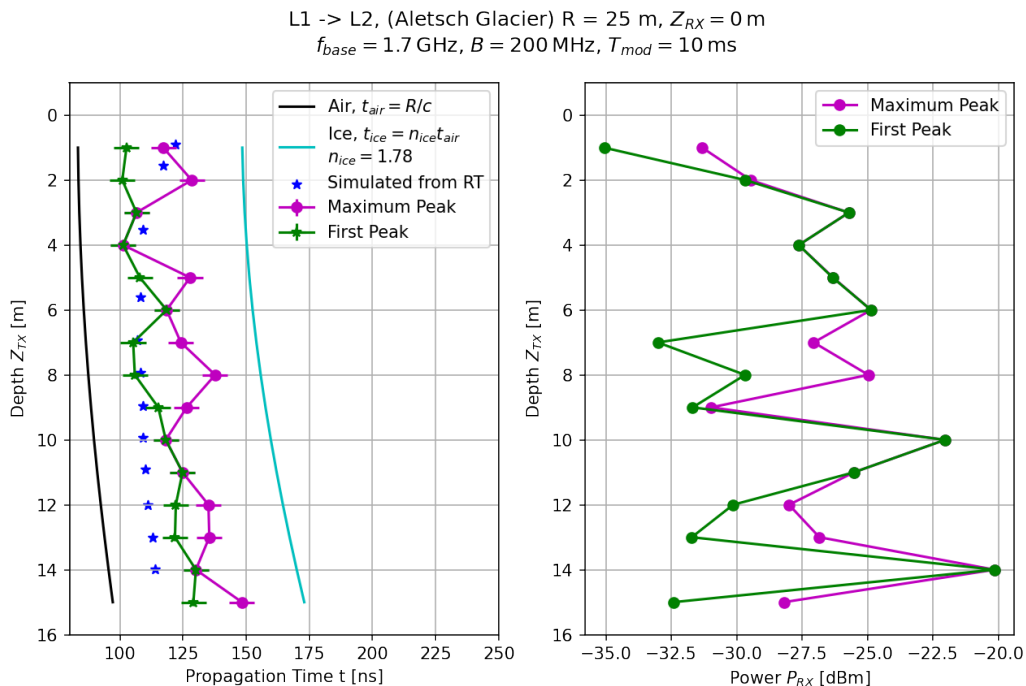
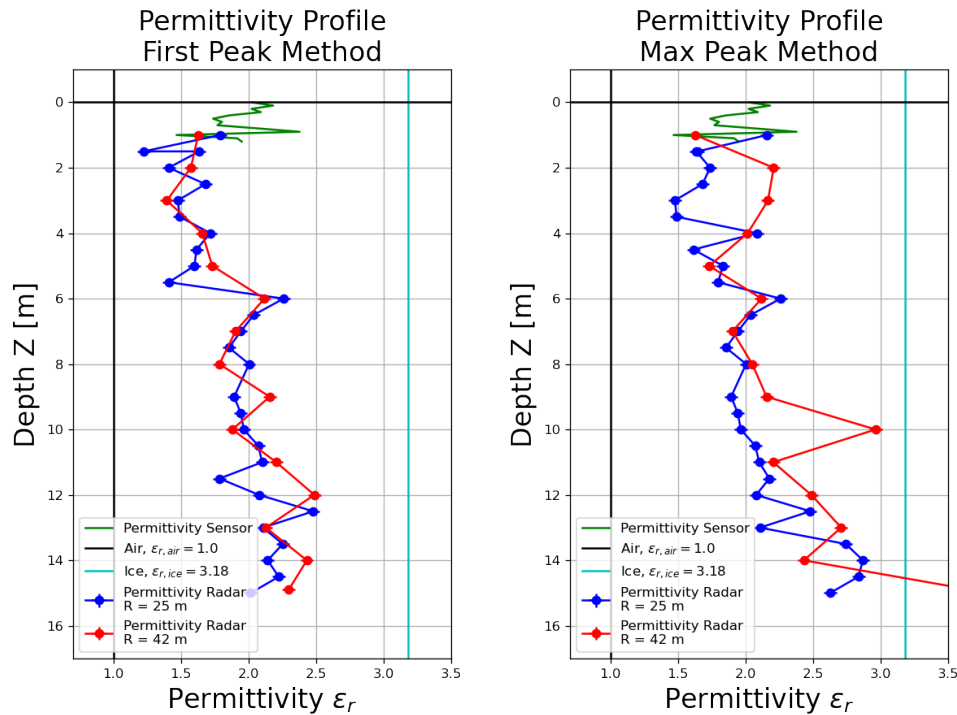


Figure 7.14: The time of flight of the peaks selected in the L1-L2 cross borehole radar (left), with the power shown on the right.



(a) $\epsilon_r(z)$ from ‘first peak’ method. (b) $\epsilon_r(z)$ from ‘maximum peak’ method.

Figure 7.15: The estimated permittivity profile ϵ_r' , as estimated from the refractive index measured using the first and maximum peaks of the signal recorded at distances of $R = 25$ m (blue) and $R = 42$ m (red).

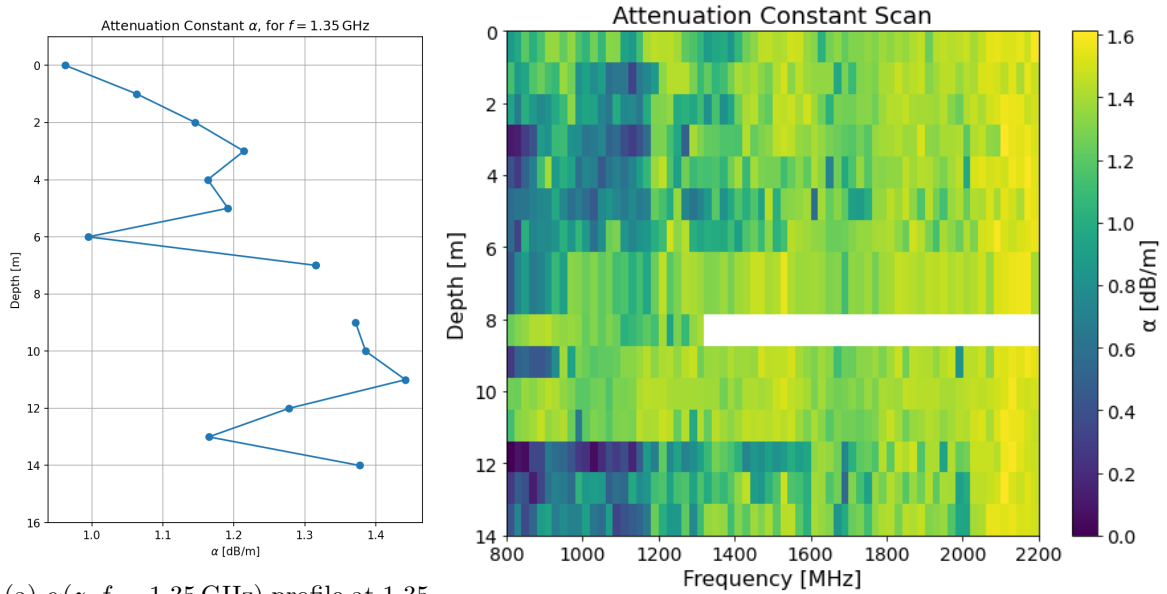
of 1 m, while the 25 m profile has a depth resolution of 50 cm. There is clear evidence of re-frozen ice layers at 4 m depth, 10 m depth, and 14 m depth, also observed in the UAV SAR measurements taken by the FAU team[82]. These are hypothesized to correspond to the summer of 2021, 2020, and 2019, respectively. Density fluctuations between on the scale of 40 m are thought to explain the difference in permittivity between the 25 m and 42 m baselines.

7.5 Attenuation Measurement

Attenuation profiles were measured to a depth of 15 m, utilizing the 25 metre baseline. The attenuation rate α was calculated by simply measuring the RF power loss compared to observations in air, given the laboratory-derived antenna gain G , wavelength λ , and antenna separation distance R . The attenuation was measured across the entire frequency of the permittivity radar (800 MHz to 2200 MHz). A software error prevented measurements from being taken at 8 m for $f > 1.3$ GHz, explaining the gap in the attenuation profile seen in Fig. 7.16.

$$P_{RX} = P_{TX} \frac{G^2 \lambda}{4\pi R^2} e^{-\alpha R} \quad (7.3)$$

A 2D color plot showing the attenuation for each depth (in increments of 1 metre) and each frequency (in increments of 50 MHz) is shown in Fig. 7.16b. The attenuation $f = 1.35$ GHz (utilized by the FAU transponder) is shown in Fig. 7.16a. As expected, the attenuation rate increases linearly with frequency, within a minimum of 0.3 dB/m at 800 MHz (seen in Fig. 7.17), and a maximum of 1.6 dB/m measured at 2200 MHz. The highest attenuation was observed at a depth of 11 m which does not obviously correlate with the ice layers. This result is as of yet



(a) $\alpha(z, f = 1.35$ GHz) profile at 1.35 GHz

(b) $\alpha(z, f)$ profile across the frequency span of the system.

Figure 7.16: The derived attenuation profile of the Jungfraufirn. In fig 7.16b a 2D color-map showing measured attenuation for all depths (resolution of 1 metre) and frequencies (resolution of 50 MHz). The attenuation profile measured at 1.35 GHz $\alpha(z, f = 1.35$ GHz) is shown in fig 7.16a.

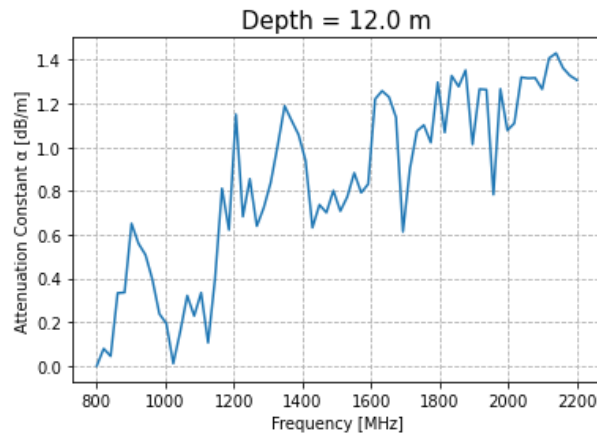


Figure 7.17: The attenuation rate $\alpha(z = 12$ m, f) at $z = 12$ m, as function of frequency f .

unexplained, as attenuation is broadly proportional to permittivity, but it is possible that this layer features a higher level of salinity (and therefore conductivity). The lowest attenuation was found at 6 m of the depth, possibly owing the trapping of radio emission within a relatively high density layer. Such effects are being investigated using the PE-based inversion analysis described previously. The measure attenuation is consistent with an ice conductivity of $\sigma = 500 \pm 100 \mu\text{S}/\text{m}$.

7.6 Summary

The cross-borehole permittivity radar concept was successfully demonstrated at the Aletsch Glacier field test. Time-of-flight and power spectra were measured to a maximum depth of $Z = 15$ m at distances of 10 m, 25 m and 42 m respectively, with the permittivity distribution estimated by selecting the peak of highest amplitude in the time-of-flight spectra. However, the volume of data was limited by a range of factors: failure of amplifier in the first week of the test, heavy snowfall in the second week of the test, leaving only 4 days of time for effective data taking with a well-functioning system. The desired goal of measuring down to the depth of the glacial ice could not be achieved.

Chapter 8

Analysis of Field Test Data

In the previous chapter (chapter 7), a preliminary estimate of the permittivity profile of the upper glacial firn at the test site near the Jungfrauoch based on the ‘peak analysis method’ was described. In this chapter, the physical implications of the data with respect to glaciology are examined. Additionally, this chapter describes an application of the GA-based reconstruction of the permittivity profile of the upper Jungfrau firn. For this, the cross-borehole measurements between boreholes L1 and L2 at a range of $R = 25$ m are used, for which the base-frequency was $f_{base} = 1.7$ GHz, and bandwidth of $B = 200$ MHz.

8.1 Glacier Modelling

The refractive index of firn n is directly proportional to the bulk firn density ρ via the empirical relationship [69],

$$n(z) = 1 + b\rho(z), \quad (8.1)$$

In which ρ is in units of g/cm^3 and $b = 0.845 \text{ cm}^3/\text{g}$. It is possible to calculate the density profile from the densification rate $d\rho/dt$ of a glacier and the accumulation rate of the glacier, i.e. the falling mass flux on the surface of the glacier. This is found by invoking an empirical relationship known as ‘Sorge’s law’ which related the ‘vertical velocity’ of firn to be equal to the accumulation rate $A(t)$ divided by the density the density ρ ,

$$\frac{dz}{dt} = \frac{A}{\rho}. \quad (8.2)$$

The densification rate itself can be determined via the Herron-Langwey model (described in detail in appendix B), which relates the densification rate to a densification rate factor k and the accumulation rate A via a differential equation:

$$\frac{d\rho}{dz} = k\rho(\rho_{ice} - \rho). \quad (8.3)$$

From this differential equation, the exponential-like relationship between density and depth can easily be derived. Hence one can find $d\rho/dt$:

$$\frac{d\rho}{dt} = k\left(\frac{A}{\rho_w}\right)^\beta(\rho_{ice} - \rho) \quad (8.4)$$

Where the densification rate factor k is itself a function of temperature, and changes above a density threshold $\rho = 550 \text{ kg/m}^3$:

- $\rho < 550 \text{ kg/m}^3$: $\beta = 1$ and $k = 11 \exp\left(-\frac{10160}{RT}\right)$
- $\rho > 550 \text{ kg/m}^3$: $\beta = 0.5$ and $k = 575 \exp\left(-\frac{21400}{RT}\right)$

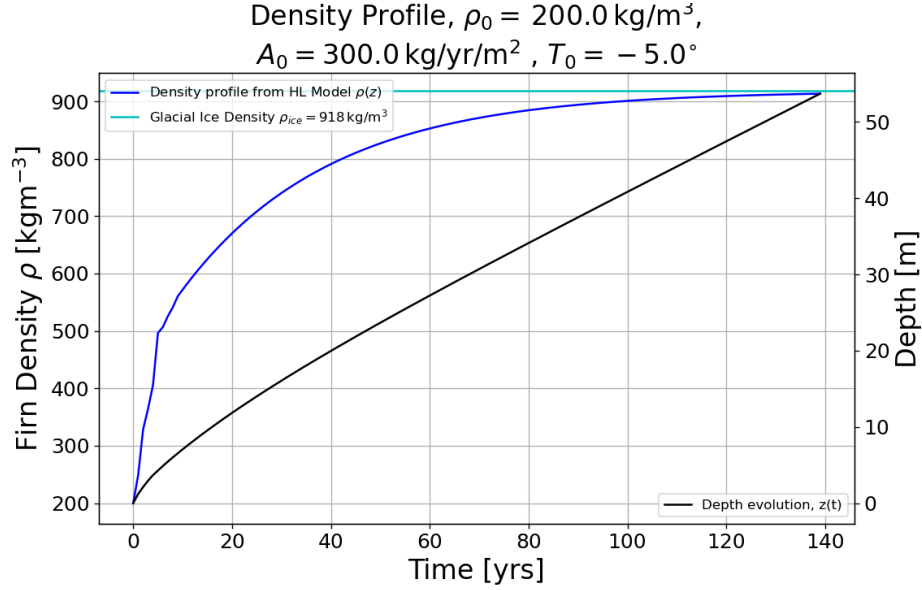


Figure 8.1: The density evolution of the Aletsch glacier, inferred from historical snow-fall data and the Herron-Langwey model[37]. The red-line shows the density $\rho(t)$ as a function of time, while the black line shows the depth $z(t)$ of the corresponding density as a function time. For example, a density of $\rho = 800 \text{ kg/m}^3$ is reached after 40 years of snow fall, at which time this layer should be $\sim 18 \text{ m}$ below the surface.

The change in k reflects a change in the densification process from being dominated compaction from overburden pressure to being dominated by sintering (see appendix B). Using climatic records of the snowfall rate at the Aletsch glacier over a period of 10 years, and the yearly average temperature at the Aletsch glacier over the same period, an estimate of the density $\rho(t)$ and depth as a function of time $z(t)$ was computed for a period of 140 years, with the results being shown in Fig. 8.1. An average accumulation rate of $A_{ave} = 300 \text{ kg/m}^2/\text{yr}$ is assumed for the time period prior to 2012. The model predicts that the density reaches an excess of $\rho > 900 \text{ kg/m}^3$ beyond a depth of $z = 53 \text{ m}$, and the overlying firn is the result of approximately $\sim 120 \text{ yr}$ of accumulation. Interestingly, the ‘inflection point’ at $\rho = 550 \text{ kg/m}^3$ is within the depths probed in the field test measurements, and this density would have been reached from $\sim 10 \text{ yr}$ of snowfall. Furthermore, it was possible to perform a fit to the data using a simple

Winter Period	Total Snow Fall [cm]	Snowfall Days	Highest Daily Snowfall [cm]
2012 2013	383	36	30
2013 2014	200	22	25
2014 2015	154	21	25
2015 2016	179	25	20
2016 2017	97	16	25
2017 2018	694	34	54
2018 2019	292	15	35
2019 2020	240	21	25
2020 2021	466	29	50
2021 2022	267	21	30

Table 8.1: 10 Years of snow fall data at the Aletsch glacier from 2012 to 2022 [54]. The average snowfall rate over this time period is $A_{ave} = 297 \text{ kg/m}^3$, or 297 cm/yr

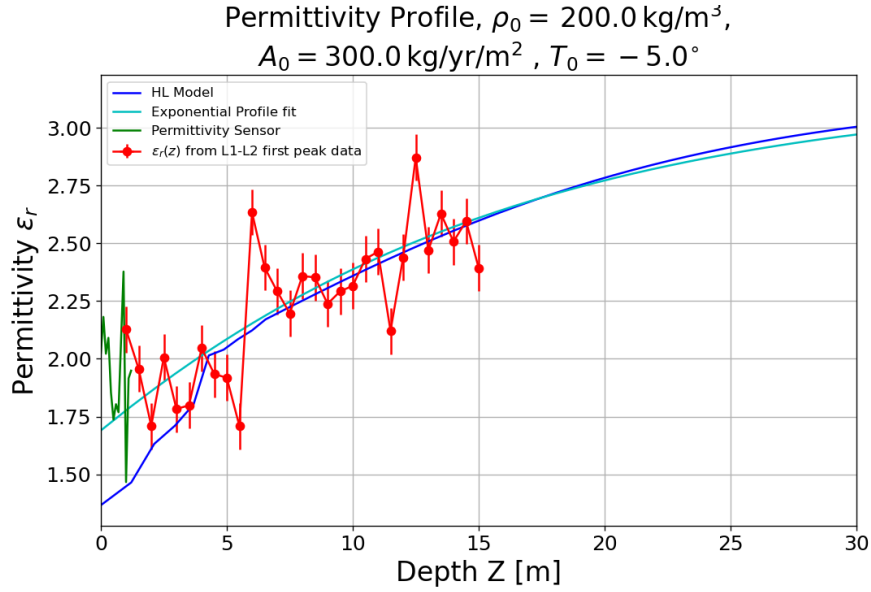


Figure 8.2: ϵ_r profile for the field-test data (first peak method measured for the parallel depth profile L1-L2), compared with the estimated density profile using snowfall data and the Herron-Langwey model. Also shown is the best-fitting exponential profile.

exponential profile model, based on the analytical fit to Spice Core data,

$$n(z) = n_{ice} + (n_0 - n_{ice})e^{-z/z_{scale}}, \quad (8.5)$$

Where $n_{ice} = 1.78$, n_0 is the refractive index at the surface, and z_{scale} is the ‘scale depth’ of the glacier (analogous to the scale height of the atmosphere). In this case, n_0 and $z_{surface}$ are allowed to be free parameters to the data. A comparison between the permittivity profile derived using snowfall data from the Aletsch glacier $\epsilon_{r,HL}(z)$, and the best functional fit $\epsilon_{r,exp}(z)$ to the data using the equation 8.5. In Fig. 8.2, the results are compared with the ‘first peak’ profile derived from the L1-L3 parallel depth profile described in the previous chapter. The best-fit values of the exponential function were found using a chi-squared fitness test and were found to be $n_0 \sim 1.312$ and $z_{surface} \sim 14 \text{ m}$. The derived profile $\epsilon_{r,HL}(z)$ shows good agreement with the data permittivity values for $3 \text{ m} \leq z \leq 4.5 \text{ m}$ and $8 \text{ m} \leq z \leq 11 \text{ m}$ and $z > 13 \text{ m}$. The largest discrepancies are seen at $z \sim 6 \text{ m}$ and $z \sim 12.5 \text{ m}$ may correspond to layers of ice resulting in the refreezing of melt-water from recent summer melting events, likely in 2020 and 2021.

8.2 Comparison of Field Test with RT and PE Simulations

Having obtained estimates for the permittivity profile based on the parallel depth measurements between boreholes L1 and L2, it is possible to assess the accuracy of this estimate by comparing the results of other measurements against the predictions from parabolic equations (PEs) and ray tracing (RT). Therefore, the ‘first peak’ and ‘maximum’ peak-derived profiles were used to generate and simulate RF propagation for a set of transmitters corresponding from the positions used in the field test, and sampled at the corresponding receiver positions also used in the field test. Both modeling methods implicitly assume range independence of the refractive index in the ice, a perfectly flat surface, and no attenuation. The RT simulation also takes the infinite frequency limit of the wave equation and hence will neglect any wave-like properties of the propagation.

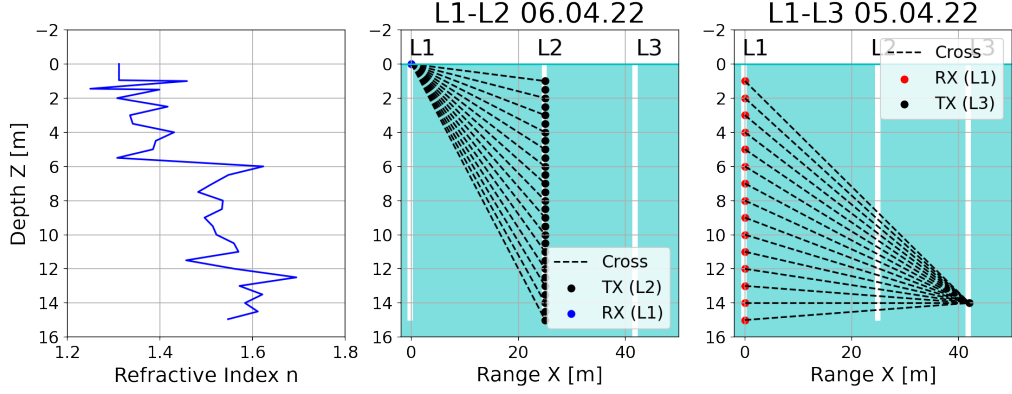


Figure 8.3: On the left, the refractive index model; first peak profile derived from L1-L2 parallel depth measurement, used for the RT and PE simulation shown in section 8.2. The middle image is the L1-L2 borehole cross-depth profile from the field test, with a fixed receiver position at $z = 0$ and the transmitter moving with depth from $z_{min} = 1.0$ m to $z_{max} = 15$ m at $R = 25$ m. The right image is the L1-L3 borehole cross-depth profile from the field test, with the transmitter fixed at $z = 14$ m and the receiver moving from $z_{min} = 1.0$ m to $z_{max} = 14$ m at a distance of $R = 42$ m.

8.2.1 RT Simulation

The implementation of RT-based simulation of RF propagation involves the definition of ‘rays’ as vectors in a Cartesian space, which in this example is limited to two dimensions. The ray vector is defined with the symbol $\hat{\mathbf{r}}$, which has an origin point $\hat{\mathbf{r}}_O$ and a direction defined by $\Delta\hat{\mathbf{r}}$. A vector magnitude is defined as the distance traveled $\Delta r = c\Delta t/n$ in a predefined time interval Δt , and the local refractive index n at the origin point of the vector $\mathbf{r}_O = (x_O, y_O)$. For any given path through the geometry, a list of ray segments is computed \mathbf{r}_{list} .

$$\mathbf{r}_{list} = [\mathbf{r}_0, \mathbf{r}_1, \dots] \quad (8.6)$$

An initial ray $\hat{\mathbf{r}}_0$, has its origin point at the range and depth of the TX: $x_{RX} = 0$ and $z_{RX} = 14$ m. Its propagation direction is defined using some polar angle θ_0 . The ray then propagates a distance defined by $\Delta s = c\Delta t/n_0$, where $n_0 = n(x_{TX}, z_{TX})$. A new position $\mathbf{r}_O = (x_1, z_1)$ is computed, and the refractive index at this position n_1 is $n_1 = n(x_1, z_1)$. Now, the refractive index of the origin and end position is compared, and the next step is decided:

- If $n_1 = n_0$, then the new ray $\hat{\mathbf{r}}_1$ is appended to the list of rays. This is called the *propagation* operation.
- If $n_1 \neq n_0$, then the ray must undergo refraction or reflection.
 - Calculate the polar angle of a refracted ray $\hat{\mathbf{r}}_{1,t}$, using Snell’s law $n_1 \sin(\theta_1) = n_0 \sin(\theta_0)$
 - If this angle is less than the critical angle θ_c , $\theta_1 < \theta_c$, where $\theta_c = \arcsin(n_1/n_0)$, the refracted ray is appended to the list. This is called the *refraction* operation.
 - If $\theta_1 > \theta_c$, then refraction is not possible, and instead the ‘reflected’ ray $\hat{\mathbf{r}}_{r,1}$ is calculated, where $\theta_1 = -\theta_0$. The reflected ray is then appended to the list. This is the *reflection* operation

Thus the new ray $\hat{\mathbf{r}}_1$ is defined using the *propagation*, *refraction* or *reflection* operations. The new ray travels a distance $\Delta\mathbf{r}_1 = c\Delta t/n_1$, and the origin and direction of the next ray $\hat{\mathbf{r}}_1$ is found from the same procedure. This process is repeated until the ray leaves the limits of the simulation geometry, or the propagation time $T = \sum^N \Delta t$ exceeds a predefined limit. A total path is computed by adding all ray path lengths $\Delta\mathbf{r}_i$: $S = \sum^N \mathbf{r}_i$. A list of ray paths $\hat{\mathbf{r}}_{list} = \hat{\mathbf{r}}_{list}(\theta, n)$ from

start point $\hat{\mathbf{r}}_0$ to end point $\hat{\mathbf{r}}_{\text{end}}$ can be defined simply with the starting angle θ_0 and refractive index profile $n(x, z)$.

In this example, the ray tracing can run via ‘ray casting’, where a large number of rays are propagated from z_{TX} with a range of starting angles θ , and the rays are propagated until they leave the simulation geometry or a set maximum time has been surpassed. Another method is to seek ‘ray convergence’, where we seek rays that will converge to a receiver point $RX = (x_{RX}, z_{RX})$. In this case, a minimization routine is employed which seeks a starting angle θ_0 which finds results in an endpoint $(x_{\text{end}}, z_{\text{end}})$ which is within some tolerances Δx and Δz . However, due to total internal reflections, there may be configurations of TX and RX for which no convergent solution will be found. If a convergent solution is found, the time of flight is added from the number of ray increments N needed to travel from TX to RX,

$$t_{\text{propagation}} = \sum^N \Delta t. \quad (8.7)$$

It is also possible that multiple solutions may be found, in which case the ray path with the smallest time is chosen. The longer time solutions may indicate reflection from layers within the ice.

For this study, rays were propagated from $z_{TX} = 14$, m, with bounds $15 \text{ m} < z < -1 \text{ m}$, and $0 \text{ m} < x < 50 \text{ m}$, in intervals $\Delta t = 1 \text{ ns}$ and a maximum simulation time of $T_{\text{max}} = 600 \text{ ns}$. For the ‘ray casting’ approach, rays were propagated from a range of starting angles from $\theta_{\text{min}} = 1^\circ$ to 179° in increments of $\Delta\theta = 0.1^\circ$. The results of this ray casting are shown in Fig. 8.4a and discussed in the section 8.2.3. In the ‘ray convergence’ approach, convergent solutions are searched for the receiver positions are at ranges $R = 25 \text{ m}$ and $R = 42 \text{ m}$ and at depths from a minimum of $z_{RX, \text{min}} = 1.0 \text{ m}$ to $z_{RX, \text{max}} = 15.0 \text{ m}$, in increments of $\Delta z = 1.0 \text{ m}$, the results of which are discussed in section 8.2.3.

8.2.2 PE Simulation

The same simulation geometry used for the RT simulation is utilized for the paraProp simulations. An FD simulation was run within the geometric bounds, with a resolution of $\Delta x = 0.2 \text{ m}$ and $\Delta z = 0.05 \text{ m}$, with a frequency of $f = 1.3 \text{ GHz}$. The resulting FD simulation is displayed in Fig. 8.4b and discussed in section 8.2.3. A TD simulation of Gaussian pulse with a central frequency of $f_{\text{central}} = 1.3 \text{ GHz}$ and a bandwidth of $B = 200 \text{ MHz}$ was made for the same simulation geometry, from $z_{tx} = 14 \text{ m}$ and sampled at the receiver positions defined in the previous section.

8.2.3 Simulation Results

The ray paths for the start angle sweep are visible in Fig. 8.4a. Some notable features are the absence of ray paths in the for ranges $R > 30 \text{ m}$ across all depths except for 4 m, 6 m, 12 m and 14 m, depths which may correspond to ice layers in the refractive index model. Within these layers, rays undergo repeated internal reflections and propagate horizontally in an effect analogous to a wave-guide. At ranges $R > 30 \text{ m}$ and outside of these layers, we observe a ‘shadow region’ where no convergent solutions exist. The PE simulation in Fig. 8.4b shows similar evidence of wave-guide-like behavior, with enhanced RF power seen, and structures in the data that look similar to the trapped rays seen in 8.4a. The paraProp simulation is able to model RF emission with a power on the order of $P \sim -50 \text{ dBm}$ in the so-called ‘shadow region’ seen in Fig. 8.4a, although it is substantially lower by $\sim 20 \text{ dB}$ than for the regions for which RT can find convergent rays.

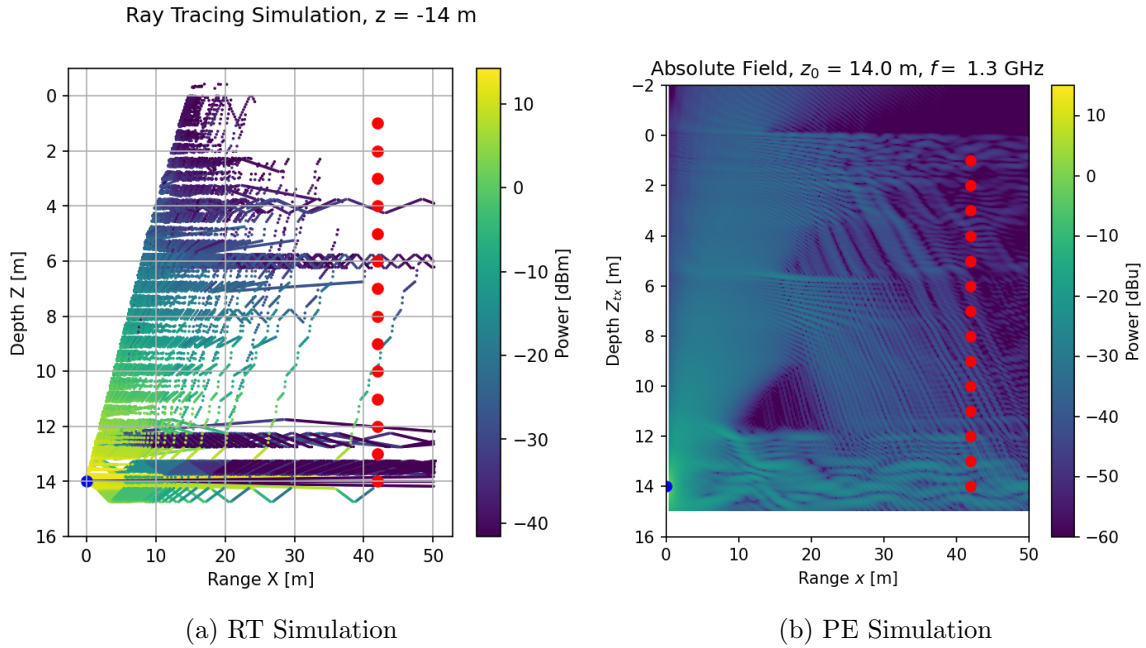


Figure 8.4: (a) RT simulation of RF propagation from $Z_{tx} = 14$ m from the Aletsch glacier, using the L1-L2 first peak permittivity profile. (b) shows the simulation with paraProp at $f = 1.3$ GHz. The position of the receiver’s RX is indicated by the red dots in both.

In Fig. 8.5, the propagation time calculated from the RT and PE simulations is compared with the signal propagation times in the cross-depth profiles between boreholes. In general, RT and PE’s prediction of the time of flight follow a similar trend to what is seen with the data, i.e. the time of flight for the L1-L2 profile lies roughly mid-way between the expectations for a homogeneous air and ice medium, and increases with transmitter depth. Another interesting trend is that the RT simulation mostly under-predicts the propagation time, while the PE mostly over-predicts it, a feature which is obvious in Fig. 8.6. Both simulation methods are more successful at predicting the time of flight of the L1-L3 profile than for the L1-L2 profile. In the L1-L3 profile, the estimated propagation time from PE simulations agrees with data 12 depths out of 14 matches within the nominal propagation time error of $\Delta t = \pm 5$ ns. For the L1-L2 profile, the PE estimated times can only be said to agree within the nominal error range 8 out of 14 times for the ‘max’ peak and 2 out of 14 times for the ‘first peak’, with the remaining data point tending to be offset by approximately ~ 12.5 ns. In both cases, the agreement between PE and the data is poor at shallow depths $z > 5$ m. The poor agreement between the measured data and the output of the simulations from the first peak derived model might be explained by short-comings of the refractive index model. Since the resolution of the depth in the model is at best $\Delta z = 0.5$ m, structures in the glacial ice smaller on smaller scales will not be represented in the model. Furthermore, the assumption of a range-independent refractive index profile is certainly not true, and the measurements between L1 and L2 will be more sensitive to inhomogeneities in the firn between L1 and L2 than the L1 and L3 measurements.

8.3 Reconstruction of the Refractive Index profile with PEs

In this final section, the GA-based inversion method is tested on some of the permittivity radar data obtained in the field test (chapter 7). Here, we utilize the same settings for the genetic operators, initialization, and selection routines as were used in the examples of the Guliya and Brueggen glaciers (chapter 5). However, the fits obtained examples assumed a highly idealized ‘Gaussian pulse’ with a bandwidth of $B = 200$ MHz. To attempt an accurate reconstruction, it

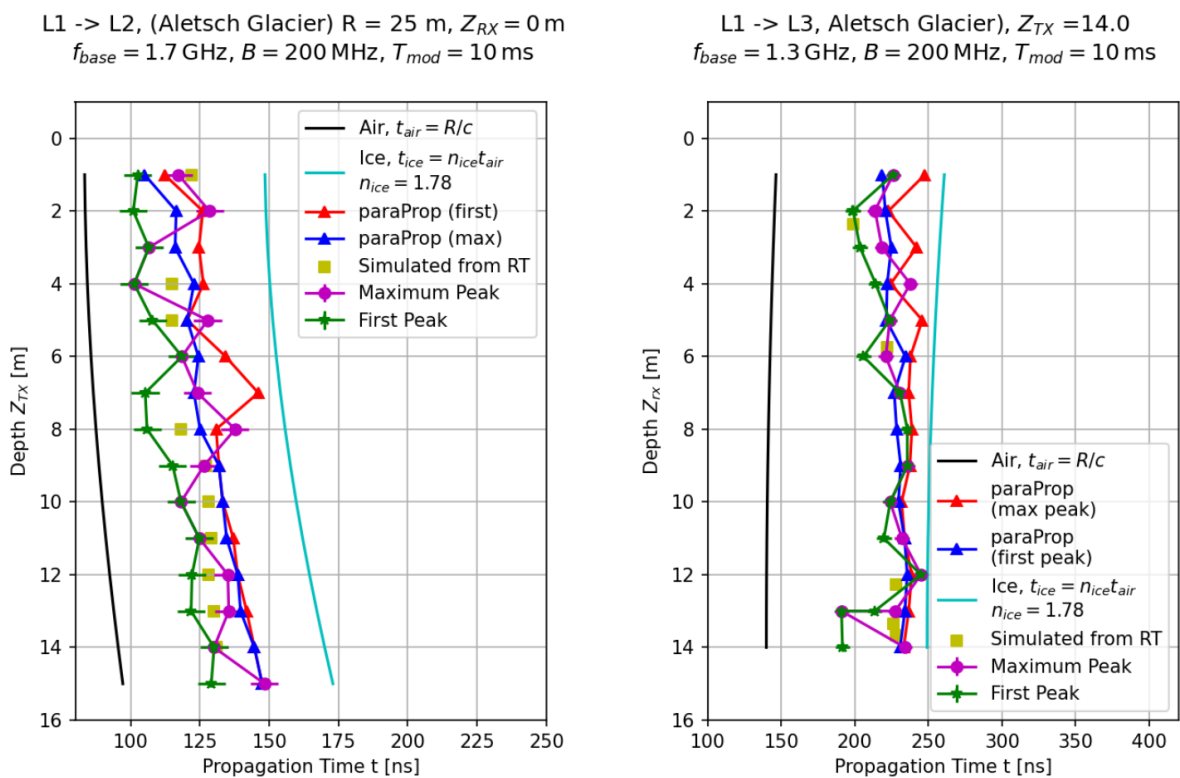


Figure 8.5: The measured time of flight of the ‘first’ and ‘maximum’ peak in the cross borehole profiles, shown with the time of flight expected from ray tracing (RT) simulations and PE simulations (with the ‘first’ and ‘maximum’ peaks also displayed). The left plot shows the results for the L1-L2 cross-depth profile, and the right shows the results for the L1-L3 cross-depth profile.

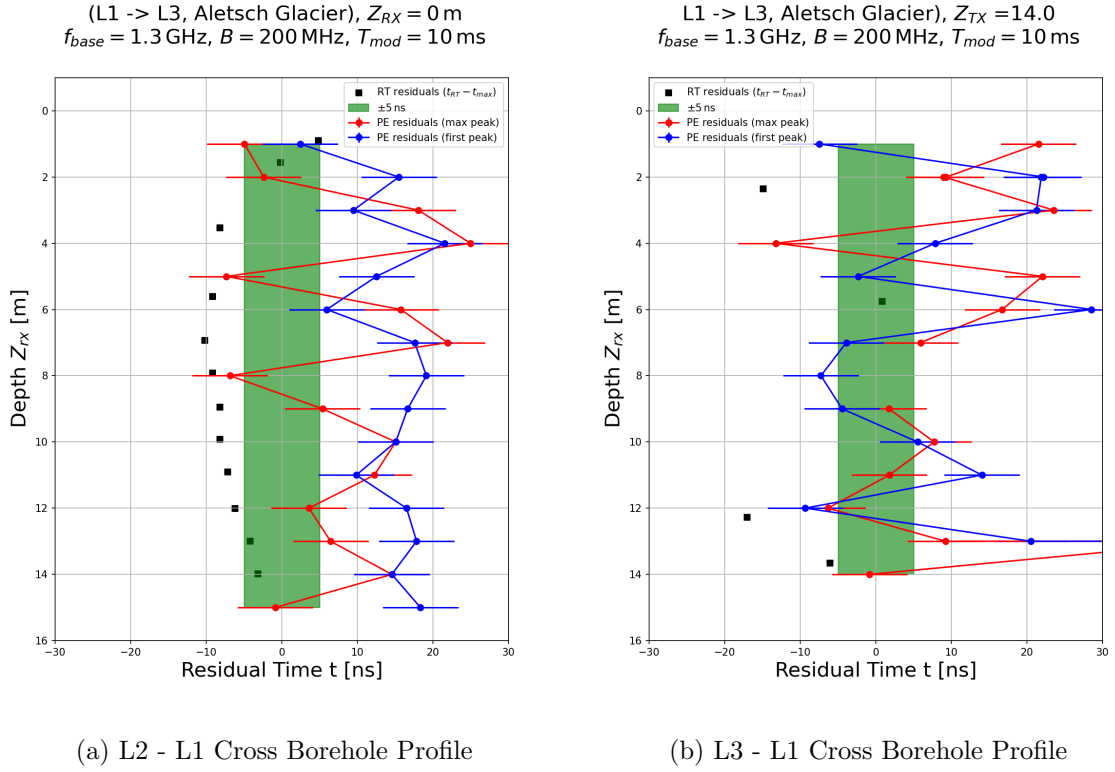


Figure 8.6: The residuals between the measured time of flight for the maximum peak in the data, and the predictions from RT and PE simulations (the absolute values of which are shown in Fig. 8.5). The green shaded area corresponds to the desired uncertainty range of ± 5 ns.

was necessary to attempt to simulate the transmitted waveform generated by the permittivity radar's frequency synthesizer as accurately as possible, which will be discussed in section 8.3.1.

8.3.1 Simulating the transmitted signal

To model the transmitted signal from the permittivity radar, a simulation chain was devised which replicates each stage of the signal transmission:

1. The signal's generation from the frequency synthesizing circuit.
2. Conversion of this signal as it passes through the power amplifier (PA).
3. The emission of the electric field E_{TX} from the transmitting antenna.
4. Propagation of the field through the ice.
5. Conversion of the electric field at the receiver into a current at the receiving antenna
6. Amplification of the current through an amplifier
7. Multiplication of the signal in the mixer circuit

Each step in this chain of signal modeling is illustrated in Fig. 8.7. The first step is the generation of the reference signal at the surface, from which the frequency synthesizer generates $V_{RF,TX}(t)$. This signal then passes through the PA, which will have some response to the signal as defined by its impulse response function $h_{TX,PA}(t)$. The PA used in the hardware was specified by the manufacturer to have a flat response spectrum (to 1dB) in the frequency range under test, and this was verified in testing at the university. The amplified signal is the convolution of $V_{RF,TX}$

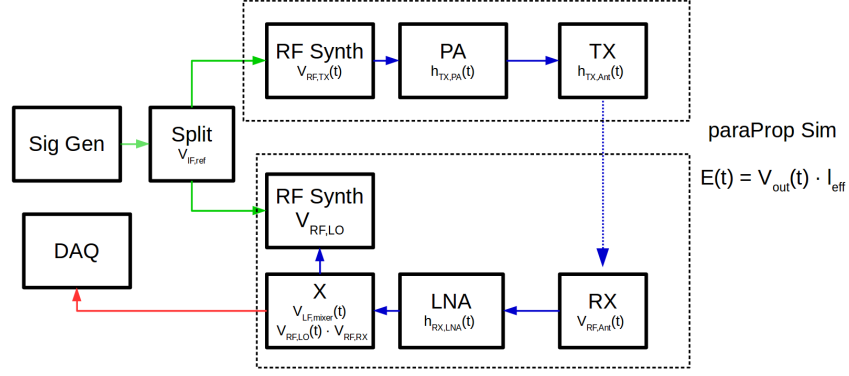


Figure 8.7: The simulation chain used to replicate the Field Test data, utilizing the PE simulation method.

and $h_{PA,TX}$, which, from the Fourier identity of convolution, can simply be found by multiplying the spectrum of the emitted signal and the Fourier transform of the impulse response $H_{PA,TX}(f)$.

$$V_{RF,PA}(t) = V_{RX,TX}(t) * h_{PA}(t) \quad (8.8)$$

Next the amplified signal is applied to the port of the transmitting antenna, which will produce an electric field as defined by its ‘effective length’ l_{eff}

$$E_{TX}(t) = E(x = 0, z, t) = V_{RF,PA}(t) \cdot l_{eff}(t) \quad (8.9)$$

Effective length can be expressed in terms of the impulse response of the antenna. The spectrum of the subsequent signal $E_{TX}(t)$ is used to define the zeroth step $x = 0$ of the simulation in paraProp.

The next step is a time-domain solution in paraProp for each transmitter position utilized in the field test data. In this case, these are between depths of 1 m and 15 m in increments of 0.5 m. The complex amplitude is sampled at receiver positions in the procedure described in chapter 4.

The next step is finding the measured voltage at the junction of the receiving antenna, which will be defined by the receiving antenna’s impulse response $h_{RX}(t)$:

$$V_{RX}(t) = I_{RX}(t)Z_0 \quad (8.10)$$

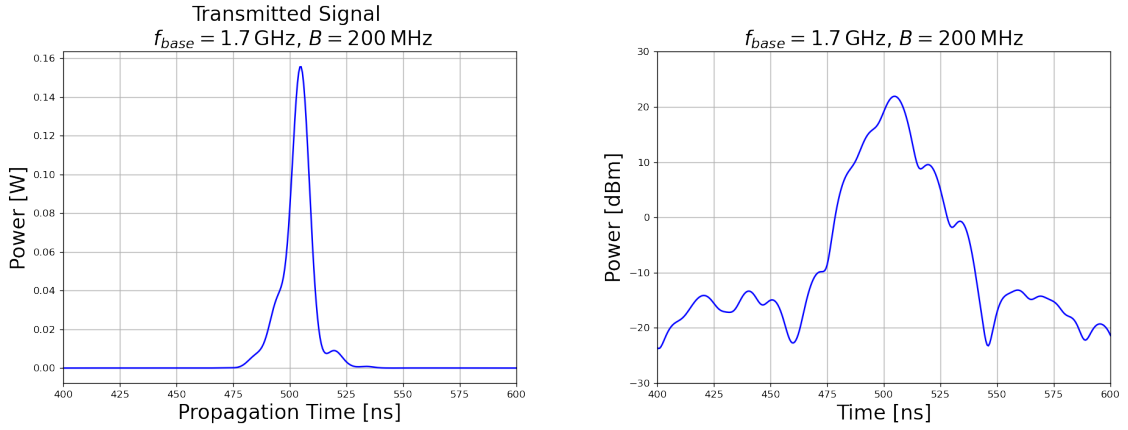
$$I_{RX}(t) = E_{RX}(t) * h_{RX}(t) = E(x = x_{RX}, z = z_{RX}, t) * h_{RX}(t) \quad (8.11)$$

Where the induced current $I_{RX}(t)$ is found from the incoming electric field $E_{RX}(t)$, and the voltage is using the current and the impedance of the system $Z_0 = 50 \Omega$. The next step is folding in the response function of the mixer’s amplifier:

$$V_{RF,LNA}(t) = V_{RX}(t) * h_{LNA}(t) \quad (8.12)$$

Finally, we find the signal measured by the oscilloscope by multiplying the amplified received signal with signal of the local oscillator $V_{LO}(t)$.

The transmitted signal applied to the transmitting antenna is shown in Fig. 8.8. The simulated transmitter signal shows ‘side lobes’ on either side of the maximum peak with a power < 0.1 that of the maximum peak.



(a) TX signal from the permittivity radar (linear scale). (b) TX signal from the permittivity radar (dB scale).

Figure 8.8: The modeled transmitted signal from the permittivity radar at $f_{base} = 1.7$ GHz and a bandwidth of $B = 200$ MHz, folding in the antenna impulse responses of Cage Antenna 1 from chapter 6.

8.3.2 Settings

The GA-based reconstruction algorithm uses identical control parameters as described in chapter 4 for the reconstruction of the Brueggen and Guliya glaciers from PE generated ‘pseudo-data’. The simulation ran for 100 generations, with 200 refractive index models being used as the individuals populating these generations, and the refractive index values from depths $z_{min} = 1.5$ m to $z_{max} = 15$ m being the ‘genes’.

- Number of Generations $N_{Generations} = 100$
- Number of Individuals $N_{Individuals} = 200$
- Number of Genes $N_{genes} = 28$
- Minimum Depth of Genes $z_{min} = 1.5$ m
- Maximum Depth of Genes $z_{max} = 15$ m

Parent Selection Settings

- Fraction of Elites: $f_{elites} = 0.05$
- Fraction of Parents: $f_{parents} = 0.85$
 - Fraction of Parents selected by Roulette: $f_{Roulette} = 0.7$
 - Fraction of Parents selected by Tournament: $f_{Tournament} = 0.3$
- Fraction of Immigrants $f_{immigrants} = 0.1$

Operator Settings

- Mutation Fraction: $f_{mutation} = 0.4$
- Cross-Breeding Fraction: $f_{cross-breed} = 0.6$

Initialization Settings

- $f_{fluctuations} = 0.8$

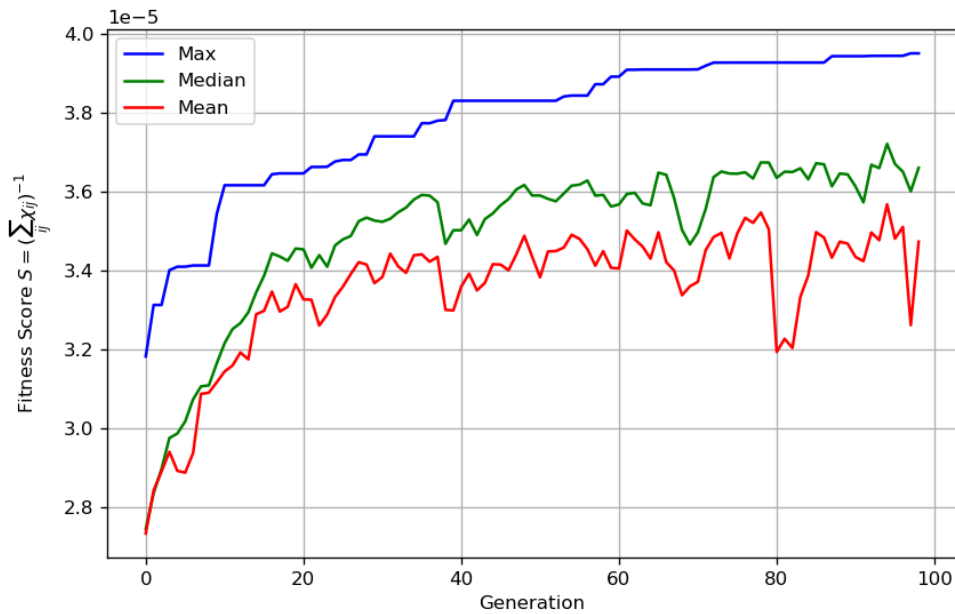


Figure 8.9: Evolution of the fitness score for the fitting of the GA based inversion to the field test data.

- $f_{sine} = 0.05$
- $f_{flat} = 0.05$
- $f_{exp} = 0.1$

8.3.3 Results

Evolution of the fitness score can be seen in Fig. 8.9. The mean and median of the score distribution increases in the first 40 generations by a factor of 25 % and 37 % respectively, after which both values fluctuate around a fitness score of $S_{mean} = 3.4 \times 10^{-5}$ and $S_{median} = 3.6 \times 10^{-5}$. The highest score of the distribution continues to increase throughout the inversion process, but the rate of increase $dS/dGen$ also slows down at generation 10 and then slows down further at generation 40. The refractive index of the best result is shown in Fig. 8.10. This best-fit result is similar to within an error of $\Delta n < 0.1$ of the initial ‘best guess’ profiles obtained by peak selection, a result consistent with the pseudo-data analysis in chapter 5, with a very visible exception at $z > 14.5$ m. At this depth, the reconstructed profile shows an anomalously low refractive index value consistent with freshly fallen snow. Such a ‘cavity’ is difficult to explain from firn densification models, and could well be an artifact of the reconstruction method. At the time of writing, no satisfactory answer has been found. Moreover, a comparison between the simulated signals with the measured signals shows the agreement of the temporal position of the ‘maximum peaks’ to within ± 5 ns as can be seen in Fig. 8.11. This trend was observed at all depths. Fig. 8.11a shows the ‘side lobes’ visible in the data can also be replicated with some accuracy using the aforementioned simulation chain, but the field test data features small scale peaks for $t > 200$ ns which were not replicated by the simulation. It is not clear whether these features are small-scale reflections caused by smaller-scale ice inhomogeneities or by fluctuations in the antenna emission properties.

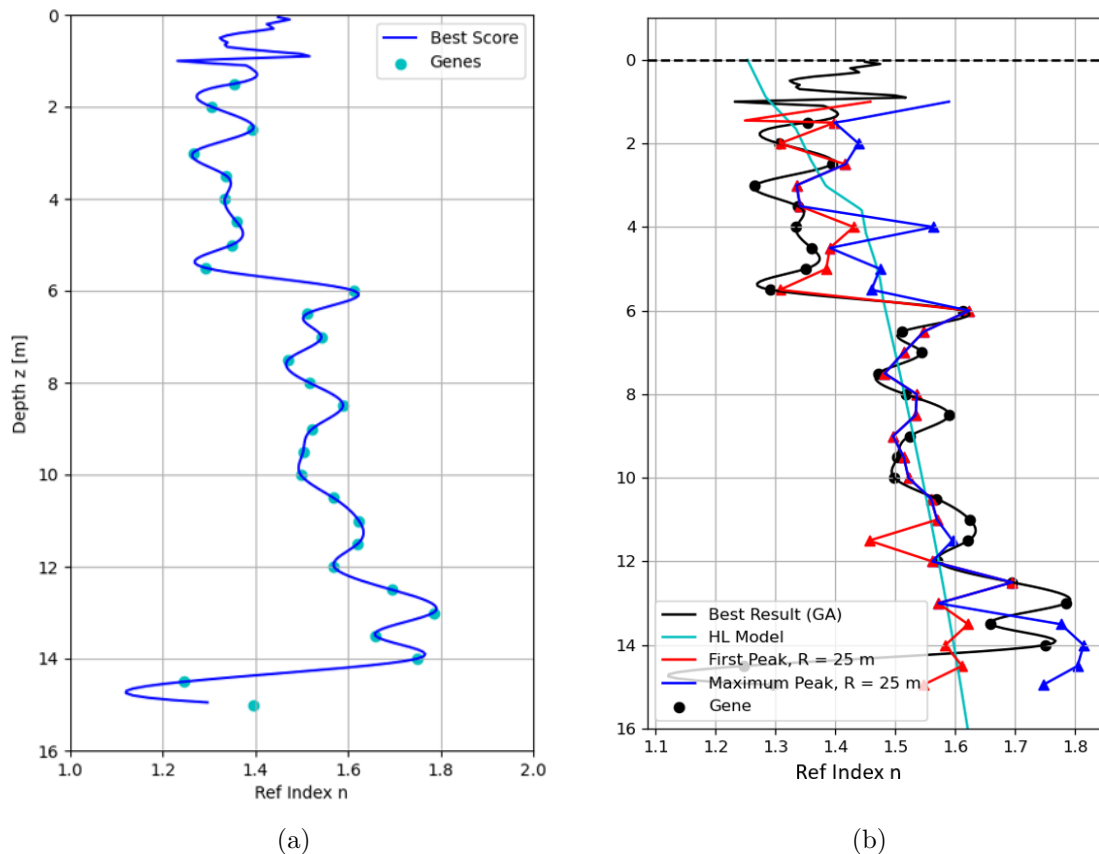


Figure 8.10: The best fit refractive index $n(z)$ profile from the GA based inversion method. The profile is shown with its ‘genes’ in Fig. 8.10a. The best fit from the GA is shown (8.10b) in comparison with the profiles obtained from the ‘first’ and ‘maximum’ peaks in Fig. 7.15

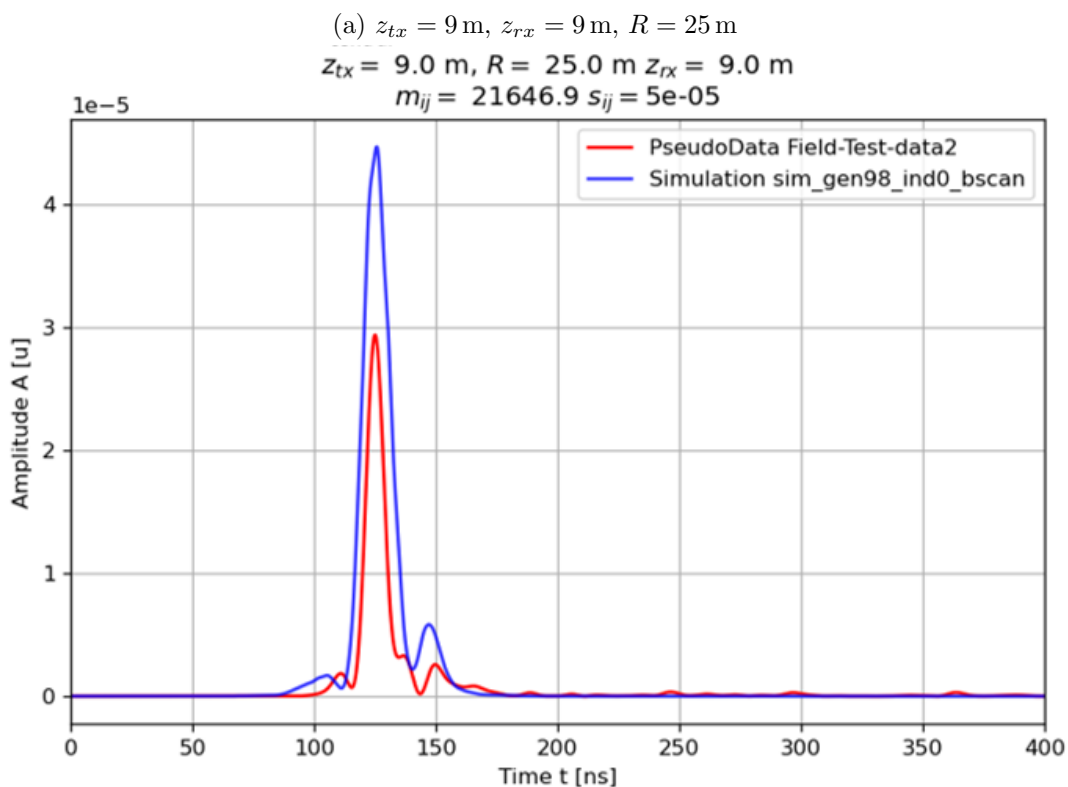
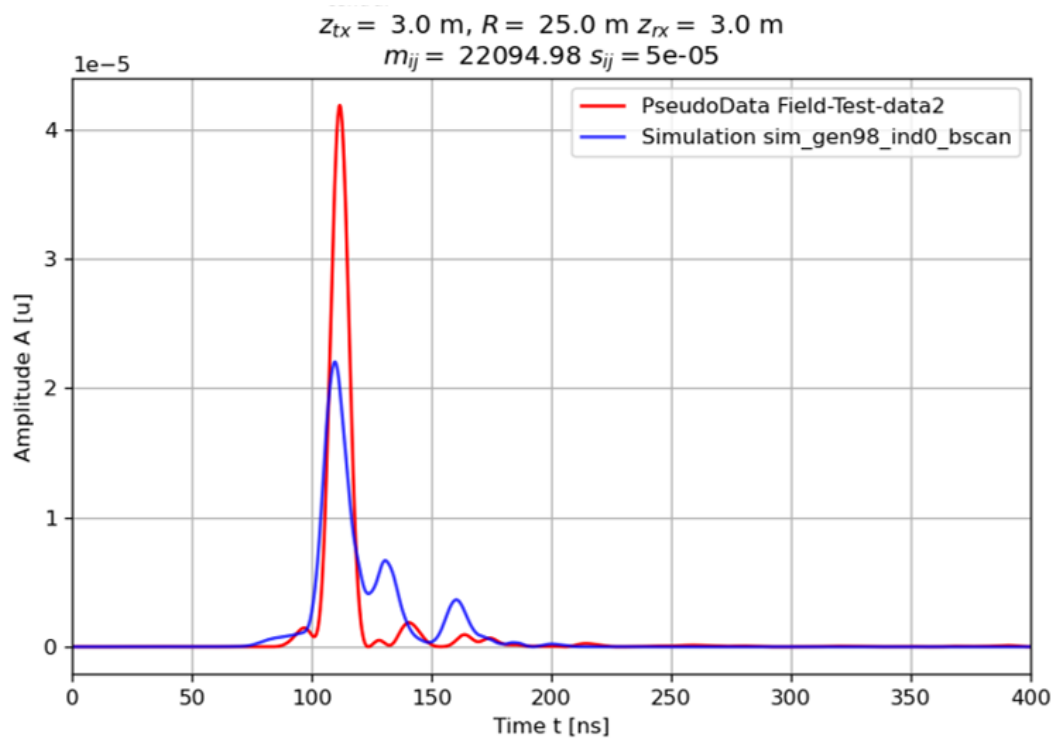


Figure 8.11: A comparison between the simulated (using the ‘best fitting profile’ and measured signal transmission from z_{tx} to z_{rx} at the same depth over a range of $R = 25 \text{ m}$. Fig. 8.11a TX and RX at $z = 9 \text{ m}$, while Fig. 8.11b has the TX and RX at the surface $z = 3 \text{ m}$.

8.3.4 Discussion

Although the best-scoring refractive index profile is consistent within the residual error of the peak-selection method, and can replicate the time of flight of the highest amplitude peaks in the spectrum, there are good reasons to be skeptical whether the resulting $n(z)$ estimate is closer to ‘the truth’ profile than that found from the peak-selection.

From the examples of the South Pole and Guliya ice caps in chapter 4, important differences between ‘smooth’ refractive index profiles and ‘layered’ profiles can be seen in the pulsed emission between a source and receiver at equal depths, for range independent profiles on size scales of $R < 100$ m. In the former, the emission can be simply described with a direct arriving component and a surface reflection component, with the direct component having the highest amplitude and being the earliest arriving component. However, for firn with numerous ‘refrozen’ ice layers, there are far more reflections, and the maximum amplitude signal is not necessarily the earliest arriving signal, due to interference between different reflected signals or through the refraction of the signal through a lower density layer at a nearby depth. Emission between layers may also be ‘amplified’ with respect to the value expected for a smooth profile. Therefore accurate reconstruction of the refractive index is contingent on reconstruction of the amplitude and time of the ‘direct’ arriving signal and of reflections. Thus, it is of paramount importance that the form of the transmitted signal is well understood, that the receiver’s impulse response to a propagating signal is likewise well understood, and that the noise level is minimal. These conditions may not have been adequately satisfied in the field test measurements; primarily due to high phase noise and unstable antenna characteristics.

Experimental Uncertainties

In chapter 6, the implementation of custom-built omnidirectional broadband antennas, which utilized a cage dipole design, was discussed. However, it was observed that the antennas proved to have inconsistent S_{11} parameters, and their efficiency was often below the 50% level normally expected for antenna design. The small-scale peaks seen in the FMCW spectra for times greater than 50 ns after the ‘maximum peak’ may be caused by noise associated with the antenna response or, perhaps by phase noise associated with the ‘maximum peak.’ This complicates the reconstruction of the signal.

Environmental Uncertainties

In addition to the limitations of the permittivity radar, the accuracy reconstruction analysis was also limited by the assumptions necessary to run the analysis. It is explicitly assumed in the analysis that the refractive index profile of the ice is range-independent and only varies with respect to depth on a scale of $R \sim 50$ m, that the surface is flat within a range of $\Delta z < 0.02$ m, and that there are no significant sources of reflections outside of the examined space, i.e. the bedrock beneath the glacier, or a crevasse outside of the measurement range.

8.3.5 Summary of GA reconstruction

The field test data underwent a preliminary application of the GA-based inversion method. Although the simulated signal obtained from the best-fit refractive index profile successfully replicated the “maximum peak” observed in the field test data for parallel depth transmission, the reconstruction of secondary peaks, potentially associated with reflections, and the cross-depth measurements were not satisfactorily achieved. The comparison of the fitness score between the field test data reconstruction and the “pseudo-data” examples presented in Chapter 5 revealed that substantial improvements to the performance of the GA-based inversion method are necessary.

Chapter 9

Conclusions

9.1 Summary of Results

Through this work, methods to model the propagation of high frequency radio-waves through a variety of realistic ice environments were developed, in addition to techniques to reconstruct the permittivity of ice through in-situ measurements with a cross-borehole radar system. The major outcomes of this thesis are divided into the following categories and summarized in the following sections; simulation radio-wave propagation through ice and in-situ measurements of ice permittivity.

9.1.1 Simulating radio-wave propagation through ice

Development of parabolic wave simulation technique

This work has tested the parabolic wave equation (PE) approximation of Maxwell's equations as a simulation method to model UHF radio-wave propagation through realistic ice environments, as defined by firn density data obtained from real-world glaciers; including the South Polar ice cap, the Guliya ice cap[45], Colle-Gnifetti glacier and Brueggen glacier. PEs are able to model RF emission in so-called 'forbidden regions' where ray-tracing can not find solutions. The simulation method has been developed through an open-source simulation code paraPropPython, which has been developed to allow for modeling of emission through environments with non-flat surfaces, inhomogeneities such as crevasses, boulders, aquifers and can model for dielectric attenuation.

Permittivity reconstruction via inversion

A genetic algorithm-based inversion technique was developed to reconstruct a permittivity profile that varies with depth but remains independent of the range. This technique demonstrated the reliable reconstruction of the time-of-flight for both the direct traveling signal and the first-order reflection of horizontally propagating signals through ice. By employing simplified models of real-world glaciers like Brueggen and Guliya, the inversion method achieved a refractive index resolution of $\Delta n \leq 0.05$. However, thus far, the method has only optimized the refractive index within a scale of $\Delta z = 0.5$ m, while the remaining depth points were obtained through spline interpolation. This interpolation process resulted in a loss of the observed "roughness" typically present in real-world glaciers. Notably, small-scale inhomogeneities in the ice, such as thin ice layers, introduce signal features that cannot be effectively reconstructed without significantly increasing the depth resolution.

9.1.2 In-situ measurements of ice permittivity

Permittivity measuring radar

Over the course of this work, a bistatic cross-borehole radar for measuring permittivity was designed, built, and tested. It utilized the frequency-modulated continuous wave (FMCW) modulation technique to measure the propagation time of radio waves between the transmitter TX and the receiver RX. It could operate in a frequency range from 800 MHz to 2200 MHz, and generate a linear frequency ramp with a bandwidth of $B = 200$ MHz with a modulation time of $T_{mod} = 10$ ms. The operational bandwidth B resulted in a nominal propagation time resolution of $\Delta t = 5$ ns. The transmitter TX and receiver RX, could be deployed down to a maximum depth of 30 m and a maximum range of 100 m. For homogeneous ice media, or media with a smoothly increasing and continuous refractive index, the permittivity radar could achieve a ‘nominal’ refractive index measurement resolution of $\Delta n_{nominal} = 0.05$ for a TX and RX deployed at equal depth at a range of $R = 40$ m.

However, the signal processing of the measurements obtained from the permittivity radar was hindered by systematic uncertainties in crucial components of the radar. The primary sources of uncertainty were related to the stability of the frequency synthesizer, and phase noise, in addition to unstable and inconsistent antenna properties. When testing the radar with both the TX and RX in air, the propagation time spectra often displayed ‘side lobes’ on either side of the highest amplitude signal, which corresponded to the ‘direct transmission’ with a propagation time $t = R/c$. The side lobes had amplitudes on the order of ~ 0.1 of the maximum amplitude, and lay within ± 10 ns of the maximum peak. This makes it difficult to differentiate between these ‘side lobes’ and reflected signal components arriving within a time window of 10 ns. Additionally, the phase noise associated with the highest amplitude peak meant that the power of the signal’s noise floor was ~ 20 dB lower than the power of the maximum peak. This meant naturally that any secondary signals in the data associated with reflections would be undetectable if their power was less than 20 dB and indeed would be difficult to distinguish from noise if they were weaker than 10 dB relative to the highest amplitude signal. For this reason, the data analysis in the field test was limited to examining signal peaks above a threshold of $P > 0.1P_{max}$, where P_{max} is the power of the maximum amplitude signal.

As a consequence of the systematic uncertainties in the frequency stability and antenna properties of the radar, only the ‘brightest’ component of the signal can be detected with a high degree of confidence, while secondary reflections are difficult to distinguish from systematic effects. This suggests that the effective uncertainty in the measured refractive index profile may be $\Delta n_{eff} \sim 0.1$, approximately twice that of the nominal uncertainty $n_{nominal} = 0.05$.

Field testing of radar at the Aletsch Glacier

The permittivity radar was tested in a field campaign at the Aletsch Glacier in March and April of 2022. During the campaign, it was used to measure the propagation time between the transmitter TX and receiver RX which were deployed in three boreholes to a maximum depth of 15 m. The measurements sampled the upper firn layer of the test site, the ‘Jungfraujochnfirn’ on ranges of $R = 25$ m and $R = 42$ m, utilizing base frequencies of $f_{base} = 1.7$ GHz and $f_{base} = 1.3$ GHz respectively. The permittivity profile was estimated utilizing ‘peak selection’ methods, applied to measurements where the depth of the transmitter z_{TX} and receiver z_{RX} are equal. In this method, a hypothesis is made that assumes that the refractive index is range-independent and that the brightest signal component, i.e. the ‘maximum peak’ corresponds to a horizontal propagation signal where the propagation time is equal to that of the propagation over the direct distance in a vacuum multiplied by the refractive index $t_{propagation} = n(z = z_{TX} = z_{RX})R/c$. Alternatively, the ‘first peak’ hypothesis considers all peaks in the waveform with power at least

10% of the maximum and assumes that the first one corresponds to the direct traveling signals. The resulting permittivity profile estimates exhibit a combination of a smoothly increasing firn density and distinct layers of increased permittivity that may correspond to refrozen ice layers from previous melt seasons. The derived density profile from the permittivity is found to be consistent with the firn density derived from seasonal snowfall over a period of 40 years, using the Herron-Langwey densification model[37]. A preliminary application of the GA-based inversion was applied to the field test data. The simulated signal from the best-fit refractive index profile was able to replicate the ‘maximum peak’ of the field test data for parallel depth transmission, but the secondary peaks (possibly associated with reflection) and the cross-depth measurements have not been satisfactorily reconstructed. The low fitness score of the field test data reconstruction in comparison with the ‘pseudo-data’ examples shown in chapter 5, indicate that the GA-based inversion is as of yet inadequate to the task.

However, it must be emphasized that these estimates neglected smaller scale structures in the ice $\Delta z < 0.05$ m and particularly variations of the density in the horizontal direction on a scale of ~ 50 m. The GA inversion method derived in the course of this thesis was applied to the field test data, but given the systematic uncertainties in the field test data, and the structural limitations in the range-independent, spline interpolated refractive index model used by the inversion method, only a marginal improvement was made in fitting to the data.

9.2 Future Work

Science is never complete, and much of the work in this thesis shows promising avenues for future development and improvement of the radio propagation simulation and reconstruction techniques presented here. In this section, potential directions that can build upon the work made in this thesis.

9.2.1 Parabolic Equation Simulations

The use of the parabolic equation simulation method for radio propagation is still relatively novel, and there is much fertile ground for improvement of the simulation method and its implementation to model the results of ice-penetrating radar:

- **Speeding up simulations:** When using paraProp, the solution of the parabolic equation at each step in range relies on the Fast Fourier Transform (FFT) algorithm, which must be applied twice per range step. This is the slowest part of the solution, requiring ~ 3 ms to solve for a single step in range when using a maximum depth of $Z_{max} = 200$ m and a depth resolution of $\Delta z = 0.05$ m. Currently, paraProp is written in Python and the solution of the PE uses the FFT function from the NumPy library. An investigation into faster solution methods, perhaps utilizing algorithms such as FFTW that optimize the local computer architecture to solve the algorithm or partial implementation of the PE solver in C++ via Cython, is planned in the near future.
- **Three-dimensional simulations with paraProp:** So far, the paraProp code is restricted to simulation in two dimensions, with the assumption of a cylindrically symmetrical field $\psi(x, z, \phi) = \psi(x, z)$. Naturally, the implementation of azimuth dependence of the refractive index $n(x, z, \phi)$ and the antenna properties would increase the utility of paraProp as a tool for simulating forward propagation of radio waves from a source in ice. However, the simulation of back-scatter in three dimensions is a far more computationally demanding task, requiring the computation of different Electric field vectors from multiple directions. Such a task would likely require substantially faster solution speeds in paraProp.

9.2.2 Inversion of PE and RT simulations

The development of a method to invert the output of PE simulations to find a fit to ice penetrating radar data is still at an early stage, and work is currently underway both to substantially improve the reconstruction resolution of the refractive index and the depth resolution of genetic algorithm (GA) based inversion method. Other points of investigation include:

- **Adaptive GAs:** So far, the GA has utilized fixed settings for its genetic operators (mutation, cross-breeding, cloning, immigration) and selection routines (roulette and tournament). Of course, selection pressures in biological evolution are not fixed, but change with time. Adaptive Genetic Algorithms (AGAs) have utilized in the past to solve known problems with the output of GAs: notably the problem of premature convergence.
- **Testing different inversion methods:** While genetic algorithms have demonstrated their effectiveness in optimizing solutions for the ice's refractive index, it is crucial to conduct comprehensive comparisons with alternative inversion methods to gain a deeper understanding of its relative strengths and limitations. The inversion procedure outlined in chapter 5 could be modified to utilize different optimization algorithms: including steepest-descent gradient, Newton and quasi-Newton methods, and damped least-squares.
- **Applying GAs to RT simulations:** Just as the GA component of the inversion method can be substituted for an alternative optimization routine, the PE generation of simulated ice-penetrating radar data can be substituted for RT-based simulations.
- **2D refractive index reconstruction:** Reconstruction of the refractive index $n(x, z)$ in 2D is a necessary step for understanding the structure or real world ice environments from radar data. While this increases the complexity of the problem, a possible approach could be a two-stage optimization, where range-independent refractive index $n(z)$ is estimated, and then 'perturbed' as a function of distance to obtain an improved fit to data. Of course, such an approach would benefit from a large number of measurements taken in different ranges as well as depths.
- **Testing of inversion method using FDTD simulations:** The solution to Maxwell's equations via Finite Difference Time-Domain (FDTD) is considered the most robust method for simulating RF signals through ice, although it is computationally expensive. A potential way to evaluate the performance of PE inversion techniques is to utilize FDTD to generate simulated pulses for novel refractive index profiles to act as test data, which PEs can attempt to reconstruct. The resulting refractive index model can be evaluated against the independently generated FDTD pulses and the refractive index models used to generate them.

9.2.3 Permittivity Radar

The bistatic cross borehole permittivity radar prototype acted as a good 'proof of concept', but the uncertainties in the antenna emission efficiency and instability in the signal generation hindered the reconstruction of the refractive index. Several improvements can be envisioned:

- **Replace antennas:** The permittivity radar utilized custom-built omnidirectional broadband antennas, which utilized a cage dipole design. However the antennas proved to have inconsistent S_{11} parameters, and their efficiency was often below the 50% level normally expected for antenna design. Future improvements to the permittivity radar would include either redesigning the antennas to a design with higher efficiency and consistent emission properties.

- **Improved system calibration:** Future improvements to the permittivity radar will require more extensive and careful calibration measurements than were carried out in the course of this work. Specifically, measurements for radio propagation from the TX to RX should take place in an anechoic chamber, in which reflections from the environment are minimized if not entirely eliminated. This would allow discrimination between systematic effects and physical reflections when the permittivity radar is used in glaciers.
- **Adding receivers:** In the course of this thesis, it was intended for the permittivity radar to be a ‘single-input-multiple-output’ system, in which the signal transmitted from a single TX can be sampled from multiple points simultaneously. This would both aid in permittivity reconstruction analysis, and in controlling for systematic errors. An example of this would be variability in the emitted power from the TX during measurements. A second receiver would make it possible to independently monitor systematic variability from the TX.

9.2.4 Use of Permittivity Radar in Field Tests

The Aletsch glacier field campaign was a verification of the permittivity radar concept and obtained an estimate of the permittivity profile of the upper 15 m of the Jungfraujochfirn. Due to limitations imposed by equipment issues and poor weather, the volume of data was limited to two parallel depth profiles and two cross-depth profiles, acquired over two days. Future field campaigns in alpine glaciers or polar ice caps would benefit from additional measurements:

- **More boreholes:** The measurements at the Aletsch glacier field test utilized a linear array of boreholes. Future measurements should utilize a circular pattern of boreholes, allowing the radar to sample the ice structure in multiple directions, with the possibility of observing any dependence of the ice properties on the flow direction of the glacier.
- **Verification using ice-core measurements:** Ultimately the accuracy of any reconstruction technique should be tested against direct measurements of the firn permittivity, or of a property that determines the permittivity, i.e. the density. Therefore, it would be desirable to use a coring drill to obtain an ice core which can then be studied with a near field permittivity sensor. This would yield an independent measurement of the permittivity profile for comparison with the output of the inversion of the radar data.

References

- [1] Enceladus: Facts & figures. <http://solarsystem.nasa.gov/>. Accessed: 2022-01-30.
- [2] Pleiades cluster at the university of wuppertal <https://pleiades.uni-wuppertal.de/>.
<https://pleiades.uni-wuppertal.de>. Accessed: 2023-05-30.
- [3] R. A. J. R. A., A. R.G., and B. J. J. et al. The gravity field of the saturnian system from satellite observations and spacecraft tracking data. *The Astronomical Journal*, 132(6):2520, nov 2006.
- [4] O. Abramov, D. Raggio, P. Schenk, and J. Spencer. Temperatures of vents within enceladus' tiger stripes. In *Lunar and Planetary Science Conference*, number 1832, page 1206, 2015.
- [5] O. Abramov and J. R. Spencer. Endogenic heat from enceladus' south polar fractures: New observations, and models of conductive surface heating. *Icarus*, 199(1):189–196, 2009.
- [6] J. A. Aguilar, P. Allison, D. Besson, A. Bishop, O. Botner, S. Bouma, S. Buitink, M. Cataldo, B. A. Clark, K. Couberly, Z. Curtis-Ginsberg, P. Dasgupta, S. de Kockere, K. D. de Vries, C. Deaconu, M. A. DuVernois, A. Eimer, C. Glaser, A. Hallgren, S. Hallmann, J. C. Hanson, B. Hendricks, J. Henrichs, N. Heyer, C. Hornhuber, K. Hughes, T. Karg, A. Karle, J. L. Kelley, M. Korntheuer, M. Kowalski11, I. Kravchenko, R. Krebs, R. Lahmann, U. Latif, J. Mammo, M. J. Marsee, Z. S. Meyers, K. Michaels, K. Mulrey, M. Muzio, A. Nelles, A. Novikov, A. Nozdrina, E. Oberla, B. Oeyen, I. Plaisier, N. Punsuebsay, L. Pyras, D. Ryckbosch, O. Scholten, D. Seckel, M. F. H. Seikh, D. Smith, J. Stoffels, D. Southall, K. Terveer, S. Toscano, D. Tosi, D. J. V. D. Broeck, N. van Eijndhoven, A. G. Vieregg, J. Z. Vischer, C. Welling, D. R. Williams, S. Wissel, R. Young, and A. Zink. Radiofrequency ice dielectric measurements at summit station, greenland, 2022.
- [7] G. Apaydin and L. Sevgi. *Radio Wave Propagation and Parabolic Equation Modeling*, chapter 1, pages 1–14. John Wiley Sons, Ltd, 2017.
- [8] ARA Collaboration, P. Allison, J. Auffenberg, and B. et al. Design and initial performance of the Askaryan Radio Array prototype EeV neutrino detector at the South Pole. *Astroparticle Physics*, 35(7):457–477, Feb. 2012.
- [9] G. A. Askar'yan. Excess negative charge of an electron-photon shower and its coherent radio emission. *Zh. Eksp. Teor. Fiz.*, 41:616–618, 1961.
- [10] J. Avva, J. M. Kovac, C. Miki, D. Saltzberg, and A. G. Vieregg. An in situ measurement of the radio-frequency attenuation in ice at summit station, greenland. *Journal of Glaciology*, 61(229):1005–1011, 2015.
- [11] H. Bader. Sorge's law of densification of snow on high polar glaciers. *Journal of Glaciology*, 2:319 – 323, 1953.
- [12] S. Barwick, E. Berg, D. Besson, G. Gaswint, C. Glaser, A. Hallgren, J. Hanson, S. Klein, S. Kleinfelder, L. Köpke, I. Kravchenko, R. Lahmann, U. Latif, J.-H. Nam, A. Nelles,

- C. Persichilli, P. Sandstrom, J. Tatar, and E. Unger. Observation of classically ‘forbidden’ electromagnetic wave propagation and implications for neutrino detection. 04 2018.
- [13] S. Barwick, D. Besson, P. Gorham, and D. Saltzberg. South polar in situ radio-frequency ice attenuation. *Journal of Glaciology*, 51(173):231–238, 2005.
- [14] E. A. Bell, P. Boehnke, T. M. Harrison, and W. L. Mao. Potentially biogenic carbon preserved in a 4.1 billion-year-old zircon. *Proceedings of the National Academy of Sciences*, 112(47):14518–14521, 2015.
- [15] A. Benedikter, K. Wickhusen, H. Hussmann, A. Stark, F. Damme, M. Modriguez-Cassola, and G. Krieger. Periodic orbits for interferometric and tomographic radar imaging of saturn’s moon enceladus. *Acta Astronautica*, 191:326–345, 2022.
- [16] M. T. Bland, W. B. McKinnon, and P. M. Schenk. Constraining the heat flux between enceladus’ tiger stripes: Numerical modeling of funiscular plains formation. *Icarus*, 260:232–245, 2015.
- [17] E. Bozdağ, J. Trampert, and J. Tromp. Misfit functions for full waveform inversion based on instantaneous phase and envelope measurements. *Geophysical Journal International*, 185(2):845–870, 05 2011.
- [18] C. Buizert and M. Helsen. Firn. In A. Fowler and F. Ng, editors, *Glaciers and Ice Sheets in the Climate System. Springer Textbooks in Earth Sciences, Geography and Environment*, chapter 11, pages 255–277”. Springer, Cham, 2020.
- [19] B. J. Buratti. Enceladus: Surface Texture and Roughness as clues to what lies beneath. In *45th Lunar and Planetary Science Conference*, Lunar and Planetary Science Conference, page 2038, Mar. 2014.
- [20] I. Collins. Phase-locked loop (pll) fundamentals, jul 2018.
- [21] J.-P. Combe, T. B. McCord, D. L. Matson, T. V. Johnson, A. G. Davies, F. Scipioni, and F. Tosi. Nature, distribution and origin of co2 on enceladus. *Icarus*, 317:491–508, 2019.
- [22] D. J. Daniels. *Surface Penetrating Radar*. The Institution of Electrical Engineers, London, UK, 1996.
- [23] W. Degruyter and M. Manga. Cryoclastic origin of particles on the surface of enceladus. *Geophysical research letters*, 38(16), 2011.
- [24] R. P. Di Sisto and M. Zanardi. Surface ages of mid-size saturnian satellites. , 264:90–101, Jan. 2016.
- [25] M. K. Dougherty, B. J. Buratti, P. K. Seidelmann, and J. R. Spencer. Enceladus as an Active World: History and Discovery. In P. M. Schenk, R. N. Clark, C. J. A. Howett, A. J. Verbiscer, and J. H. Waite, editors, *Enceladus and the Icy Moons of Saturn*, page 3. 2018.
- [26] D. Eliseev, D. Heinen, K. Helbing, R. Hoffmann, U. Naumann, F. Scholz, C. Wiebusch, and S. Zierke. Acoustic in-ice positioning in the enceladus explorer project. *Annals of Glaciology*, 55(68):253–259, 2014.
- [27] L. W. Esposito. Planetary rings. *Reports on Progress in Physics*, 65(12):1741–1783, Dec. 2002.
- [28] B. R. et al. Observations in the saturn system during approach and orbital insertion, with cassini’s visual and infrared mapping spectrometer (vims). *Astronomy and Astrophysics*, 446:707–716, 2006.

- [29] J. A. Fleck, J. R. Morris, and M. D. Fleck. Time-dependent propagation of high energy laser beams through the atmosphere. *Applied Physics*, 1976(10):129–160, jul 1976.
- [30] P. Friend and A. Kyriacou. Dielectric Profiling of Enceladus’ Surface in the Tiger Stripe Region. In *52nd Lunar and Planetary Science Conference*, Lunar and Planetary Science Conference, page 2586, Mar. 2021.
- [31] M. Grab, E. Mattea, A. Bauder, M. Huss, L. Rabenstein, E. Hodel, A. Linsbauer, L. Langhammer, L. Schmid, G. Church, and et al. Ice thickness distribution of all swiss glaciers based on extended ground-penetrating radar data and glaciological modeling. *Journal of Glaciology*, 67(266):1074–1092, 2021.
- [32] B. Gundlach, J. Ratte, J. Blum, J. Oesert, and S. Gorb. Sintering and sublimation of micrometre-sized water-ice particles: The formation of surface crusts on icy solar system bodies. *Monthly Notices of the Royal Astronomical Society*, 479(4):5272–5287, 2018.
- [33] B. R. H., C. R. N., and B. B. J. et al. Composition and physical properties of enceladus’ surface. *Science*, 311(5766):1425–1428, 2006.
- [34] K. Helbing, R. Hoffmann, U. Naumann, D. Eliseev, D. Heinen, F. Scholz, C. Wiebusch, and S. Zierke. Acoustic properties of glacial ice for neutrino detection and the enceladus explorer, 2016.
- [35] D. Hemingway, L. Iess, R. Tajeddine, and G. Tobie. The interior of enceladus. *Enceladus and the icy moons of Saturn*, pages 57–77, 2018.
- [36] A. Herique, B. Agnus, and E. A. et al. Direct observations of asteroid interior and regolith structure: Science measurement requirements. *Advances in Space Research*, 62(8):2141–2162, 2018. Past, Present and Future of Small Body Science and Exploration.
- [37] M. M. Herron and C. C. Langway. Firn densification: An empirical model. *Journal of Glaciology*, 25(93):373–385, 1980.
- [38] L. Iess, D. J. Stevenson, M. Parisi, D. Hemingway, R. A. Jacobson, J. I. Lunine, F. Nimmo, J. W. Armstrong, S. W. Asmar, M. Ducci, and P. Tortora. The gravity field and interior structure of enceladus. *Science*, 344(6179):78–80, 2014.
- [39] A. P. Ingersoll, S. P. Ewald, and S. K. Trumbo. Time variability of the enceladus plumes: Orbital periods, decadal periods, and aperiodic change. *Icarus*, 344:113345, 2020. Cassini Mission Science Results.
- [40] W. Kang and G. Flierl. Spontaneous formation of geysers at only one pole on enceladus’s ice shell. *Proceedings of the National Academy of Sciences*, 117(26):14764–14768, 2020.
- [41] S. Kempf, U. Beckmann, and J. Schmidt. How the enceladus dust plume feeds saturn’s e ring. *Icarus*, 206(2):446–457, 2010.
- [42] M. R. Kirchoff and P. Schenk. Crater modification and geologic activity in enceladus’ heavily cratered plains: Evidence from the impact crater distribution. *Icarus*, 202(2):656–668, 2009.
- [43] K. Konstantinidis, C. L. Flores Martinez, B. Dachwald, A. Ohndorf, P. Dykta, P. Bowitz, M. Rudolph, I. Digel, J. Kowalski, K. Voigt, and R. Förstner. A lander mission to probe subglacial water on Saturn’s moon Enceladus for life. *Acta Astronautica*, 106:63–89, Jan. 2015.
- [44] K. Konstantinidis, C. L. F. Martinez, B. Dachwald, A. Ohndorf, P. Dykta, P. Bowitz, M. Rudolph, I. Digel, J. Kowalski, K. Voigt, et al. A lander mission to probe subglacial water on saturn s moon enceladus for life. *Acta astronautica*, 106:63–89, 2015.

- [45] S. Kutuzov, L. G. Thompson, and I. e. a. Lavrentiev. Ice thickness measurements of guliya ice cap, western kunlun mountains (tibetan plateau), china. *Journal of Glaciology*, 64(248):977–989, 2018.
- [46] A. Kyriacou, P. S., and C. Sbrocco. paraproppython. <https://github.com/prchyr/paraPropPython>, 2020.
- [47] H. Looyenga. Dielectric constants of heterogeneous mixtures. *Physica*, 31(3):401–406, Mar. 1965.
- [48] K. A. Ludwig, C.-C. Shen, D. S. Kelley, H. Cheng, and R. L. Edwards. U–th systematics and 230th ages of carbonate chimneys at the lost city hydrothermal field. *Geochimica et Cosmochimica Acta*, 75(7):1869–1888, 2011.
- [49] J. I. Lunine, A. Coustenis, G. Mitri, G. Tobie, and F. Tosi. Future Exploration of Enceladus and Other Saturnian Moons. In P. M. Schenk, R. N. Clark, C. J. A. Howett, A. J. Verbiscer, and J. H. Waite, editors, *Enceladus and the Icy Moons of Saturn*, page 453. 2018.
- [50] M. Mansuripur. The Ewald-Oseen extinction theorem. *Optics & Photonics News*, 9(8):50–55, Aug. 1998.
- [51] C. P. McKay, A. Davila, C. R. Glein, K. P. Hand, and A. Stockton. Enceladus Astrobiology, Habitability, and the Origin of Life. In P. M. Schenk, R. N. Clark, C. J. A. Howett, A. J. Verbiscer, and J. H. Waite, editors, *Enceladus and the Icy Moons of Saturn*, page 437. 2018.
- [52] W. B. McKinnon, J. I. Lunine, O. Mousis, J. H. Waite, and M. Y. Zolotov. The Mysterious Origin of Enceladus: A Compositional Perspective. In P. M. Schenk, R. N. Clark, C. J. A. Howett, A. J. Verbiscer, and J. H. Waite, editors, *Enceladus and the Icy Moons of Saturn*, page 17. 2018.
- [53] W. B. McKinnon, J. I. Lunine, O. Mousis, J. H. Waite, and M. Y. Zolotov. The Mysterious Origin of Enceladus: A Compositional Perspective. In P. M. Schenk, R. N. Clark, C. J. A. Howett, A. J. Verbiscer, and J. H. Waite, editors, *Enceladus and the Icy Moons of Saturn*, page 17. 2018.
- [54] Meteoblue. Simulated historical climate weather data for aletsch glacie <https://meteoblue.com>, 2022.
- [55] J. Meyer and J. Wisdom. Tidal evolution of mimas, enceladus, and dione. *Icarus*, 193(1):213–223, 2008.
- [56] F. Nimmo, A. C. Barr, M. Běhounková, and W. B. McKinnon. The thermal and orbital evolution of enceladus : observational constraints and models. 2017.
- [57] Y. Ohtomo, T. Kakegawa, A. Ishida, T. Nagase, and M. T. Rosing. Evidence for biogenic graphite in early Archaean Isua metasedimentary rocks. *Nature Geoscience*, 7(1):25–28, Jan. 2014.
- [58] O. Ozgun, V. Sahin, M. E. Erguden, G. Apaydin, A. E. Yilmaz, M. Kuzuoglu, and L. Sevgi. PETOOL v2.0: Parabolic Equation Toolbox with evaporation duct models and real environment data. *Computer Physics Communications*, 256:107454, Nov. 2020.
- [59] G. W. Patterson, S. A. Kattenhorn, P. Helfenstein, G. C. Collins, and R. T. Pappalardo. The Geology of Enceladus. In P. M. Schenk, R. N. Clark, C. J. A. Howett, A. J. Verbiscer, and J. H. Waite, editors, *Enceladus and the Icy Moons of Saturn*, page 95. 2018.

- [60] C. Porco, D. DiNino, and F. Nimmo. How the geysers, tidal stresses, and thermal emission across the south polar terrain of enceladus are related. *The Astronomical Journal*, 148(3):45, jul 2014.
- [61] C. Porco, D. DiNino, and F. Nimmo. How the geysers, tidal stresses, and thermal emission across the south polar terrain of enceladus are related. *The Astronomical Journal*, 148(3):45, 2014.
- [62] C. Porco, L. Dones, and C. Mitchell. Could It Be Snowing Microbes on Enceladus? Assessing Conditions in Its Plume and Implications for Future Missions. *Astrobiology*, 17:876–901, Sept. 2017.
- [63] C. C. Porco, P. Helfenstein, P. C. Thomas, A. P. Ingersoll, J. Wisdom, R. West, G. Neukum, T. Denk, R. Wagner, T. Roatsch, S. Kieffer, E. Turtle, A. McEwen, T. V. Johnson, J. Rathbun, J. Veverka, D. Wilson, J. Perry, J. Spitale, A. Brahic, J. A. Burns, A. D. DelGenio, L. Dones, C. D. Murray, and S. Squyres. Cassini observes the active south pole of enceladus. *Science*, 311(5766):1393–1401, 2006.
- [64] F. Postberg, R. N. Clark, C. J. Hansen, A. J. Coates, C. M. Dalle Ore, F. Scipioni, M. Hedman, and J. Waite. Plume and surface composition of enceladus. *Enceladus and the icy moons of Saturn*, pages 129–162, 2018.
- [65] F. Postberg, R. N. Clark, C. J. Hansen, A. J. Coates, C. M. Dalle Ore, F. Scipioni, M. M. Hedman, and J. H. Waite. Plume and Surface Composition of Enceladus. In P. M. Schenk, R. N. Clark, C. J. A. Howett, A. J. Verbiscer, and J. H. Waite, editors, *Enceladus and the Icy Moons of Saturn*, page 129. 2018.
- [66] F. Postberg, S. Kempf, J. Schmidt, N. Brilliantov, A. Beinsen, B. Abel, U. Buck, and R. Srama. Sodium salts in e-ring ice grains from an ocean below the surface of enceladus. *Nature*, 459(7250):1098–1101, 2009.
- [67] F. Postberg, N. Khawaja, B. Abel, G. Choblet, C. Glein, M. Gudipati, B. Henderson, H.-W. Hsu, S. Kempf, F. Klenner, G. Moragas-Klostermeyer, B. Magee, L. Nölle, M. Perry, R. Reviol, J. Schmidt, R. Srama, F. Stolz, G. Tobie, and J. Waite. Macromolecular organic compounds from the depths of enceladus. *Nature*, 558, 06 2018.
- [68] S. Prohira, C. Sbrocco, and A. P. et al. Modeling in-ice radio propagation with parabolic equation methods. *Physical Review D*, 103(10), may 2021.
- [69] G. D. Q. Robin. Velocity of radio waves in ice by means of a bore-hole interferometric technique. *Journal of Glaciology*, 15(73):151–159, 1975.
- [70] J. Rolla, A. Machtay, A. Patton, W. Banzhaf, A. Connolly, R. Debolt, L. Deer, E. Fahimi, E. Ferstle, P. Kuzma, C. Pfindner, B. Sipe, K. Staats, and S. A. Wissel. Using evolutionary algorithms to design antennas with greater sensitivity to ultra high energy neutrinos, 2021.
- [71] R. I. Saragih, N. F. Saragih, and M. Aritonang. Improving performance genetic algorithm on knapsack problem by setting parameter. *Journal of Physics: Conference Series*, 1361(1):012034, nov 2019.
- [72] G. Schubert, J. D. Anderson, B. J. Travis, and J. Palguta. Enceladus: Present internal structure and differentiation by early and long-term radiogenic heating. *Icarus*, 188(2):345–355, 2007.
- [73] M. Schwikowski, M. Schläppi, P. Santibañez, A. Rivera, and G. Casassa. Net accumulation rates derived from ice core stable isotope records of pío xi glacier, southern patagonia icefield. *The Cryosphere*, 7(5):1635–1644, 2013.

- [74] W. Shockley. The theory of p-n junctions in semiconductors and p-n junction transistors. *The Bell System Technical Journal*, 28(3):435–489, 1949.
- [75] B. S. Southworth, S. Kempf, and J. Spitale. Surface deposition of the enceladus plume and the zenith angle of emissions. *Icarus*, 319:33–42, feb 2019.
- [76] B. S. Southworth, S. Kempf, and J. Spitale. Surface deposition of the enceladus plume and the zenith angle of emissions. *Icarus*, 319:33–42, 2019.
- [77] F. Spahn, J. Schmidt, N. Albers, M. Hörning, M. Makuch, M. Seiß, S. Kempf, R. Srama, V. Dikarev, S. Helfert, G. Moragas-Klostermeyer, A. V. Krivov, M. Sremčević, A. J. Tuzolino, T. Economou, and E. Grün. Cassini dust measurements at enceladus and implications for the origin of the e ring. *Science*, 311(5766):1416–1418, 2006.
- [78] J. Spencer, F. Nimmo, A. P. Ingersoll, T. A. Hurford, E. S. Kite, A. R. Rhoden, J. Schmidt, and C. J. A. Howett. Plume origins and plumbing (ocean to surface). The University of Arizona Press, 2018.
- [79] J. R. Spencer and F. Nimmo. Enceladus: An active ice world in the saturn system. *Annual Review of Earth and Planetary Sciences*, 41(1):693–717, 2013.
- [80] J. N. Spitale, T. A. Hurford, A. R. Rhoden, E. E. Berkson, and S. S. Platts. Curtain eruptions from enceladus’ south-polar terrain. *Nature*, 521(7550):57–60, 2015.
- [81] J. N. Spitale and C. C. Porco. Association of the jets of enceladus with the warmest regions on its south-polar fractures. *Nature*, 449(7163):695–697, 2007.
- [82] M. Stelzig, J. Audehm, B. F., A. Benedikter, M. Giang Do, A. Kyriacou, K. Helbing, C. Wiebusch, G. Krieger, and M. Vossiek. Validation of sensor systems in an analogue scenario for icy moon exploration, international foundation hfsjg, activity report 2022, 2022.
- [83] M. Stockham. Radio Frequency Attenuation Length Estimates In Ice from Antarctic and Greenlandic Radar Depth Sounding Data. In *APS April Meeting Abstracts*, volume 2014 of *APS Meeting Abstracts*, page S8.006, Mar. 2014.
- [84] F. Swiss Federal Spatial Data Infrastructure. Maps of switzerland <https://map.geo.admin.ch/>, 2023.
- [85] R. Tajeddine, K. M. Soderlund, P. C. Thomas, P. Helfenstein, M. M. Hedman, J. A. Burns, and P. M. Schenk. True polar wander of enceladus from topographic data. *Icarus*, 295:46–60, 2017.
- [86] P. C. Thomas, R. Tajeddine, M. S. Tiscareno, J. A. Burns, J. Joseph, T. J. Lored, P. Helfenstein, and C. Porco. Enceladus’s measured physical libration requires a global subsurface ocean. , 264:37–47, Jan. 2016.
- [87] R. H. Tyler, T. P. Boyer, T. Minami, M. M. Zweng, and J. R. Reagan. Electrical conductivity of the global ocean. *Earth, Planets and Space*, 69(1):156, Nov 2017.
- [88] J. Waite, J. H., W. S. Lewis, B. A. Magee, J. I. Lunine, W. B. McKinnon, C. R. Glein, O. Mousis, D. T. Young, T. Brockwell, J. Westlake, M. J. Nguyen, B. D. Teolis, H. B. Niemann, R. L. McNutt, M. Perry, and W. H. Ip. Liquid water on Enceladus from observations of ammonia and ^{40}Ar in the plume. , 460(7254):487–490, July 2009.

Appendices

Appendix A

Dielectric Properties of Ice

A.1 Permittivity: Theory

This work was primarily concerned with understanding the dependence of high frequency (i.e. MHz to GHz scale) radio emission through icy media, which can be described entirely with the complex permittivity ϵ profile of the medium in question. The permittivity ϵ , also called ‘absolute permittivity’ of a material, is a property that determines how much energy is stored in the charge separation of the medium in response to an external electric field. The relative permittivity ϵ_r , is the ratio of the absolute permittivity of the material and the permittivity of free space ϵ_0 .

$$\epsilon_r = \frac{\epsilon}{\epsilon_0} \quad (\text{A.1})$$

The relative permittivity is the factor by which the electric field in the medium \mathbf{E} is reduced relative to what it would be in a vacuum. Cold pure ice $T < 0^\circ$ is predominantly a dielectric material, but even pure ice has a small level of conductivity. A dielectric is a material where the electric charges do not move freely in response to an external field but are instead displaced from their equilibrium position within some small bounded distance, resulting in ‘polarization.’ The positive charges are displaced in the direction of the external field, while the negative charges move in the opposite direction, creating an internal electric field that acts against the external field, with this effect being quantified by the ‘electric susceptibility’ χ_E . The susceptibility is a constant of proportionality (which can be expressed as a tensor in an anisotropic medium) which relates the electric field in the medium \mathbf{E} to the dielectric polarization density \mathbf{P} (also known as the ‘polarization field’):

$$\mathbf{P} = \epsilon_0 \chi_E \mathbf{E} \quad (\text{A.2})$$

where \mathbf{P} is the divergence of the bound charge density ρ_b

$$\nabla \cdot \mathbf{P} = \rho_b \quad (\text{A.3})$$

And the related electric displacement field \mathbf{D} , the gradient of the free charges

$$\nabla \cdot \mathbf{D} = \rho_f \quad (\text{A.4})$$

with the total charge density within the volume of interest being $\rho = \rho_f + \rho_b$. Thus from Maxwell’s formulation of Gauss’ law, we express \mathbf{D} and \mathbf{P} in terms of χ_E and \mathbf{E} :

$$\mathbf{D} = \epsilon \mathbf{E} = \epsilon_0 \mathbf{E} + \mathbf{P} = (1 + \chi_E) \mathbf{E} = \epsilon_0 \epsilon_r \mathbf{E} \quad (\text{A.5})$$

Electric susceptibility is related to the relative permittivity by:

$$\epsilon_r = 1 + \chi_E \quad (\text{A.6})$$

In general, a material cannot be polarized instantaneously from an applied electric field. The response of the polarization as a function of time is described with a convolution:

$$\mathbf{P}(t) = \epsilon_0 \int_{-\infty}^t \chi_E(t-t')E(t')dt' \quad (\text{A.7})$$

With the time delay Δt being expressed as $\Delta t = t-t'$. Through a Fourier transform the equation A.7 can be expressed conveniently in frequency space as:

$$\mathbf{P}(\omega) = \epsilon_0 \chi_E \mathbf{E}(\omega) \quad (\text{A.8})$$

Consequently, permittivity is expressed as a complex function of the angular frequency of the applied field:

$$\epsilon = \epsilon(\omega) \quad (\text{A.9})$$

$$\epsilon = \epsilon' + i\epsilon'' \quad (\text{A.10})$$

Where ϵ' is the real part of the permittivity and ϵ'' the imaginary part. From Maxwell's equations it can be derived that the real part of the relative permittivity of the material directly determines the speed of light inside a material $v = c/n$, as expressed by the material's refractive index n :

$$n = \sqrt{\epsilon'_r} \quad (\text{A.11})$$

Intuitively this can be understood from the response of the bound charges within the material, which as previously mentioned, align with the applied field and create a field in the opposite direction. Thus, as the fields are vector quantities, the electric field in the material is the sum of the external field and the field caused by the induced charge separation. Paradoxically, both of these fields should propagate at the speed of light c , not at the slower speed of light in the material v . But, as postulated in the Eswald-Oseen extinction theorem, the field produced by the separated charges has a component that travels at c and a component that 'looks' like it travels at v , and the component traveling at c completely cancels out the external field[50]. As a result, the only field inside the material is traveling at v , with the same angular frequency ω as the external field and a longer wavelength $\lambda = 2\pi cn/\omega$. The Eswald-Oseen theorem has been derived from Maxwell's equations in several works[50].

A.1.1 Atomic Model

In the classical approach to the dielectric, the material is made up of atoms. Each atom consists of a cloud of negative charge (electrons) bound to and surrounding a positive point charge at its center. This can be reduced to a simple dipole using the superposition principle. A dipole is characterized by its dipole moment, a vector quantity shown in the figure as the blue arrow labeled M. It is the relationship between the electric field and the dipole moment that gives rise to the behavior of the dielectric. When the electric field is removed the atom returns to its original state. The time required to do so is called relaxation time; an exponential decay.

A.1.2 Debye Model

Because charges move at finite velocities, there exists a threshold value of f for which the charges can not move fast enough to keep up. In other words, the frequency of the external field oscillation can be greater than that of polarization charge oscillation, and therefore the charges remain separated and in motion. The frequency at which this happens is known as the relaxation frequency. Below the relaxation frequency, the permittivity plateaus at low-frequency, or 'static' limit ϵ_s , sometimes known as the dielectric constant. At frequencies above the relaxation frequency, the permittivity also plateaus at the high-frequency limit ϵ_∞ .

$$\epsilon(\omega) = \epsilon_\infty + \frac{\Delta\epsilon}{1 + i\omega\tau} \quad (\text{A.12})$$

Appendix B

Formation of Glacial Firn

On Earth, firn is the transitional stage between fallen snow and glacial ice. Following drifting, disintegration, and packing of snow crystals, surface snow has a density of $280 - 420 \text{ kg/m}^3$, or a volume filling ratio of approximately one-third. The overburden pressure from shallower fallen snow or firn squeezes out the air gaps until the firn density approaches that of solid ice $\rho_{ice} = 920 \text{ kg/m}^3$. In addition to the densification, the firn grains themselves go through grain growth, sintering, and recrystallization.

B.1 Densification

Snow crystals can have a large variety of distinct shapes, some very complex, which can lead to very low-density values for freshly accumulating snow ($40\text{--}200 \text{ kg/m}^3$), as the snowflakes are packed inefficiently. During and after a snowfall event, wind action induces the breakup of the complex snow crystals. This causes the disintegration of the snowflakes, turning them into more rounded snow grains, which can settle efficiently by sliding into a more organized, stacked pattern. In addition, recrystallization by diffusion and sublimation occurs immediately after snowfall events, resulting in reduction of the surface area of the crystal. Reduction of the surface area reduces the free energy, so the formation of spherical grains is favored. Large snow grains grow at the expense of smaller grains because this also reduces the free energy. Grain growth, the settling effects of wind reworking, and the more effective stacking of grounded grains lead to a fast consolidation of snow after a snowfall event. Aged surface snow has typical densities of $200\text{--}400 \text{ kg/m}^3$.

A phenomenon related to sublimation is the formation of depth hoar. This is a low-density layer ($100\text{--}300 \text{ kg/m}^3$) consisting of coarse, pyramidal, or cup-shaped crystals. These layers are formed when cooling occurs at the surface while the snowpack below remains warmer. The steep temperature gradient that results causes rapid vapor flux towards the surface, and recrystallization occurring along this pathway leads to the formation of faceted, coarser grains.

Settling and grain growth dominate the relatively fast firn compaction process in the first stage until a density of $\sim 550 \text{ kg/m}^3$ is reached. The spherical grains are organized in their most effective configuration at this density. Further compaction occurs by increasing the contact area between the neighboring ice crystals via sintering, involving the transfer of material to the contact points between grains to form bonds. Initially, this process was also dominated by vapor transport, but with increasing density, the porosity decreased, and hence, the influence of vapor transport was greatly reduced. As the overburden pressure and the contact area between grains both increase, recrystallization is favored: molecular diffusion changes the size and shape of crystals, thereby reducing the stress at the contact points. This last process is controlled by temperature, the overburden pressure and the corresponding compaction rates are much slower than during the initial settling phase.

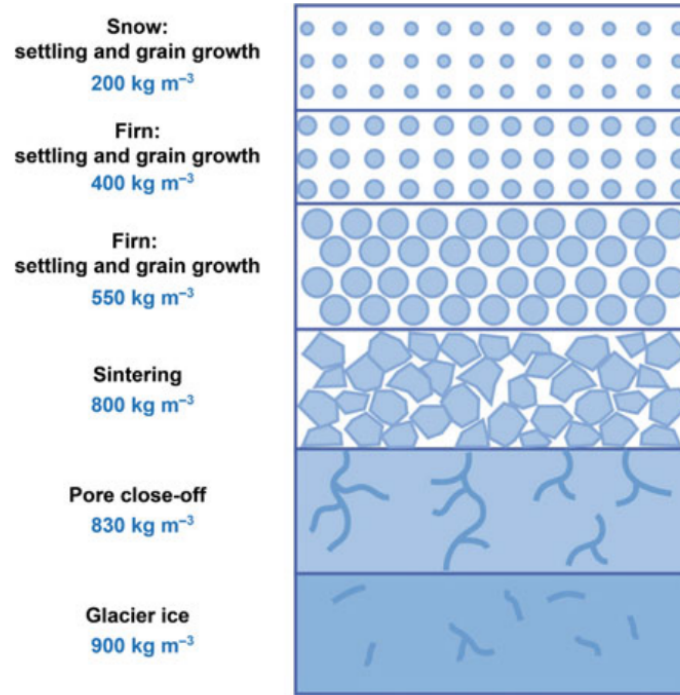


Figure B.1: Illustration of densification processes of dry snow and firn from snow settings to the formation of glacial ice [18]

At a density of $\sim 730 \text{ kg/m}^3$, the densification rate further slows down. The contact area between grains has reached a maximum, and the remaining air occupies thin channels between the grain boundaries. The main process that can further increase the density of the medium is the internal deformation (creep) of crystals. The final stage of densification of the ice matrix occurs below pore close-off: due to increasing overburden pressure, the air bubbles are reduced in volume. At the close-off density, the hydrostatic pressure in the ice is around 4–7 times as large as the (near-ambient) air pressure in the bubbles. The bubbles will be compacted until their pressure matches the surrounding ice. At depths below $\sim 600 \text{ m}$, this process eventually forms clathrates.

B.1.1 Densification Models

The process outlined above is a qualitative description of what happens in ‘cold glaciers’ where temperatures are still below freezing and can be quantitatively described with empirical, the most widely known of which is the Herron-Langway model[37]. The model assumes that the change in the air gap is linearly proportional to the change in stress caused by the weight of the above snow, with the change in the vacuum fraction v :

$$\frac{dv}{v} = -k\rho dz \quad (\text{B.1})$$

with ρ being the firn density, z the depth and k is a densification rate constant. The vacuum fraction can be represented by the density difference between solid ice and firn:

$$v = \frac{\rho_{\text{ice}} - \rho}{\rho_{\text{ice}}} \quad (\text{B.2})$$

By substituting equation B.2 into B.1 and solving by integrating, it was found that:

$$\log\left(\frac{\rho}{\rho_{\text{ice}} - \rho}\right) = k\rho_{\text{ice}}z \quad (\text{B.3})$$

The linear proportionality between the left and right-hand terms implies an asymptotic relationship between the firn density and depth, which is indeed observed with terrestrial glaciers in zones of accumulation. One can further derive a differential equation model for the density change with depth:

$$\frac{d\rho}{dz} = k\rho(\rho_{\text{ice}} - \rho) \quad (\text{B.4})$$

Herron and Langway further invoke an empirical relationship known as ‘Sorge’s Law’ which states the ‘vertical velocity’ dz/dt of material in firn is equal to the accumulation rate (the mass flux of falling snow) A divided by the density, with A being in units of mass per unit area per unit time[11]. This allows us to obtain the equation for the densification rate:

$$\frac{dz}{dt} = \frac{A}{\rho} \quad (\text{B.5})$$

and:

$$\frac{d\rho}{dt} = kA(\rho_{\text{ice}} - \rho) \quad (\text{B.6})$$

It is implicitly assumed that the temperature and accumulation rate are independent or can be treated as independent. Herron and Langway subsequently make k a function of temperature T using an Arrhenius-type law. One then arrives at the following expressions for the densification rate.

$$\frac{d\rho}{dt} = k\left(\frac{A}{\rho_w}\right)^\beta(\rho_{\text{ice}} - \rho) \quad (\text{B.7})$$

with ρ_w the density of water. In this model, there are two distinct values of k and for β at a transition point of $\rho = 550 \text{ kg/m}^3$, with R being the ideal gas constant:

- $\rho < 550 \text{ kg/m}^3$: $\beta = 1$ and $k = 11 \exp -\frac{10160}{RT}$
- $\rho > 550 \text{ kg/m}^3$: $\beta = 0.5$ and $k = 575 \exp -\frac{21400}{RT}$

The inflection point at $\rho = 550 \text{ kg/m}^3$ marks the point where densification becomes dominated by sintering instead of compaction. This model allows one to derive the ice density profile from available data on snowfall rates and temperature. It also explains the quasi-exponential function of firn density observed in many glaciers and hence also explains empirical models of refractive index profiles. n is directly proportional to ρ [69]:

$$n(z) = 1 + 0.845\rho(z) \quad (\text{B.8})$$

B.1.2 Melting and Refreezing

While gravity playing the dominant role in the densification process, but other factors; namely thermal forcing and horizontal motion also play their roles. The most important effect in our case is the melting of surface snow during summer months. This melt-water may refreeze at the surface or may percolate downwards through pores in the firn to refreeze at a greater depth, forming ice layers or ice lenses.

Appendix C

The Permittivity Profile of the Tiger Stripe Region

In this chapter, the dielectric profile of Enceladus' upper ice crust to a depth of a few hundred m in vicinity to the tiger stripes is investigated. Doing so requires, at first, the modeling of the plume deposits of the south polar geysers and the resulting ice deposition on the surface. Further possible changes to the deposited ice due to physical parameters such as temperature or pressure must also be considered. From these models, the physical and chemical properties of the ice, such as density and salinity, are then estimated to derive the respective permittivity and attenuation values. The analysis includes modeling the plume ice deposition on two scales. First, the global plume deposition is simulated, originating from all known geysers across the whole south polar region (latitudes below 60° S), with a lower resolution of 1 deg x 1 deg per bin. In addition, higher resolution modeling with a higher resolution of plume ice deposits from a single geyser located in Damascus Sulcus with bin sizes of 10 m x 10 m is performed.

C.1 Ice Deposition on a Global Scale

C.1.1 Geyser deposition modeling

The surface of Enceladus' south polar region is mainly composed of pure crystalline water ice with only minor traces of CO_2 ([28], [64]). Those ice grains are sediment constantly from the geysers located inside the tiger stripes. Over 200 active geysers have been identified in the South Polar Region of Enceladus, with their positions aligning with the 4 tiger stripes. The first 9 geysers, correlating with known infrared hot spots, were found in [81]. An additional 98 geysers were identified by [61] and a further 115 by [80]. These geysers erupt water vapor at a total rate of 200 kg/s and ice and dust particles with radii between 0.5 and 15 μm at a rate of 25 kg/s [75]. The water vapor, traveling at speeds of ~ 700 m/s, as well as 10 % of the erupted particles escapes from Enceladus' gravitational forces and fall into orbit around Saturn as parts of the E-Ring. However, the remaining ~ 90 % of the ice particles fall back on Enceladus' surface, with the fraction of grains depositing back on the surface approaching 1 for particles with a radius $r_{\text{grain}} > 2$ m (Fig. C.2), building up constantly as an unconsolidated loose packed layer of snow. The deposition rate thereby decreases with increasing distance to the Geysers. Kempf et al. 2010 ([41]) simulated the deposition rate to be up to 0.5 mm/yr in close vicinity to the vents and down to 10^{-5} mm/yr at the equator of Enceladus. The velocity distributions of the erupting ice grains of different radii are shown in Fig. C.1, with the distributions being scaled by the relative abundances of the ice grains by radius. It can be seen that both the mean velocity and velocity variances decrease for larger ice grain radii. The size of the ice particles that fall back to the surface thereby decreases with increasing distance to the vents ([41], [23]). These deposits are described henceforth as the 'snow layer'.

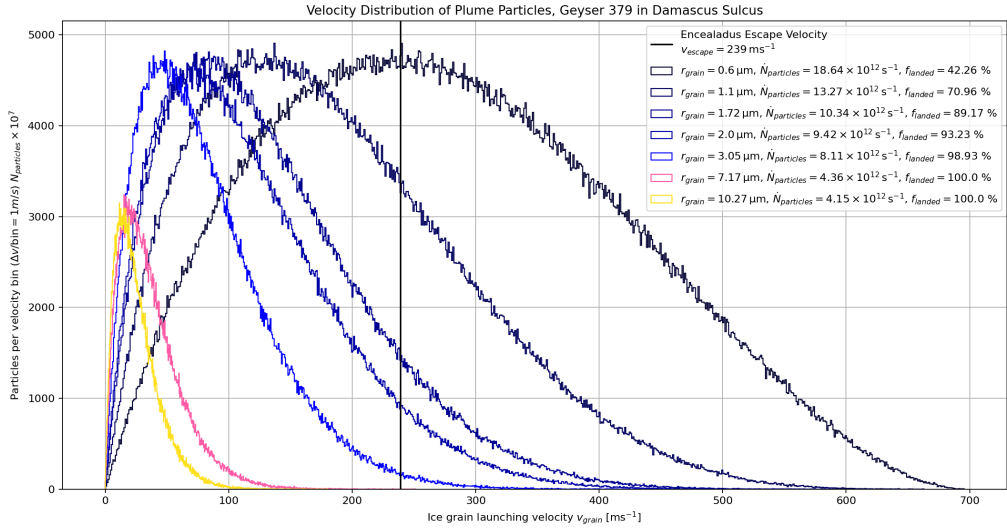


Figure C.1: The modeled ice particle velocity distribution at the geyser for ice particles with radii from $r_{\text{grain}} = 0.5 \mu\text{m}$ to $r_{\text{grain}} = 15 \mu\text{m}$. The relative numbers of the ice particles are found by integrating these distributions. The escape velocity of Enceladus $v_{\text{escape}} = 239 \text{ m/s}$ is displayed with a vertical line

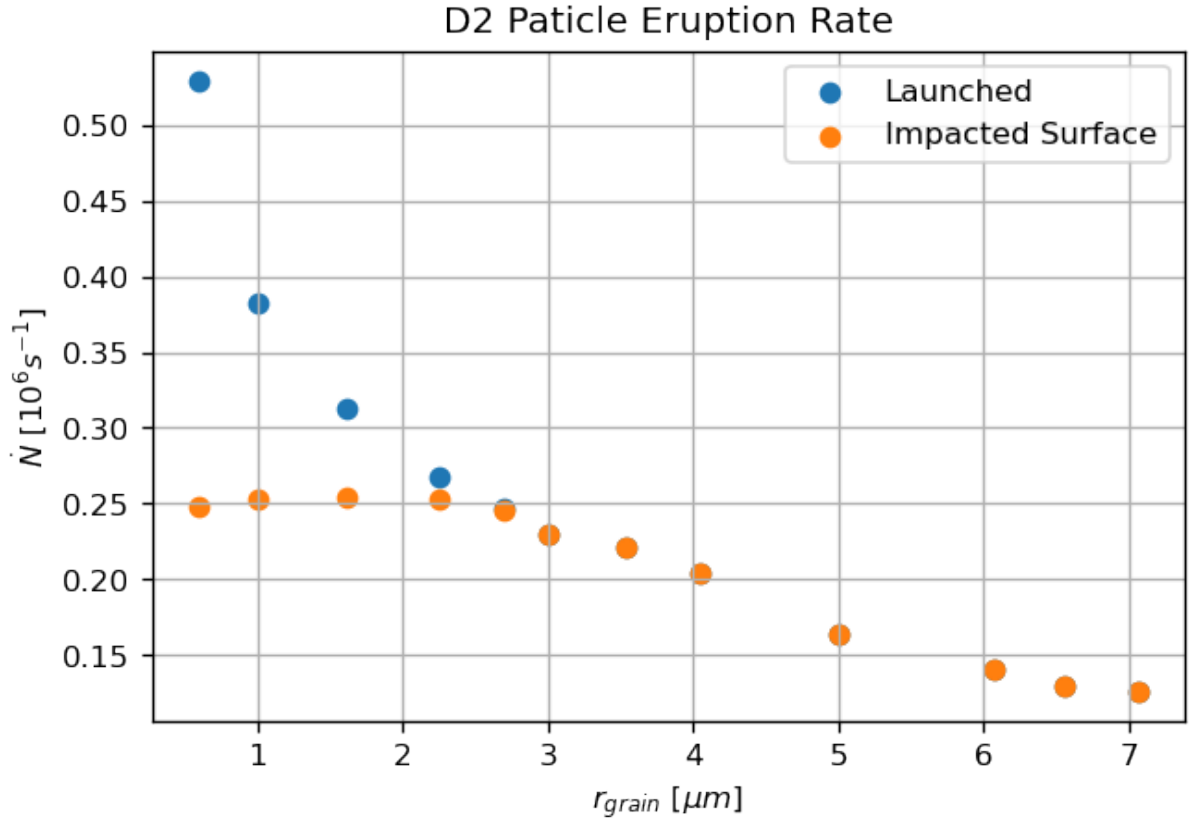


Figure C.2: The ice grain eruption rate from a geyser located at ‘D2’ (a hot-spot observed in Damascus Sulcus), with a comparison between the fraction of particles erupting vs how many land back at the surface as a function of r_{grain} . Ice grains with radii $r_{\text{grain}} > 2 \mu\text{m}$ will all fall back to the surface. Data is taken from [75]

Southworth et al. 2019 [75] simulated the impact rate of ice grains on the surface as a function of latitude, longitude (bin sizes of 1 deg x 1 deg) and particle radius, creating arrays of 180 x 360 for each of the particle radii simulated [75]. In total, they simulated 12 distinct particle radii for the first 9 geysers identified in [81] and 7 sizes for the remainder of geysers found by [61] and [80]. The impact rate is converted into the deposition rate dz/dt on the surface:

$$\frac{dz}{dt}(\lambda, \phi, r) = \frac{dN}{dt dA}(\lambda, \phi, r) \frac{4}{3} \pi r^3 \quad (\text{C.1})$$

Where λ is the latitude, ϕ is the longitude and r the particle radius. The particle flux $dN/dtdA$ gives the number of particles dN landing in a unit area dA per unit time dt . Therefore the total volume of particles landing on a unit area on the surface is found by multiplying the number of particles by the volume of each particle. To further obtain absolute values for the number flux from the data files from [75], which only provides relative values, the number flux was integrated over the surface of Enceladus and across particle radii.

$$\frac{dM}{dt} = \int R_E^2 d\Omega \int dr \frac{dN}{dt dA}(\lambda, \phi, r) \rho_{\text{ice}} \frac{4}{3} \pi r^3 \quad (\text{C.2})$$

Where the particle mass rate dM/dt is set equal to 25 kg/s [75], R_E is the Enceladus radius of 252 km, and $d\Omega$ gives the solid angle. To obtain values of the total accumulated ice deposition Z on Enceladus surface, deposition rate dz/dt was integrated over the probable time of geyser activity on the South Polar Region T_{activity} , assuming constant activity over this time.

$$Z(r, \lambda, \phi, T_{\text{activity}}) = \int^{T_{\text{activity}}} dt \frac{dz}{dt}(r, \lambda, \phi) \frac{\rho_{\text{ice}}}{\rho_{\text{bulk}}(\lambda, \phi, t)} \quad (\text{C.3})$$

Note that the resulting total thickness of the accumulated ice particles layer will also depend on the local bulk density of the layer. Scenarios for the densification of the ice grains on the surface are discussed later in this section.

C.1.2 Results for Deposition

Figure C.3a shows the derived deposition rate dz/dt on Enceladus Surface for ice grains with a radius of 15 μm . The regions of the highest intensity of deposition with $\sim 10\text{mm/yr}$ closely matches with the positions of the tiger stripes. In the surrounding terrain, the mean deposition rate decrease constantly down to only $\sim 1\text{mm/yr}$ south of -80° . Three profile lines in Fig. C.3b are drawn, for which the total deposition for a time of constant geyser activity of 100 kyr can be inferred (fig C.3b). Profile 1 passes the south pole of Enceladus and cuts through all four tiger stripes. Profile 2 runs in parallel with profile 1 but with an offset of about 141 km, and profile 3 goes perpendicular to the other profiles and pass just along the single tiger stripe feature of Damascus Sulcus (see Fig. C.3).

In profile 1, all peaks of deposition which correlate each with one of the tiger stripes reach similar magnitudes. Only Alexandria Sulcus shows two separated peaks which are both slightly lower than the peaks of the other tiger stripes. In profile 2, the peak of Damascus Sulcus has the lowest magnitude which is also decreased in respect to the corresponding peak in profile 1. The maximum deposition rates of the tiger stripes in profile 2 then decreases in Baghdad Sulcus and is strongest in Cairo Sulcus, where it reaches total deposition of 10^3 similar as in profile 1. Profile 3 shows the deposition rate along Baghdad Sulcus. However, as the profile runs in a straight line, it does not always hit the tiger stripe center exactly which has a natural curved shape.

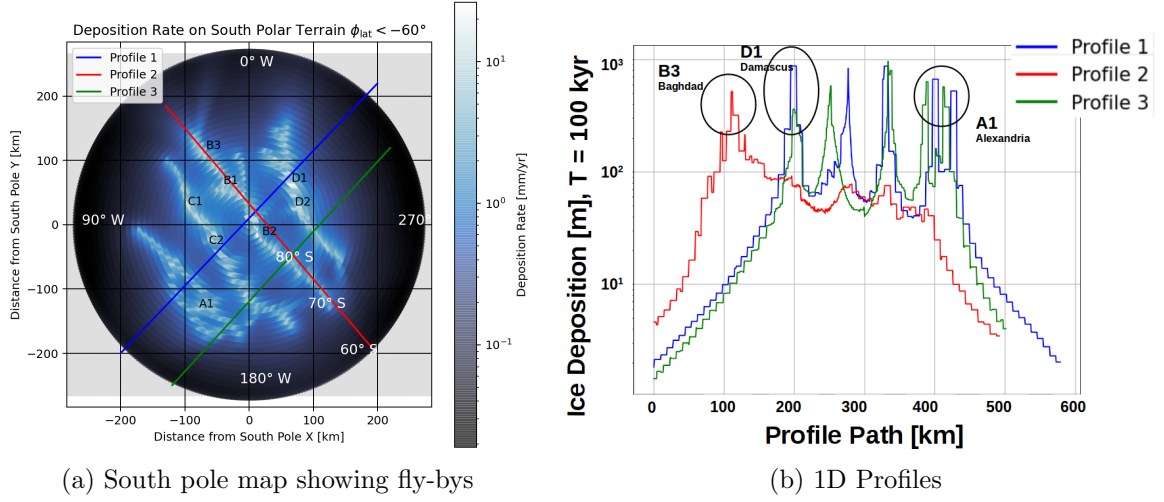


Figure C.3: A map of the accumulative ice deposition above the South Polar Terrain (SPT) over 100 kyr, as based off the numerical modelling from Southworth et al 2018 [75]. The ice deposition peaks at the position of the four tiger stripes as seen in C.3a. Also shown in the plots are 3 different paths over the South Polar Terrain, with Profile 1 bisecting all four tiger stripes and going over the South Pole, Profile 2 running approximately parallel over Baghdad Sulcus, and Profile 3 running parallel to Profile 1 but offset by around 50 km to the north. In C.3b, you can see the ice deposition along these paths, with clear peaks in deposition intensity at the position of the hotspots identified in Porco et al 2006 [63]).

C.1.3 Sintered snow layer

As Enceladus surface gravity is low $g_E = 0.113 \text{ m/s}^2$ (around 1% of the Earth's gravity)[79], and the ice grains surface layer has a low density $\rho \approx 92 \text{ kg/m}^3$ [19] there will be little compressive pressure or stress acting on the deposited grains. For example, compressive stresses could be approximately 1 kPa at 100 m depth in a layer of unconsolidated ice grains. Additionally, owing to Enceladus' surface temperature of 80 K, melting and refreezing processes analogous to Earth's glaciers will not occur. This leaves sintering as the dominant mechanism for densification, a mass transport process that leads to the formation of a 'neck' between neighboring particles, which occurs in the presence of relative heat and reduces porosity and thereby increases density ([32]). As illustrated in Fig. C.4a, the sinter neck radius r_s increases to a maximum, due to mass transport of molecules to the neck region and sublimation of molecules from the neck region and the grains itself. As this process continues, the distance between the center of mass of both grains decreases, and the pore space between the grains decreases in volume, leading to a decrease of total porosity within the ice grain depositions and, hence, an increase in density. The densification process is described as a function of time using the formula:

$$\rho(t) = \rho_0(1 + ke^{\alpha t}) \quad (\text{C.4})$$

Where ρ_0 is the initial bulk density of the grained material, and $k + 1 = P_i/P$ is the ratio of the initial porosity P_i and final porosity P , and $\alpha = 1/\tau$, with τ as time taken to reach maximum sintering from adhesion time. The density of the bulk layer reaches a maximum value as time approaches the sintering time. The bulk densities of the respective layers are found by multiplying the porosity (P) within the ice particle layer and the density of the particles:

$$\rho_{\text{bulk}} = (1 - P)\rho_{\text{grain}} \quad (\text{C.5})$$

From Cassini's surface measurements, the initial porosity of the ice particle sediments (the snow layer) of $P_0 = 0.9$ [19], and a final porosity after complete sintering of $P_f = 0.4$ and a grain density of $\rho_{\text{grain}} = 920 \text{ kg/m}^3$, according to the density of pure hexagonal crystalline ice. Gundlach

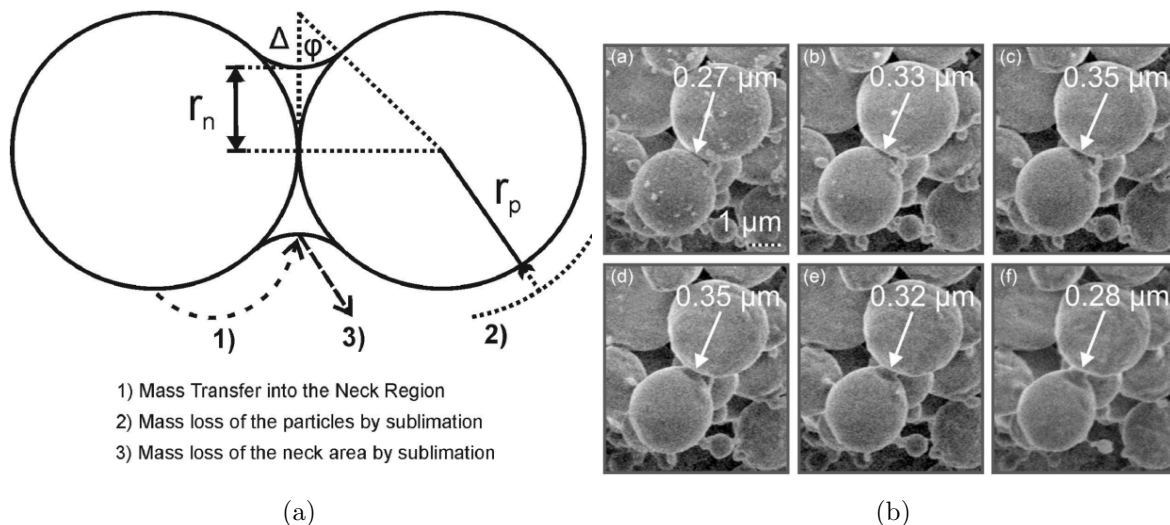


Figure C.4: C.4a is an illustration of the sinter geometry and the three main sintering processes from [32]. An example of sinter neck evolution of microscopic ice grains observed by an electron microscope in a chamber cooled to 163 K [32].

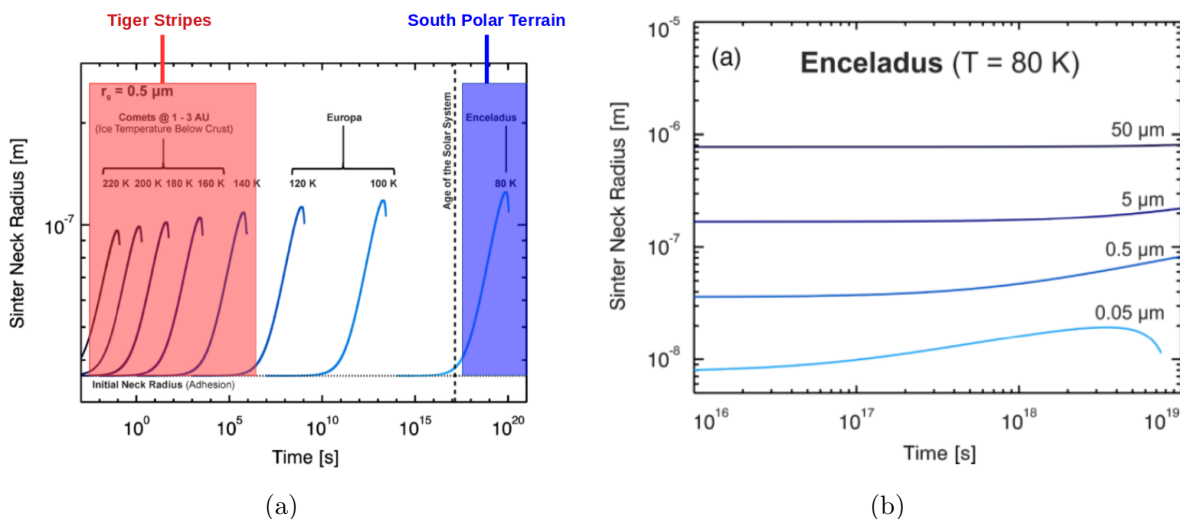


Figure C.5: Example of sinter neck evolution times from the Gundlach model for $0.5 \mu\text{m}$ ice grains on different ice surfaces in the solar system in general (C.5a) and for Enceladus in particular (C.5b), with temperatures ranging from 220 K to 80 K. The evolution time is strongly temperature dependent, from taking place in seconds on the surface of comets in the inner solar system to longer than the age of the solar system on the South Polar Terrain (blue-shaded area). It can be noted that the temperature within the tiger stripes is comparable to the cometary temperatures, as indicated by the red-shaded area. Both plots are taken from Gundlach et al. (2018) [32], with the highlighted regions in C.5a added by the author.

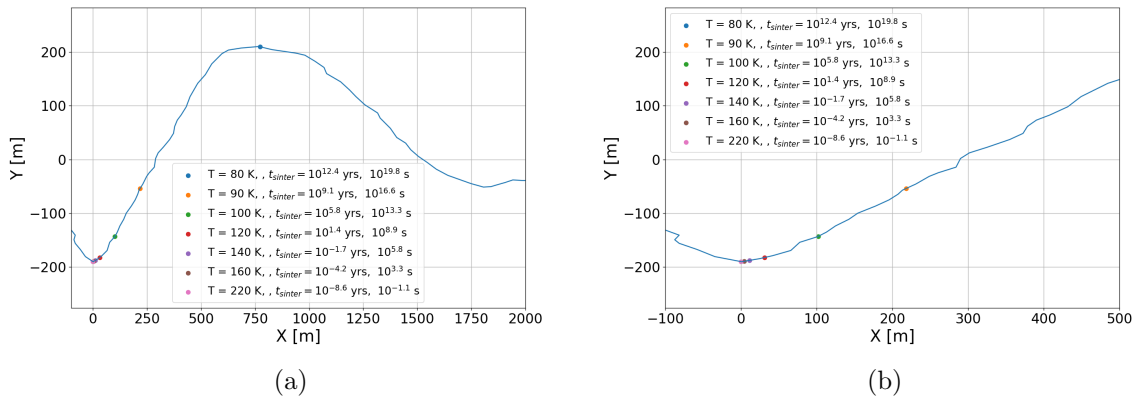


Figure C.6: A topographical cross-section of Damascus Sulcus at the location of Geyser 389, with surface temperature of different points indicated with coloured dots. C.6a shows the valley and ridge extending outwards to a 2 km range from the geyser, with temperatures already falling to 80 K at 750 m from the geyser. C.6b shows temperature variation within 500 m of the geyser, showing the rapid rise of temperature to 160 K.

et al. (2018) found a strong temperature dependence of sintering-neck formation time τ , and that the surface temperatures on Enceladus are too low to drive sintering processes within the lifetime of the Solar System (fig C.5). Yet the tiger stripes themselves are recognizable hotspots on the surface, and inside the chasm, the temperatures rise to a relatively balmy 225 K [5], where sintering processes take place within a time scale of minutes. However, the temperature falls down again rapidly within a short distance from each Tiger Stripe. Fig. C.6 shows the topography of Damascus Sulcus taken from data from stereoscopic observations[4] as an example, with the receptive temperatures derived from modeling [5] indicated at the horizontal distance to the center of the Tiger Stripe depression. The decrease from 225 K to 160 K occurs on a scale of only 5 m, which is hardly resolvable within the scale of the figure. At a distance of 250 m, the temperatures fall to 90 K and reach the normal SPT surface temperature of 80 K at a distance of 750 m. This distance corresponds to the peak of the ridge of Damascus Sulcus. Therefore, sintering processes at the surface are only possible near the geysers, and sintered snow layers could also occur only inside the ridges themselves.

Due to the small scale of temperature variation leading to a transition from non-sintering to sintering regions, it was necessary to model the ice deposition on a smaller dimension than that employed by [76]. The methodology and results of this study are reported in the next section.

C.2 Ice Deposition on a Local Scale

The data used for the global deposition mapping lacked the resolution to observe the deposition on the scale of the tiger stripes, which have widths of 5000 m. The geyser plumes were re-simulated using a simple numerical model to derive the deposition distributions on a local scale within the base of the fracture. The example of Geyser 379, located in Damascus Sulcus at a latitude of -80.628 and longitude 302.18 is used, for which topographic data obtained through stereoscopic methods from an image of Damascus Sulcus was available [19].

Numerical Modelling

For the simulation of a single geyser, the mass production rate of 25 kg/s was assumed is equally distributed among the geysers, and from this the number of particles emitted per second from the

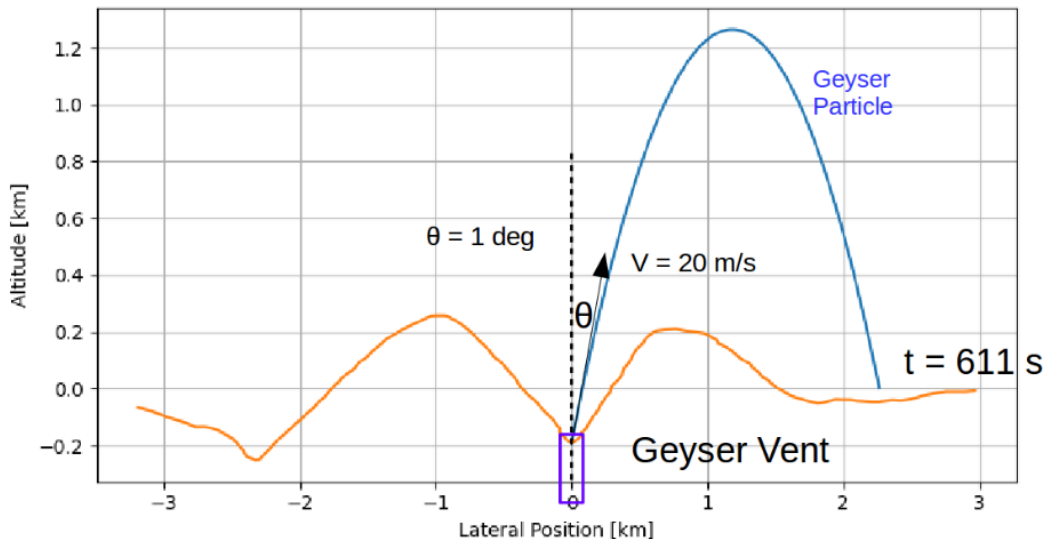


Figure C.7: The trajectory of an ice particle from Geyser 379 in Damascus Sulcus in the gravitational field of Enceladus. An ice particle is given a starting velocity of 20 m/s (the median velocity for ice grains of radius $r_{\text{grain}} = 20 \mu\text{m}$) and a zenith angle of $\theta = 1^\circ$. It travels for 611 s, reaching a maximum altitude of 1.2 km above the surface, and lands 2.2 km south of Geyser 379. The reader should note that other forces (such as the Coriolis force or the Saturnian gravitational field) are neglected.

individual geyser can be inferred. Additionally, the simulation used the estimated zenith 1° and azimuth angle 3° of the Geyser 379, as well as the opening angle of 15° [30]. The particle launch rate $dN/dt(r_{\text{grain}})$ for particles of different radii r_{grain} is determined by a power law relationship (see Fig. C.1), with larger particles being less abundant in the plumes. As large particles are heavier, their starting velocities will also be slower. The starting velocity distribution for the vent using the model was taken from Southworth et al. (2018) [76]:

$$p(v, r_{\text{grain}}) = \left(1 + \frac{r_{\text{grain}}}{r_c}\right) \left(\frac{r_{\text{grain}}}{r_c}\right) \frac{v}{v_c^2} \left(1 - \frac{v}{v_{\text{gas}}}\right)^{\frac{r_{\text{grain}}}{r_c} - 1} \quad (\text{C.6})$$

Where $r_c = 0.5 \mu\text{m}$ is the critical radius of the particles and v_{gas} is the gas velocity of the plume. The starting angle of the particle is chosen randomly from the range of the geyser's opening angle.

For $N = 10^5$ particles launched from the geyser, each particle trajectory in the gravitational field was simulated. The simulation is stopped when it lands on the surface or when it travels further than 10 km from the geyser (as illustrated in Fig. C.7).

We then count the number of particles landing on the surface in bins of distance from the geyser. From the obtained data, the deposition rate can be estimated as a function of distance from the geyser and integrated over the active time τ_{active} . For this same geyser, temperature data of the surface was obtained, and from this, it was possible to conclude that sintering could only occur within 100 m of the geyser's origin. The depth of the deposited ice layer (or snow layer) can be seen for different active time scenarios in Fig. C.8. As discussed in chapter 2, the active time of the SPT is unknown and still under discussion, with the crater count inferred surface of 1 Myr acting as a constraint on the possible scenarios. Therefore, there are a number of different probable active time scenarios, ranging from 1 kyr to 1 Myr, assuming a constant eruption rate.

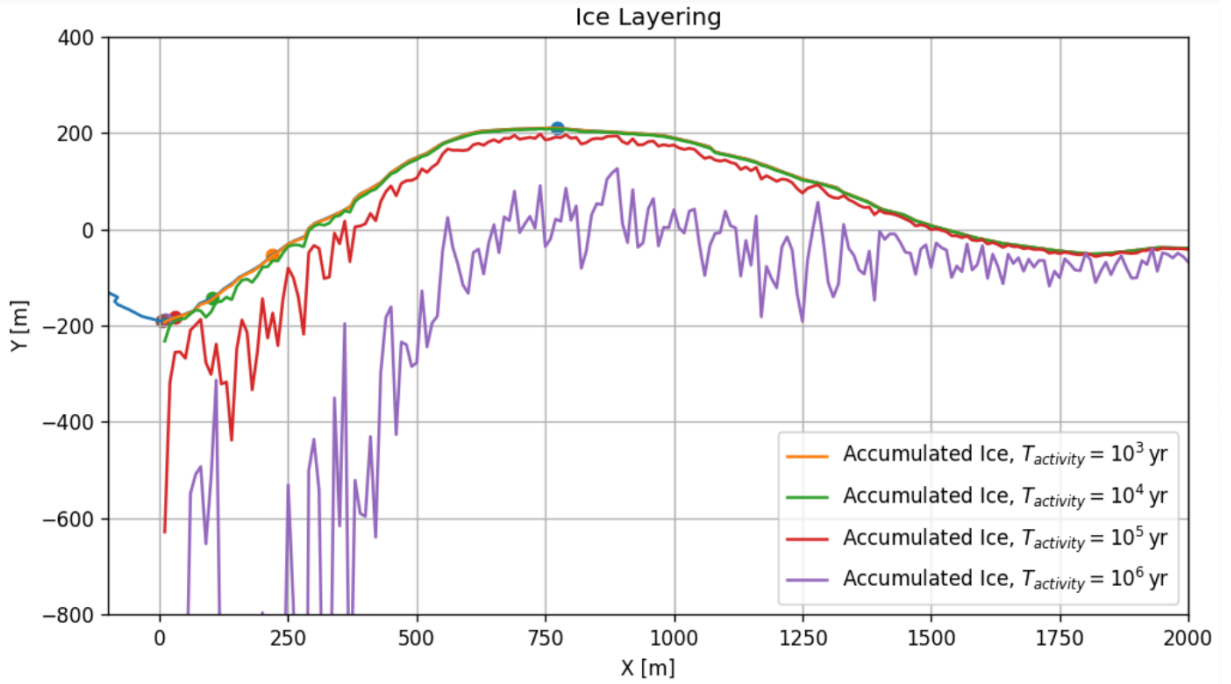


Figure C.8: The simulated depth of the ice particles subtracted from the surface topography, for different scenarios of T_{active} , ranging from 10^3 to 10^6 years.

C.3 Permittivity Profile

C.3.1 Layering

The modeling showed that the highest deposition occurs within a 1000 m of the geyser, with this being dominated by the slow-moving and more massive particles with $v < 20$ m/s and small zenith angles. From the surface temperature, these grains rapidly sinter and approach a maximum density of 552 kg/m^3 .

Hence the highest level of deposition is expected very close to the vents, and these are completely sintered. With further distance to the geysers, the deposition rate falls by an approximately exponential distribution. For a scenario of 100 kyr of constant geyser activity, the accumulated ice grain depth is:

1. $Z(x = 100 \text{ m}) \sim 300 \text{ m}$ (inside tiger stripe ridge).
2. $Z(x = 1000 \text{ m}) \sim 20 \text{ m}$ (immediately outside tiger stripe ridge).
3. $Z(x = 10000 \text{ m}) \sim 2 \text{ m}$ (general landscape of the SPT).

At around 100 m distance, 100 m sintered ice grain deposits are expected, whereas, at 1000 m distance, a depth of 20 m of unsintered snow deposits can be expected, with this reducing to 2 m at a distance of 10 km from the geyser. The results of this modeling make it unlikely that 3-layer terrain near the geysers will be observed, with unconsolidated ice grains gradually evolving into a sintered layer as a function of depth. Instead, a sharp transition from a sintered layer to a snow layer is likely, owing to the rapid temperature variation of the surface within the tiger stripes.

A first approximation of the permittivity profile can be found from the measured porosity [19] of the surface and our two-layer model, using the empirical relationship:

$$\epsilon_r = (1 + 0.845\rho)^2 \quad (\text{C.7})$$

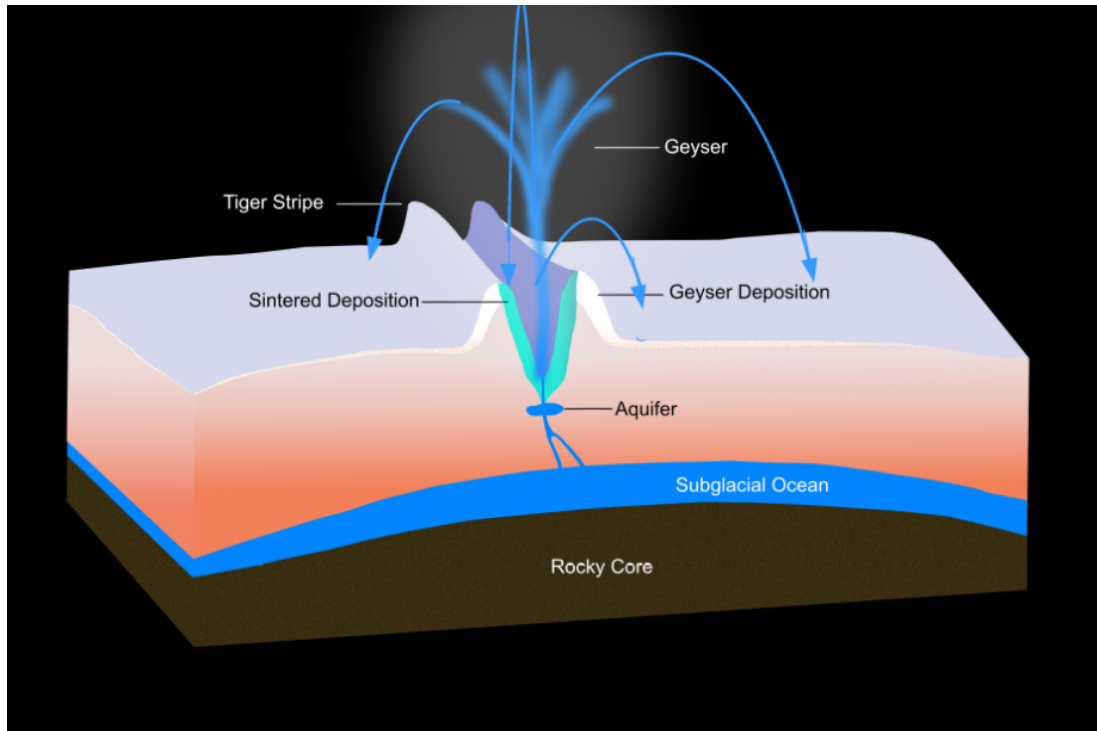


Figure C.9: An illustration of a geysir plume eruption from a vent within Damascus Sulcus. Dark blue indicates erupting ice particles surrounded by escaping water vapor. The arcs correspond to the trajectory of the ice particles falling to the surface. The sintered ice layer is only significant within the ridge, while the unconsolidated ice layer becomes steadily thinner with distance from the geyser (Plot from private communication with Dr. Pia Friend).

With ρ as the bulk density defined in units of g/cm^3 . From Buratti et al. [19], the unsintered grain deposits on Enceladus' surface have a porosity of 0.9, resulting in a permittivity of $\epsilon_r = 1.2$. In the regions where sintering occurs, the porosity of the material decreases to a value of 0.4, as inferred by Gundlach et al. [32], leading to a permittivity of $\epsilon_r = 2.3$. The lithospheric ice crust of Enceladus has a porosity of 0.1, resulting in a permittivity of $\epsilon_r = 2.95$. A schematic of the relative thickness and distribution of the three distinct layers around Geyser 379 is shown in Fig. C.9.

C.3.2 Chemical Composition

Having considered the depth and density of the deposited ice (both the 'snow' and 'sintered' layers) in the previous section, one must also consider the concentration of salts and organic species in the grains to derive the bulk conductivity of the Enceladus ice layers, from which the attenuation length of the surface can also be inferred.

The measurement of the mass spectrum of a wide sample of ice grains in the plume by Cassini's CDA, makes it possible to model the bulk conductivity of the deposited ice layers. However, first, the bulk conductivity of ice from the specific conductivity of *pure* ice grains was derived. The bulk is described as a heterogeneous mixture of vacuum and spherical ice crystals, with the volume packing ratio v . Empirically, the permittivity of such a mixture is:

$$\epsilon_\infty(v) = (1 + 0.496v)^3 \quad (\text{C.8})$$

We used a model from Looyenga (1965)[47] relationship between powder and bulk at microwave and radio frequencies, that is, a scenario with such a dielectric mixture dependent on the volume

packing fraction v to describe its high-frequency behavior $\sigma_{\infty,pure}$. For a two-component mixture of permittivity ϵ_1 and ϵ_2 , the bulk permittivity is defined:

$$\epsilon^{1/3} - \epsilon_1^{1/3} = v(\epsilon_2^{1/3} - \epsilon_1^{1/3}) \quad (\text{C.9})$$

By combining equations C.8 and C.9, and taking the imaginary components of permittivity

$$\epsilon_r = \epsilon_r' - i\epsilon_r'' = \epsilon_r' + i\omega\sigma \quad (\text{C.10})$$

We obtain the expression for the conductivity of the bulk:

$$\sigma_{\infty,pure}(v) = \sigma_{\infty,pure}(v=1)v(0.68 + 0.32v)^2 \quad (\text{C.11})$$

Doping an ice crystal with impurities leads to an increase in conductivity. In the high-frequency limit, the conductivity σ_{∞} is expressed as a linear sum of the conductivity components of all the species of impurities:

$$\sigma_{\infty}(v) = \sigma_{\infty,pure}(v) + \sum_i \beta_i(v)c_i \quad (\text{C.12})$$

Where β_i is the molar conductivity of species i , and c_i is their molar concentration. The molar conductivity obeys the same relationship as for pure ice in equation C.11.

As described in chapter 2, the ice grains are classified as Type I (salt poor), Type II (organics rich), and Type III (salt-rich). Since the evidence suggests that Type III particles are heavier and hence more likely to land in vicinity of the geysers, the ice deposits at the tiger stripes can be assumed to be dominated by Type III particles. The dominant species in Type III particles is sodium cations Na_+ , which has a molar conductivity of $\beta_{\text{Na}^+} = 1.5 \frac{\mu\text{S}}{\mu\text{M}}$ [66]. Type III ice particles having sodium to water ratio of up to $\text{Na}/\text{H}_2\text{O}10^{-3}$, and hence a maximal concentration of $c_{\text{Na}^+} = 5.1334 \odot 10^4 \mu\text{M}$. All other species were found to have negligible contributions to the conductivity, hence:

$$\sigma_{\infty}(v) = \sigma_{\infty,pure}(v) + \beta_{\text{Na}^+}c_{\text{Na}^+} \quad (\text{C.13})$$

Thus, for unsintered ice grains with porosities of $P = 0.9$ and hence volume filling ratios of $v = 0.1$, the conductivity:

$$\sigma_{\infty,TypeIII}(v=0.1) \approx 3.889 \cdot 10^3 \mu\text{Sm}^{-1} \quad (\text{C.14})$$

Resulting in an attenuation factor $\alpha = 3.5 \text{ dB/m}$.

C.4 Discussion

The very high deposition rate near the vent implies a depth of 100 m of sintered ice very close to the vent. This poses the question of what happens to this much ice. At constant activity times of 1 Myr, the total accumulated ice would be enough to fill the fracture of Damascus Sulcus. Such accumulated ice would further seal the vent with deposited ice, leading to a build-up of pressure and explosive eruption. Such a scenario has been proposed by Porco et al 2014 to explain cycles of activity and inactivity observed in a third of observed geysers over 6.5 years of observation[61]. It is also unclear how stable the geysers are in local position and in time, with such effects not being considered in this model.

C.5 Conclusions

Overall, the small-scale deposition analysis allowed us to conclude that the highest deposition occurs within 1 km of the geyser, mainly consisting of the heaviest (and hence slowest moving) ice particles. From temperature data, it was found that these grains rapidly sinter and approach a bulk density of 552 kg/m^3 . Hence the highest depositions occur within the valley of the tiger stripes, with the deposited grains subject to rapid sintering. The conclusions of the respective properties of the layers are summarized in table C.1.

Layer	ϵ_r'	ϵ_r''	P	ρ [g/cm ³]	$\sigma(f = 1 \text{ GHz})$ [$\mu\text{S/m}$]	v m/ μs	α
Snow Layer (Pure Ice)	1.159	$7.93 \cdot 10^{-6}$	0.9	0.0917	0.441	278	0.000308
Sinter Layer (Pure Ice)	2.131	$7.14 \cdot 10^{-5}$	0.4	0.551	3.969	205.49	0.002
Snow Layer (Type I)	1.159	$4.336 \cdot 10^{-5}$	0.9	0.0917	2.411	278	0.0017
Sinter Layer (Type I)	2.131	$3.9 \cdot 10^{-4}$	0.4	0.551	21.701	205.49	0.0112
Snow Layer (Type III)	1.159	0.0036	0.9	0.0917	197.472	278	0.1382
Sinter Layer (Type III)	2.131	0.032	0.4	0.551	1777.173	205.49	0.917
Primordial Ice	2.856	0.00013	0.1	0.826	7.337	177.528	0.003

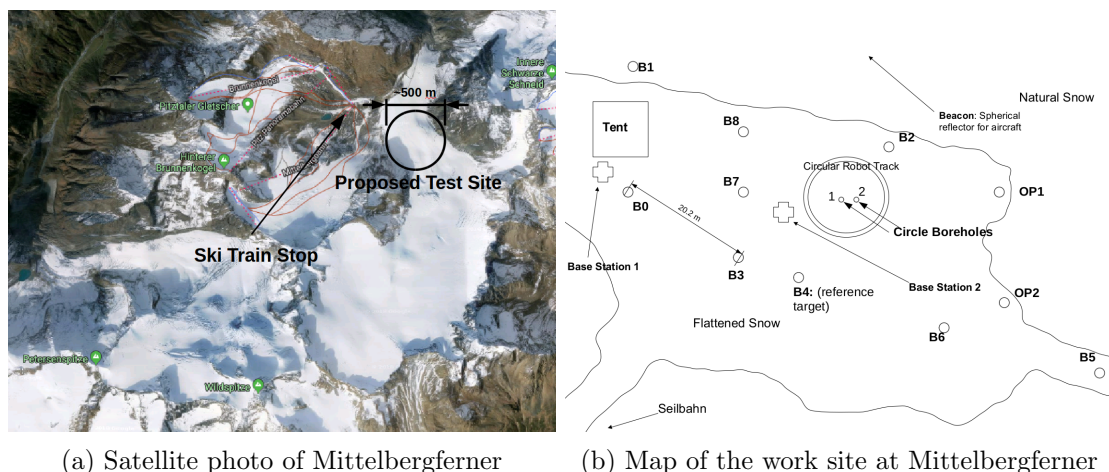
Table C.1: A summary of the estimated physical and dielectric properties of the primordial ice sheet and the snow and sintered layers (i.e. the deposited layers) above them. The changes in the estimated imaginary permittivity and conductivity values of the deposited layers for three different ice grain salt concentrations are shown: pure ice (assuming no salt content), ‘salt poor’ Type I particles ($\text{Na}/\text{H}_2\text{O} = 10^{-5}$), and ‘salt rich’ Type III particles ($\text{Na}/\text{H}_2\text{O} = 10^{-3}$)

Appendix D

Field Test 1

D.1 Field Test 1: Mittelbergerferner

The first field test in the project took place in February 2019 at Mittelbergerferner in Pitztal, Austria. This was primarily selected based on DLR-HR's previous experience in flying the area. In addition, the Mittelbergerferner is one of the most accessible glaciers in the Alps, making logistics and accommodation comparably easy to arrange. The accommodation was located in the adjacent valley, which meant that the team had to take a lift to the glacier every day. The material could be brought directly to the ski area by inclined cable car and from there directly onto the planned field test camp by Snowcat. A sketch of the camp at 2760m a.s.l. is shown in Fig. D.1b. At the time the field test took place, there was a continuous snow cover with a thickness of about 2m in the area of the camp. The part of the Mittelbergerferner, where the test camp lay within the ablation area of the glacier. Hence the beginning of the actual glacier ice is directly under the snow cover and there is no firn layer of densified snow. The field test lasted a total of two weeks between arrival on Feb. 10, 2019, and departure on Feb. 24, 2019. The main objective of BUW was to measure the permittivity and the attenuation of the snow and ice in respect to the depth within the glacier. Another objective was to test the self-melting reference targets (Figure D.2). As described in section 6, the measurements of the permittivity and the attenuation are made using a pair of antennas: one transmitting and one receiving. The measurements were then done by lowering down the antennas, each into one borehole in line of sight to each other, and then sending a frequency-modulated wave signal between the antennas. The travel time of the signal was used to reconstruct the permittivity, and the difference in the amplitude between the transmitting and receiving antenna was used for



(a) Satellite photo of Mittelbergerferner

(b) Map of the work site at Mittelbergerferner

Figure D.1: The Mittelbergerferner test site.



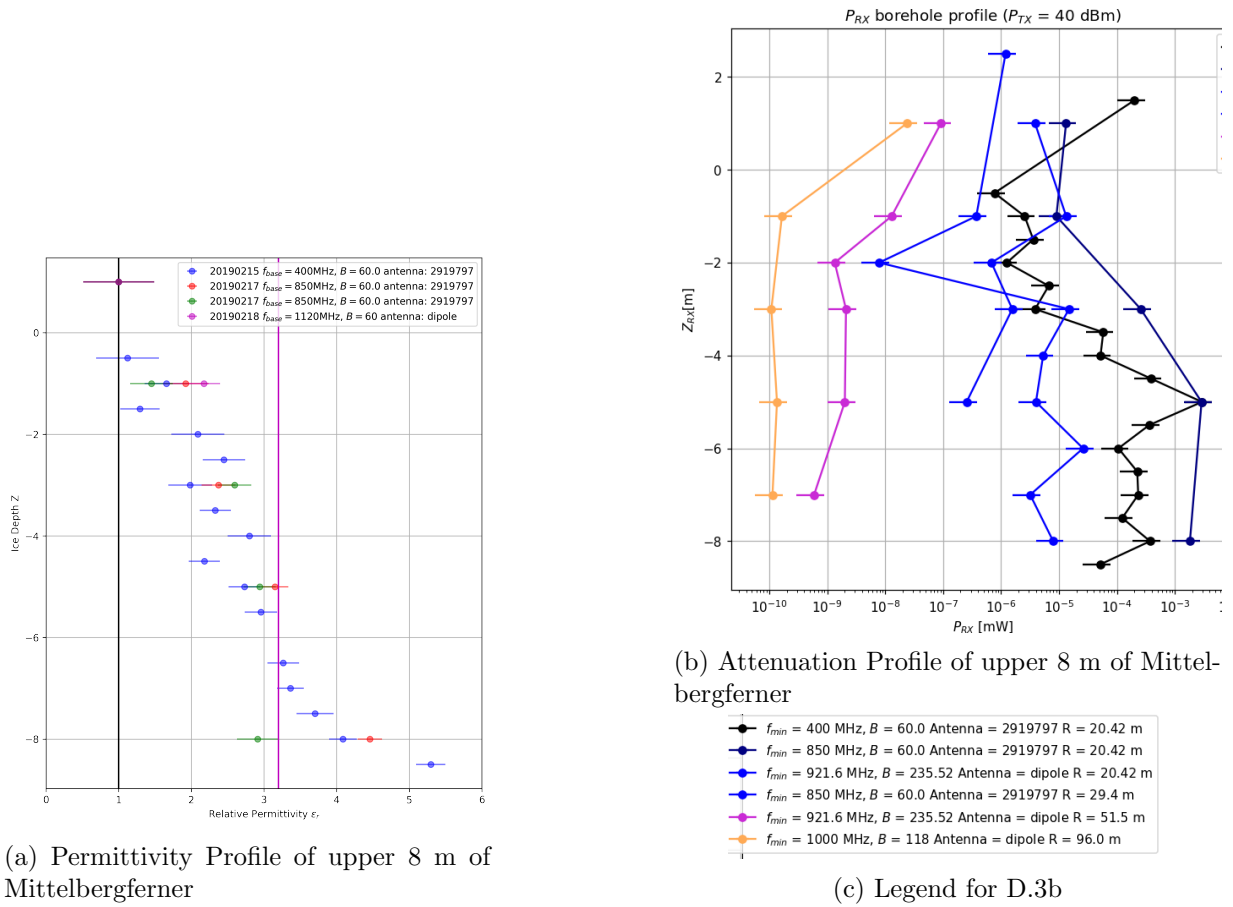
Figure D.2: Deployment of the reference targets at the Mittelbergferner

the attenuation measurements. The measurements were done for different distances between the antennas by using different boreholes. And for each borehole pair, multiple measurements were done using different frequencies and in various different depths, which was well documented to later reconstruct the data with respect to the depth of the glacier.

D.1.1 Results

Figure D.3a shows the resulting permittivity profile of the Mittelbergferner glacier at the area of the test side, with a clearly seen linear increase in the permittivity. High permittivity values below 6 m of depth $\epsilon_r > 3.2$ show evidence of water content in the glacier. Consistent real-part permittivity was measured from 400 MHz to 1.2 GHz. The data correlate well with literature data on the density of the glacier.

Figure D.3b shows the respective gain or power profile from which the attenuation rate can be measured. Multiple measurements were taken across the boreholes shown in Fig. D.1b, with borehole separations R from 8 m to 100 m. For power transmission measurements for ranges: $8\text{ m} < R < 50\text{ m}$, a gain of power relative to the air was measured, with the gain maximized at depths of 5 - 6 m. This is explained due to lensing effects occurring due to the surface (air-snow boundary) and the relatively shallow layer of high density. Beyond 50 m, attenuation of the signal was observed. From the power profiles, the average attenuation constant at 1 GHz of $\alpha(f = 1\text{ GHz}) = 0.26\text{ dB/m}$ was measured. The maximum observed attenuation was found at 3 m, with 30 dB loss over 100 m. The observed time-of-flight spectra were complex due to complex ice stratification, and there was evidence of deeper boundary layers, water pockets & bedrock (Figure D.4), but these could not be unambiguously verified. One self melting reference target was also brought to the glacier for testing. It was possible to melt itself up to 1.5m into the glacier. However, as it couldn't be recognized from the radar signal inside the snow and ice, one result of this field test was that another system had to be designed instead of the self-melting reference targets.



(a) Permittivity Profile of upper 8 m of Mittelbergferner

(b) Attenuation Profile of upper 8 m of Mittelbergferner

(c) Legend for D.3b

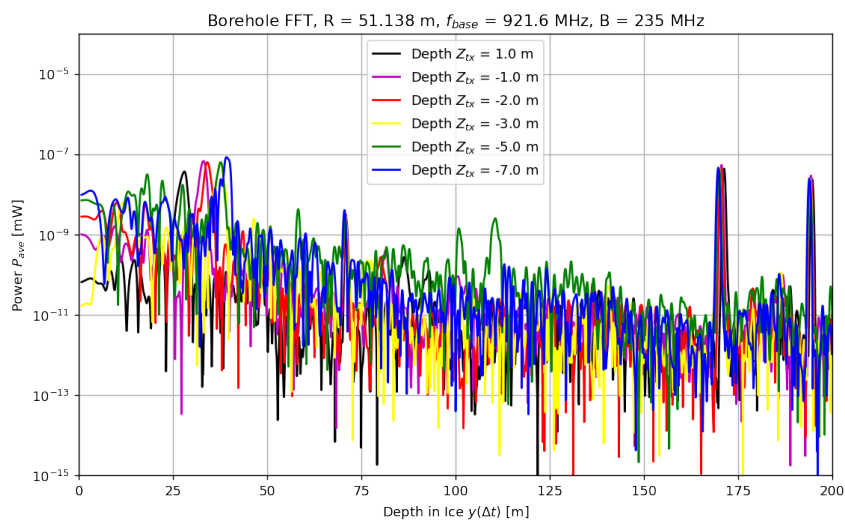


Figure D.4: Reflection spectra at Mittelbergferner

Appendix E

Comparison of PEs to FDTD

To verify the accuracy of the PE method, a comparison study was made between paraProp and an FDTD package Meep. This was motivated because the initial form of paraProp contained an error in the formulation of the Parabolic Equation, which led to an escalating phase velocity error that increases linearly range as can be seen in the pulse shown in Fig. E.1. The amplitude of the fields estimated with Meep and paraProp are shown in Fig. E.2. The simulation settings used were:

- Maximum Horizontal Range of the Simulation $X = 100$ m
- Maximum Ice Depth $Z = 74.9$ m
- Horizontal Resolution: $\Delta x = 0.08$ m
- Vertical Resolution: $\Delta z = 0.08$ m
- Frequency: $f = 100$ MHz
- Source Depth: $z_0 = 9.9$ m
- Refractive Index Model: $n(z) = +Be^{-Cz}$ for $z > 0$

As seen in Fig. E.1, the pulse was offset from the value expected analytically $t = Rn/c$ by 77 ns. When simulating pulses over varying distances, the error was found to be proportional to the value n at the surface of the transmitter and receiver. Thus the estimated travel time of the pulse was $t' \propto Rn^2/c$. When the refractive index is constant over the frequency range, the phase velocity is equal to the group velocity. The received pulses showed no sign of ‘dispersion’ and had the same width as the transmitted pulse. Thus, the error in the pulses’ group velocity suggested an error in the calculation of the phase velocity. Thus, a comparison was made between the phase velocity as a function of distance for both Meep and paraProp. The phase velocity was calculated numerically, first by calculating the wave vector as a function of distance from the transmitter.

$$k(x_i) = \frac{d\phi(x_i)}{dx} = (\arccos \frac{\Im[u(x_i + dx, z_0)]}{\Re[u(x_i + dx, z_0)]} - \arccos \frac{\Im[u(x_i, z_0)]}{\Re[u(x_i, z_0)]})/dx \quad (\text{E.1})$$

Where $d\phi$ is the local phase offset, as defined by the difference in argument of the complex amplitude between x_i and $x_{i-1} = x_i - \Delta x$. From this the phase velocity as function of x can be estimated simply:

$$v_p = \omega/k(x_i) = \omega/\frac{d\phi(x_i)}{dx} \quad (\text{E.2})$$

The resulting phase velocity as a function of distance is shown in Fig. E.3. This demonstrated that pulse velocity error indeed came from the phase velocity error from the FD solution, with

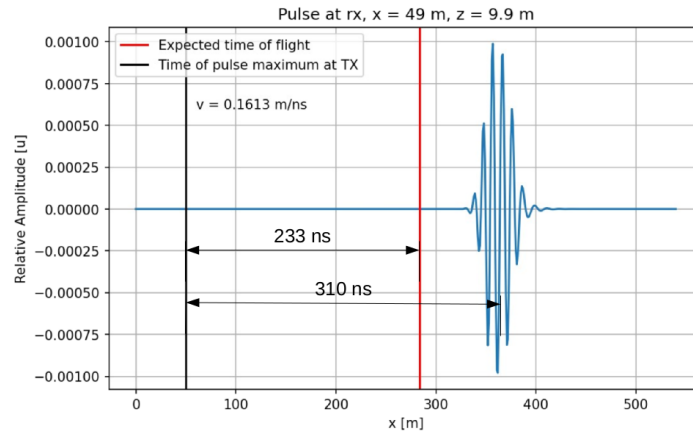


Figure E.1: The time of flight of a pulse in the old version of paraProp. The pulse measured at receiver $rx(x = 25 \text{ m}, z = 10 \text{ m})$. The pulse's central frequency $f_c = 400 \text{ MHz}$ and bandwidth $B = 200 \text{ MHz}$ emanating from a dipole antenna at source depth $z_0 = 10 \text{ m}$

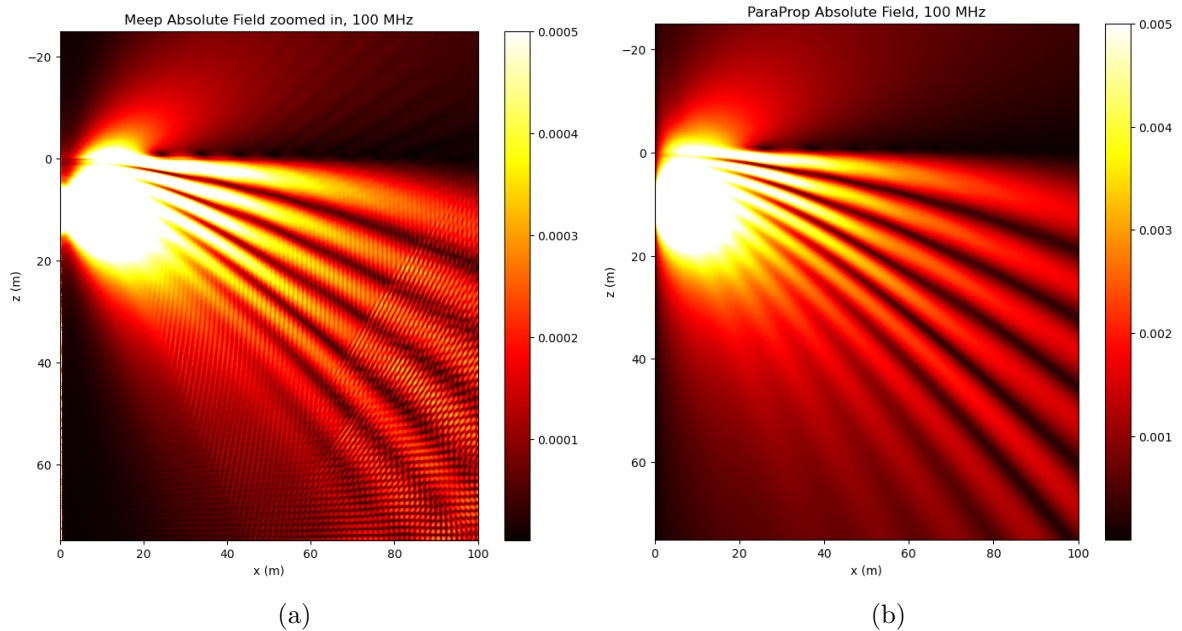


Figure E.2: The absolute field of 100 MHz radio emission from a 9.9 m dipole transmitter in South Pole (functional) ice. With a solution from Meep E.2a and from paraProp E.2b

the phase velocity of Meep shown in green and that for the old version of paraProp shown in blue. The Meep phase velocity is in good agreement with analytical expectations with the phase velocity old paraProp is reduced by a factor $1/n$. To create the parabolic equation one can define the reduced field $u(x, z)$ from a cylindrically symmetric field $\psi(x, z)$.

$$\psi(x, z) = \frac{e^{ik_0x}}{\sqrt{x}} u(x, z) \quad (\text{E.3})$$

We have the parabolic partial-differential equation:

$$\frac{\partial u}{\partial z} = e^{ik_0\Delta x(Q-1)} \quad (\text{E.4})$$

We make the approximation of the Q-operator $Q_{\text{ice}} \approx Q$ as written in paper:

$$Q_{\text{ice}} = \sqrt{1 + \frac{\partial_z^2}{k_0^2}} + n\sqrt{1 + \frac{1}{n_0^2}} - \sqrt{1 - \frac{n^2}{n_0^2}} \quad (\text{E.5})$$

For Q_{ice} the equations are redefined by replacing vacuum wave-vector $k_0 = \omega/c$ to using the source wave-vector $k'_0 = \omega n_0/c$, with the reference refractive index $n_0 = n(z_0)$ with z_0 being the source depth. In the original code equations E.3 to E.5 use k'_0 (which was expressed simply as k_0). However I proposed that the conversion between Ψ and u must use the vacuum wave-vector k_0 .

$$\psi(x, z) = \frac{e^{ik_0x}}{\sqrt{x}} u(x, z) \quad (\text{E.6})$$

instead of:

$$\psi(x, z) = \frac{e^{ik'_0x}}{\sqrt{x}} u(x, z) \quad (\text{E.7})$$

I therefore rewrite equations E.4 and E.5

$$\frac{\partial u}{\partial z} = e^{ik_0n_0\Delta x(Q-1)} \quad (\text{E.8})$$

$$Q_{\text{ice}} = \sqrt{1 + \frac{\partial_z^2}{n_0^2 k_0^2}} + n\sqrt{1 + \frac{1}{n_0^2}} - \sqrt{1 - \frac{n^2}{n_0^2}} \quad (\text{E.9})$$

By making this simple change to equation E.6 one can naturally obtain the ‘correction factor’ $\times 1/n_0$. The results show very good agreement with Meep and analytical expectations, as can be seen by the overlap between the orange points (the phase velocity for the corrected PE solution) and the green points (showing the phase velocity found with Meep). In essence the change to the Q-operator is linked to a change in the definition wave-vector to be dependent on the refractive index at the source. But the solution of the field from the *reduced field* has to be multiplied by the factor $e^{ik_0\Delta x}$ and the previous code used $e^{ik_0n_0\Delta x}$ leading to the accumulative phase error which was $\propto n_0$. With this error removed, the estimated phase velocity and amplitude are in good agreement between Meep and paraProp, adding confidence to the predictions of PE methods for radar propagation through ice.

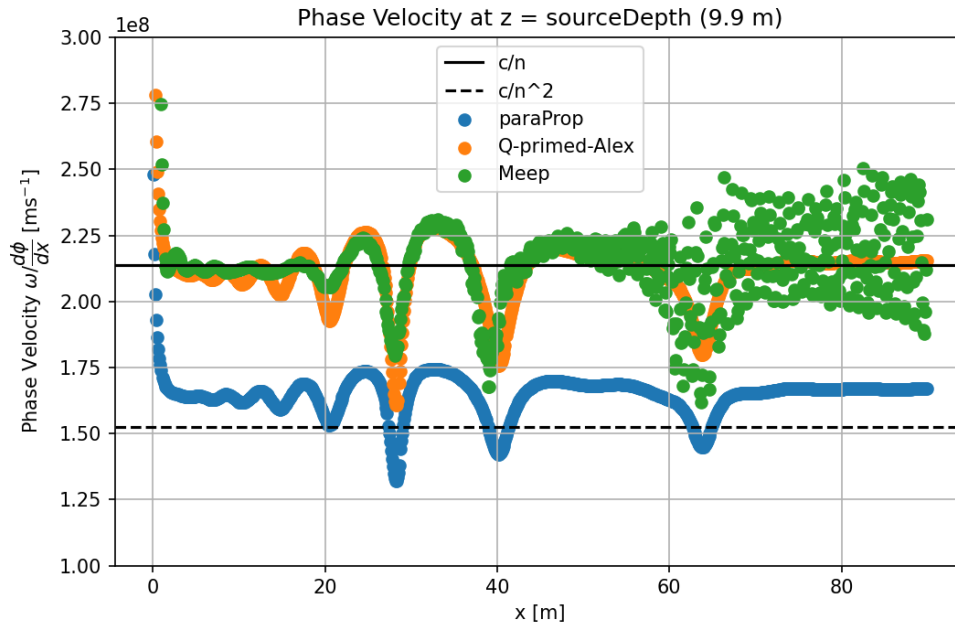


Figure E.3: The phased velocity of the E-field $z = 9.9$. The blue points show the phase velocity calculated with the original paraProp [68] versus that calculated using Meep. The orange displayed the corrected solution for paraProp found by applying equation E.6.

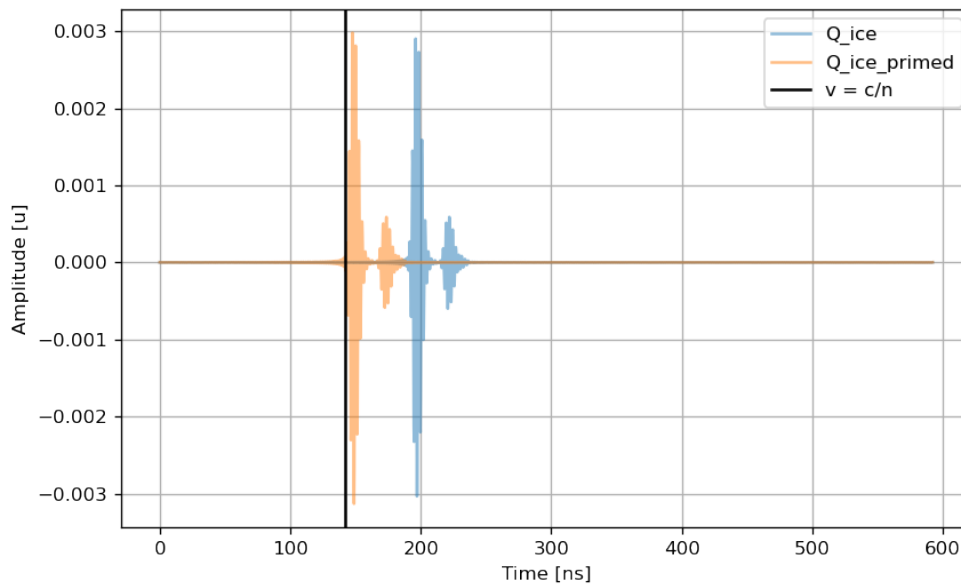


Figure E.4: A pulse shown with the correction of the Q operator

Appendix F

Non-Flat Surface Simulations with paraProp

F.1 Non-flat Surfaces

In all examples of simulations with paraProp given in this thesis, the ice environment was assumed to have a flat surface, with an underlying refractive index profile that varied along the range by the same function $n(x, z) = n(z)$, except for the examples with anomalies shown section 4.4. However, it is possible to simulate while taking into account non-flat surfaces by adding a digital elevation model (DEM) after setting the refractive index profile. This is accomplished in two ways:

- Cutting mode: If any depth coordinates $z_0 = z(x) < z_{DEM}(x)$, then $n(x, z_0) \rightarrow 1.0$
- Shifting mode: If any $z_0 = z(x) < z_{DEM}(z)$, then $n(x, z_0) \rightarrow n(x, z - z_{DEM})$

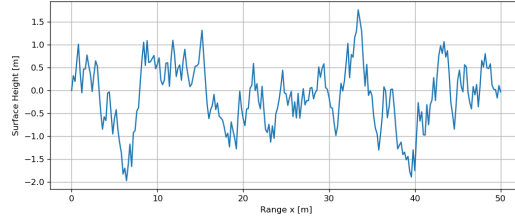
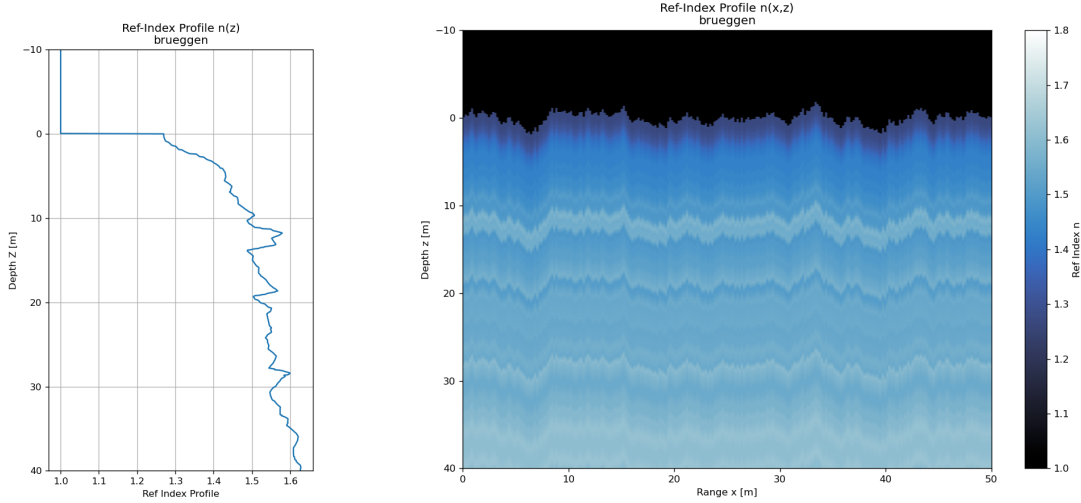
Cutting mode simply removes the ice above a certain depth without effecting the underlying refractive index profile, while shifting mode shifts all the refractive index up or down by the same amount as the difference of the surface elevation from a flat surface at $z = 0$.

F.2 Example: Brueggen glacier

To demonstrate the effect of non-flat surfaces on the simulate RF signal, consider the Brueggen glacier located in Patagonia in South America [73]. A ‘rough surface’ is added to the surface using ‘shifting mode’, using a digital elevation model ‘DEM’ $z_{DEM}(x)$ which is simply,

$$z_{DEM}(x) = f_{LP}(z_0 + R, \Delta x), \quad (\text{F.1})$$

where R is a random number between bounds (in this case $-2 \text{ m} < R < 2 \text{ m}$), z_0 defines the flat surface ($z_0 = 0 \text{ m}$, $f_{LP}(z(x), \Delta x)$ is a low pass filter. The randomized surface is shown in Fig. F.1a. The 2D refractive index of the Brueggen firn, accounting for the change in topography is shown in Fig. F.1c. The simulated E -field power as a function of depth and range $|E(x, z)|^2$ is shown for the case of a flat surface in Fig. F.2a, and for the rough surface in Fig. F.2b, for a transmitter located at $z_{TX} = 4 \text{ m}$ and transmitting CW emission at a frequency $f = 200 \text{ MHz}$. The flat surface case (Fig. F.2a) shows refracted signal ‘bands’, which appear as bands of enhanced emission $\sim -40 \text{ dBm}$ separated by narrow gaps with low emission $\sim -70 \text{ dBm}$. This is due to the refraction of the signal due to the increasing refractive index with depth. There is also a clear case of ‘horizontal emission’ for ranges $x > 40 \text{ m}$ and $z < 10 \text{ m}$, caused by trapping of the RF emission by ice layers. The rough surface (Fig. F.2b, has the effect of ‘blurring’ the bands, leading to an emission that appears more homogeneous below the surface. In both cases we see a shadow region immediately above and below the surface $-5 \text{ m} < z < 5 \text{ m}$, with reduced

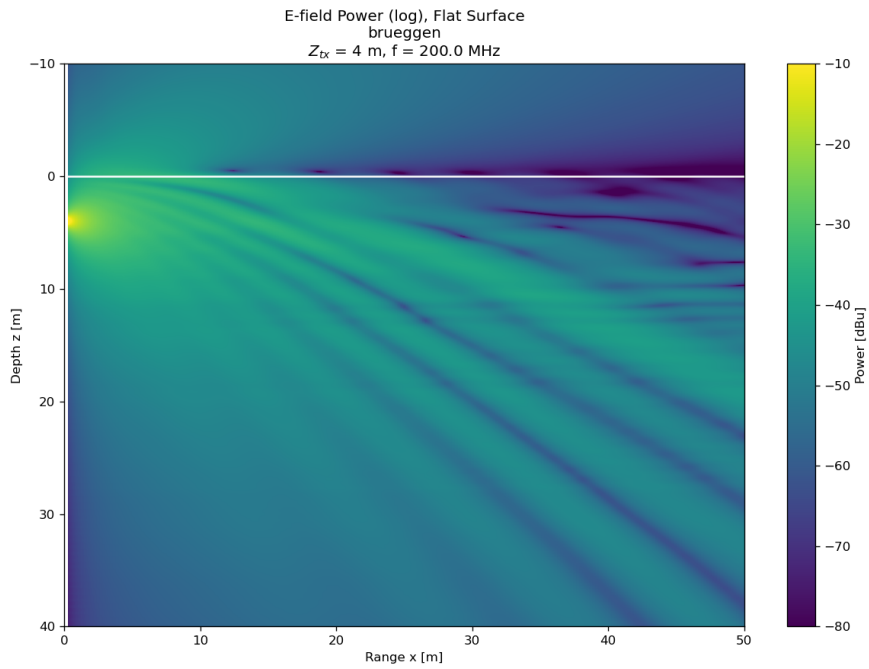
(a) Rough Surface $z_{DEM}(x)$ (b) 1D refractive index $n(z)$ (c) 2D refractive index $n(x, z)$ Brueggen (rough surface)

emission. The change in the RF emission between the cases of a flat and rough surface, can be more clearly see by seeing the ‘gain’ G of the RF power in the ice in the case of the ‘rough’ surface P_{rough} relative to the flat surface case P_{flat} . The gain is here defined as the ratio between P_{rough} and P_{flat} in logarithmic space and is displayed in decibel ‘dB’ units:

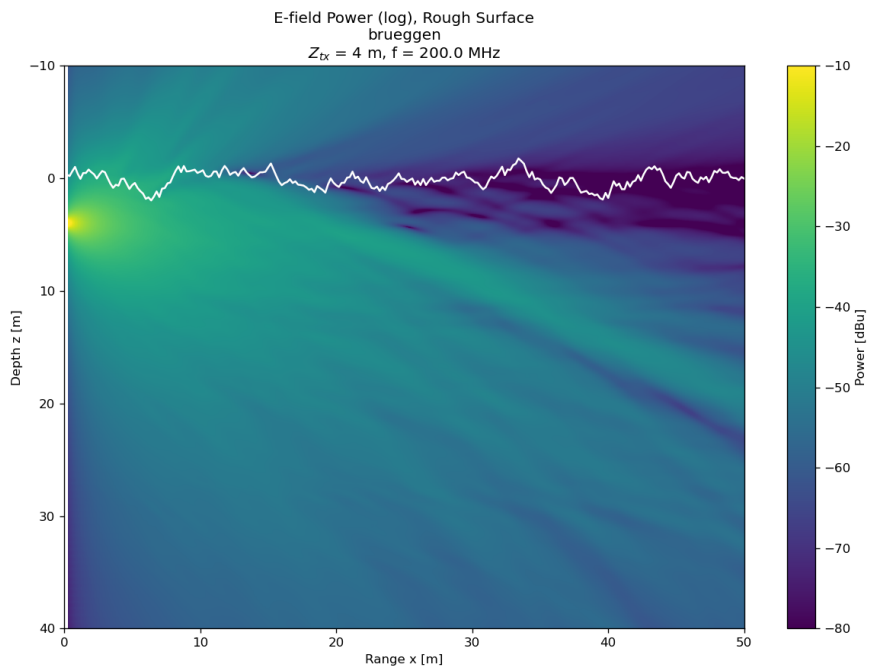
$$G = 10 \log_{10} \left(\frac{P_{rough}}{P_{flat}} \right). \quad (\text{F.2})$$

The gain as a function of depth and range is shown in a heat map shown in Fig. F.3. It can be seen that the refraction bands are smoothed out by the rough surface geometry, as the ‘hot bands’ (with $G \sim 30$ dB) in the gain plot correspond to the dark regions in Fig. F.2a, while the cold bands correspond to the bright refracted bands in Fig. F.2a. Other interesting effects can be seen when the gain map is zoomed in to the upper 5 m of the surface in Fig. F.4a. Here there are clearly identifiable ‘hot spots’, localized circular regions of $G \sim 30$ dB, with a radius $r < 1$ m which appear within $0 \text{ m} < z < 2 \text{ m}$. Notably this is within the range of the maximum surface fluctuation. Co-currently, the region below shows cold spots within $-2 \text{ m} < 0 < 0 \text{ m}$, which appear at similar ranges to the aforementioned cold spots. Fig. F.4b shows RF emission through the same surface geometry when the transmitter TX is placed at a lower depth of $z_{tx} = 22 \text{ m}$. Here the ‘hot’ and ‘cold’ spots are apparent but have moved laterally, away from the range of the transmitter. These hot and cold spots are likely caused by changes in RF interference caused by the change in the surface topography relative to the flat surface.

The significant changes in the modeled RF emission close to the surface 30 dB indicated that surface roughness may be an important effect to consider in the case of cross-borehole RF transmission in realistic ice environments. This effect is worth continued investigation.



(a) The E field power of Brueggen in space, with a flat surface



(b) The E field power of Brueggen in space, with a rough surface

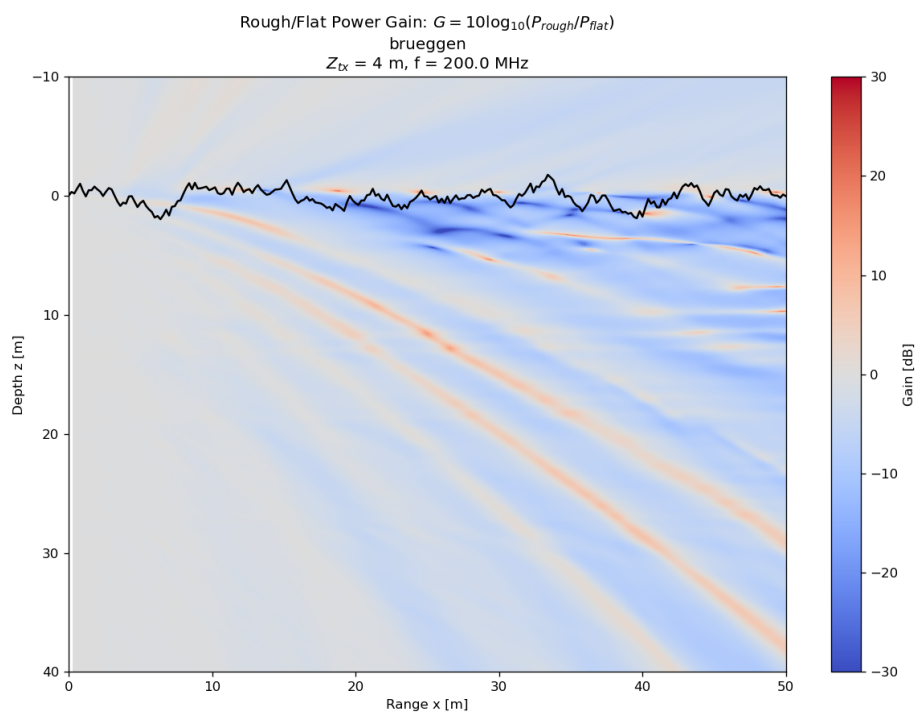


Figure F.3: The gain of the RF emission for a 'rough surface' scenario for the Brueggen glacier relative to the 'flat surface' case.

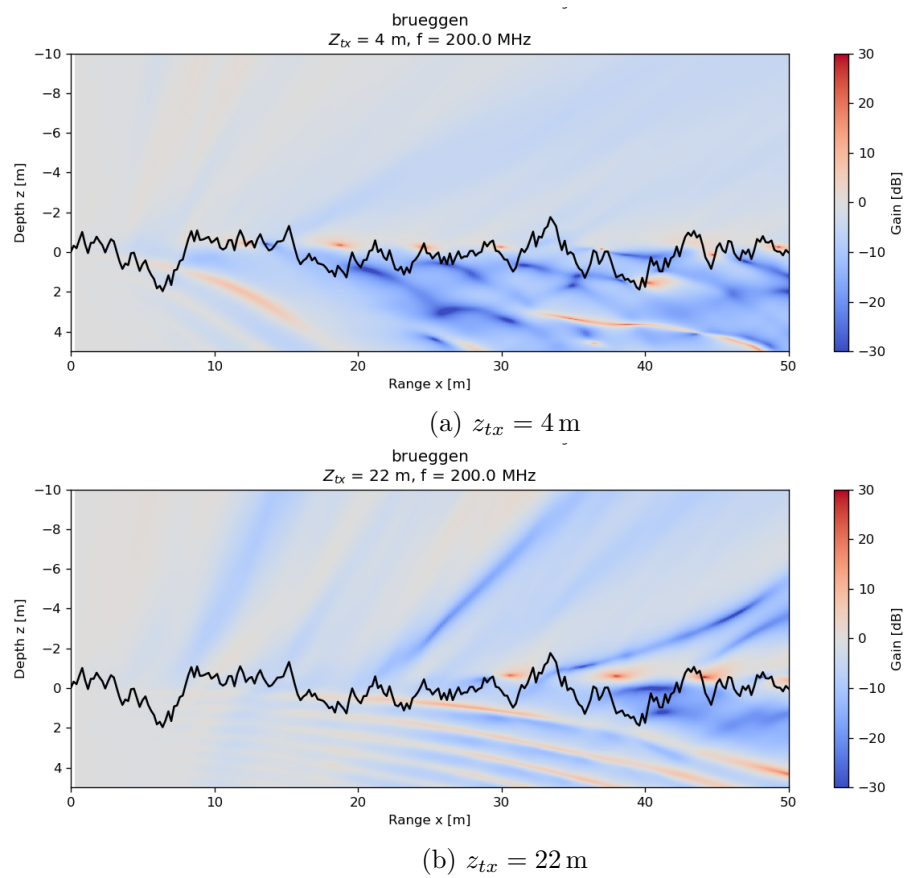


Figure F.4: The gain of the RF emission for a rough surface relative to a flat surface. The upper 5 m is displayed, with the upper plot showing the TX at a shallower depth $z_{TX} = 4$ m (F.4a) and the lower plot showing the TX at a deeper depth $z_{TX} = 22$ m (F.4b).